Impurity Transport and Radiation at the Stellarator Wendelstein 7-X

Inauguraldissertation

zur

Erlangung des akademischen Grades eines
Doktors der Naturwissenschaften
(Dr. rer. Nat.)

der

Mathematisch-Naturwissenschaftlichen Fakultät

der

Universität Greifswald

vorgelegt von
Philipp Scholl, geb.
Hacker
geboren am 15.06.1994
in Demmin

Greifswald, 05.03.2024

Dekan	Prof. Dr. Gerald Kerth
1. Gutachter	Prof. Dr. Thomas Klinger
2. Gutachter	
Tag der Promotion:	

The work may be hard, and the discipline severe; but the interest never fails, and great is the privilege of achievement.

(John Strutt, 3rd Baron Rayleigh)

for my family

Zusammenfassung

Strahlungsverlusts im Rahmen der Leistungsabfuhr ist für den Betrieb bestehender und die Entwicklung künftiger Fusionsreaktoren ist von großer Bedeutung. Die gezielte Verunreinigung mit Fokus auf den Ablöseprozess für die Abfuhr von Wärmeenergie und Schutz der Maschine ist von großem wissenschaftlichen Interesse. Eine zuverlässige und stabile kontrollierte Strahlungskühlung im magnetisch eingeschlossenen Bereich, im Plasmarand und im Divertor mit Anteilen der Strahlungsleistung von $\geq 95\%$ ist daher notwendig. Während OP1.2b wurde am Stellarator W7-X ein Rückkopplungssystem des Bolometers mit Echtzeit-Funktion für die Gasinjektion von Verunreinigungen mit niedriger Kernladungszahl entworfen und implementiert. Damit wurde ein stabiles Wasserstoffplasma mit kontrollierter Strahlungskühlung durch Helium bei $f_{\text{rad}} \geq 85\%$ erreicht. Eine Verringerung der Wärmebelastung des Targets um mindestens den Faktor zwei wurde gleichzeitig gemessen, während die Ablösung der Strahlung aus C^{3+}-Ionisationen bereits für $f_{\text{rad}} \sim 50\%$ sichtbar war. Ein Satz von mindestens drei Sichtlinien wurde als Proxy für schnelle Extrapolationen der Strahlungsverluste validiert.
Die Erkundung des entsprechenden Parameterraums ergab keine Korrelationen für Experimente mit Rückkopplung bei Verunreinigungen mit niedrigem Z. Gaseinlässe von moderater Stärke und Länge waren im Allgemeinen zuverlässig in der Lage Strahlungskühlung ohne terminale Plasmastörungen zu bewirken. Rudimentäre Modelle für diesen Injektionsprozess sind in der Lage, beispielhafte Strahlungsmessungen von Rückkopplungsexperimenten darzustellen. Detektoren, welche die Separatrix- und Plasmarand-Region betrachten, erwiesen sich als am brauchbarsten für diesen Ansatz. Eine Auswahl von drei-sieben vertikalen und/oder horizontalen Bolometerkanälen erreichen eine Vorhersagegenauigkeit von $\geq 85\%$ im Vergleich zum vollständigen System. STRAHL wurde in Kombination und zum Vergleich mit experimentellen Daten aus Rückkopplungsszenarien. Verunreinigungen durch Kohlenstoff stellen hier den größten Beitrag zum Emissionsgrad am

Plasmarand, während die Verringerung der Diffusivität, der Elektronentemperatur und -dichte um die Separatrix zu Experiment-ähnlichen Strahlungsprofilen führte. Eine Verschiebung von außerhalb nach innerhalb der Separatrix war für $f_{\text{rad}} \to 1$ zu beobachten.
Die Zuverlässigkeit eines optimierten Minimum Fisher Tomographie Algorithmus in Kombination mit dem W7-X-Bolometersystem wurde durch rigorose Störungstests der Geometrie nachgewiesen. Ein ~~groß angelegter~~ Benchmark hat gezeigt, dass es einen idealen Satz von k_{ani} für eine gegebene Emissivitätsverteilung gibt. In der Transmissionsmatrix $\mathbf{T}$ wurde eine intrinsische Asymmetrie in Richtung des oberen SOL- und Separatrixbereichs festgestellt. Variationen des Gewichtungsfaktors haben gezeigt, dass $k \leqslant 1$ in der Rekonstruktion gut mit lokalisierten bzw. glatten Strahlungsstrukturen korreliert. Die Auswertung von künstlichen Phantombildern mit zweidimensionalen Qualitätskoeffizienten zeigte eine signifikante Diskrepanz zwischen diesen und χ^2. Bei den künstlichen Strahlungsbildern unterschätzten die errechneten P_{rad} konsequent die tatsächliche, darin enthaltene Gesamtstrahlungsleistung.

Abstract

The importance of radiative power exhaust towards the operation of existing and the development of future fusion reactors is well-understood. Exploration of deliberately impurity seeded and feedback controlled scenarios with focus on detachment physics for heat energy dissipation and machine safety is of great interest. Reliable and stable controlled radiative cooling in the confined region, in the SOL and divertor with radiation power fractions of $f_{\mathrm{rad}} \geq 95\%$ is therefore necessary.
During OP1.2b at the stellarator W7-X, a real-time bolometer radiation feedback system for thermal gas injection of low-Z impurities has been designed and implemented. It achieved stable hydrogen plasma with controlled helium radiative edge cooling at $f_{\mathrm{rad}} \geq 85\%$. Here, reduction of target heat loads of at least a factor of two was measured, while detachment of C^{3+} ionization radiation was visible already for $f_{\mathrm{rad}} \sim 50\%$. A limited set of at least three lines of sight was validated as a proxy for fast radiation power loss extrapolations.
Exploration of the corresponding parameter space did not present correlations for low-Z impurity seeded feedback experiments. It was established however that moderately scaled gas puffs generally and reliably performed edge cooling without terminal plasma perturbation. Rudimentary models for this injection process have been found to be capable of representing exemplary radiation measurements of feedback activations. Detectors viewing the separatrix and SOL region presented to be most viable for *a priori* real-time bolometer feedback configurations. A robust selection of three-seven vertical and/or horizontal bolometer camera channels can be provided that achieves $\geq 85\%$ prediction accuracy when compared to the full data set. STRAHL was used in combination with experimental data from feedback scenarios and input parameters modelled for comparison purposes. Carbon impurities were found to be the dominant contributor to SOL emissivity, while reduction of diffusivity, electron temperature and density around the

separatrix provided radiation profiles similar to experimental findings, seeing an inward shift from outside to inside the separatrix for $f_{\mathrm{rad}} \to 1$.
Significant robustness and reliability for a radially dependent anisotropy weighting Minimum Fisher regularization algorithm in combination with the W7-X bolometer system have been established through rigorous geometry perturbation testing. A large scale benchmark thereof has suggested the existence of an ideal set of k_{ani} for a given emissivity distribution. An intrinsic bias towards the upper SOL and separatrix area in the transmissivity matrix $\mathbf{T}$ was found. Limited interval weighting factor variations have shown $k \lesseqgtr 1$ to correspond well to localised or smooth radiation structures in reconstruction, respectively. Evaluation of phantom images with two-dimensional quality coefficients demonstrated misalignment between those and χ^2. For the artificial brightness profiles, presented P_{rad} consistently underestimated the actual, total power contained in the phantom.

to the very end ...

Acknowledgements

This thesis to a large part is the result not only of my own work but of the collaboration of many people. I could not have succeeded with this project without the support and effort that every one of them invested.

This work was not possible without the help of many people. Fist and foremost, I would like to thank my supervisor Prof. Dr. Thomas Klinger, research group leader and mentor Dr. Felix Reimold and Dr. Daihong Zhang for their unending patience and enlightening guidance throughout the many years.

My gratitude and best wishes goes to all the scientist and colleagues contributing now, in the past and the far future to the endeavour that is the fusion plasma experiment Wendelstein 7-X. Back before attending university I only dreamt of working with the stellarator myself and contributing a meaningful part to its advancement.

Most importantly, there is a small group of people that made this possible in the first place and supported me every step of the way. From the bottom of my heart, my sincerest and deepest love to all of you - my wife, Stella, for sharing the burden more than I would have ever wanted and my parents, for always holding me up and on whose shoulders I stand tall and proud.

This work has been carried out within the framework of the EUROfusion Consortium and has received funding from the Euratom research and training programme 2014-2018 and 2019-2020 under grant agreement No 633053. The views and opinions expressed herein do not necessarily reflect those of the European Commission.

Contents

Introduction

In light of the depletion of conventional, natural and fossil fuels for energy production, as well as their negative impact of their consumption on the environment, renewable, clean - virtually emissionless - and readily available alternatives are direly called for. Despite its, for now more than 70 years persisting technical and economical challenges, magnetically confined plasma nuclear fusion is a prime candidate for such and has the potential to be the final answer to issues of ongoing climate change, the associated accelerated growth in energy consumption, costs and the discrepancy of global resource distribution[1, 2].

1.1. Nuclear Fusion

Nuclear fusion is the process of two lighter atoms or nuclei interacting and forming a heavier element. This phenomenon has been thoroughly studied since its discovery in the early 20th century on our solar systems central star *sol*[3]. Ironically, initial research around nuclear fusion was based on weapons development surrounding the *Manhattan project*[I] *thermonuclear bombs* and later iterated upon by scientist in the United Kingdom and finally brought to a first concept individually in 1950/51 by Lyman Spitzer[II] in

[I] a program of research and development during WWII to produce nuclear weapons, led by the United States in collaboration with the United Kingdom, resulting in two bombs dropped on Japan

[II] Lyman Spitzer, Jr. * Jun. 26, 1914 Toledo; † Mar. 31, 1997 Princeton

the USA, as well as Andrei Sacharow[III] and Igor Tamm[IV] in the USSR. All postulated magnetic plasma confinement as way to a thermonuclear reactor, however with different approaches, i.e. the *stellarator* and *tokamak*. Since then, nuclear fusion has been experimentally demonstrated in laboratory environments and hence associated with the fourth state of matter, *plasma*[4]. Fusion processes involving light nuclei, i.e. hydrogen or helium isotopes are energetically most advantageous, as they produce the most energy per nucleus mass. In the case of confined, high-temperature plasma applications, such large kinetic energies and therefore velocities are necessary to overcome the electrostatic Coulomb force repulsion between the positively charged nuclei, reducing the distance so that the *strong nuclear force* dominates and fusion reactions are induced. Rate coefficients $\langle \sigma v \rangle$ towards the total yield $Q = P_{\text{fus}}/P_{\text{ext}}$, with P_{fus} the power from fusion reactions and P_{ext} the input, are convolutions of kinematic cross-sections and Maxwell-Boltzmann distributions. Of those, only a Deuterium-Tritium interaction has a large enough contribution at energies $\leq$64 keV due to an intermittent resonance in a volatile ${}^{5}_{2}\text{He}$[5].

$$ {}^{2}_{1}\text{D} + {}^{3}_{1}\text{T} \longrightarrow {}^{5}_{2}\text{He}^{*} \longrightarrow {}^{4}_{2}\text{He}\,(3.5\,\text{MeV}) + {}^{1}_{0}n\,(14.1\,\text{MeV}) \tag{1.1} $$

Resulting kinetic energies of the products are noted accordingly. Plasma temperatures of 20 keV have been achieved regularly and by a large range of devices, underlining the superiority of DT fusion in this regard. The vast energy gain on the right-hand-side in equation (1.1), particularly the fast neutrons can be used to heat a water repository in a future power plant, similar to a conventional nuclear fission reactor. Additionally, only minor secondary radioactive waste from neutron activation is expected from such a device, alleviating the issue of dismantlement and final storage of other nuclear machines. Deuterium has a sufficient natural abundance and hence can be distilled effectively from water, while Tritium does not but can be *bred* using the penetrating neutrons and a supplementary Lithium blanket around the vessel.

This thesis is concerned with the properties of radiation in the stellarator *Wendelstein-7X* (W7-X), particularly from intrinsic and extrinsic impurities,

[III] Andréj Dmítrievič Sácharov, * May 21, 1921 Moscow; † Dec. 14, 1989
[IV] Igor' Evgen'evič Tamm, * Jun. 26, 1895 Wladiwostok; † Apr. 12, 1971 Moscow

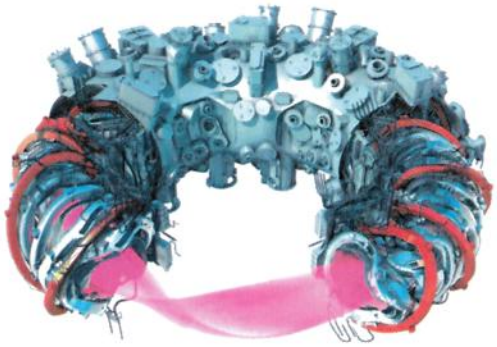

Figure 1.1.: Stellarator Wendelstein 7-X: Cut-away rendering of the outer vessel, superconducting magnetic coils, cooling and supporting structure. The translucent red band is the plasma tube (last closed magnetic flux surfaces). ©IPP

their transport and effects on the overall plasma performance. After an introduction to the machine, presented results will be centred around the core diagnostic responsible for measuring radiation at W7-X: the *multicamera, metal resistor bolometer*. The next sections will introduce the core concepts relating to the investigations performed in this work.

1.2. Wendelstein 7-X

Wendelstein 7-X is the latest iteration in a long line of stellarator experiments conducted by scientists at the Max-Planck Institute for Plasma Physics, beginning in the 1950s. The first W1-A stellarator went into operation in 1960 at the Max-Planck Institute for Physics and Astrophysics, providing a foundation for the continuing development of which this device is the culmination.
Stellarators generate the necessary rotational transform, the twist of the magnetic field, (majorly) by external coils. Consequently, the stellarator magnetic field is deliberately configured using said coils and its plasma essentially current-less and more stable compared to a tokamak. Wendelstein 7-X is designed to be modular, i.e. have a discrete symmetry that enables entire subsections to be replaced or exchanged. The iterative optimisation process towards such a modular device was shaped to satisfy multiple criteria,

including small magnetic islands, good plasma equilibrium and magneto-hydrodynamic (MHD) stability, reduced neoclassical transport, minimized bootstrap current and fast particle confinement. Its modular designed, five-fold symmetric superconducting magnetic field coils encompass the whole machine. The coil system consists of 70 superconducting magnets of seven different shapes, 50 non-planar coils producing the twisted magnetic field and 20 planar coils for increased flexibility in magnetic configuration space - it can be seen in figure 1.1[6–9].

The W7-X stellarator is the largest of its kind, with a major and minor radius of 5.5 m and 0.53 m (depending on magnetic coil currents) respectively, volume of 30 m^3, 3 T maximum magnetic field strength, heating power of 14 MW and expected plasma temperatures of up to 130 MK. W7-X has performed three successful experimental campaigns since its first plasma in 2015. After multiple upgrades, the machine has demonstrated improved, longer confinement and increased overall power, with the ultimate goal being a discharge duration of 30 min at 10 MW of external heating, demonstrating a capability essential to a future fusion power plant: continuous operation[10].

Development of this stellarator reactor line was defined by the qualification of a viable divertor concept. Divertors - interfaces deliberately contacting and *diverting* (interacting) with the hot plasma - in stellarators cannot be toroidally symmetric. The cross-section of W7-X varies strongly from triangular to bean-shape and exhibits natural magnetic islands, i.e. smaller, from the core separated and confined flux tubes which do not extend far toroidally. Hence, so-called *island divertors* are placed at the edge where the rotational transform has a resonance close to unity. This field line pitch ι is defined as the number of poloidal transits per single toroidal transit of a field line on a toroidal flux surface. Assuming toroidally nested magnetic flux surfaces, the rotational transform is given by $\iota/2\pi = \mathrm{d}\psi/\mathrm{d}\Phi$, with ψ the poloidal magnetic flux, and Φ the toroidal magnetic flux. The tube of the last closed flux surface (LCFS) and cuts through the magnetic field structure for characteristic points can be found in figure 1.2. On each magnetic field period, one pair of island divertor modules is installed where the cross-section of the magnetic field is predominately bean-shaped. Magnetic islands intersect these targets, providing a well-defined flow of particles from the plasma *scrape-off layer* (SOL) to the wall and decoupling the core plasma region in the process. Divertors therefore have to withstand a heat flux of up to 10 MW/m^2. Wendelstein 7-X was not yet equipped with water-cooling and

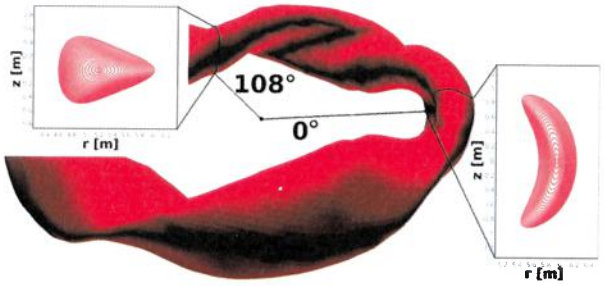

Figure 1.2.: Flux tube of the last closed flux surface around the W7-X torus and cross-sections in the triangle- (left) and bean-shaped (right)plane. At 108° toroidally, the bolometer camera system is located.

plasma contact points are only inertially cooled in experiments discussed for this thesis[9, 11].

1.3. Plasma Physics

At the given temperatures, matter only exists as plasma, an ionized gas where atoms are fully ionized and interact with electric and magnetic fields. Hence, fusion energy research is the study of high-temperature plasma physics in large devices with strong magnets. Challenges here are the long-time confinement of particles and exhaust of thermal energy, while a lower limit for a self-sustaining or -heating fusion plasma $Q > 1$ is given by the *triple product* or *Lawson criterion*. Introduction of non-hydrogenic species into the plasma via deliberate gas puffing, solid-state seeding, sputtering of wall material or intrinsic impurities has to be taking into account due to its parasitic and diluting effect on the system:

$$n_{\mathrm{i}}\tau_{\mathrm{E}} \geq \frac{12 f_{\mathrm{tot}}}{\langle \sigma_{\mathrm{DT}} v \rangle f_{\mathrm{H}}^2 E_\alpha - 4 L_{\mathrm{Z}}(T)} T \tag{1.2}$$

with n_{x} the number densities and T the equilibrated temperatures of electrons, ions and atomic hydrogen respectively, $f_{\mathrm{H}} = n_{\mathrm{H}}/n_{\mathrm{e}}$ the hydrogens fractional abundance, $f_{\mathrm{tot}} = \sum_i n_{\mathrm{i}}/n_{\mathrm{e}}$ the ion-electron dilution, E_α kinetic alpha particle energy and L_{Z} the radiative loss function. Plasma conditions described by satisfying the Lawson criterion in equation (1.2) require a strong magnetic confinement, trapping charged particles in the magnetic

field using the Lorentz force to restrict their motion perpendicular to its field and travelling in a *gyro-motion* on helical trajectories along those lines. In stellarators, additional drift effects are compensated by the secondary poloidal magnetic field from the sophisticated magnetic coil setup[12, 13]. In current and future plasma fusion devices, large heat loads on plasma facing components are a challenge and topics surrounding it of great scientific interest, as steady-state operation at large powers is central to the ultimate goal of a nuclear fusion power plant. The expected huge power flux onto divertors for such a scenario of continuous operation are significantly larger than the material limits. Distribution of this energy and thermal load through electromagnetic radiation into the full 4π solid angle and onto the entire vessel wall is one possible solution to this problem. *Bremsstrahlung* P_{brems} of accelerating charged particles on field lines and line radiation from ionisation and excitation processes P_{line} contribute to the *cooling* of the core. Steady-state, the plasma confinement power balance can be written as $P_\alpha + P_{\text{h}} = P_{\text{n}} + P_{\text{rad}}^{\text{core}} + P_{\text{SOL}}$, with P_α the alpha particle *heating* of the plasma, P_{h} the external input, P_{SOL} the total power in the SOL and $P_{\text{rad}}^{\text{core}} = P_{\text{brems}} + P_{\text{line}}$. Introduction or seeding of extrinsic, high-Z impurities into the core, which radiate strongest in the hotter confinement center can be used to increase the latter and hence reduce the power that enters the SOL[14–16]. The impact of deliberate plasma pollution however has drawbacks. Dilution is increased because of their greater number of charge states and are likely to accumulate in the core due to transport dynamics. Furthermore, oversaturation with impurities can lead to plasma termination, radiative collapses or disruptions. Varying operational and machine conditions, as well as impurity combinations inside the plasma and their different behaviour under those circumstances make the experimental evaluation particularly difficult[17]. This topic is center of ongoing investigations and ultimately motivation for the methodology and application developed over the course of this thesis. In the hypothetical first plasma fusion power plant prototype DEMO, it is expected that $0.7P_{\text{h}}$ is radiatively exhausted from the core and the remainder has to be further reduced through radiation in the SOL, finding at least a radiation fraction $f_{\text{rad}} = P_{\text{rad}}/P_{\text{h}} \geq 0.95$. *Radiation in the divertor* has several benefits, like a reduced total heat flux onto and broadening of the contact area with the target, decreasing chemical and physical sputtering of wall material and additional reaction loss channels with neutral particles. At the lower densities and temperatures outside the

LCFS, low-Z impurities can be used to control the radiation here such that fuel dilution, impurity retention and radiative saturation of the divertor are of adequate levels[18–20].

1.3.1. Transport

Transport plays a very important role in the performance of fusion devices. They transfer energy, mass and charge spatially via collisions between particles or by flows, thermodynamically equilibrating the plasma. Commonly, plasma transport refers to the combination of classical, neoclassical and anomalous or turbulent processes. Turbulent transport dissipates energy through non-linear, chaotic flows, which are themselves usually generated by instabilities in the plasma, and is very effective in transporting energy and mass.

Classical Transport

Classical transport considers diffusive collisions between ions, eventually leading to a net particle loss from the confinement to the SOL and vessel walls. Due to the presence of charged particles, plasma diffusion significantly differs from diffusion in gases or liquids. The interaction between the positive and negative particles results in ambipolar diffusion with a diffusion coefficient that is dissimilar to that of either electron or ion species separately. The rate of diffusion scales with $1/B^2$, implying that confinement times can be greatly improved with small increases in field strength. Such collisions change the center of the particles gyrating motion, with displacements the size the Larmor radius r_L. Same species Coulomb collisions yield no net transport but may contribute to energy transfer and heat flux. With impurities, friction effects between all species need to be taken into account. Ion-impurity collisions dominate the impurity transport due the large collision frequency ν, causing convection. The impurities diamagnetic velocity v_{dia} is directed into the same direction as the diamagnetic velocity of the hydrogen ions. However, due to the charge dependence of v_{dia} there exists a velocity difference between ions and impurities. The resulting friction force is amplified by the respective ion charge of the impurities. Due to the electrostatic repulsion, this translates into an inward convection of impurities and an outward convection of hydrogen. Radial temperature gradients however may change the convection proportionality due to the decrease in friction

at larger relative velocities. Fluid models find an extra term $\propto \nabla T$ related to Coulomb friction, ultimately causing an outward flux of impurities. For an impurity of charge q, the total flux $\vec{\Gamma}_q$ including diffusive and convective transport can be written as

$$\vec{\Gamma}_q = \frac{r_{L,q}^2 \nu_{q,H}}{2} \left(-\nabla n_q + n_q q \left(\frac{\nabla n}{n} - \frac{\nabla T}{2T} \right) \right) .$$

Neoclassical Transport

In practice, the rates suggested by classical diffusion have not been found in real world machines, where a host of previously unknown plasma instabilities caused the particles to leave confinement at rates closer to B, as had been seen in Bohm diffusion. The failure of classical diffusion to predict real-world plasma behaviour led to a deeper understanding of the diffusion process, known as neoclassical transport.

The *neoclassical transport model* provides a model for the transport of particles, momentum, and heat due to Coulomb collisions in confined plasmas in complex magnetic geometries, assuming that the plasma is in an equilibrated state, i.e. not including fluctuations. The classical model is extended by the incorporation of geometrical effects, which lead to complex particle orbits and drifts that were ignored in the latter.

Writing the Boltzmann equation with the particle distribution function $f_x = f_x(\vec{x}, \vec{v}, t)$ for particle species x, the *Fokker-Planck*[I] expression for a collisionality operator and an additional source term S_x gives a kinetic equation for neoclassical transport from which the respective moments can be derived[21].

$$\frac{\partial f_x}{\partial t} + \vec{v} \nabla f_x + \frac{Z_x e}{m_x} \left(\vec{E} + \vec{v} \times \vec{B} \right) \nabla_v f_x = - \frac{\partial}{\partial v_i} \left(f_x \langle \Delta v_i \rangle \right) + \frac{1}{2} \frac{\partial^2}{\partial v_i \partial v_j} \left(f_x \langle \Delta v_i \Delta v_j \rangle \right) + S_x \qquad (1.3)$$

In a collisionless regime, this reduces to the *Vlasov equation*, describing temporal evolution of f_x for plasma of charged particles only coupled by

[I] Adriaan Daniël Fokker; * Aug 17, 1887 Buitenzorg; †Sep. 24 1972 Beekbergen

long-range interaction such as Coulomb interaction[22]. Equation 1.3 satisfies momentum, particle and energy conservation and assumes that collisions only have small random effects on the particle velocity and are sufficiently frequent for the resulting particle trajectory to be described also as random. Neoclassical transport theory provides a set of equations for the temporal evolution of a species moments. It accounts for all particle motion associated with toroidal geometry, specifically ∇B and curvature drifts, passing and trapped particles, i.e. *banana orbits*. The theory is valid for all collisionality regimes, and includes effects due to resistivity and viscosity. An important prediction of the theory is the *bootstrap current*[23–25].
In a neoclassical fluid picture, diamagnetic flows drive parallel flows, satisfying continuity equation. Similarly to classical transport, convection also may be written with the diamagnetic drift and the related friction between particles entering into the resulting drift velocity. Hence, a neoclassical radial flux for impurity of charge q for the types of transport orbits $O = \{\text{classic}, \text{banana}, \text{Pfirsch-Schlüter}\}$ is given by:

$$\vec{\Gamma}_{\mathrm{q}} = \sum_{x}^{O} D_{\mathrm{x}} \left(-\nabla n_{\mathrm{q}} + n_{\mathrm{q}} q \left[\frac{\nabla n}{n} - H_{\mathrm{x}} \frac{\nabla T}{T} \right] \right) = -D_{\mathrm{neo}} \nabla n_{\mathrm{q}} + v_{\mathrm{neo}} n_{\mathrm{q}} \, .$$

In any case, the convection is proportional to the charge of the impurity and its contribution consists of one term into the direction of the density gradient and one opposite depending on the parameter H_{x}. The latter is given through plasma parameters, geometry, and the mass ratio between collision partners. For similarly oriented temperature and density gradients, H_{x} is positive and an effect of temperature screening is observed. Convection here is proportional to the charge of the impurity, such that effects due to the neoclassical drifts are enhanced for higher charge states. Realistically, multiple impurity species lead to a critical friction equilibrium between them towards their transport fluxes[26, 27].

Anomalous Transport

Research often finds that transport exceeds neoclassical expectations by an order of magnitude or more. Differences between measurement and the above prediction are called *anomalous* or turbulent transport, generally assumed to be generated by non-linear effects driven by micro-instabilities. An

important argument for turbulence significantly contributing to the total transport to this degree is its scaling with heating power and machine size. In contradiction to neo-/classical predictive scaling laws, confinement decreases with temperature, potentially explained by greater turbulence and transport at higher T. Furthermore, deliberate suppression of turbulent effects, either actively or passively, sees a reduction in transport, supporting the previous assumption. The general assumption is that anomalous transport is the consequence of microscopic instabilities, caused by steep density, temperature, and pressure gradients, e.g. ion and electron temperature gradient instabilities (ITG, ETG)[28, 29]. Similarly, an integrated impurity flux can simply be written as the sum of all previous phenomena:

$$\vec{\Gamma}_q = -\left(D_{neo,q} + D_{an,q}\right)\nabla n_q + \left(v_{neo,q} + v_{an,q}\right) n_q = -D_q \nabla n_q + v_q n_q \,.$$

Usually, dominant turbulent transport $D_{neo} \ll D_{an}$ so that neoclassical diffusion may be neglected. Only when turbulent transport is suppressed or small, neoclassical diffusion becomes important. For very large q or high-Z impurities, charge dependent terms inflate the neoclassical convection so that it is noticeable outside those cases. Recent studies have identified plasma rotation to cause asymmetries of impurities on flux surfaces and also improving non-turbulent transport. Strongly rotating plasmas redistribute particles with centrifugal forces, making neoclassical transport a significant contributor though turbulent transport is present. If neoclassical transport is important, density gradients of high-Z elements become large due to the charge dependence, leading to strongly peaked density profiles of high-Z elements in the core[30, 31].

1.3.2. Plasma Radiation

Electromagnetic radiation from plasma particles is a core aspect of nuclear fusion research and its understanding more so crucial to the development of a future power plant. As noted above, P_{rad} plays a key role in the exhaust of power from the core and SOL, dissipating large amounts of energy into a larger surface area and protecting plasma facing components from damaging heat loads. The process of radiative power loss is intrinsic to magnetically confined gaseous discharges, as the most important contribution

to the emissive exhaust channel is *Bremsstrahlung* P_{brems}. Acceleration of the individual charged species in a plasma along field lines, under heating or due to collisions, i.e. Coulomb scattering will produce electromagnetic radiation.

$$P_{\text{brems}} = c_{\text{b}} n_{\text{e}} \sqrt{T_{\text{e}}} \sum_i n_{\text{i}} \left\langle \overline{Z}_{\text{i}} \right\rangle^2 = c_{\text{b}} n_{\text{e}}^2 \sqrt{T_{\text{e}}} Z_{\text{eff}} \tag{1.4}$$

A Bremsstrahlung constant is given by $c_{\text{b}} = 5 \times 10^{-43}\,\text{MWm}^3/\sqrt{\text{keV}}$[32]. This expression trivially contracts for purely hydrogenic Deuterium-Tritium plasma, with the effective atomic number $Z_{\text{eff}} = 1$ because of the average charge state of particle i $\left\langle \overline{Z}_{\text{i}} \right\rangle = 1$ and $n_{\text{D}} + n_{\text{T}} = \sum_{\text{i}} \left\langle \overline{Z}_{\text{i}} \right\rangle^2 = n_{\text{i}}$. In practice however, $Z_{\text{eff}} \neq 1$ due to the contamination with intrinsic or deliberate seeding of extrinsic impurities. In a simplified, quantum-mechanical approach, the Bremsstrahlung emissivity $p_{\text{brems}}(v, \nu)$ which is the power emitted per solid angle in photon velocity space times the photon frequency, summed over all photon polarizations can be given by equation (1.5). This is an approximate classical result, with a *Kramers-Gaunt* factor g_{ff} accounting for respective corrections - see *Kramers' opacity law*[I].

$$p_{\text{brems}}(v, \nu) = \frac{8\pi}{3^{3/2}} \frac{Z^2 \overline{e}^6 n_{\text{i}}}{c_0^3 m_{\text{e}}^2 v} g_{\text{ff}}(v, \nu) \tag{1.5}$$

This uses the scaled electronic charge $\overline{e} = e/\sqrt{4\pi\varepsilon_0}$.[33]
Additionally, emissive losses also may occur through synchrotron, line and recombination radiation. The prior is also called *magnetobremstrahlung* and comes from acceleration effects perpendicular to the kinematic $\vec{v}$ of particles with relativistic velocities. *Synchrotron* radiation is, similar to normal Bremsstrahlung a gyromagnetic radiation. Its contribution is expected to be negligible in the current status of operations at W7-X. In a purely hydrogenic plasma, line and recombination radiation do not play an essential role except for the significantly cooler plasma edge and SOL, where all ions are fully ionized while the central plasma is too hot for recombination. This obviously changes again under the influence of pollution by nuclei of bigger charge number[34].

[I] describing the opacity of a medium, assuming it is dominated by bound-free (light during ionization of a bound electron) or free-free (light when scattering a free ion) absorption

1.3.3. Impurities

Intrinsic Impurities

In the plasma fusion process produced helium must be removed in to reduce fuel dilution. Its confinement time is significantly larger than that of the plasma particles and the energy confinement time, because of an increased wall recycling and decreased divertor pumping and compression. However, fast helium nuclei are needed for additional heating effects of the plasma core until thermalization. In the case of the experiments examined in this thesis, thermal helium gas is deliberately injected or ejected from the walls in which it was implanted during wall conditioning and cleaning glow discharges[35–37].

More common intrinsic impurities like O, C or heavier elements of wall material are eroded from the walls by the impinging ions and accelerated in the plasma sheath electric field. Due to conservation of charge and the resulting ambipolar fluxes to the wall, electron and ion temperatures majorly define the erosion process. Large heat fluxes to the wall can lead to melting or sublimation wall material, potentially causing electric arcing or dust production as a secondary impurity source. Introduction of macroscopic particle in the process may lead to considerable increase in radiative power loss due to the large cascade of associated ionisation, excitation and charge exchange[38–40].

Extrinsic Impurities

Injection of low-Z impurities like He, Ne, S or Ar can be designed to control localized heat fluxes at the plasma edge by radiative cooling without disturbing the core plasma confinement. Applications therefore are being investigated and obligatory for a reactor grade device, since steady-state operation total heat loads scale faster with the machine size than its inner surface area. An estimated 95% of the fusion power from the plasma core has to be exhausted in the edge and SOL for wall protection purposes. In an exemplary case at the tokamak *ASDEX Upgrade*[I], radiative cooling is achieved for externally injected nitrogen concentrations in the range of 1%–3%.

[I] Axially Symmetric Divertor Experiment; divertor tokamak at the Max-Planck-Institute for Plasmaphysics, Garching that went into operation in 1991; second-largest fusion experiment after W7-X in Germany

in the plasma core.[41–45]

Experiments on earlier tokamak devices with wall elements of heavy metals have demonstrated that instead of a gradual increase of radiation, e.g. with increased heating, the losses can start to grow explosively when the density exceeds a certain critical level. This behaviour is caused by sudden accumulation of heavy, high-Z impurity particles in the plasma core. Conclusive engineering and physics research developments have led to changes in approach to wall materials and handling of discharge pollution as discussed previously. Nevertheless, even in the case of deliberate low-Z impurity seeding, the plasma behaviour does not necessarily obey simple laws. The radiating edge layer attached to the plasma boundary can become unstable when the plasma density is ramped up above a threshold value. Under some conditions, this manifests itself in a radial contraction of the plasma, preserving its poloidal and toroidal homogeneity. By such a *detachment* of the plasma from the vessel interface, a large fraction of the input power is lost through radiation from impurities a thin toroidally enclosing shell at the plasma edge and in the SOL. Detachment may terminate the discharge through disruption but can also lead to the formation of a quasi-stationary *detached plasma. Multi-Faceted Radiation From the Edge* (MARFE), toroidal strings of high density, high radiation plasma can occur at the high field side (HFS) of the device during detachment, spawning close to the divertors and near X-points[46]. Deliberate seeding of low- or medium-Z impurities like He, Ne, Si, Ar etc. can increase the f_{rad} in the edge and SOL to 95% without MARFEs or plasma detachment, while avoiding accumulation in the plasma core. A *radiating edge* can lead to, under definite condition impurity seeding, a reduction of anomalous heat and particle loss from the plasma, hence indicating that impurities are essential also to anomalous transport and corresponding micro-instabilities[47–49].

Neutral particle impurities enter the plasma through either intrinsic, i.e. erosion, initial contamination or plasma-wall interaction, or extrinsic, i.e. deliberate gas-puffing, pellet injection, laser-physical sputtering etc. processes. Radiation losses from all impurity charge states can be calculated for all ionisation stages Z as follows:

$$P_{\text{rad}} = \sum_{\text{Z}} n_{\text{e}} n_{\text{Z}} L_{\text{Z}} \ .$$

Here, L_{Z} the *cooling rate*, i.e. power lost from a unit volume for ~~one electron and ion~~. Two major processes contribute to the energy loss through electron-impurity interaction. On one hand, *line radiation* arises when the impurity is excited by electron impacts and relaxes spontaneously by radiating photons and cooling the plasma., On the other hand, an additional Bremsstrahlung term ~~due to electrostatic attraction of the electrons has to~~ be added. At the edge, line radiation dominates the emission from impurities, however Bremsstrahlung becomes more relevant in the core for increasing ionisation levels and therefore larger cross-sections. For example, the lower charge states of the intrinsic impurity carbon are excited at around 5–10 eV and radiate mostly in the SOL and plasma edge, while its higher ion stages with $E_{\text{exc}} \sim E_{\text{ion}} \gtrsim 300\,\text{eV}$ only yield radiation in the confinement volume[50].
In the plasma core, the impurity cooling rate is usually described in a *corona approximation*, where the processes of ionisation and recombination dominate the particle balances for different charge states and their densities are governed by the relations:

$$k^{\text{ion}}_{\text{Z-1}} n_{\text{Z-1}} + k^{\text{rec}}_{\text{Z+1}} n_{\text{Z+1}} = \left(k^{\text{ion}}_{\text{Z}} + k^{\text{rec}}_{\text{Z}}\right) n_{\text{Z}} \ .$$

Rate coefficients for ionisation and recombination are only a function T_{e} and given by k_{ion} and k_{rec} for the respective charge states.
At the plasma edge, low-Z impurity ions have enough time to diffuse into hot plasma regions through potentially very strong anomalous transport before ionizing into less intensely radiating higher charge states. Hence, transport processes increase cooling rates and make it less temperature sensitive compared to the corona approximation without transport. In the vicinity of intense localized impurity sources, e.g. diagnostic beams or gas valves, time-dependence and three-dimensionality of the impurity transport has to be accounted for. During their lifetime, individual ionisation stages move along the magnetic field and diffuse in the direction perpendicular to the field. While the diffusion area is small compared to he occupied flux surface, lifetime and rate coefficients constitute them as intense but localized sources for the neighbouring charge states, forming a set of nested shells evolving in time.

Radiating Edge Layer

As discussed before, a stable radiation edge layer is crucial towards the development of high performance fusion plasma in large reactors. Consider the stationary heat balance at the edge, i.e.homogeneous along the magnetic field:

$$P_{\mathrm{rad}} = \kappa_{\perp} \frac{\mathrm{d}^2 T}{\mathrm{d}r^2} \,, \tag{1.6}$$

with $\kappa_{\perp}$ the parallel heat conduction, r the distance from the LCFS and $T_{\mathrm{i}} = T_{\mathrm{e}} = T$[51]. Under several assumptions, i.e. $P_{\mathrm{rad}}(T) = P_{\mathrm{rad}} = \text{const.}$, $\kappa_{\perp}(\mathrm{d}T/\mathrm{d}r) = P_{\mathrm{h}}$ limited by the heating power in the core at the LCFS and a temperature profile decay in the SOL λ_{T} so that $\mathrm{d}T/\mathrm{d}r = T/\lambda_{\mathrm{T}}$ for $r = 0$, an analytical and stable solution to equation (1.6) and the separatrix temperature can be found:

$$T_{\mathrm{LCFS}} = \frac{\lambda_{\mathrm{T}}}{\kappa_{\perp}} \left(P_{\mathrm{rad}} \lambda_{\mathrm{T}} + \sqrt{P_{\mathrm{rad}}^2 \lambda_{\mathrm{T}}^2 + P_{\mathrm{h}}^2 - 2 P_{\mathrm{rad}} \kappa_{\perp} T_{\mathrm{max}}} \right) . \tag{1.7}$$

In 1.6, T_{max} is the temperature at the interface layer of SOL and plasma core. The maximum radiation level $\gamma_{\mathrm{rad}} = \Delta P_{\mathrm{rad}}/P_{\mathrm{h}}$, corresponding to a critical level of P_{rad} gives[51]:

$$\gamma_{\mathrm{rad}}^{\mathrm{max}} = 1 - \frac{\kappa_{\perp} T_{\mathrm{max}}}{P_{\mathrm{h}} \lambda_{\mathrm{T}}} + \sqrt{\left(\frac{\kappa_{\perp} T_{\mathrm{max}}}{P_{\mathrm{h}} \lambda_{\mathrm{T}}} \right)^2 - 1} \,. \tag{1.8}$$

Understanding the second term in equation (1.8) as a functional parameter, it is evident that going from Ohmic plasmas with low transport, small $\kappa_{\perp}$ and intrinsic carbon impurity for $T_{\mathrm{max}} \sim 60\,\mathrm{eV}$, to discharges with increased transport, large $\kappa_{\perp}$ and seeding of extrinsic neon at $T_{\mathrm{max}} \sim 200\,\mathrm{eV}$, the $\gamma_{\mathrm{rad}}^{\mathrm{max}}$ increases continuously[30, 52, 53].
Exceeding a critical P_{rad} inevitably leads to a steadily cooling plasma edge. For T_{LCFS} below the excitation energy of low-Z impurity ions of 5–10 eV, the radiating layer shrinks towards the plasma axis, while the heat flux density from the core increases because of the constriction of the plasma tube. Therefore, current density and ohmic heating in the core increase and resulting *plasma detachment* develops[51].

Quite limiter specific. Other relevant instabilities?

Instabilities

Regarding plasma instabilities due to impurities, it is important to note the difference between radiative and collisional perturbations. Instabilities can occur due to the impurity ionisation electron production, electron heat losses on impurity excitation and ionisation or Coulomb collision heat transfer from the hydrogen ions with impurities. Let $k = 2\pi/\lambda$ and λ the perturbations wave length, γ its spatial growth rate, $Q_{\mathrm{coll}} = 3\nu_{\mathrm{Z,i}} n_{\mathrm{Z}} (T_{\mathrm{i}} - T_{\mathrm{Z}})$ the Coulomb collision heat loss, $\kappa_{\mathrm{e/i}}^{\parallel}$ the electron heat conduction parallel to the magnetic field and $T_{\mathrm{e}} = T_{\mathrm{i}} = T$, $n = n_{\mathrm{e}} = n_{\mathrm{i}}$ on a magnetic flux surface. For a dominant electron cooling perturbation with variations $\Delta T_{\mathrm{e}} \gg \Delta T_{\mathrm{i}}$ one yields equation (1.9), while for opposite Coulomb ion cooling scenarios equation (1.10) applies[51].

not properly introduced or motivated

$$\gamma = \frac{n_{\mathrm{Z}}}{2}\left(\frac{L_{\mathrm{Z}}}{2T} - \frac{\mathrm{d}L_{\mathrm{Z}}}{\mathrm{d}T}\right) - \frac{k^2 \kappa_{\mathrm{e}}^{\parallel}}{2n} \tag{1.9}$$

→ discuss on a simpler cartoon level

$$\gamma = \frac{Q_{\mathrm{coll}}}{T} - \frac{k^2 \kappa_{\mathrm{i}}^{\parallel}}{2n} \tag{1.10}$$

Small reduction in plasma temperature lead to heat losses both from electrons through increasing radiation and Coulomb collisions of ions with impurities. In both cases, plasma heat conduction inhibits the growth of perturbations. Instabilities develop $\gamma \geq 0$ from spontaneous variations if with increasing density or impurity content the plasma heat losses exceed the critical level, described by the parameter $\eta = n_{\mathrm{Z}} n / k^2$. For electron radiation instabilities this yields[51]:

$$\eta_{\mathrm{rad}} = \frac{2\kappa_{\mathrm{e}}^{\parallel}}{L_{\mathrm{Z}}/T - 2\mathrm{d}L_{\mathrm{Z}}/\mathrm{d}T} ,$$

while for Coulomb cooling instabilities induced by heat transfer to impurity ions this gives:

$$\eta_{\mathrm{coll}} = \frac{\kappa_{\mathrm{i}}^{\parallel} T}{Q_{\mathrm{coll}}} .$$

Due to the intrinsic differences in magnetic configuration between low- and high-field side, radial temperature gradient and heat flux from the plasma

core are weaker and density higher at the latter. Hence, critical heat losses and consequential radiation instabilities, leading eventually to MARFE formation, develop here first. One has to mention that also other mechanisms for the energy loss are of importance for the MARFE formation. For typical parameters in a Deuterium plasma with carbon impurities and edge temperatures below 50 eV, ion collision instabilities can develop for plasma and impurity densities several times smaller than those required for the development of an electron radiation instability[51].

Detachment

In divertor equipped machines, radiation of impurities can be localized in the divertor volume, where the plasma state is essentially controlled by the recycling of charged particles and energy loss to the target plate. In the *recycling zone* very close to the interface, heat is transported by the convection of plasma particles. Further into the plasma than neutrals from the plasma boundary can penetrate, the intensity of the charged particle source and hence plasma flux drop. In this *conduction zone*, the energy is transported predominantly by the heat conduction. Neutral impurity particles eroding from the divertor and entering the SOL are ionized earlier than hydrogen, i.e. in the recycling region. Resulting friction between the plasma and impurity ion flux leads to a significantly shortened life cycle without excitation and radiative exhaust thereof. However, neutrals produced sufficiently far into the interface between the zones can escape from the plasma layer into the gas volume and return via the conduction region[54]. A full derivation is beyond the scope here, but a significant divertor plate temperature

$$R \sim P_{\mathrm{h}}^{2.7} \langle n \rangle^{-4.7}$$

is necessary for adequate cooling of the plasma close to the target through impurity radiation and therefore detachment, given a strong enough input heating power and reduced average density[48, 51].

Thesis Overview

The importance of impurities, both intrinsic and extrinsic towards not only the overall performance of a fusion plasma but explicitly its control and the machine safety is well-established. Exploration of radiative power exhaust scenarios corresponding to detachment physics and its research under the influence of deliberate and feedback controlled impurity seeding is of great interest. This thesis aims to establish a diagnostic foundation and framework for and conclusively implement a real-time global radiation power loss feedback system with the bolometer diagnostic for achieving stable detachment through low-Z impurity thermal gas seeding. Based on experimental achievements thereof, a multidimensional, statistical parameter analysis is performed, focusing on the sensitivity of the application with respect to emissivity distributions and plasma scenarios. At last, a custom tailored tomographic inversion algorithm is benchmarked using artificial radiation profiles and its robustness under geometric perturbations evaluated.

Bolometry of Fusion Plasmas This chapter introduces and focuses on the bolometer diagnostic system implemented at the Wendelstein 7-X stellarator, covering the requirements, construction, and operational principles used to measure spatial and temporal evolution of plasma radiation. It further details the specific challenges faced in the fusion environment and describes the used metal resistor type, emphasizing its advantages and limitations within this context. The bolometer system at Wendelstein 7-X is highlighted for its reliability and capability to withstand extreme conditions and provide critical data for power balance and transport studies.

Plasma Radiation Feedback Control This chapter focuses on the configuration and operational details of a real-time radiation feedback control system developed for Wendelstein 7-X. It outlines the system's design, performance, and experimental achievements, showcasing how the system contributes to controlling plasma radiation levels. The chapter illustrates the feedback system's impact on plasma parameters under the influence of bolometer data and its comparison with other feedback control strategies, emphasizing the significance of maintaining optimal plasma conditions and enhancing the overall efficiency of fusion experiments.

Feedback Impact and Line of Sight Sensitivity Analysis Chapter 4 presents a comprehensive analysis of the feedback controls' impact on plasma parameters, including impurity seeding modelling and line of sight sensitivity evaluation. It discusses the theoretical predictions and experimental validation of feedback effects on plasma behaviour, offering insights into the optimization of impurity seeding strategies. The chapter also delves into the sensitivity analysis of bolometer camera lines of sight and their implications for accurate measurement and control of plasma radiation, highlighting the use of STRAHL modelling to understand and mitigate feedback-related challenges.

Two-dimensional Radiation Inversion The focus of chapter 5 is on the techniques and challenges associated with two-dimensional radiation profile inversion in fusion plasmas with regard to the W7-X bolometer. It explores the application of minimum Fisher regularization and discusses the sensitivity of camera geometry to line of sight perturbations. The chapter introduces phantom radiation profiles to assess the inversion process's accuracy and discusses the tomography of experimental data. It emphasizes the importance of accurate radiation profile inversion for understanding plasma behaviour.

Bolometry of Fusion Plasmas

The word bolometer is derived from the greek βολή (*boli*), meaning "beam" or "cast", and μετερ (*meter*), "to measure". Therefore, the purpose of a bolometer can be noted as *to measure beams of light.* Its principle was invented by american astronomer *Samuel Pierpont Langley*[I] in 1878 and was later used for infrared measurements at the Allegheny Observatory[55, 56]. Their results were involved in first calculations made by *Svante Arrhenius*[II] in 1896 regarding the greenhouse effect[57].

A bolometer consist of an absorber, which is (thermally) linked to a reservoir with ideally constant properties. Incident energy, either through photons, impinging particles or even non-observable dark matter results in a change of state, i.e. temperature, of the absorber in relation to the reservoir. In proportion to the amount of absorbed energy this difference increases, which is relaxed into the reservoir at a speed defined by an intrinsic time constant, specific capacity and conductance between absorber and reservoir. In the case of thermal detectors the absorber works as a resistive thermometer, whose cooling time, heat capacity and thermal conductance can be used to calculate incident power from a change in temperature.
Bolometers are widely used today in both industry and different fields of science. At ultra-low temperatures, e.g. below 10 K or less, they can be used as particle detectors, or in the case of the *Herschel Space Observatory*[58] and *Stratospheric Observatory for Infrared Astronomy* (SOFIA), as detect-

[I]Samuel Pierpont Langley * Aug. 22, 1834 † Feb. 27, 1906
[II]Svante August Arrhenius * Feb. 19, 1859 † Oct. 2, 1927

ors for cosmic radiation.[59] Thermal cameras consist of a large array of *microbolometers* that acquire radiation in the spectral infrared range[60].

The following chapter will briefly introduce the bolometer diagnostic in plasma fusion devices and specifically characterize the one implemented at the stellarator Wendelstein 7-X.

2.1. Overview

The purpose of bolometers in fusion devices is to measure the spatial and temporal evolution of the irradiated power from the plasma within their field of view and sensitive spectral range. Depending on the type and construction, this can be, but not limited to, from infrared to soft X-ray. Additionally, the diagnostic has to conform to high operational demands governed by the circumstances in such machines[61]. The performance of bolometers in plasma fusion devices has to be unaffected by large changes in ambient temperature, as well as high thermal loads for extended durations, e.g. as is the case at Wendelstein 7-X. They need to withstand neutron radiation and consequently a radioactive contamination, while being insensitive to large electromagnetic fields and pressure perturbations. The most crucial requirement to a bolometer is however the consistency and reliability of its measurements due to very limited access to and maintenance of the diagnostic after it has been installed in a fusion device. As we will see later in section 5.2, this especially holds true for the geometry of the diagnostic. Because of the application of methods of inversion on the bolometric measurements in order to find the local radiation distribution, the line of sight geometry has to be as accurate as possible. Perturbations by thermal and mechanical stresses exerted on the machine during evacuation and cooling need to be negligible. Furthermore, in the case of the bolometer at W7-X, an *in-situ* calibration of the above-mentioned parameters, which provides information about the current state of the diagnostic, needs to be carried out reliably. Finally, the small measurement signals need to be transferred outside the vacuum vessel for a long distance to the data acquisition hardware in environments with strong interference and background noise.
The following chapter will present the bolometer diagnostic that has been implemented and established at W7-X, which the enclosed results of this

work will rest upon. The conception, implementation and deployment of a ***real-time radiation system*** that is designed to provide information about the radiation power loss for plasma feedback-control purposes is a key issue of this thesis. Starting with section 2.2, the necessary theoretical and experimental background will be provided in order to properly introduce the bolometer as such, as well as the radiation feedback system later on in chapter 3.

2.1.1. Detector Species

Over the past forty years[62], bolometers have been widely adapted in plasma fusion devices. The most prevalent concepts are the metal resistor bolometer, *absolute extreme ultraviolet* (AXUV) photo diode bolometer and *infrared imaging video bolometer* (IRVB), while there exist other designs like ferroelectric[63] or semiconductor[64] bolometers, which are not applied in fusion devices.

Metal Resistor Bolometer The metal resistor bolometer is the most common concept found in plasma fusion devices. Modern designs consist of highly sensitive thin metal film absorbers, residing on electrically non-conductive thermal transmission layers that are connected to a metal resistor. Additional to the thin metal film, a nanometer thick carbon coat can be applied to enhance the spectral responsiveness of the absorber in the infrared range[65]. They generally feature operational reliability, resilience against the hostile environments found in fusion devices and low sensitivity for perturbations in parameters like pressure or ambient temperature[66].

Absolute Extreme Ultraviolet Bolometer The absolute extreme ultraviolet bolometer uses p-n junction photodiodes with a sensitive spectral range from ultraviolet to X-ray radiation, very fast temporal responsiveness and insensitivity to impinging neutral particles as detectors.[67, 68] While being comparatively cheap and easy to use, their working principle of inner photoelectric effect limits them to a specific spectral range for acquisition, e.g. $h \cdot \nu > E$[I,II]. Due to their nonlinear frequency response and degradation

[I] photon energy: h *Planck* constant, ν frequency, E energy
[II] Max Karl Ernst Ludwig Planck * April 23, 1858, † Oct. 4 1947

in fusion environments they are not applicable for absolute radiation power measurements. Additionally, photodiodes degrade over time, especially due to the incoming neutron flux from D-T processes and strong γ radiation. Therefore, AXUV bolometers are more likely to be used complimentary to other bolometric diagnostics in order to resolve fast events and complement commonly resistive systems.[69]

Infrared Imaging Video Bolometer Infrared imaging video bolometers or segmented mask infrared imaging bolometer (*SIB*) measure radiation with a single, large metal foil behind a slit aperture or pinhole. The change in foil temperature due to incident radiation is measured from the carbon coated backside with an infrared camera, between which an IR transmitting vacuum window is placed to eliminate cooling through convection. In case of the SIB, the thin metal film is clamped between two masks, in most cases made out of copper as a heat sink, exposing an array of pixels on both sides. Properties and performance of the bolometer therefore are governed by pixel size, material thicknesses and mask attributes. The IRVB does not use masks on either side and thus has to rely on a delicate calibration for the thermal diffusion model of the metal film, which in turn rewards with an increase of detector area of ca. 40% and the removal of shadowing from mask to pixel[70, 71]. The local power deposition is derived by solving the two-dimensional heat transport equation on the thin foil. At the Large Helical Device (*LHD*) a reliable calibration method has been established[72, 73]. Like the metal resistor detector, it can be used in demanding conditions such as plasma fusion devices, while having good spatial and temporal resolution. Drawbacks include the complicated diffusion modelling, the spectral sensitivity and the dependency between responsiveness and thickness, balancing the range of photons energies than can be absorbed and time resolution[74].
In the following chapter the thin metal film resistor bolometer, as implemented at the stellarator Wendelstein 7-X will be discussed. Their kind is the most promising candidate for long term usage at future deutereum-tritium plasma fusion reactors, as they potentially meet all projected operation requirements[75], although IRVB bolometer types have been discussed for future fusion devices such as ITER[I] as well.

[I]ITER: International Thermonuclear Experimental Reactor

2.2. Bolometry at W7-X

The bolometer diagnostic at the stellarator W7-X measures the irradiated power from the plasma. It provides the total radiated power loss for global power balance studies and information about transport. In terms of plasma diagnostics, one important property under investigation is the radiation power loss. The overall radiation distribution and transport, mainly through impurities but also neutral particles, as well as the global power balance are of large importance.
The metal resistive bolometer detectors at W7-X consist of thin metal film absorbers that are thermally connected to a resistor. Incident power by radiation or particles heats up the absorber and therefore the resistor, which in turn leads to an increase in resistance. Measuring the change in resistance, combined with knowledge about the thermal properties of the sensor, yields the absorbed power of the detector.
In order to provide spatially resolved radiation distributions from the individual line integrated measurements of each absorber an array of detectors that view the plasma through a pinhole in a camera is needed. This introduces the challenge to balance good spatial resolution, i.e.small viewing angles and narrow lines of sight, with high signal-to-noise ratios and large temperature changes in the absorber. A possible way to measure small resistance changes with high precision is the *Wheatstone bridge*, where a slightly asymmetric electrical circuit of resistors experiences imbalances due to temperature change[76]. Each bolometer detector at W7-X is connected in groups of two by a Wheatstone bridge, with two ideally symmetric reference absorbers and resistances also located inside the circuit. Setups like this have also been applied at tokamak fusion plasma experiments in the past[77].
The detectors of the bolometer at W7-X are intrinsically very sensitive to thermal interference and non-absorbed input microwave heating[65]. Considerations regarding the construction and diagnostic placement were made to avoid overestimation regarding the calculation of the irradiated power from the plasma. Further requirements for the detectors are, sufficient time resolution and resistance against deterioration over long term exposition inside the vessel, since later adjustments during operational campaigns are not possible. Furthermore, calibrations can only be done prior to construction and, once assembled, inside the device, so that only an in-situ procedure

gives access to any detector parameters needed for calculations.

This section is devoted to introducing the measurement principle and design of the bolometer at W7-X. One will thoroughly present the implemented construction of the device and the resulting features in regard to the experimental environment. To start, the requirements imposed by the fusion experiments itself, which in turn lead to decisions regarding the design will be discussed.

2.2.1. Requirements

Wendelstein 7-X is designed to be capable of a steady-state operation at 10 MW of 140 GHz microwave electron cyclotron resonance heating for at least 30 min. The total non-absorbed microwave power will be limited to 1 MW, which equals an ECRH stray radiation flux density of 90 kW/m^2 on plasma facing components. Higher values are expected close to the heating beam launchers and about a factor of ten less in places opposite to the ECRH launching antennas[78]. This microwave stray radiation will impact on plasma facing components and diagnostics after multiple path reflections inside the vessel. Therefore, diagnostics facing the plasma which are susceptible to the microwave disturbance like the bolometer need special considerations in design[65]. A potential bolometer detector and data acquisition (DAQ) system at W7-X are also expected to be able to continuously measure the radiation power coming from the plasma for 30 min without degradation. As mentioned earlier, due to restrictions on in-vessel work, the diagnostic ideally requires no repetitive or extensive servicing, i.e. calibration, repair or exchange of aging components.
The radiative power loss from the plasma and non-absorbed microwave radiation are expected to average to multiple 10 kW/m^2 thermal load on plasma facing structures. Components closer to emitting microwave antennas or with higher absorption coefficients face additional challenges[79, 80]. Due to its design the metal resistor bolometer is especially susceptible to stray microwave radiation and thermal perturbations. During machine preparation components are conditioned by "*baking*" them for a long duration with a radio frequency discharge at around 150 °C. A thermal siphon has to be attached to the detector to provide a large enough mass and short cooling time, which prevents the absorber from damaging through thermal loads.

Finally, possible deuterium plasma operation imposes the question about neutron resilience and lifecycle of the detector.
The goal of the bolometer is to measure the global radiation power and local emissivity. The lines of sight have to be carefully planned in order to achieve the best possible spatial resolution while covering as much poloidal cross-section as possible at their respective toroidal position. Due to the intrinsic design of W7-X, the insertion port for the diagnostic is cylindrical shaped, thus limiting the geometry of a possible bolometer camera. Radiation from the plasma should be absorbed evenly across a wide spectral range, e.g. visible light to soft X-ray, so an absolutely calibrated power measurement is possible.

2.2.2. Construction

The bolometer diagnostic at W7-X consists of a two-camera system of thin metal film resistive detectors. The schematic of a single detector can be seen in figure 2.1. The $3.8 \times 1.3\,\mathrm{mm}$, $5\,\mathrm{mm}^2$ absorber consists of a $5\,\mu\mathrm{m}$ thick gold film, enclosed by a 0.6 mm thick Si front plate frame, which resides on a $5\,\mu\mathrm{m}$ Si_3N_4 layer. On top of the gold, nitrate membrane and silicon frame a 150 nm aluminium layer has been sputtered onto. The detector area above the Al layer is covered by a thin 50 nm carbon coat. The silicon-nitrate substrate is connected via two, $1\,\mathrm{k}\Omega$ Pt meanders to the electrical circuit for data acquisition. Both of the $30\,\mu\mathrm{m}^2 \times 200\,\mathrm{nm}$ connections have been sputtered onto the backside of the SiN membrane. Besides this *main* absorber design there also exist *secondary*, beryllium or aluminium covered absorbers that can be used for the focused analysis of high impurity plasma, soft X-ray radiation and high energy photons due to their respective spectral properties.
Behind the silicon frame, four of the eight total absorbers per detector chip are hidden, so that they are shut off from radiation and therefore should not experience a change in temperature. This chip of absorbers, electrical circuit and meander is placed between the silicon frame and an aluminium backplate, which resides on a ground plate with pin connectors for data acquisition. The top to bottom, i.e. from plasma side to pins, assembly schematic can be seen in figure 2.2b. Two of each absorber type, measurement and reference are connected in a Wheatstone bridge on the chip like figure 2.2a. The non-exposed reference absorbers can be seen on the right half of the chip

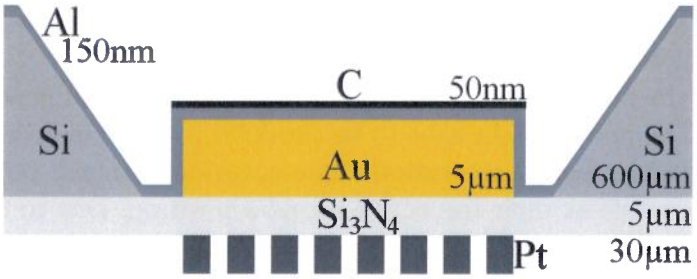

Figure 2.1.: Detector schematic. Diagram of a single blackened detector foil with frame, substrate and meander. Layer dimensions are noted, however not pictured to scale

in figure 2.2b, where the solid part of the front plate is covering them in contrast to the recesses on the left. Small drill holes in the front plate close to the reference foils are dedicated to equilibrating ambient pressure changes for both absorbers, while still providing full coverage from radiation. The exposed measurement and closed-off reference absorber form the Wheatstone bridge for data acquisition. The schematic of an electrical circuit for a Wheatstone bridge as constructed by reference and measurement absorbers can be seen in figure 2.9a. Further details on its physical measurement principle will be discussed in section 2.2.4 when introducing the bolometer equations.
The bolometer system at W7-X incorporates two cameras that are each made up out of multiple detector arrays that consist of 32 measurement and reference absorbers. The detector arrays are located behind a graphite camera front plate with pinholes through which each views the plasma individually. Between the two pinholes in each camera front plate and the detector arrays located behind there is a rotary shutter that is capable of blocking any radiation entering the housing. The detector holder, camera housing and aperture are all cooled via the central water cooling system of W7-X, which is coupled to a several hundred cubic meter large reservoir. Temperature changes of the camera array are monitored by a Pt100 resistive thermometer integrated into the back. A full camera head assembly with two detector arrays inside can be seen in figure 2.3. The individual arrays are located as close to each other as possible so that their resulting lines of sight view approximately the same plasma volume. The absorber chips with their

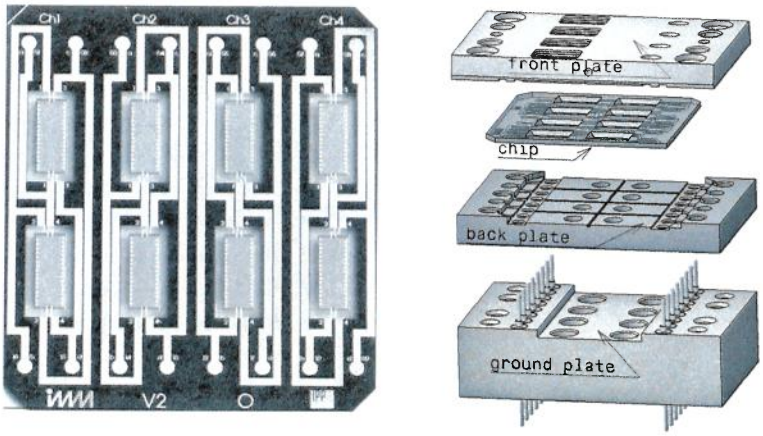

(a) Detector chip **(b)** Bolometer head

Figure 2.2.: (Left) Detector chip backside with four reference and measurement absorbers each connected in Wheatstone bridges as pairs. (Right) Bolometer group head assembly from plasma side (top) to cable connection pins (bottom).

assembly in figure 2.2b are collected in a group head with four channels per unit each. These group heads are angled individually towards the pinhole inside the camera array in a fan-shape to achieve the best possible line of sight coverage of the plasma at small viewing angles.
The detector system is connected via shielded ultra-high vacuum (UHV) proof, low resistance, low impedance, 40 m long cables, which are terminated in ten pole LEMO® connectors on both sides, to the data acquisition chassis outside the fusion device. Four master base printed circuit boards (PCB) connect to 32 individual data acquisition (DAQ) cards each, which contain the analog-to-digital converter (ADC) AD7730 from National Instruments®,[I]. Every individual measurement-reference absorber pair is connected via the cables to on of the DAQ cards. The four master PCBs are connected via ribbon cables with individual pins for each DAQ card to a NI® 7813R. The entire 128 channel system is controlled via a LabVIEW®,[II] software program, consisting of both controls for the analog-to-digital converters (ADC), as

[I]National Instruments (NI), NASDAQ: NATI; Austin, TX. USA, founded 1976
[II]Laboratory Virtual Instrumentation Engineering Workbench, National Instruments 1986

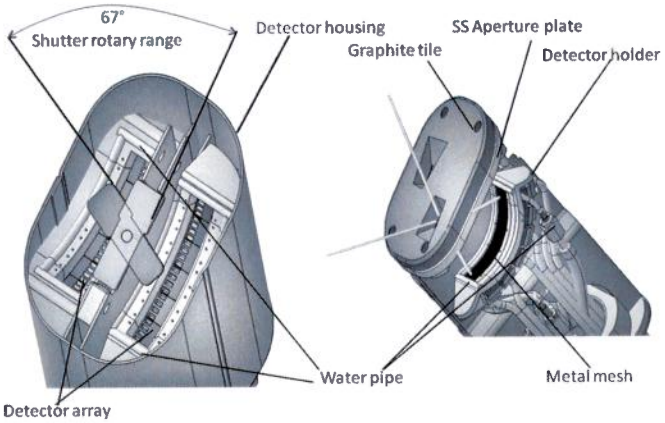

Figure 2.3.: Overview of one (vertical bolometer) camera head. (Left) Two subdetector arrays mounted on two water cooled detector holders, separated with an optic baffle, behind a rotating shutter inside the ellipsoidal camera head at the front of the diagnostic port. (Right) Graphite tile cap in front of the stainless steel aperture plate as thermal protection with indicated line of sight cone, wire mesh microwave protection and backplate connectors.

well as graphical user interface for diagnostics and debugging. Data of an ongoing measurement is stored in volatile random access memory (RAM). Before it is uploaded via an Ethernet link to the central Wendelstein 7-X archive data vault for redundancy, an individual local copy is stored on the onboard hard drive disk (HDD).

2.2.3. Line of Sight Geometry

To achieve the best possible results when evaluating the line of sight integrated data from each detector and calculating the radiated power distribution, the camera geometry has to provide good coverage of the plasma cross-section. The two cameras are located at slightly offset toroidal positions around 108° toroidally, in the *triangular* plane of W7-X. One camera head is located on the outer side of the vessel, watching the plasma horizontally, while the other is positioned below, viewing vertically into the vessel. Both devices are angled in toroidal direction due to the design of the vessel diagnostic mounting. Their identical intrinsic tilt is 68.75°, which

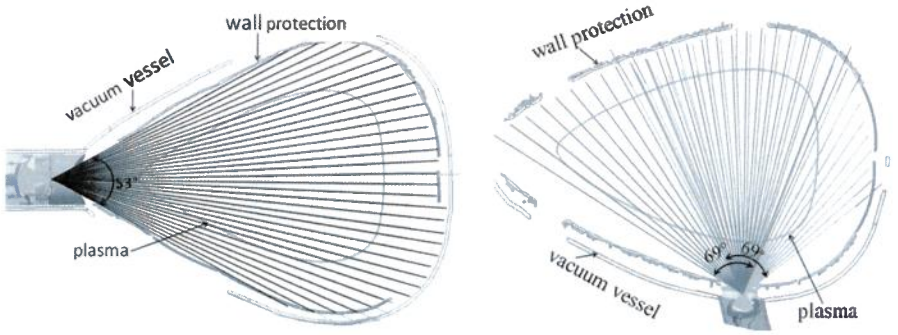

Figure 2.4.: Lines of sight of (left) horizontal bolometer camera, consisting of 32 individual detectors, and (right) vertical bolometer possessing two subdetector arrays of 20 channels each, viewing the plasma through their own respective apertures.

gives the detector lines of sight a toroidal reach of $\approx 5°$. The center-center, i.e. center of detector traced through the center of the aperture, line of sight distribution for both camera heads can be seen in figure 2.4.
The horizontal bolometer camera (HBC) is divided into two 32 channel subarrays, where one is designed and built as described in section 2.2.2, while the other contains secondary and backup detectors. The same is true for the vertical bolometer camera (VBC). In the latter case, the two arrays are made up out of 32 channels each, however both have 24 standard channels like before, where their lines of sight overlap around the poloidal center of the vessel. The remaining detectors again work as specialized, filtered absorbers.
The HBC covers the entire vessel cross-section horizontally, which guarantees complete coverage for plasma radiation in varying magnetic configurations. The VBCs lines of sight do not cover the full scrape-off layer at the bottom of the machine, but only the magnetically confined plasma area. The intersecting lines of sight of HBC and VBC provide the possibility to perform tomographic inversion of the line-integrated measurements. For further reference one can look at chapter 5 where such mathematical tools will be applied to the bolometer data.
Due to their relative position to the plasma, and thus different requirements for the opening angle, the aperture to detector distance varies between the cameras. The detectors of the horizontal camera are 175 mm and of the

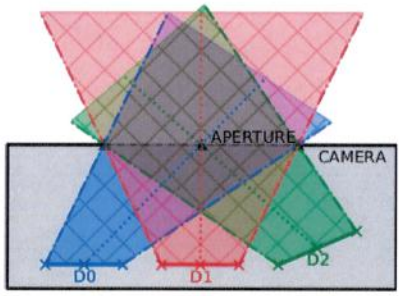

Figure 2.5.: Mockup of how detectors are located in relation to their respective aperture **A** inside the camera housing **C**. **D0** and **D1** are located on the same subarray and hence in the same plane. **D2** is on another part of the camera array that is angled differently towards the pinhole.

vertical camera 84 mm equidistantly placed behind the pinhole. Each of the detectors lines of sight are collimated through their respective pinhole. They are arranged in a shape of an arch or fan, as shown in figure 2.3, around the rectangular pinholes. The vertical camera features two individual apertures for the left- (VBCl) and right-facing (VBCr) subarrays to accommodate their different poloidal orientations, while the horizontal face plate only has one pinhole of 5×10 mm, or 50 mm^2. The elongated side of the detectors are aligned in toroidal direction, with the apertures being perpendicular to it. This is due to space limitations inside the device, which vice versa leads to a horizontal and vertical viewing angle of 53° and 138° for VBC and HBC - the angle between upper- (outer) and lowermost (innermost) line of sight vector.

In general, each camera head is made up out of two subsystems that are slightly offset toroidally and separated by a plate to limit the signal *crosstalk* between them. The displacement is small however, so that the observed plasma volume is approximately the same for both subarrays. Furthermore, the toroidal distance between the cameras and the extent of the lines of sight in this direction are small. They are within the cameras spatial resolution around the magnetic center of the plasma of 5 cm.

The camera arrays are made up out of four-by-two detector subcompartments, where each of the doubles consist of a reference and measurement absorber on a single chip. All the chips are angled individually towards the aperture to maximize their optical transmission as shown in figure 2.5. The

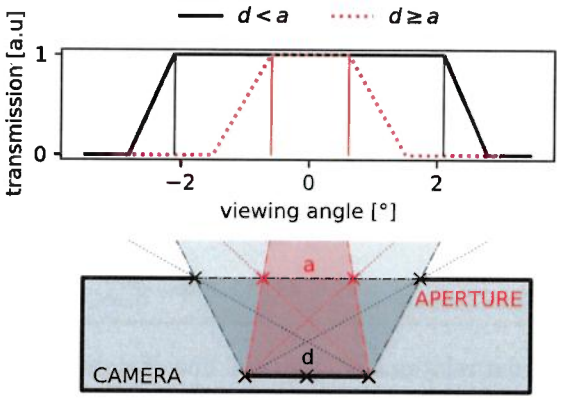

Figure 2.6.: Normalized arbitrary transmission functions of different size relations of aperture a to detector d. The W7-X core bolometry is built with $d < a$.

lines of sight of detectors from the same subarray are qualitatively depicted by D0 and D1. They share the same plane with a small displacement in direction of the camera, i.e. along the direction of the aperture, which results in a different angle of the line of sight cones. Consequently, detectors from other subarrays, like D2, are angled differently towards the pinhole to maximize their optical transmission - as is the entire camera around the front plate aperture.
An example of how the transmission function of a camera pinhole in relation to the projected widths of the pinhole and detector looks like can be seen in figure 2.6. Camera, aperture and detectors shown here are not to scale and only schematically resemble the bolometers' setup. Theoretically, in a two-dimensional approximation there are two different line of sight shapes for the projection of a detector through a pinhole: trapezoidal and triangular. In the case of $d > a$ or $d \geq a$, i.e. the detector is larger or smaller than the aperture, the line of sight is of a trapezoidal shape. For the latter, the width of the *cone* that is created by tracing the rectangular detector through the pinhole geometry widens the greater the distance to the aperture. The cone becomes trapezoidal. Conversely, if the pinhole is smaller than the detector the cone tapers. In relation to the distance from the pinhole, a narrowing line of sight eventually intersects with itself and therefore becomes triangu-

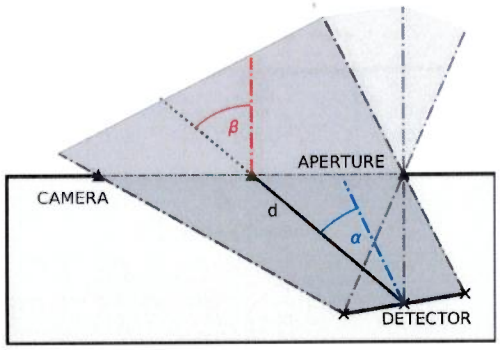

Figure 2.7.: Angular relations of aperture, line of sight and detector. Angles of β and α denote the angles between normals and line of sight. The distance between detector and aperture is called d. A lighter shade of grey indicates the partially shadowed section.

lar.
For all detectors of the bolometer at W7-X their respective aperture width is greater than their length, i.e. $d < a$. Hence, for this estimation we will assume the raw transmission across the line of sight cone to be unity. Investigations in section 5.2 regarding the discretization of the line of sight and their respective contribution to the line integral will show for this assumption to remain valid.
Figure 2.6 also introduces a challenge for the quantitative assessment of the line of sight geometry: there exist parts of the detector that are not entirely covered by the line of sight cone where the optical transmission onto the absorber is decreased. In order to address this one needs to find the absolute light yield onto the detector through the pinhole. Assume an infinitesimal part of the detector M (measurement) $\mathrm{d}A_M$ and aperture A $\mathrm{d}A_A$. The line of sight cone becomes a projection from $\mathrm{d}A_M$ through $\mathrm{d}A_A$. Let β and α be the angles between the direction of the line of sight and the normals of aperture and detector, respectively. The distance between the aperture and detector is d. For reference, see figure 2.7. It also more explicitly shows the partial shadowing of the detector by the projection through a pinhole. The transmission $\widetilde{K}_M$ can therefore be calculated using:

$$\widetilde{K}_M = \iint_{A,M} \frac{\cos(\alpha)\cos(\beta)}{4\pi d^2}\,\mathrm{d}A_M \mathrm{d}A_A\ . \tag{2.1}$$

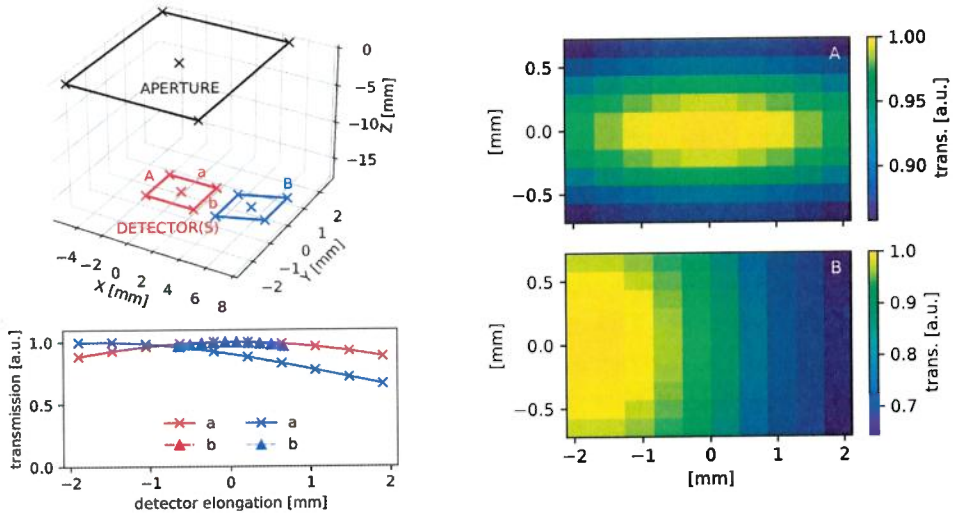

(a) Etendue **(b)** Transmission

Figure 2.8.: (a): (top) Detector A and B behind aperture with bolometer-like geometry. (bottom) Normalized transmission for both dimensions of the detectors. **(b)**: Map of the normalized etendue for both absorbers on the left along a and b. Their sizes and distances are representative of the W7-X bolometer.

Equation 2.1 is called *etendue* and is a measure for the light-yield onto the detector through the pinhole. The etendue addresses the problem of partial coverage of the absorber with the incident angles α and β inside the integral. Furthermore, the previously addressed spatial resolution of the bolometer camera is defined by the width of the cone where the optical transmission or light yield is maximum. A more detailed discussion of the mathematical approach to the line of sight geometry and impact on radiation power calculations can be found in section 5.2.

An example of how the transmission of a bolometer detector-pinhole pair looks like at W7-X can be seen in figure 2.8. Equation 2.1 has been numerically solved for an as-build combination, where both distances and orientations are the same as for the horizontal bolometer camera. Detector A and B, as well as the aperture have been transformed into their own coordinate system for exemplary reasons. Figure 2.8a shows the general geometry with elongations of the detectors a and b, as well as the transmission along those

directions across the absorbers. The partial shadowing has a small impact on the light yield onto the outermost parts in the direction of the camera array, i.e. along a towards B. However, perpendicular thereto the normalized transmission does not deviate. Figure 2.8b combines these results in a map across the absorbers A and B. The detector parallel to the aperture has a maximum in the center with varying gradients in both directions a and b. Partial shadowing perpendicular to the lateral extent of the camera array has a stronger effect because of the orientation and dimensions of the aperture and detectors. The normalized yield onto absorber B gradually decreases along a, i.e. further away from the pinhole. It is important to note that the exact details of this discussion change for the actual geometry of the VBC and HBC geometry.

2.2.4. Bolometer Equations

In the following section the measurement principle of the metal resistive bolometer detector and the Wheatstone bridge will be introduced. Subsequently, the *in-situ* calibration method, performed before every measurement, and its conclusions for the calculation of the radiation power onto the absorber will be outlined. Enclosed therein is a simplified derivation of the bolometer equation used to estimate the plasma radiation from the entire device, as well as a very general and exemplary approach to reproductions of local radiation distributions.

Measurement Principle

The electrical circuit schematic as an example can be seen in figure 2.9a. Measurement (M) absorbers are thermally connected to the R_M, whereas the non-exposed reference (R) detectors are connected to R_R. Generally the idea is to apply a large excitation voltage U_{ex} across one *diagonal* of the bridge and measuring the small resulting ΔU across the other. In a "dark" scenario one assumes $R_M = R_R = R$ both resistances to be equal and the bridge to be balanced, hence $\Delta U = 0$. Through incident power the measurement absorber heats up, causing the temperature of R_M to rise and its value to increase by ΔR. For this unbalanced bridge one finds:

$$\frac{\Delta U}{U_{\text{ex}}} = \frac{R + \Delta R}{2R + \Delta R} - \frac{R}{2R + \Delta R} \approx \frac{\Delta R}{R} \,. \tag{2.2}$$

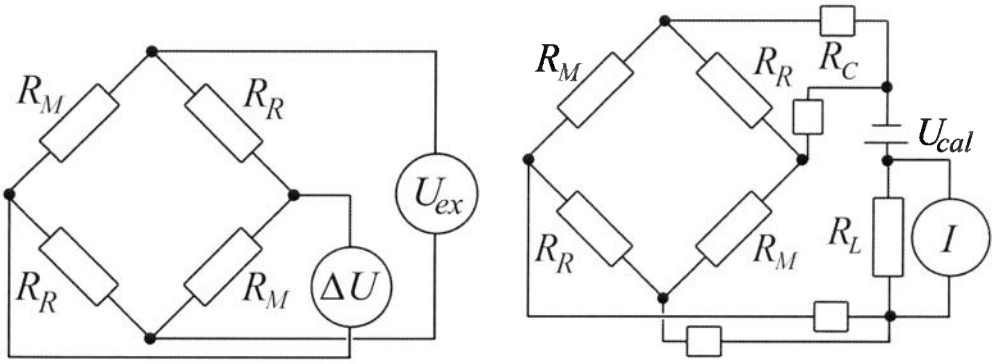

(a) Measurement **(b)** Calibration

Figure 2.9.: **(a)**: Schematic Wheatstone bridge with measurement (M) and reference (R) resistors R_M and R_R respectively. Both are thermally linked to an absorber, while the measurement part only is exposed to incident power. The bridge is connected with a voltmeter and AC excitation source. **(b)**: Equivalent circuit for calibration of the Wheatstone bridge, with DC voltage U_{cal}, cable resistances R_{C} and an additional load R_{L} for current measurement I.

Since the bridge balance is perturbed by the temperature change in both R_M simultaneously, the signal-to-noise is doubled since the noise of the measurement is governed by external factors such as cables and acquisition electronics.
The excitation voltage U_{ex} has an amplitude and alternation frequency (AC) of 20 V and 19.2 kHz, respectively. Direct current (DC) coupled excitations are not well suited to this problem, since the already small resistance perturbation ΔR is superimposed by a dominating noise component that scales $\propto 1/f$ the frequency in the power spectrum[76, 81]. When applying the AC current one measures the resistance at the frequency of the excitation and thereby removes a large uncertainty by discarding the rest of the spectrum. Assume an AC excitation U_{ex} of frequency ω, amplitude $\hat{U}_{\mathrm{ex}}$ and the bridge output, measured in U with an amplitude ΔU and phase shift ϑ. To find ΔU and therefore ΔR and ΔT, the change in temperature through radiation,

one has to combine the measurement with a reference voltage of frequency ω and integrate:

$$\int_0^{2\pi} \Delta U \sin(\omega t + \varphi) \sin(\omega t)\, \mathrm{d}(\omega t) \stackrel{!}{=} \frac{\Delta U}{2} \cos(\varphi) \equiv A \tag{2.3}$$

The demodulated result A in equation (2.3) is achieved by assuming that ΔU is constant. Because the phase shift φ itself is influenced by mechanical and thermal stresses of the acquisition circuit, there is no way of predicting or adjusting the phase shift reliably across a single measurement period or beyond. In order to alleviate the issue one repeats the previous step with a *quadrature* of the signal, i.e. a quarter period out of phase modulation, which transforms $\sin(\cdot)$ to $\cos(\cdot)$.

$$\begin{aligned} \int_0^{2\pi} \Delta U \sin(\omega t + \varphi) \cos(\omega t)\, \mathrm{d}(\omega t) &\stackrel{!}{=} \frac{\Delta U}{2} \sin(\varphi) \equiv B \\ \Delta U = 2\sqrt{A^2 + B^2}\,, \qquad \varphi &= \arctan\left(\frac{B}{A}\right) \end{aligned} \tag{2.4}$$

The results of equation (2.4) can in practice be carried out by frequency programmable gate arrays (FPGA) on an analog-digital-converter. This measurement principle is very reliable and comes with greatly reduced systematic errors[77, 82].
For the bolometer diagnostic at W7-X however this is not the case. The demodulation and *quadrature* of the signal is not carried as described above, but the bridge imbalance is directly measured as ΔU for an excitation cycle with the connected electric circuit including cables in mind. The equivalent circuit for such bridge measurements can be seen figure 2.14 and the conclusive equation (2.12). Derivations in respect thereof are largely based on the work provided by Giannone et. al[61].
After having defined the measurement voltage ΔU and resistance change ΔR for the detector one can now calculate the temperature change ΔT and consecutively incident power P_{bolo} onto the absorber. Let us assume the resistance to increase linearly with the temperature, i.e. $\hat{R} = \alpha R$. The temperature change can be written using equation (2.2) in terms of ΔU.

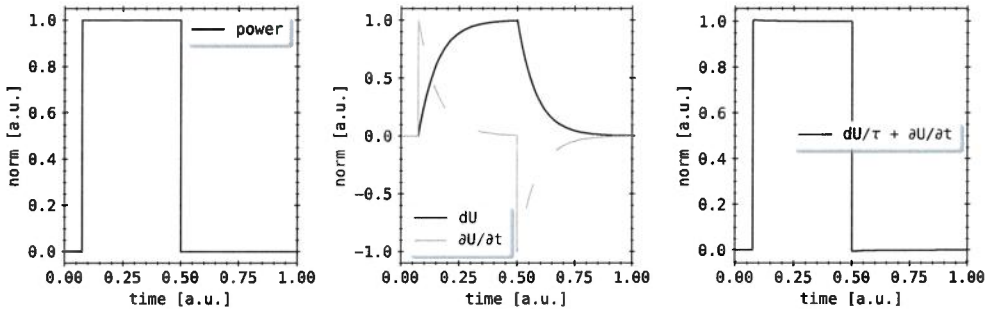

Figure 2.10.: An example for a normalized single power stage of 0.5 s and resistive absorber response as described above. Shown on the left is the incident power. In the center are both the gain and time derivative of the voltage drop across the absorber. The final image on the right shows the sum of the latter, which again yields the input power.

Finally, the temperature change ΔT is given by the incident power P_{bol}, the heat capacity κ and the cooling time τ of the absorber.

$$\begin{aligned} \Delta T &= \frac{\Delta R}{\hat{R}} = \frac{2\Delta U}{\alpha U_{\mathrm{ex}}} \\ \kappa \frac{\mathrm{d}(\Delta T)}{\mathrm{d}t} &= P_{\mathrm{bol}} - \kappa \frac{\Delta T}{\tau} \end{aligned} \tag{2.5}$$

$$P_{\mathrm{bol}} = \frac{2R\kappa}{U_{\mathrm{ex}}\hat{R}\tau}\left(\Delta U + \tau \frac{\mathrm{d}(\Delta U)}{\mathrm{d}t}\right) \tag{2.6}$$

Equation 2.6 only depends on the intrinsic characteristics of the absorber, i.e. its thermal properties and the measurement voltage ΔU. The heat capacity κ measures how much power the absorber can store. While the cooling time τ expresses the exponential rate and time constant at which the element dissipates heat. An example for this can be seen in figure 2.10: for a single stage of incident power, e.g. a heating pulse of microwaves, the sum of $\mathrm{d}(\Delta U)/\mathrm{d}t$ and $\mathrm{d}\Delta U/\tau$ represents the input radiation (arbitrary units). While normalized quantities are shown in this figure, given that the thermal properties are known, i.e. heat capacity etc., one can accurately calculate the power using this approach. In order to accurately calculate the bolometer detector power in practice one needs to calibrate the absorber and find its respective properties.

Calibration

A reliable, accurate, *in-situ* calibration procedure is needed to find the total incident power onto the absorber. Because of manufacturing processes, no detector is created equal, especially with regard to layer and substrate thickness. Variations in absorber composition lead to changes in heat capacity, resistance or cooling time across a camera or even a single Wheatstone bridge. Also, deterioration due to exposition to heavy plasma radiation also might contribute to a change in response of the detector. Continuously monitoring the systems characteristics is key, especially in context of the application in this experiment. Therefore, a calibration method based off an *Ohmic heating phase*, involving reference resistors for comparison and taking cable properties into account has been established and used in past experiment campaigns. One should note that this is, with minor changes, based off of the derivations made by Giannone et al.[61].
An equivalent circuit for the calibration of the previously discussed Wheatstone bridge can be seen in figure 2.9b. Two concurrent voltage levels are applied to either the two measurement or reference resistors, while the respective others are short-circuited. The NI® AD7300 is capable of both voltage and current measurement - although consecutively and not in parallel. An example of two current stages for one pair of measurement and reference resistor from the same Wheatstone bridge can be seen in figure 2.11.
First, the current flowing through the resistor at floating potential I_0 is measured as a baseline. It is assumed that element M has the resistance R_M before the calibration. For two values of $U_{\mathrm{cal}} = 1.2\,\mathrm{V}$ and $2.5\,\mathrm{V}$ the stages are run each for 1.6 s. The current through the resistor evolves with $I(t)$ and eventually equilibrates, i.e. $t \to \infty$. One therefore finds for the resistance from the current in the first stage:

$$R_M = 2\left(\frac{U_{\mathrm{cal}}}{I(t \to \infty) - I_0} - R_{\mathrm{L}} - R_{\mathrm{C}}\right) . \tag{2.7}$$

Here, $R_{\mathrm{L}} = 10\,\Omega$ is an additional load resistor in the acquisition circuit outside the Wheatstone bridge and $R_{\mathrm{C}} = 40\,\Omega$ accounts for the connected cables. The electric power leads to an Ohmic heating of the foil, increasing the temperature, which, due to a temperature change of the resistor, changes the resistance and therefore again the current flowing through the detector.

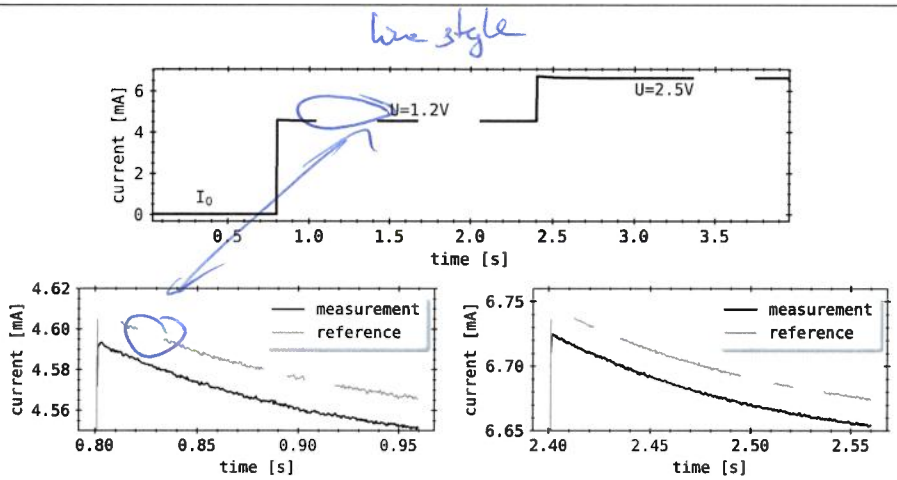

Figure 2.11.: Example of the first (left) and second (right, both - top) Ohmic heating stages as described for measurement and reference absorbers. One easily notices the difference in absorber response between reference and measurement part of the same bridge. The maximum current before the exponential decay during the first heating pulse corresponds to $\Delta I\,(0)$.

One assumes a current perturbation due to the Ohmic heating $\Delta I\,(t)$ to be superimposed onto $I\,(t)$. The cooling time rate towards equilibrium, i.e. $\Delta I \to 0$ can be expressed by an exponential decay function:

$$\Delta I\,(t) = -\Delta I\,(0)\left[1 - \exp\left(-\frac{t}{\tau_M}\right)\right] . \tag{2.8}$$

Here, τ_M yields the temperature decay or cooling time constant of the resistor M. The time t is measured relative to the occurrence of the ohmic heating stage, and $\Delta I\,(0)$ is the resulting maximum current thereof. By a numeric fitting procedure of the previous function in equation (2.8) to the response of the detector one easily finds the values of τ_M and $\Delta I\,(0)$.
Differences in foil and substrate thicknesses result in different heat capacities κ of each absorber, while the thermal contacting to the body of the bolometer chip holder also varies and results in variations in cooling time τ. Hence, the initial response to the Ohmic heating stage can be significantly different to an exponential decay. However, the cooling is dominated by the carbon coated gold and aluminium layer in-between. Therefore, the first few milliseconds of the heating stage are excluded from the numerical fit of the function in equation (2.8) in order to find τ and κ. Important to note is that in this

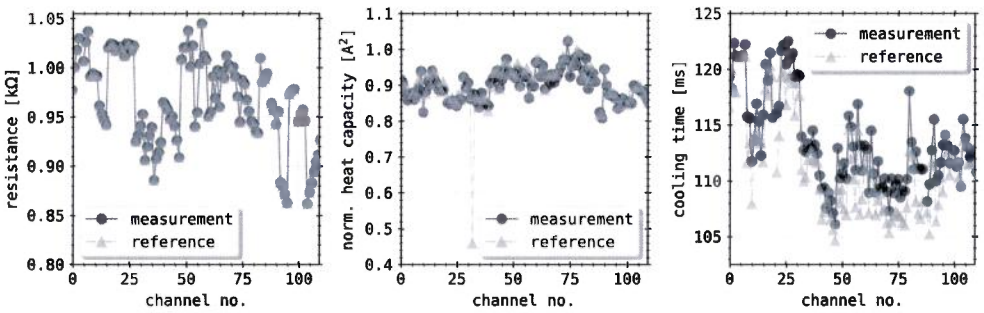

Figure 2.12.: Example for a set of calculated normalized heat capacities, resistances and cooling times for both measurement and reference detectors as described below. Small groups of four consecutive detectors in each property hints at similarities in composition irregularity. Reference channel number 32 in the middle figure shows an especially low heat capacity, indicating an issue with the thermal contact of the meander bridge.

case, the change of the current $I(t)$ does not yield the maximum current through the detector, as noted above by $\Delta I(0)$. This property is measured independently at the peak of $I(t)$ during the Ohmic heating pulse.
The current when heated up $\Delta I(0)$ can be used the find the (normalized) heat capacity κ_M. By linearization of the change ΔR in resistor value R_M one can write the power balance during the current stage as:

$$\frac{U_{\text{cal}} I_0^2}{I(\infty) - I_0} + \frac{I(\infty)\, I_0 R_M}{2} = -\kappa_M \frac{4U_{\text{cal}}}{I_0^2} \left[\frac{\mathrm{d}\Delta I}{\mathrm{d}t} + \Delta I \right] . \tag{2.9}$$

Substituting equation (2.8) for ΔI and calculating for the steady state case, i.e. $t \to \infty$ hence $\mathrm{d}I/\mathrm{d}t \to 0$ and $\Delta I \to 0$, equation (2.9) can be rewritten to:

$$\kappa_M = \frac{\Delta I^4(0)}{4I(\infty)\left(I(\infty) - I_0\right)} . \tag{2.10}$$

With the previously outlined setup it is possible to do the above measurements for all measurement and reference resistors of the Wheatstone bridge, which results in the values of τ, κ and R for each individually. Those are important not only for the calculation of the plasma radiation power, but

A is the surface area of the insides of the camera housing, ΔT the relative temperature change to a baseline and ε an emissivity efficiency. In a more accurate model this is in fact frequency dependent with $\varepsilon(\nu)$, since the camera enclosure is not adequate described as a black body. To add to that, perturbations of the integrated camera holder water cooling have also presented strong, thermally induced signal drifts. An example for this can be seen in figure 2.13.
Previously, Zhang et al. have modelled the temperature impact on detector properties for the above equations[86]. It was concluded that the detector characteristics become functions of the temperature increments in all parts of the bridge, i.e. ΔT_M and ΔT_R of measurement and reference absorber respectively, and that the major impact on signal form is imposed by thermal changes in the resistance R and heat capacity κ. It was found that the drift and offset are in the range of 50–150 µV/K, depending on the composition of the absorber[86]. A simultaneous measurement of both bridge voltage ΔU and current through the Wheatstone bridge for parallel data acquisition and calibration has not been implemented. The similarly designed bolometer at the future large tokamak fusion device ITER will feature a real-time calibration parallel to data acquisition[87].
For long pulse experiments this issue can be avoided by systematically looking up known calibration values at given absorber temperatures and ambient pressures. The future *divertor bolometer system* at W7-X will pursue this strategy. As further reference, the literature notes the change in heat capacity, cooling time and resistance of a gold with a rate of 25 J/(K mol), 0.13 ms/K and 0.008 nΩ m/K respectively. This behaviour is mostly linear beyond a threshold of 275 K[88–92]. This again underlines the necessity of active cooling of the bolometer camera.
The temperature increase of the resistor and absorber due to voltages applied for excitation during the measurement process is expected to be 25 K. The calibration itself also heats up the foil through the Ohmic heating phase. It can be assumed that the increase in temperature is similar during both and this effect will be neglected in later considerations[86]. The future divertor bolometer will conduct absorber calibrations while also applying the measurement excitation.

for information on detector status and reliability as well. An example for a set of calculated κ, R and τ for both exposed and hidden counterparts can be seen in figure 2.12.

In reality, the above equations have to be corrected to account for the temperature dependence of all three quantities. This has not been pursued for the bolometer system at hand. Furthermore, Zhang et al. addressed the influence[83] of ambient pressures and concluded, that an increase of up to 20 Pa leads to an equivalent, non-negligible pseudo signal of 2–8 $\mathrm{W/(m\,Pa^2)}$, while the expected change in pressure during experiments is 0.5–1 Pa. However, the expected maximum pressure of plasma discharges in W7-X is $\approx 1 \times 10^{-2}$ Pa, therefore this is not an issue. Tests in *VINETA*[I] have found that the detector characteristic is susceptible to strong ambient pressure and temperature changes. A *strain-gauge* factor as a function of the resistivity and pressure was defined, which was found to have a hysteresis and change with the line integrated power[84]. Nevertheless, one would need an individual gauge to measure local baseline pressures or flow rates through or at the pinhole to most accurately address this problem. Another approach would be to install one or more blind absorbers that are not exposed, so they can be used to subtract a bias from the signals of the corresponding camera.
For the validity of the bolometer measurements its performance under conditions of high neutral gas density is of concern, where an additional component of the bolometer signal comes from localized, high energy neutral particles from charge exchange processes at the plasma edge. First order corrections to the bolometer equations can be made by incorporating neutral gas simulation codes with charge exchange to numerical simulations of the measurement[85]. This has not been exercised for the bolometer at W7-X. The expected $10\,\mathrm{kW/m^2}$ high thermal loads on plasma facing components and conclusive temperature perturbations of the camera enclosure of the bolometer may lead to additional signal drifts due to infrared radiation from inside the diagnostic housing. As a simplest estimate of *grey body radiation*, such a drift is $\propto \varepsilon A \Delta T^4$ according to the *Stefan-Boltzmann*[I,II] *law*, where

[I]VINETA: Versatile Instrument for Studies on Nonlinearity, Electromagnetism, Turbulence and Application

[I]Jožef Štefan * Mar. 24, 1835 † Jan. 7, 1893

[II]Ludwig Eduard Boltzman * Feb. 20, 1844 † Sep. 5, 1906

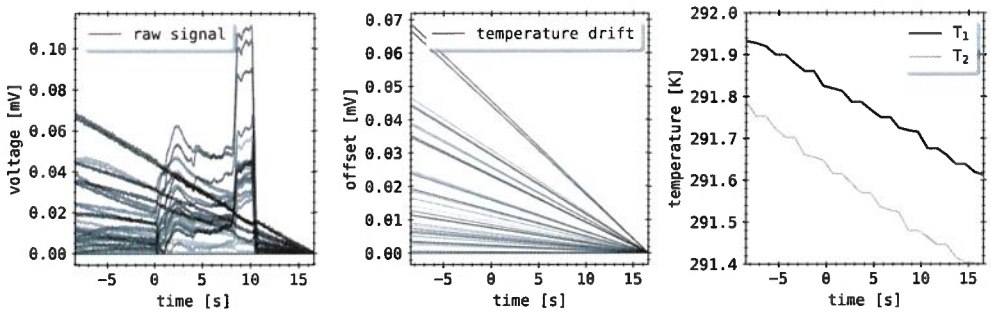

Figure 2.13.: The left image shows the unaltered detector signal as measured by the data acquisition for the main HBC array in the W7-X experiment XP20180927.37. The middle is the subtracted, assuming linear, temperature drift for each of those channels. Note how either every channel has different drift functions or entirely different temperatures. The right picture shows the measurement results of two *Pt100* resistive thermometers from the back of the HBC array over the course of the experiment

Radiation Power Measurement

After a successfully performed calibration the power onto the absorber can be calculated. Following will be an outline of this process, accompanying the equations to calculate the incident radiation power.
In general, the radiation from the plasma along the line of sight (LOS) of an absorber can be written as:

$$P_{\text{rad}} \propto \int_{LOS} \sum_{Z} n_e \cdot n_Z \cdot L_Z \left(T_e, T_i, T_Z, \ \ldots\right) \frac{\mathrm{d}l}{4\pi} \ . \tag{2.11}$$

Here, P_{rad} shall be the total incident power as measured by the bolometer absorber. This is, in theory, proportional to the sum over all *(line) radiation functions* L_Z of elements Z, which describes the combined emission from both continuum and atomic processes at a given set of plasma parameters, e.g. electron and ion temperature $T_{e,i}$, as well as the condition of the device.
Consider that ΔU the output voltage of the Wheatstone bridge is being measured in the equivalent circuit shown in figure 2.14. In accordance to equation (2.6) the radiation power onto the measurement absorber can be expressed in P_{bol}. Adjusting equation (2.6) to the details of the measurement

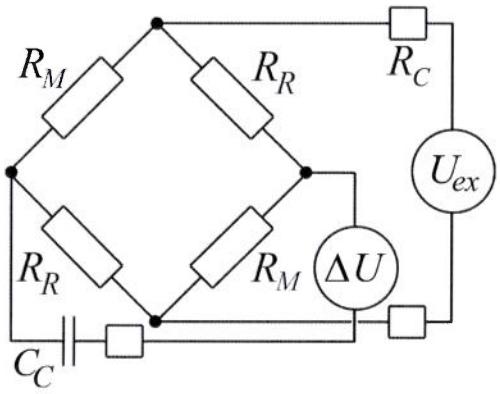

Figure 2.14.: Equivalent circuit for bridge imbalance measurements ΔU of Wheatstone bridge, with AC excitation voltage U_{ex}, cable resistances and capacity R_{C} and C_{C}.

circuit for absorber M of the Wendelstein 7-X bolometer diagnostic, one arrives at the *bolometer equation*:

$$\widetilde{P}_M = \frac{2}{V_{\mathrm{eff}}} \left(R_M + 2R_{\mathrm{C}}\right) \kappa_M \sqrt{g_{\mathrm{C}}} \left(\tau_M \frac{\mathrm{d}(\Delta U_M)}{\mathrm{d}t} + f_\tau \Delta U_M\right) . \tag{2.12}$$

The corresponding parameters of the data acquisition setup for equation (2.12), i.e. V_{eff}, f_τ, g_{C}, β, ω etc. are shown below in equation (2.13). The Wheatstone bridge frequency is $f_{\mathrm{bridge}} = 2500\,\mathrm{Hz}$ and cable parameters are measured to be $R_{\mathrm{C}} = 40\,\Omega$ and $C_{\mathrm{C}} = 2\,\mathrm{nF}$ respectively.

$$\begin{aligned} V_{\mathrm{eff}} &= \frac{(5\,\mathrm{V}) \cdot R_M}{R_M + 2R_{\mathrm{C}}} \\ g_{\mathrm{C}} &= 1 + \left(\omega \left(R_M + R_{\mathrm{C}}\right)\right)^2 \\ \beta &= \frac{1 - \left(\omega R_M\right)^2 + \left(\omega R_{\mathrm{C}}\right)^2}{1 + \left(\omega \cdot \left(R_M + R_{\mathrm{C}}\right)\right)^2} \\ \omega &= 2\pi \cdot f_{\mathrm{bridge}} C_{\mathrm{C}} \\ f_\tau &= 1 - \frac{V_{\mathrm{eff}}^2 \cdot \beta}{4\kappa_{\mathrm{M}} \left(R_M + R_{\mathrm{C}}\right)^2} \end{aligned} \tag{2.13}$$

As previously pointed out, equation (2.12) is only a valid estimator for the radiation power in a single detector within a small temperature range and

at constant neutral gas pressures. During manometer tests where the vessel pressure was continuously increased, detector signals rose in the absence of plasma or radiation. Additionally, each detector is only accepted for evaluation if its calibration values are within a 3% deviation window from their reference counterpart.
In summary, the absorbed radiated power is expressed as a function of voltage drop across the Wheatstone bridge as shown in absorber and the corresponding time derivative. Assuming $R_M \approx 1\,\mathrm{k\Omega}$, $\tau_M \approx 110\,\mathrm{ms}$ and $\kappa_M \approx 0.8\,\mathrm{mW/k\Omega}$, which gives $\omega = 3.14 \times 10^{-5}\,\mathrm{Hz\,F}$, $\beta \approx 1$, $\sqrt{g_C} \approx 1$, $V_{\mathrm{eff}} = 4.63\,\mathrm{V}$ and $f_\tau \approx 1$, equation (2.6) can be written for a sample time of 1.6 ms as:

$$\tilde{P}_M \approx 25.74\,\mathrm{W/V}\,(\mathrm{d}(\Delta U_M) + 0.014\Delta U_M) \ . \tag{2.14}$$

Commonly one finds during a measurement of plasma radiation at W7-X $\Delta U \sim 10^{-3}\,\mathrm{V}$ and the change in signal on the time basis given above $\mathrm{d}(\Delta U) \sim 10^{-5}\,\mathrm{V}$. Hence, the predominant part of the equation is the raw signal, however during transient phases with fast changes of plasma radiation distribution the dynamic part may play a more important role therefore set the time resolution of the system by requirements regarding the signal-to-noise ratio.
The raw signal has to be offset corrected. e.g. for temperature drifts. By design of the system, the detector temperature changes naturally due to ohmic heating by the excitation voltage and incident radiation. The calibration process however already saturates the absorber temperature through ohmic heating, so that an additional heating during the actual measurement is not experienced. External thermal interference through the perturbations of the water cooling and heating of the camera enclosure (and other plasma facing components) and subsequent infrared radiation also may add to possible thermal drifts or signal errors.
In summary, the baseline offset is calculated from the mean voltage ΔU in the first few (hundred) milliseconds of measurement before plasma startup at T_0 in order to account for an initial imbalance of the Wheatstone bridge before the experiment.

$$V_{\mathrm{off}} = \frac{1}{t_2 - t_1} \int_{t_1}^{t_2} \Delta U_M\,(t)\,\mathrm{d}t \ , \ t_1 < t_2 < T_0 \tag{2.15}$$

An expected temperature and signal drift is compensated using the *least squares* method to fit a linear function $f(t, \beta_1, \beta_2)$ as offset between the detector signal before the start and end of experiment. This approach is based on the assumption of linearity in first order temperature dependency of the calibration properties, as well as a slow linear temperature rise due to a large enough thermal inertia or reservoir of the machine. Data points beyond the end of the experiment, where incident radiation no longer heats up the absorber, are not included since the detector already begins to exponentially cool down. Let t_1 be the point in time just before the start of the plasma heating, t_2 right after it shutting off and $\overline{\Delta U}(t)$ be a 50-100 sample median of the signal around t. Then $\vec{\beta} = (\beta_1, \beta_2)$, $\vec{f} = \left(f\left(t_1, \vec{\beta}\right), f\left(t_2, \vec{\beta}\right)\right)$, $\Delta\vec{U}_M = \left(\overline{\Delta U}_M(t_1), \overline{\Delta U}_M(t_2)\right)$ become the component forms of the parameters, fit and target function at those given times. The drift problem therefore is:

$$\begin{aligned} r_i =& \Delta U_{\mathrm{M}}(t_i) - f(t_i, \beta_1, \beta_2) \\ R_{\mathrm{res}} =& \sum_{i=1}^{n} r_i^2 = \|\vec{f}\left(t, \vec{\beta}\right) - \Delta\vec{U}_{\mathrm{M}}\| \\ & \underset{\vec{\beta}}{\operatorname{argmin}} \left[\|\vec{f}\left(t, \vec{\beta}\right) - \Delta\vec{U}_{\mathrm{M}}\|\right] \end{aligned} \tag{2.16}$$

Solving the minimization problem in equation (2.16), given that $\beta_i \in \mathbb{R}^+$ are positive for direct proportionality between the absorber response and temperature, one yields:

$$V_{\mathrm{drift}}(t) = \begin{cases} 0 & , \ t < t_1 \,\&\, t > t_2 \\ \beta_1 \cdot t + \beta_2 & , \ \text{else} \end{cases} \tag{2.17}$$

Let the resulting signal, i.e. offset- and drift-corrected be ΔU_M^*. To save one step in calculation, one can easily see that $\beta_2 = 0$ either becomes zero for an offset-corrected ΔU_M as a training set, or $\beta_2 = V_{\mathrm{off}}$ else. Additionally, the latter approach ensures that $\Delta U_M^* \approx 0$ around $T = T_0$ where no plasma radiation or thermal interference is expected.
To avoid larger contributions of the derivative term $\mathrm{d}\left(\Delta U_M^*\right)/\mathrm{d}t$ for small $\mathrm{d}t$ or large signal noise one applies a filter. A frequency gate via a low pass *Savitzky Golay* polynomial fit of order p and width N or boxcar filter (moving mean) of width N have been successfully tested and deployed with similar, adequate results. The filtered, *corrected* voltage becomes $\Delta\widetilde{U}_M$. In

the discretized, i.e. analog-to-digital converted case, the j-th sample at time t_j of $\Delta\widetilde{U}_M$ becomes a convolution of N surrounding points with coefficients c_i weighting the corrected data. In the case of the Savitzky Golay filter the coefficients $c_i = f\left(\Delta U_M^*\right)$ become a function of the convoluted signal:

$$\begin{aligned} \Delta\widetilde{U}_{M,j} &= \sum_{i=\frac{1-N}{2}}^{\frac{N-1}{2}} c_i \Delta U^*_{M,j+i} \\ c_i &= \begin{cases} 1/N & \text{, boxcar} \\ 1/35\left(-3f_{i-2} + 12f_{i-1} + \right. & \\ \qquad \left. 17f_i + 12f_{i+1} - 3f_{i+2}\right) & \text{, S. G.} \end{cases} \end{aligned} \tag{2.18}$$

Finally, starting from equation (2.12) and combining prefixes into detector specific factors, i.e. F_M and f_M, as well as applying equation (2.17) and equation (2.18), one yields:

$$\begin{gathered} F_M = \frac{2\tau_M}{V_{\text{eff}}}\left(R_M + 2R_{\text{C}}\right)\kappa_M\sqrt{g_{\text{C}}}\,, \quad f_M = \frac{f_\tau}{\tau_M} \\ \boxed{P_M := \tilde{P}_M\left(\Delta\widetilde{U}_M\right) = F_M \cdot \left(\frac{\mathrm{d}\left(\Delta\widetilde{U}_M\right)}{\mathrm{d}t} + f_M\Delta\widetilde{U}_M\right)} \end{gathered} \tag{2.19}$$

The equation (2.19) is the final form of the bolometer equation (2.6) as it has been used in the past at the stellarator Wendelstein 7-X and will be during the course of this thesis for the results shown further below. Equation 2.19 is also again only a function of the absorber specific properties F_M and f_M, as well as the post-processed Wheatstone bridge imbalance measurement ΔU.

2.2.5. Performance

The efficiency of gold absorbers has previously been found to be close absolute wavelength range between 1×10^3–1 nm for black nickel layer coatings[93]. The results can be seen in figure 2.15a. Meister et. al[94] have measured the photoresponse of pure thin film platin absorbers of varying thickness, which are very similar to the carbon blackend gold film detectors at W7-X, and compared their results to photoabsorption calculations

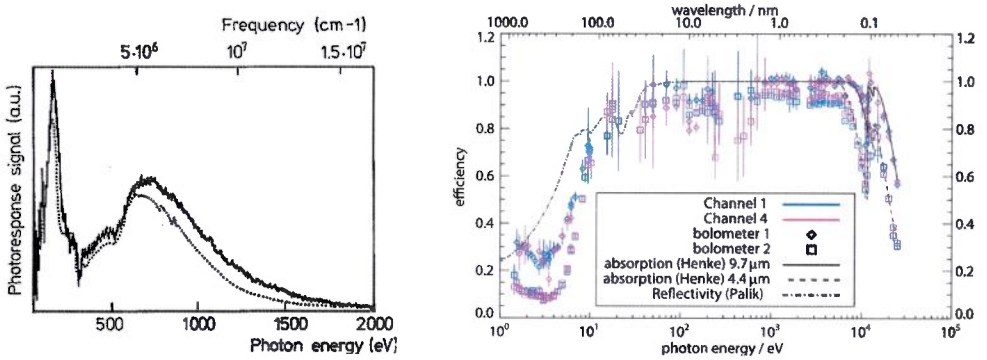

(a) Au absorber[93] **(b)** Pt absorber[94]

Figure 2.15.: **(a)**: Photoresponse signals for a thin gold foil bolometer absorber (solid) and gold diode (dotted) to synchrotron radiation[93]. **(b)**: Efficiency of bolometer absorber over incident photon energy as derived and measured by Meister et. al[94].

by Henke et. al[95] for atomic (crystal) scattering, reflection and transmission. The results are shown in figure 2.15b. The efficiency with the highest uncertainties correlate to measurements at the lowest powers of the radiation source - channel no.1 and channel no.4 with respective thickness of 9.7 µm and 4.4 µm. The continuous, dashed and dotted-dashed black line are achieved by atomic scattering calculations[95, 96]. The obtained results of a thick absorber for photon energies above 200 eV agree within their uncertainties with the literature. Efficiencies obtained for a thin absorber also matches but shows slightly lower values. The photoresponse of a 5 µm thick gold absorber is therefore assumed to be unity in the range of 600–0.2 nm, where reflectivity is greatly reduced due to the coating, while the sensitivity of 200 nW is still low. This provides the capability of absolutely calibrated measurements of the expected plasma radiation at W7-X.
The silicon frame and aluminium layer are used as thermal contact to diffuse the power load from the sensitive gold film resistor onto the graphite and stainless steel camera housing in order to limit the detector from reaching its maximum allowable temperature of 250 °C.
As previously mentioned, the bolometer diagnostic is required to manage at least 10 kW/m^2 of microwave stray radiation at its plasma facing front plate without degradation of the actual measurement. Therefore, any of the

four detector arrays - two per camera each - are covered by a conductive wire-mesh of 90 µm thickness and 0.24 mm rectangular spacing in order to reduce the impact of non-absorbed microwave radiation through the pinhole. The optical transmission changes with detector location for the HBC because of differences in angle between line of sight and wire mesh normal, which reduces the light yield onto each absorber. However, this is not the case for both vertical camera arrays, where the arrangement is mounted individually directly in front of the subarrays. The resulting total optical transmission can be seen in figure 2.16b. The insides of the cameras have been coated with a special ceramic titanium oxide and aluminium oxide layer to enhance the microwave absorbance of the camera body and reduce the reflectance thereof. Additionally, special copper beryllium springs in the camera front plate mounting ensure a tight fit of the plasma facing component to reduce leakage of microwave radiation. Coating, holding plate springs and wire mesh all greatly improve the cameras' response to the microwave ECRH stray radiation[97, 98]. Long duration tests with 140 GHz strayfield microwave radiation onto the camera body and detector housing have been performed in MISTRAL[I]. The results show the impact to be reduced to 3% of its total $\approx$ 10 mW per detector, or $<$ 0.1 mW. The results can be seen in figure 2.16. For an expected 10 kW/m^2 microwave stray radiation, aperture size of 50 mm^2 and 175 mm distance to a 5 mm^2 absorber, the resulting 0.5 W through the pinhole arrive at 0.04 µW on the detector. This is orders of magnitude smaller than commonly measured experiment plasma radiation powers.

The previously described absorber, electrical circuit and hardware is capable of acquiring voltages in the range of $\pm$80 mV, sampled into 16 bit, which translates to 2.44 µV acquisition resolution at maximum range. However, this changes in correspondence to the selected acquisition setting, which leads to a minimum resolution of 0.31 µV at $\pm$10 mV acquisition range. This is also important for the achievable signal-to-noise ratio, where the acquisition range setting defines the smallest possible measurement error by its voltage resolution. The temporal resolution of the ADC is limited by its master clock rate of $f_{master} = 4.9152$ MHz. However, the latency of the field programmable gate array (FPGA) inside the ADC, depending on the

[I]MISTRAL: MIcrowave STray RAdiation Launch facility; Max Planck Institute f. Plasmaphysics, Greifswald

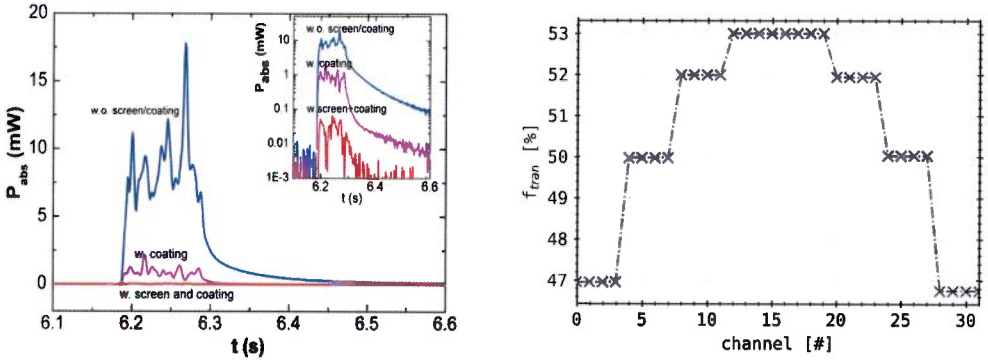

(a) Microwaves **(b)** Transmission

Figure 2.16.: **(a)**: Before and after the ceramic coating treatment and wire mesh installation in front of the detector arrays. Shown are the results of MISTRAL[I] tests with and without microwave countermeasures. (Right) Transmission factor of wire mesh over channel number. Subsets of detectors are grouped into blocks inside the larger camera array, hence the steps in this curve. Their angle between the lines of sight and mesh normal is equal, yielding the same transmission coefficient.

operation of read and write, ranges between 10–100 ns. This is a small perturbation compared to the physical limits of the detector, dominated by its cooling time. The sample frequency of the ADC is given by programmable hexa-/decimal values. Those discreet hex values are 12-bit coded, translating to $2^{12} = 4096$ possibilities of setting, to which the minimum delta in sample time or frequency becomes

$$\Delta T_{sample} = \frac{T_{s,max} - T_{s,min}}{4096} = 0.0095\,\text{ms}\,, \quad \Delta f_{sample} = 0.0254\,\text{kHz}\,.$$

Data acquisition was possible for sample times of $\{0.8, 1.6, 3.2, 6.4, 12.8\}$ms. One should note that the ADC is capable of operating at another measurement mode, where the acquisition range is sampled twice per cycle period with alternating parity, i.e. between alternating pins resulting in a change of sign, however this comes at the cost of a much smaller signal-to-noise ratio. A further characterisation of this acquisition mode has not been pursued. In measurement mode it was found that the noise background caused by small fluctuations in situations without incident radiation is in the range of

0.5–6 µV. This results in a signal-to-noise ratio in high radiation scenarios of at least:

$$\begin{aligned} \overline{\Delta U} &= \underset{t_1,t_2}{\text{median}}\left(\Delta U\left(t\right)\right) && , T_{\text{start}} < t_1 < t_2 < T_{\text{stop}} \\ \sigma_{\Delta U} &= \sqrt{\int_{t_0}^{t_0'} \left(\Delta U - \overline{\Delta U}\left(t_0, t_0'\right)\right)^2 \mathrm{d}x} && , t_0 < t_0' < T_{\text{stop}} \\ \text{SNR} &= \frac{\overline{\Delta U}}{\sigma_{\Delta U}} = 1000 \mathrel{\widehat{=}} 10\,\text{lg}\left(\frac{\overline{\Delta U}}{\sigma_{\Delta U}}\right)\text{dB} = 30\,\text{dB}\,. \end{aligned} \tag{2.20}$$

Here, $\overline{\Delta U}$ is the median value in the interval (t_1, t_2) and $\sigma_{\Delta U}$ the standard deviation. However, they are both calculated at different times: $\sigma_{\Delta U}$ describes the noise before the experiment, while $\overline{\Delta U}$ represents the median of the signal during the discharge. This avoids possibly accounting for plasma radiation fluctuations to contribute to $\sigma_{\Delta U}$.
The quality of the acquired signal and calibration results have been closely monitored throughout the past, and especially the last experimental campaign. Combined they yield information about the absorber condition and wear or possible discrepancies with the connected electronics. The results can be seen in figure 2.17 and figure 2.18. Shown there is the 99th percentile of both the calibration values and acquisition properties for each main detector across the last experimental campaign. The core bolometry system with its 61 functional detectors successfully participated in 1182 experiment programs.
Figure 2.17 presents the calibration results of the measurement absorbers, including the resistance, normalized heat capacity, cooling time and signal voltage offset without plasma. The results of equation (2.7) in figure 2.17a show very small deviation over time. Plateaus in R indicate individual experiment days, where in-between the camera array temperature slightly deviated. Towards the end of the campaign however three detectors of the vertical bolometer camera particularly diverge, indicating either deterioration or electronic problems. Solving equation (2.10) for calibrations during OP1.2b yields figure 2.17b. Similarly, the characteristics of each detector vary only slightly for each experiment. One absorber produces values that greatly diverge from its campaign average within the first ca. 350 experiments. This is likely due to systematic errors in the calibration process or algorithm, since those perturbations no longer appear after. At around

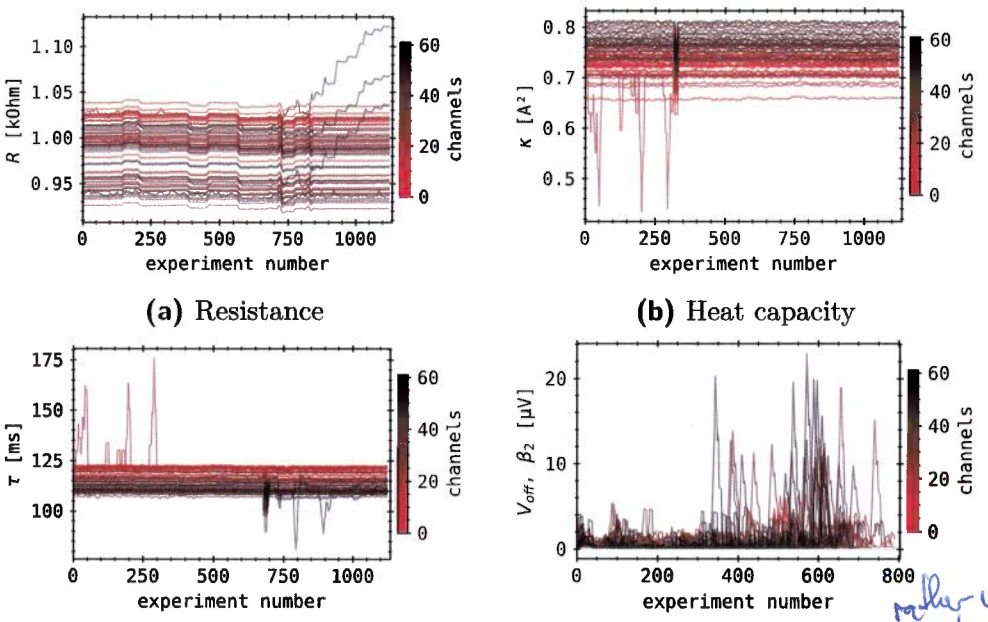

(a) Resistance **(b)** Heat capacity

(c) Cooling time **(d)** Offset

Figure 2.17.: Calibration parameters of the core bolometry system at W7-X during OP1.2b. **(a)** Resistance of the absorber as calculated by equation (2.7). **(b)** Normalized heat capacity of the detector from equation (2.10). **(c)** Cooling time from exponential decay fit to an ohmic heating stage as depicted in figure 2.11. **(d)** Absolute offset in acquisition before the discharge begins.

experiment number 350 an entire session of about 30 experiments shows collectively smaller heat capacities, which again points to an issue with the first ohmic heating stage during the calibration process or interference of the camera array temperature. Similar results are found for the cooling time data shown in figure 2.17c. The perturbations responsible for the valleys in the heat capacity data however have a reciprocal effect and lead to peaks in the cooling time. For an experiment session of about 30 discharges the cooling time collectively decreases by about 20% likely because of the above reasons. figure 2.17d shows the fit results from equation (2.17), i.e. the absolute offset at the start of the discharge when the absorber has equilibrated after engaging the measurement excitation. Generally the values are below 1–

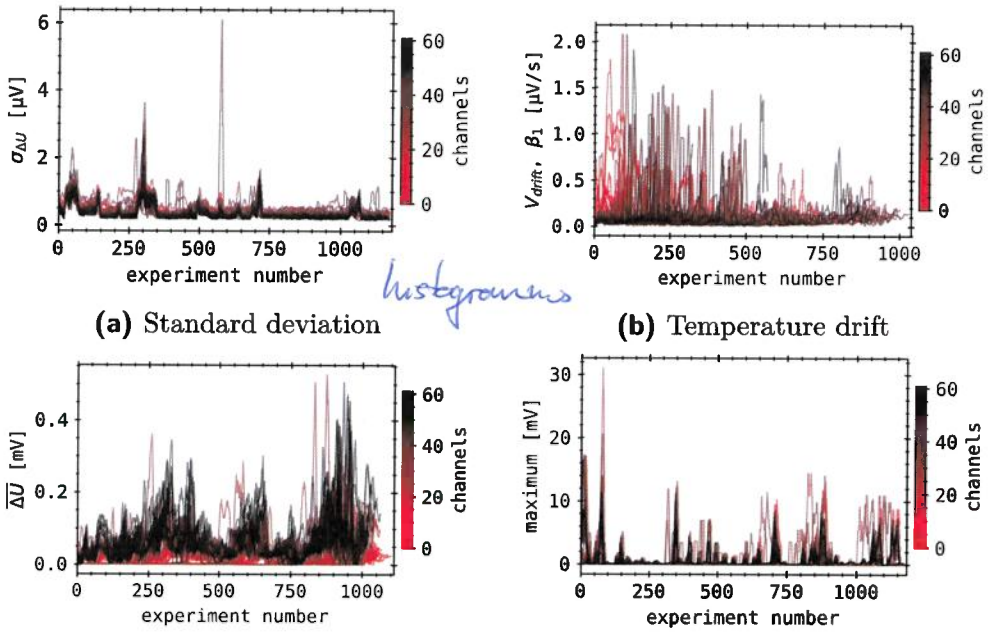

(a) Standard deviation **(b)** Temperature drift

(c) Median **(d)** Maximum

Figure 2.18.: Operational performance numbers of the core bolometry system at W7-X during OP1.2b. (Top Left) Standard deviation from measurements without plasma background, i.e. 100 samples before ECRH starts. (Top Right) Thermal signal drift (positive). (Bottom Left) Median of signal during plasma discharges. (Bottom Right) Maximum signal for every experiment.

2 µV. In single cases, perturbations in the cameras' water cooling can lead to thermal interference, which produces larger offsets and peaks in figure 2.17d. As previously lined out, at typically 10–20 mV acquisition range at 16 bit resolution this compares to the possible minimum 0.15–0.3 µV bit-noise. Figure 2.18 presents the acquisition performance, including the standard deviation, i.e. noise, temperature drift, signal median and voltage maximum. The results of equation (2.20) in figure 2.18a and figure 2.18c portray similar behaviour like the voltage offset in figure 2.17d. Generally, both signal noise and drift are low, predictably in the range of 0.5–1 µV and 0.1–0.5 µV/s respectively. This level of noise is around twofold the minimum possible voltage

property	κ_M $[A^2]$	R_M [Ω]	τ_M [ms]	V_{off} [μV]
median	0.724	0.987	110.57	0.204
deviation	0.0545	0.011	4.93	31.11

property	$\sigma_{\Delta U}$ [μV]	V_{drift} [μV/s]	$\overline{\Delta U}$ [mV]	maximum [mV]
median	0.339	0.057	0.042	1.186
deviation	12.586	27.621	0.032	3.704

Table 2.1.: Median and standard deviation of all previously discussed properties of the calibration and acquisition. Results taken from figure 2.17 and figure 2.18.

resolution, while the thermal interference drift is even smaller. However, assuming a total acquisition time of 10 s, which was a common requirement during the last experimental campaign, this leads to a baseline offset of up to 50 μV towards the end of the measurement. Longer acquisition times lead to greater perturbations, though their correction remains accessible through the simple fit method in equation (2.17). In cases where the thermal load onto the absorber or camera device is increased, this value can change significantly as depicted in the first half of the plot, where individual detectors exhibit spikes of up to 2 μV/s, which is almost ten times as much as the average expected signal drift. The background noise in figure 2.18a is largely consistent throughout the past experimental campaign, with collective peaks across multiple tens of experiments, where $\sigma_{\Delta U}$ reaches up to 2.5 μV. Those peaks extend past one single event, which means they are not linked to experimental circumstances, but revert and flatten out, indicating that they are reversible and not connected to absorber conditions. This is most likely due to issues with the excitation voltage of the Wheatstone bridge by perturbations in the electrical power supply of the diagnostic. Figure 2.18c displays results from equation (2.20), which tries to establish an average gain of the detector signal across OP1.2b. This shows that the expected signal from plasma and stray microwave radiation, as well as thermal perturbation is at least two orders of magnitude larger than the previously discussed drift and noise, and one greater than the average offset. The last figure 2.18d establishes the maximum signal per experiment. Values above

property x	ΔU	$\mathrm{d}(\Delta U)/\mathrm{d}t$	$\mathrm{d}t$	U_0	R_L	f_bridge
value s_x	0.5 µV	1 µV/s	15 µs	1 mV	1 mΩ	1 Hz

property x	C_C	$\Delta I(0)$	$\Delta I(\infty)$	R_C
value s_x	0.5 nF	1 µA	1 µA	1 mΩ

Table 2.2.: Systematic errors and standard deviation of measurement properties that contribute to the bolometer equation equation (2.19).

10 mV repeatedly occur across multiple sessions, i.e. beyond a set of tens of discharges, indicating high performance and high radiation scenarios. This also solidifies the decision to set the range of acquisition to 10–20 mV, depending on the geometric location of the channel - a channel monitoring the scrap-off layer likely yields smaller signals, and therefore performs better at high resolutions or smaller ranges -, so high radiation scenarios are measured adequately.
The previously shown results from figure 2.17 and figure 2.17 have been compiled in table 2.1. Median values are representative of the discussed quality of the calibration process and acquisition. Their standard deviations are a measure to the consistency of the performance, while also indicating how exceptional circumstances, e.g. environmental changes can significantly alter, if not corrupt the measurement results.
Besides analysing the measurement data over a longer period, one can also find an analytical approach to the measurement error. Based on bolometer equation (2.19) the *Gaussian*[I] *error propagation* or *propagation of uncertainty* can be calculated using the values from table 2.2 and the equation for variance of an analytical function with independent variables. Let s_{x_j} be either the standard deviation, if available, or systematic error of variable x_j. Therefore, the systematic error of P_M the power onto the absorber becomes:

$$s^2_{P_M} = \sum_j \left(\frac{\partial P_M}{\partial x_j}\right)^2 s^2_{x_j} = 1.599\,\mu\mathrm{W} \tag{2.21}$$

[I] Johann Carl Friedrich Gauss * Apr. 30, 1777 † Feb. 23, 1855

This error is small, especially when compared to common measurement values of >0.1 mW. Similarly, this characterisation supports the previous findings of small noise levels or large signal-to-noise ratios.

Generally, given a constant background pressure and temperature of the camera, the W7-X bolometer diagnostic performs well within the required specifications, while featuring a high signal-to-noise ratio SNR > 1000 at high temporal resolution for this type of sensor. Results that will later be discussed in this work are within those measurement specifications and have been cleared for consistency.

2.3. Plasma Radiation Power

The goal of the bolometer system at W7-X is to measure the spatial and temporal evolution of the irradiated power from the plasma within its field of view. Ultimately, the bolometer is used to provide a totally calibrated global plasma radiation power loss and the underlying local emissivity. The provided information are critical towards the protection of the machine and experiment control, with regard to plasma profiles and instabilities[65, 99]. In particular, the bolometer measurements are necessary to understand energy loss processes and transport, since the majority of the radiation power is expected to come from intrinsic impurities[100, 101]. This, in turn, is important towards the assessment of the energy confinement quality and performance of the plasma[102]. The tomographic inversion of the line-integrated channel signals can be used to investigate the diffusion and transport of the plasma as well as the impurities[103]. However, the most important task of the bolometer is to provide the radiation power from the plasma, since large radiation losses reduce the in part convective thermal loads on target components and dissipate them into 4π sr, which is highly relevant for the lifetime of the machine and its safety[104].
Following will be an introduction to the methodology of calculating the global radiation power and local emissivity, i.e. a total radiation power loss from the plasma in section 2.3.1 and a radially or two-dimensionally resolved power density at the given field of view of the camera system in section 2.3.2.

2.3.1. Global

The line of sight geometry has been thoroughly introduced and established in detail previously in section 2.2.3. Figure 2.4 shows the conceptional setup of the lines of sight inside the vessel. An understanding of the geometry and transmissivity of the detector-aperture lines of sight are crucial to the development of a global radiation power measurement. The estimation of the global radiative power loss from the plasma will be based on geometric calculations of the individual detectors lines of sight and assumptions about the irradiating plasma volume.
Previously, the total incident power onto a single detector P_M has been established in equation (2.19). Given calibration results for the resistance, cooling time and heat capacity one can thereby calculate the total power for each camera C by their respective detector numbers $M \in S_C$. In order to extrapolate the radiation power measured in the bolometer plane of W7-X to the entire torus one needs to account for the difference in volume and therefore make assumptions about the emissivity distribution along the magnetic field lines. Let the total irradiating plasma volume to be $V_{\mathrm{P,\,tor}}$. A schematic of the radiation domain can be seen in figure 2.19b, where the magnetically confined region and island chain is fully covered. In agreement to Peterson and Zhang et al.[105, 106], three-dimensional EMC3[I]-EIRENE[II] Monte Carlo plasma transport simulations of the scrape-off layer (SOL)[107, 108] indicate that the irradiating volume extends as far as $r_{\mathrm{eff}} = 1.35\, r_{\mathrm{a}}$, the minor (effective) plasma radius from the magnetic axis. Simulations focussing on the intrinsic impurities carbon and oxygen at different heating powers and radiation fractions $0.4 - 0.9$ - the ratio of total radiation power loss and input (heating) power P_{H} - show a total plasma volume of 130% of V_{LCFS}, the volume of the last closed magnetic flux surface.

$$f_{\mathrm{rad}} = \frac{P_{\mathrm{rad}}}{P_{\mathrm{H}}} \tag{2.22}$$

By design, a domain of effective radius $1.3\, r_{\mathrm{a}}$ is necessary to accommodate all lines of sight of the bolometer system adequately inside the vessel, since smaller volumetric projections do not intersect with the line of sight of the outermost channels of the cameras. Assuming the predictive quality of these

[I]EMC3: Edge Monte Carlo 3D; plasma transport simulations in island divertors
[II]EIRENE: neutral gas transport Monte Carlo code

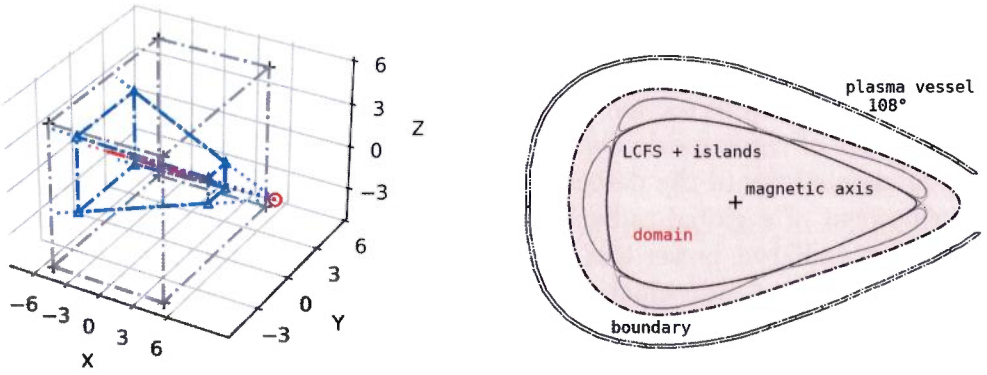

(a) Line of sight volume **(b)** Bolometer plane

Figure 2.19.: **(a)**: Trapezoidal LOS cone through an exemplary volume element. The blue lines indicate the intersection of the line of sight and domain, i.e. test cube. Marked red is the length of the center LOS inside the volume. **(b)**: A schematic assembly of the plasma vessel at 108° toroidally with outlines of the LCFS and attached 5/5-island chain from an exemplary Poincaré map. The estimation domain is marked with the dot-dashed line and red fill pattern. Approximately this equals 130% of the surface area/volume of the LCFS.

calculations to be adequate, EMC3 simulations should be performed for all magnetic configurations, experiment scenarios and machine conditions to find the corresponding irradiating plasma volume. However, this in itself is a very taxing and computationally expensive task and therefore outside the scope of this work. Ideally, the lines of sight of the bolometer cover the whole plasma domain so that the outermost channels yield $P_{\mathrm{M}} \approx 0$, which in contrast will be relevant later on in this work. This is especially important towards boundary conditions of tomographic inversion in chapter 5. The assumption of $V_{\mathrm{P,\,tor}} = f_{\mathrm{P}} V_{\mathrm{LCFS}} = 1.3\, V_{\mathrm{LCFS}}$, where f_{P} is the volumetric factor, generally yields good results, which will later be discussed in more detail for the performance of the tomographic inversion in section 5.4. On should note here that f_{P} is effectively a scaling factor towards the total radiated power loss of the plasma.
As indicated in section 2.2.3, some parts of the detectors are only partially exposed to plasma radiation by the aperture. Hence, one has to establish a relation between the line integral through $V_{\mathrm{P,\,tor}}$ and geometry of detector

and aperture to find the plasma radiation along the line of sight. Let $P_{\mathrm{rad},M}$ be the average plasma radiation along the line of sight of detector M.

$$P_{\mathrm{rad},M} = \iiint \frac{g_{\mathrm{rad}}(\vec{r})}{\widetilde{K}_M(\vec{r})}\,\mathrm{d}\vec{r} \tag{2.23}$$

In equation (2.23), $\widetilde{K}_M(\vec{r})$ is the etendue of detector M and $g_{\mathrm{rad}}(\vec{r})$ the radiation distribution of the plasma. The transmission function $\widetilde{K}_M$ describes how light enters the bolometer and reaches the detector. The measurement of power onto the detector does not distinguish between the parts of the absorber that are hit by radiation. Therefore, the total transmission or etendue no longer is a function of $\vec{r}$ but rather only of detector and aperture geometry, $\widetilde{K}_M(\vec{r}) = \widetilde{K}_M$. Equation 2.1 has already presented the etendue in section 2.2.3.
The zero-dimensional measurement of radiation power per detector and point in time includes a geometric simplification about g_{rad}: one assumes that the radiation is equally distributed along the total line of sight length L_M. In order to introduce the power onto the detector P_M from equation (2.19) to equation (2.23), we arrive at:

$$\begin{aligned}
\iiint g_{\mathrm{rad}}(\vec{r})\,\mathrm{d}\vec{r} &\overset{!}{=} \frac{P_{\mathrm{bolo},M}}{L_M} \equiv \frac{P_M}{L_M}\,, \\
K_M &= \widetilde{K}_M \cdot L_M\,, \\
\Rightarrow \quad P_{\mathrm{rad},M} &= \frac{P_M}{K_M}\,.
\end{aligned} \tag{2.24}$$

Therefore, $P_{\mathrm{rad},M}$ becomes the radiation distribution (density) along the line of sight of detector M. It is also referred to as *chord profile* or *chord brightness*, which will later be introduced more thoroughly in section 2.3.2. The final step towards a global radiation power loss is the extrapolation from the investigated volume of the bolometer camera. Let the line of sight volume of channel M inside the radiation domain be V_M. An example of how this is defined can be seen in figure 2.19a. A more detailed description and examples of volumetric calculations can be found in section 4.3. The

radiation power in the plane of camera C, $P_{\mathrm{rad},C}$ and therefore total radiation power from the plasma P_{rad} can be estimated using:

$$V_C = \sum_M^{S_C} V_M$$

$$\boxed{P_{\mathrm{rad}} \coloneqq P_{\mathrm{rad},C} = \frac{V_{\mathrm{P,\,tor}}}{V_C} \sum_M^{S_C} \frac{P_M V_M}{K_M}, \qquad C \in (\mathrm{HBC},\ \mathrm{VBC})} \tag{2.25}$$

Equation 2.25 denotes the total, global radiation power from the plasma as measured by the bolometer. This quantity will usually be introduced as P_{rad} generally, or $P_{\mathrm{rad,\,HBC/VBC}}$ to specify the camera array that is used to extrapolate from. A set of volumes V_M and etendues K_M for the magnetic standard configuration with $V_{\mathrm{P,\,tor}} = 1.3\,V_{\mathrm{LCFS}}$ for all three cameras can be seen in figure 2.20.
Figure 2.21 shows an example of how the calculations using equation (2.19) and equation (2.25), together with values taken from figure 2.20, contribute to a total radiation power estimation for an experiment in W7-X during the last experimental campaign. The total absorbed power P_M onto the detector from the HBC is roughly half of that from the VBC due to the larger distance between detector and pinhole, reducing the radiation intensity per surface area at the cameras' absorber plane. Expectedly, when accounting for the respective etendues and line of sight volumes $P_{\mathrm{rad,\,HBC}}$ and $P_{\mathrm{rad,\,VBC}}$ represent the same radiative power loss roughly within a 5% margin of error. However, in highly poloidally asymmetric plasma radiation scenarios this deviation can vary strongly. Individual assessments of the local emissivity profiles, which will be discussed further below, or tomographic inversions are necessary to address the radiative power loss adequately in this case.
Given the consistency of the calibration data, volumetric estimations for the required magnetic configuration and measurement data itself, extrapolations made using equation (2.25) have proven fit the radiation level very well when incorporating and comparing to other diagnostics that are used to provide information about the experimental performance. One metric to measure the adequacy of the total radiated power loss by is the *global power balance*. A more detailed discussion of how the accuracy of P_{rad} can be addressed will follow further below in section 2.3.2 and section 2.3.3. One should also note that a different approach, instead of estimating the irradiation plasma region

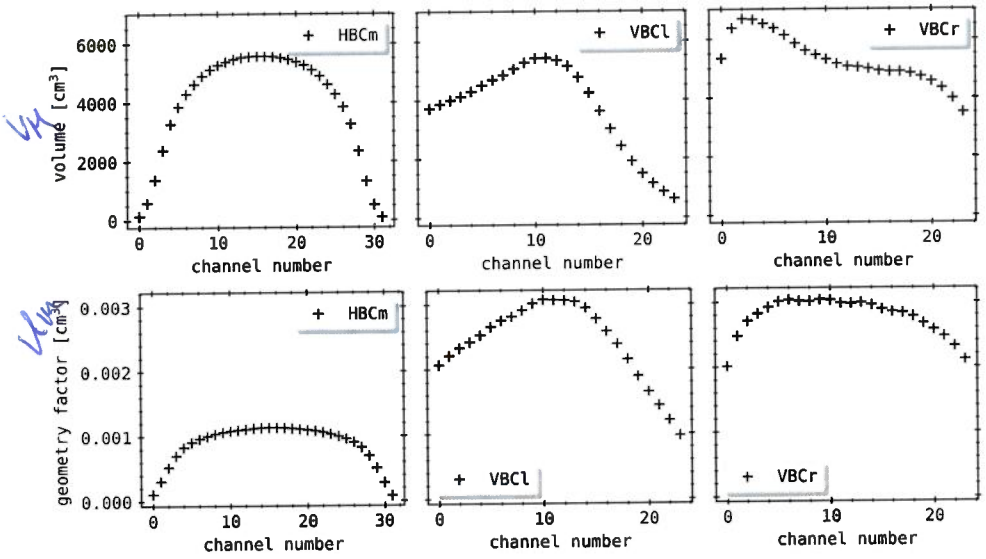

Figure 2.20.: Line of sight volumes V_M (top) and Etendues K_M (bottom) of all camera arrays. Note how the bolometers have been designed in a way that all cameras roughly contribute the same LOS volume, while due to differences in the pinhole design etendues are twice as large for the vertical arrays.

as $V_{\mathrm{P,\,tor}}$ from magnetic equilibrium calculations, is to directly calculate the volume using the boundaries of the radial radiation profile as measured by the bolometer. This will also be discussed in more detail in the next section.

2.3.2. Local

The global radiation power as measured by the bolometer diagnostic has been introduced. In addition to the absolute radiative power loss from the plasma, the local, radially or two-dimensionally resolved emissivity at the given field of view of the bolometer system is just as important in order to understand the impact of plasma impurities and transport on the radiation profile and vice versa.

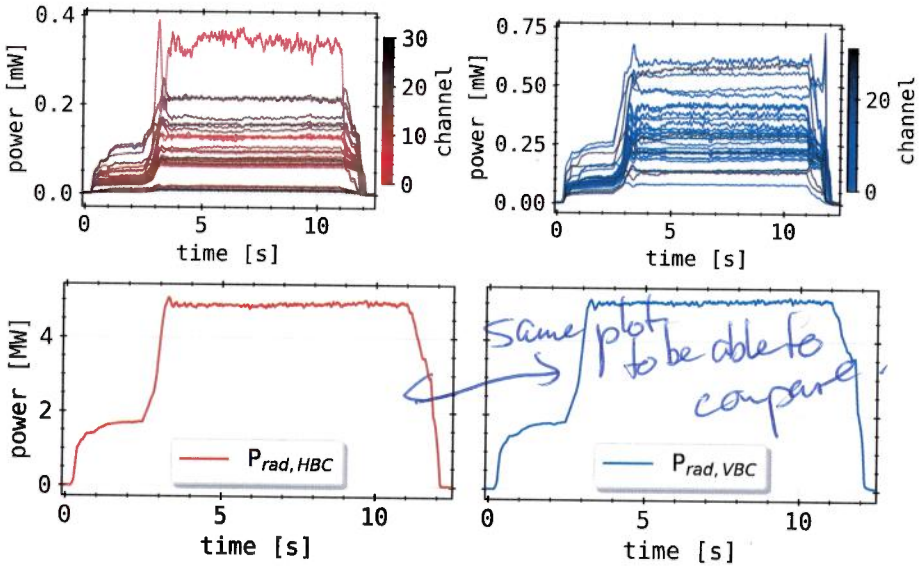

Figure 2.21.: XP20181010.36
(top) Absorbed power per channel P_M by equation (2.19) over time for HBC (left) and VBC (right). **(bottom)** Total radiative power loss as extrapolated from the above detector measurements using equation (2.25). Example discharge with thermal helium beam density control by interferometry in standard magnetic configuration and 5.72 MW input ECRH power, achieving $1.2 \times 10^{20}/\mathrm{m}^3$ and 2.5 keV electron density and temperature, respectively.

Chord Brightness Profile

Let us assume a plasma with $V_{\mathrm{P,\,tor}} = 1.3V_{\mathrm{LCFS}}$ as shown in figure 2.19b. This area can be sectioned in both radial and poloidal direction to create a two-dimensional grid in $\vec{r} = (r, \vartheta)$ from the perspective of the magnetic axis, or $\vec{r} = (r, z, \vartheta) = (r, z)$, i.e. cylinder coordinates as seen from the center of the machine, where $\varphi = 108°$ the toroidal angle in the bolometer plane. Figure 2.22 on the left shows how such a grid can potentially be constructed for any magnetic configuration. As the domain boundary is modelled after the last closed flux surface of that magnetic configuration, the width of those N_r radial sections is coupled to the minor plasma radius r_a, e.g. $\mathrm{d}r = 1.3\,r_\mathrm{a}\,/\,N_\mathrm{r}$ for a $1.3V_{\mathrm{LCFS}}$ domain. Likewise, the N_ϑ poloidal

cross-sections are calculated from the full 2π angle, $\mathrm{d}\vartheta = 2\pi/N_\vartheta$. A common setting would be $N_\mathrm{r} = 20$ and $N_\vartheta = 150$. This method will also be used later for geometric calculations towards tomographic inversions in chapter 5. One should note that increasing both radial and poloidal (and/or toroidal) step counts may introduce numerical artefacts due to overfitting during tomographic inversions of the line integrated measurements.
With equation (2.1) the concept of infinitesimal detector and aperture subdivisions has been introduced. Let us rewrite the integral over both the detector and aperture as a single integral over differential etendues, i.e:

$$\iint_{A,M} \frac{\cos(\alpha)\cos(\beta)}{2\pi d^2} \mathrm{d}A_M \mathrm{d}A_A \overset{!}{=} \int_M \mathrm{d}\widetilde{K}_M \ . \tag{2.26}$$

In order to assess the radiation distribution in the plane of the bolometer cameras one has to know where the line of sight cone is located in three-dimensional space. Therefore, the grid in figure 2.22 has to be extended in toroidal direction for $\pm 2.5°$ to account for the respective tilt of the camera and the width of the line of sight cones. This is done by repeating the same approach as before for flux surfaces of the same magnetic configuration at corresponding toroidal locations. One should note that the grid in this figure is not exactly only constructed from segmented magnetic flux surfaces calculations. This is in fact the projection of the enclosing meshes onto the actual bolometer camera plane, which one remembers to be significantly tilted in toroidal direction. Practically, the pixel corners have been traced in direction of the torus from one VMEC equilibrium to the next. The potential intersections of those lines with the bolometer plane are calculated and constructed into the presented grid. If not stated otherwise, this will be the case for all two-dimensional meshes in the triangular plane from here on.
Let us assume a voxel $v^{(i,j,k)}$, i.e. a six sided polyeder with eight corners made up out of neighbouring grid intersections. The pixels $p^{(i,j)}$ in figure 2.22 are achieved by collapsing, i.e. summation of all voxels at index (i,j) for all N_ϑ toroidal divisions. Let $T_M^{(i,j)}$ be the geometrical contribution, i.e. local sensitivity of the bolometer absorber M to radiation for pixel $p^{(i,j)}$. With $L_M^{(i,j,k)}$ the line of sight section length from differential $\mathrm{d}A_M$ through $\mathrm{d}A_A$

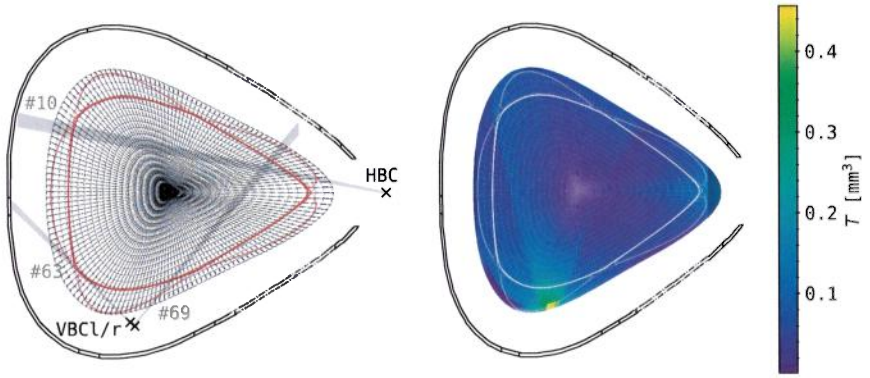

Figure 2.22.: (left): Standard magnetic configuration based grid with 20 radial and 150 poloidal divisions that covers $1.3\,V_{\mathrm{LCFS}}$. Marked are the center position of the individual apertures (black crosses) for all cameras. For reference one line of sight cone (noted in electrical channel number) per camera array has been included. **(right)**: Total geometry contribution per pixel summed up from all three camera arrays.

(see equation (2.26)) inside the voxel $v^{(i,j,k)}$, the geometrical contribution becomes:

$$T_M^{(i,j)} = \sum_{k=1}^{N_\vartheta} T_M^{(i,j,k)} = \sum_{k=1}^{N_\vartheta} \left(\int_M L_M^{(i,j,k)} \mathrm{d}\widetilde{K}_M \right) \tag{2.27}$$

$$T_M^{(i,j,k)} = \begin{cases} 0 & , \; M \text{ not in } v^{(i,j,k)} \\ L_M^{(i,j,k)} \mathrm{d}\widetilde{K}_M & , \; \text{else} \end{cases}$$

The geometrical contribution can be interpreted as the convolution of etendue and line of sight length at a given position. It describes the impact radiation at this location yields onto the absorber. The sum of all camera emissivities can be found in figure 2.22. The etendue $\widetilde{K}_M$ is contributing to $T_M^{(i,j)}$, which again is calculated from the relative camera aperture and detector geometry. For the VBC, the etendues are roughly two times larger than those of the HBC, as seen in figure 2.20, which, in turn, also yields larger $T^{(i,j)}$. Additionally, both VBC array lines of sight overlap close to their respective apertures, thus further increasing the *local sensitivity* in front of the vertical camera relative to its horizontal counterpart.
Equation 2.27 can be used to quantitatively describe the position of the

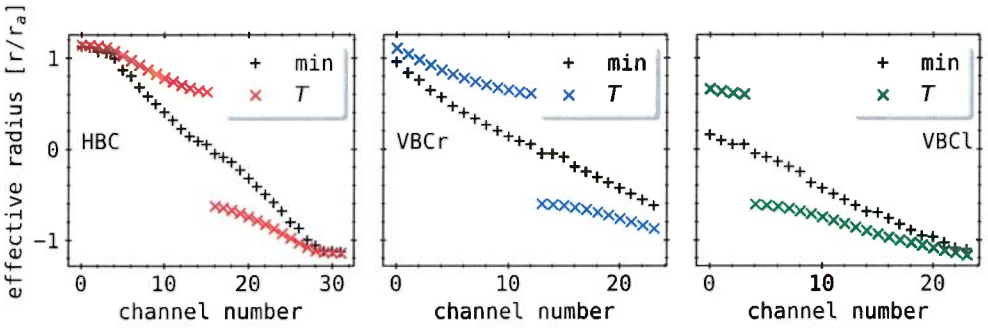

Figure 2.23.: Normalized effective plasma radius r_{eff} in units of the minor plasma radius r_{a}=0.539 m along the line of sight of each detector and camera array. Both methods from equation (2.28)(a) and (b) are shown as 'min' and 'ε', respectively.

line of sight of detector M in two-dimensional space for one toroidal position by attributing each an effective plasma radius $r_{\text{eff},M}$. From magnetic equilibrium calculations, on which the grid around the magnetic axis $\vec{r}_{\text{mag}} = (r_{\text{mag}}, z_{\text{mag}})$ is based, every pixel $p^{(i,j)}$ is given a $r_{\text{eff}}^{(i,j)}$ for their center position $\vec{p}_0^{(i,j)} = \left(r_0^{(i,j)}, z_0^{(i,j)}\right)$. The effective plasma radius of the line of sight of detector M can be written as:

$$r_{\text{eff},M} = \begin{cases} \underset{T_M^{(i,j)}>0}{\text{argmin}} \left(r_{\text{eff}}^{(i,j)}\right) & \text{(a)} \\ \sum_{i=0}^{N_r} \sum_{j=0}^{N_\vartheta} \left(T_M^{(i,j)} \, r_{\text{eff}}^{(i,j)} / \sum_{i=0}^{N_r} \sum_{j=0}^{N_\vartheta} T_M^{(i,j)} \right) & \text{(b)} \end{cases} \tag{2.28}$$

$$\text{sgn}\left(r_{\text{eff}}^{(i,j)}\right) = \begin{cases} -1, & \left(z_0^{(i,j)} < z_{\text{mag}} \vee M \in S_{\text{HBC}}\right) \wedge \\ & \left(r_0^{(i,j)} < r_{\text{mag}} \vee (M \in S_{\text{VBCl}} \vee M \in S_{\text{VBCr}})\right) \\ +1, & \text{else} \end{cases}$$

Equation 2.28(a) and (b) introduce an effective plasma radius for every detector. Method (a) returns the minimum radius along the line of sight of detector M, while method (b) calculates the effective radius by weighting the individual contributions $r_{\text{eff}}^{(i,j)}$ with their respective, normalized $T_M^{(i,j)}$. The sign convention in $\text{sgn}\left(r_{\text{eff}}^{(i,j)}\right)$ is used to distinguish between outboard/up-

side and inboard/downside lines of sight.The normalization of both equation (2.28)(a) and (b) to the magnetic standard configurations minor plasma radius r_a can be found in figure 2.23.
Equation 2.28(a) yields a nearly linear spectrum of radii up until the upper- and lowermost channels of the HBC, where the line of sights only graze the outer pixels. Qualitatively, equation (2.28)(b) yields similar results, as the effective radius is decreasing monotonous for all camera arrays. However, by weighting the individual contributions with their local sensitivity, $r_{\text{eff},M}$ represents the radial position which the respective detector M is the most sensitive to. Although all cameras have detectors covering the center of the plasma and magnetic axis (see figure 2.4), results of equation (2.28)(b) in figure 2.23 do not support this. Disentangling the convolution of line integrated measurements and locally varying emissivities, in order to assess the radiation distribution, therefore poses a great challenge. The simplest representation of the local radiation distribution is given by the chord profile:

$$\boxed{P_{\text{chord},M} := P_{\text{rad},M} \mathrel{\hat{=}} \frac{P_M}{\int_M L_M \, \mathrm{d}\widetilde{K}_M} \mathrel{\overset{!}{=}} \frac{P_M}{\sum_{i=0}^{N_r} \sum_{j=0}^{N_\vartheta} \sum_{k=0}^{N_\varphi} \varepsilon_M^{(i,j,k)}} \,.} \tag{2.29}$$

The chord profile $P_{\text{chord},M}$ describes the average power per volume or average brightness along the line of sight of detector M. Combined results of equation (2.28)(a) and equation (2.29) can be found in figure 2.24. The top figure shows the combined profiles of all cameras for one point in time. The HBC covers the entire volume, whereas a selection of detectors from both vertical arrays link together for a slightly decreased coverage. The included error bars are barely visible for channels with a significant SNR, i.e. $r_{\text{eff},M} \in (-1.0, 1.0)$. Greater uncertainties occur where the SNR is significantly smaller. One should also note that on the positive end of the horizontal camera profile, one channel reports negative values, indicating issues with offset and noise characterisation. The line integrated measurements of all cameras are generally in agreement, with congruence within the last closed flux surface and small differences around the separatrix. This is, however, rather an exception than the rule and will be discussed in more detail in section 3.2.1 and section 5.4. The temporal profile evolutions in the bottom figure show a rapid inwards transition of plasma radiation between 3.1–3.35 s. Similarly to the above, profiles for all times from the HBC and VBC indicate radiation mainly from the plasma edges, with decreased intensity in

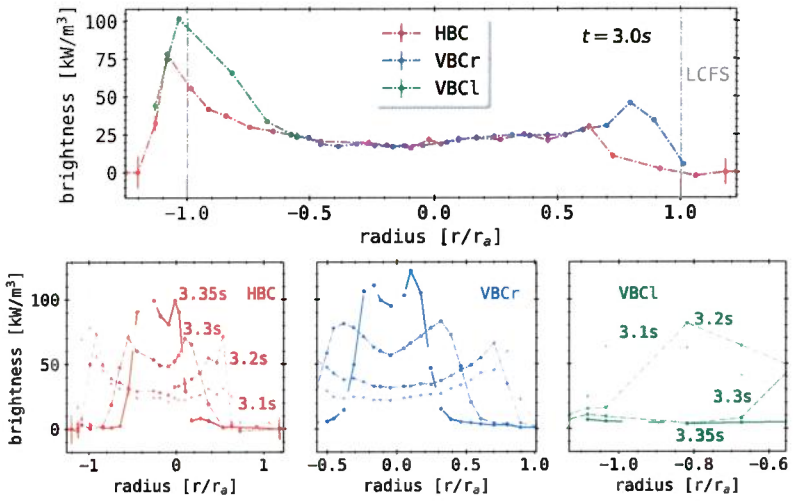

Figure 2.24.: XP20180725.44

Example chord brightness profiles for equation (2.29) at **(top)** 3.0 s and **(bottom)** a temporal evolution between 3.1–3.35 s. Plot abscissa is given by the minor plasma radius normalization of equation (2.28)(b). The location of the last closed flux surface at 1.0 (-1.0 respectively) has been marked. This discharge was performed in a high magnetic mirror configuration at 1.3 MW ECRH power.

the core of the discharge and a steep drop-off outwards. The profiles of the horizontal camera and right vertical array are not symmetric around the magnetic axis, i.e. $r_{\text{eff}} = 0$. They show a small radial displacement towards the lower, inboard side of the plasma, i.e. $r_{\text{eff}} < 0$ or $z < z_{\text{mag}}$ and $r < r_{\text{mag}}$. The chord brightness represents a convoluted radial radiation profile that can yield information on plasma asymmetry and power loss. Under certain assumptions the chord profile can also indicate dominant impurities that contribute to the cooling of the plasma. For more reference see section 4.4.

Radial Profile and Tomography

With the multichannel, multicamera bolometer system at Wendelstein 7-X the line integrated measurements can be used to perform tomographic inversions in order to obtain two-dimensional radiation distributions in one plane of the device. Tomographic reconstructions are generally used to solve

multidimensional geometric problems of inversion to find solutions for a system with a finite number of projections. Different mathematical models exist in order to invert the line integrals of the projections. In the case of the two-camera W7-X bolometer system in the triangular shaped plane, the number of free parameters, represented by the total number of pixels, is far greater than the number of constraints, i.e. the line of sight intersections. Such an *ill-posed*, or *under-constrained* problem is difficult to solve and requires mathematical effort and *a priori* information or assumptions about the potential profile.
For simplification, assume the measurement system and distribution profile to be in one plane of $(x,\, y)$. Let r be the distance to the coordinate center and ϑ the enclosed angle between $\vec{r} = (x,\, y)$ and $\vec{e}_x$ the unit vector in x direction. Also, let $f(x, y)$ be an unknown distribution. The line integral along L and its parametrisation with $x(t) = t\sin(\vartheta) + r\cos(\vartheta)$ and $y(t) = -t\cos(\vartheta) + r\sin(\vartheta)$ are used in:

$$\begin{aligned} \mathcal{R} f_L &= \int_L f(x,y)\,\mathrm{d}L = \int_{-\infty}^{\infty} f(x(t), y(t))\,\mathrm{d}t\ , \\ f(r,\vartheta) &= \int_0^{\pi}\int_{-\infty}^{\infty} \mathcal{R} f(r',\vartheta)\cdot h(r-r')\,\mathrm{d}r'\mathrm{d}\vartheta\ . \end{aligned} \tag{2.30}$$

The simplest reconstruction problem is therefore given by the *Radon*[I] *transform* $\mathcal{R} f$ and *filtered back-projection formula* in equation (2.30). The convolution function $h(r)$ is a highpass filter, thus giving the method its name, and has the *Fourier transform*[II] $\mathcal{F} h = \hat{h}(\omega) = \|\omega\|$[109]. An *ill-posed* problem requires the filter $h(r)$ to be an irregular *filter kernel* - the matrix representation of $h(r)$ is non-invertable and singular. Discrete, regular kernels can be used when regularisations are applied to the solution and filter, e.g. a certain degree of smoothness. The filtered back-projection in Equation 2.30 can be performed in the frequency domain by applying forward and backward Fourier transforms to the integral:

$$f(r,\vartheta) = \int_0^{\pi} \mathcal{F}^{-1}\left(\mathcal{F}\mathcal{R} f_{\mathrm{L}}(\omega)\,\|\omega\|\,k(\omega)\right)\mathrm{d}\vartheta\ . \tag{2.31}$$

The window function $k(\omega)$ is used as a regularisation to the solution domain and to suppress high frequency range noise[110].

[I] Johann Karl August Radon * Dec. 16, 1887, † May 25, 1956
[II] Jean-Baptiste Joseph Fourier, * Mar. 21, 1768 † May 16, 1830

The simple filtered back-projection in equation (2.30) is not suitable for an ill-posed problem such as the two-dimensional radiation distribution reconstruction from bolometer measurements in W7-X. Although fast Fourier transformations (FFT) and the Radon transform itself are computationally very efficient, applicable regularisations to equation (2.31) do not fit the underlying physical problem well since they can not correct potential errors in the imaging or measurement system (geometry), which is why the approach has widely been replaced by *iterative* solvers.
Plasma projections along the lines of sight of the bolometer diagnostic are few due to intrinsic design requirements and limited accessibility. The inversion yields a high risk of overfitting - the introduction of numerical artefacts and corrections - due to the unfavourable ratio of free parameters *(pixels) and constraints (lines of sight), i.e. *ill-posedness*. Therefore, regularisation algorithms with constraints have to be applied. They provide additional *a priori* information, e.g. smoothness or weighting based on location[111]. A commonly used, simple algebraic expression for such an algorithm is the *Tikhonov*[III] *regularisation*. Let $\mathbf{T} \in \mathbb{R}^{n \times m}$ be a known matrix of parameters and coefficients regarding the measurement or imaging systems, e.g. geometry and transmission matrix, and $\hat{\vec{b}} \in \mathbb{R}^n$ a vector representing the measurement values itself from the line integrals. The algorithm tries to find $\vec{x} \in \mathbb{R}^m$ the discretized emissivity values on a pixel or voxel grid, such that the regularisation problem becomes[112]:

$$\begin{aligned} \mathbf{T}\vec{x} &= \hat{\vec{b}} \\ \eta := \vec{x}^{(\mu)} &= \left(\mathbf{T}^\intercal \mathbf{T} + \mu^{-1}\mathbf{I}\right)^{-1} \mathbf{T}^\intercal \vec{b} \\ \eta^\intercal \eta &\xrightarrow{\min} c^{(\mu)} \\ \min_{\eta} &\left\| \left(\vec{b} - \mathbf{T}\eta\right)^\intercal \left(\vec{b} - \mathbf{T}\eta\right) + \mu \left(\eta^\intercal \eta - c^{(\mu)}\right) \right\| \\ \chi &= \vec{b} - \hat{\vec{b}} \end{aligned} \tag{2.32}$$

The diagonal identity $\mathbf{I} \in \mathbb{R}^{m \times n}$ and $\mu > 0$ are called *regularisation*. The error of the iteration in η is called χ. The matrix $\mathbf{T}^\intercal\mathbf{T} + \mu^{-1}\mathbf{I}$ has a high condition, i.e. is ill-conditioned. The solution η is therefore more sensitive to the error χ when μ is large. Because of the ill-conditioning of the matrix

[III] Andrey Nikolayevich Tikhonov, Oct. 17, 1906 † Oct. 7, 1993

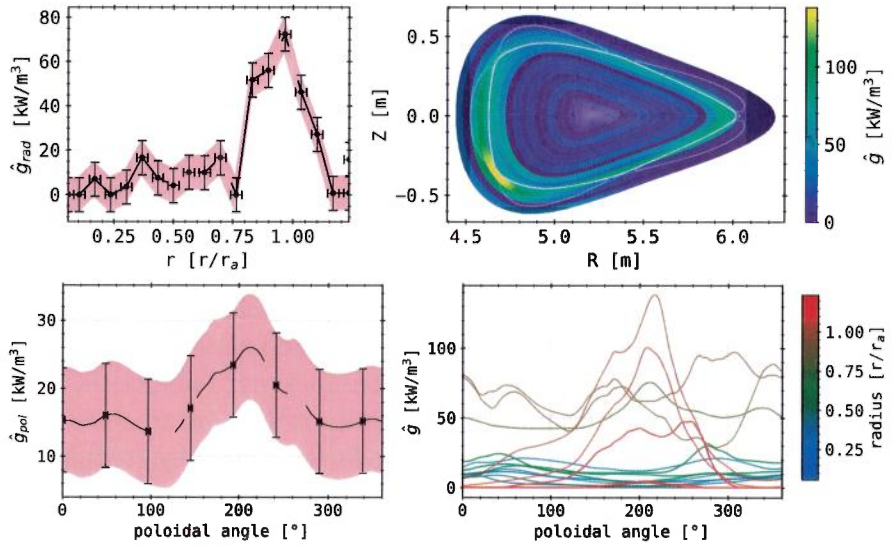

Figure 2.25.: XP20180725.44
Example of local radiation distribution profiles at $t = 3.0\,\mathrm{s}$. **(top-left)**: Poloidally averaged radial radiation profile with absolute vertical and lateral error bars. **(top-right)**: Two-dimensional radiation distribution, with Poincaré overplot of plasma islands and separatrix. **(bottom-left)**: Radially averaged poloidal radiation profile with error bars. **(bottom-right)**: Individual poloidal radiation distribution.

$\mathbf{T}$ and the error η, the vector $\vec{x}^{(\infty)}$ typically is not a sensible approximation of $\vec{x}$. Finite values of μ have to be chosen in order to obtain a meaningful solution to the above problem. Generally, by design, stronger regularisations yield reconstructions that are closer to the desired solution, but may lead to large error values[112].
There are other approaches to solve ill-posed inversion problems of line integrated measurements. The *minimum Fisher* regularisation in chapter 5 is currently being used with the bolometer diagnostic at W7-X.
Let us assume an arbitrary inversion that yields a radiation distribution

$\hat{g}(\vec{r})$ in the plane of the bolometer cameras. Both radial and poloidal maps of the radiation distribution can be written as:

$$\hat{g}_{\mathrm{rad}}(r) = \int_0^{2\pi} \hat{g}(r,\vartheta)\,\mathrm{d}\vartheta\,, \tag{2.33}$$

$$\hat{g}_{\mathrm{pol}}(\vartheta) = \int_0^{f_{\mathrm{P}} r_{\mathrm{a}}} \hat{g}(r,\vartheta)\,\mathrm{d}r\,. \tag{2.34}$$

Figure 2.25 shows an example for a two-dimensional radiation distribution and its poloidal and radial integrals in accordance to equation (2.33) and following. The map is based on geometric arguments and the grid discussed in the previous section, especially equation (2.27). Radiation has been reconstructed mainly in the shape of a three to five cell wide ring along the separatrix. The X-point on the lower inboard side however has a maximum that is approximately twofold the average intensity of the radiation ring. Consequently, assuming equal drop-off lengths around the plasma the ring is widened on the inboard side. The radial profile in $\hat{g}_{\mathrm{rad}}$ indicates that the radiation is mainly located inside the last closed flux surface, where the intensity increases sharply towards the maximum at $0.95 r_{\mathrm{a}}$. Presented error bars are, on one hand, derived from the mathematical penalty of the inversion algorithm, i.e. the absolute error in emissivity as noted by χ in equation (2.32). On the other hand, the error in resolution of the resulting profile is given by half of the width or height of the cells. Plots of individual radial position in the bottom left of figure 2.25 accentuate asymmetries that are functions of the poloidal angle. The distinct radiation peak is found here between $0.9 - 1.1 r_{\mathrm{a}}$ at the lower inboard X-point around $230 - 240°$. The average poloidal profile is similarly shaped and supports the previous observations, however at a much lower intensity. This is due to the contribution of the mostly dark areas of the reconstructed image where no emission has been reconstructed by the algorithm.
The application of an inverse reconstruction algorithm that is tailored towards the problem posed by the previously introduced bolometry system is considered to be best practice in order to assess the local radiation distribution. This however requires a number of assumptions about and *a priori* knowledge of the mathematical procedure and its behaviour, as well as the physics that govern the measurements. A mathematical tool like the

Tikhonov regularisation with the *Fisher*[I] *information* as a constraint or regulator is of great value towards the understanding of plasma radiation and the underlying impurities. The latter will be characterised in much more detail and an example algorithm outlined in chapter 5.

After having introduced local and global radiation power measurements from the bolometer one can take the next step and use this knowledge for plasma performance characterisation. The next section will discuss the power balance involving the global power estimation derived in the previous section with equation (2.25).

2.3.3. Power Balance

Addressing the power balance, and thereby the underlying conservation of energy, of input heating and external losses, i.e. perpendicular transport across magnetic field lines or radiation, is a critical tool for characterising plasmas in magnetically confined fusion devices. Furthermore, it is crucial for the desirability of magnetic fusion and therefore the success of a potential plasma fusion power reactor[113]. It is important to have an understanding of the physical processes that are connected to the heating and power exhaust, which vice versa can profit from thorough experimental investigations on the plasma power balance. For example, the power loss through impurity radiation is, in addition to being practically unavoidable especially in large scale fusion devices, mandatory in a reactor to reduce the heat flux densities to the targets by dissipation of power in the plasma volume. This radiation, plasma parameters like density and temperature, and the resulting transport are strongly and non-linearly coupled[114].
A simple approach to the (global) power balance is the zero-dimensional (0-D) treatment of the conservation of energy. This 0-D model is derived from a full set of three-dimensional fluid equations by making a number of assumptions. Let a pure plasma with $n_e \approx n_I = n$ the particle number densities of electrons and ions and $n_Z \ll n$ of impurity species Z. Similarly, the particle temperatures are $T_e = T_I = T$. The plasma is assumed to be

[I]Sir Ronald Aylmer Fisher Feb. 17, 1890 † July 29, 1962

fully ionized and in thermodynamic equilibrium. Therefore, the internal energy density U_j and particle pressure p_j of species j are

$$U_j = \frac{3}{2} n_j T_j = \frac{3}{2} p_j \ , \qquad p_j = n_j T_j \ .$$

Deriving from the conservation law for energy in fluid dynamics and using the (fluid) velocity $\vec{u}$ one yields the conservation of energy for a zero-dimensional ansatz as[113]:

$$\frac{3}{2}\frac{\partial p}{\partial t} + \frac{3}{2}(\nabla \cdot p)\,\vec{u} + p\nabla \cdot \vec{u} + \nabla \cdot \vec{q} = s \ . \tag{2.35}$$

The right-hand side of equation (2.35) combines energy sources and sinks in s. The first term on the left-hand side describes the energy density variation. A net flux of plasma energy is accredited for in the second term. The third term accounts for changes in energy density under plasma expansion or shrinkage. Finally, the fourth term on the left denotes energy losses through diffusive processes as an energy density current $\vec{q}$.
At a magnetically confined plasma fusion device the sources and sinks term can be written as[115]:

$$s = s_{\mathrm{H}} - s_{\mathrm{rad}} \ .$$

Therein noted energy density input and losses are: s_{H} the gain from the input heating and s_{rad} the dissipation via plasma radiation.
Integrating equation (2.35) over the volume of the plasma yields the simplified null-dimensional global energy balance.

$$\begin{aligned} 0 &= \frac{1}{V_{\mathrm{P}}} \int_{V_{\mathrm{p}}} \left(\frac{3}{2} \left(\frac{\partial p}{\partial t} + (\nabla \cdot p)\,\vec{v} \right) + p\nabla \cdot \vec{v} + \nabla \cdot \vec{q} - S \right) \mathrm{d}\vec{r} \\ &= -S_{\mathrm{H}} + S_{\mathrm{rad}} + S_{\mathrm{div}} + \frac{1}{V_{\mathrm{P}}} \int_{V_{\mathrm{p}}} \left(\frac{3}{2} \left(\frac{\partial p}{\partial t} \right) + p\nabla \cdot \vec{v} + \nabla \cdot \vec{q} \right) \mathrm{d}\vec{r} \\ 0 &= S_{\mathrm{H}} - S_{\mathrm{rad}} - S_{\mathrm{div}} - \frac{\mathrm{d}W}{\mathrm{d}t} = S_{\mathrm{bal}} \end{aligned} \tag{2.36}$$

In equation (2.36) the volume integral over the net plasma energy flux $3/2\,(\nabla \cdot p)\,\vec{u}$ was accounted for as the convective energy loss to a target S_{div}. The plasma stored energy is W. Experimentally there are, as of now, two possibilities of assessing this number: estimating the total kinetic energy

W_{kin} using density and temperature profiles or measuring the diamagnetic energy W_{dia} with a separate diagnostic.

$$W \approx W_{\text{kin}} = \frac{3}{2}\int_{V_{\text{P}}} \sum_j n_j T_j \frac{\mathrm{d}V}{\mathrm{d}r}\mathrm{d}r$$

Using the kinetic energy as an estimator, although while being analytical, has some drawbacks: derivation of $\mathrm{d}V/\mathrm{d}r$ is based on magnetic equilibria, the working gas ion density n_{i} is assumed to be equal to n_{e} and the contribution of plasma impurities is difficult to address experimentally. Neglecting impurities in W_{kin} shows larger values of around 25%, which again varies with species and density of said impurity, when comparing to the diamagnetic energy[115]. Furthermore, electron density and temperature profiles from the *Thomson scattering* diagnostic that have been provided during the previous experimental campaign were very sensitive to inconsistencies in both calibration and laser adjustment[116, 117]. Multiple diamagnetic loops at various locations of W7-X measure magnetic flux changes of the plasma. Those changes are directly related to the plasma stored energy. Thus,the diamagnetic energy, given an adequate model for compensating external magnetic flux contributions, has been consistently and accurately provided by a dedicated diagnostic[118].
The total time derivative of the energy balance in equation (2.36) yields the power balance of the plasma, with $P_{\text{H}} = P_{\text{ECRH}}$ the input microwave electron cyclotron heating:

$$\boxed{0 = \frac{\mathrm{d}}{\mathrm{d}t}S_{\text{bal}} \stackrel{!}{=} P_{\text{bal}} = P_{\text{ECRH}} - P_{\text{rad}} - P_{\text{div}} - \frac{\mathrm{d}W}{\mathrm{d}t}} \tag{2.37}$$

Equation 2.37 *de facto* sets the global power balance to zero. However, in practice, when characterising P_{bal} using experimentally measured values for the contributing sources and losses, each one introduces errors through simplifications in their respective models and measurement techniques.
The radiative power loss P_{rad} is based on an approximation for the irradiating plasma volume and geometric model for the lines of sight. Additionally, equation (2.25) assumes toroidal symmetry of the plasma radiation, while Zhang et al. have previously found that this is not necessarily the case. Analysis of bolometry data from past experimental campaigns, based on comparisons with other diagnostics involved in the power balance in equation (2.37),

way too low realistically (does neglect target radiation load for example)

indicate a 5% error for the proxy of the global P_{rad} from equation (2.25) derived in section 2.3.1. Recently, it was discussed that there might a previously neglected contribution of the vessel heat load through plasma radiation from the main chamber. This error is expected to be as large as 25% of P_{rad} in certain scenarios. In addition, the value of input microwave heating power P_{ECRH} is noted to have an intrinsic error of 10%[119]. Finally, the divertor target power load P_{div} has to be measured. A thermography system consisting of ten infrared cameras, observing all divertor units measure the surface temperature and provide the total power load[120]. Discrepancies in the measurement of the total target power load occur due to errors in the infrared measurement and its mapping to the individual divertor elements, as well as toroidal asymmetries and errors in the heat transport analysis code THEODOR[I]. Peak heat loads are found to have an intrinsic error of up to 10%[120].

An example for the power balance derived in equation (2.37) and the respective quantities involved can be seen in figure 2.26. The ECRH delivers, after an initial, slightly decreasing stage of 1.3 MW within the first 0.8 s of the plasma discharge, a constant 0.55 MW of microwave power for the duration of 28 s. The resulting individual divertor target heat loads are below 100 kJ per module and within the previously discussed error bar of the thermography diagnostic, indicating a toroidally symmetric heat load distribution. The total, integrated target load varies across the experiment duration, but remains below 0.5 MW with a gradual increase from $\approx$ 0.2 MW and two drops around 1.75 s and 8.5 s. After shut-off of the heating power, the remaining heat load drops below 250 kW, but immediately increases again to about 300 kW. Bolometer measurements and calculations of the global radiative power loss with equation (2.25) present a slowly increasing radiation level from 0.15 MW after the initial heating stage to 0.25 MW at the termination of ECRH. Within the first 0.5 s, P_{rad} rises to 0.25 MW drops below 0.2 MW again. After microwave heating shut-off, the radiation power peaks with 0.55 MW due to irradiating the remaining plasma energy and recombinations, before sharply decreasing to zero. The diamagnetic energy W_{dia} quickly peaks at 220 MJ within the first 0.5 s, from which a small drop and increase are followed by a gradual decline with small perturbations to 180 kJ at the end of the discharge. The resulting time derivative $\mathrm{d}W_{\text{dia}}/\mathrm{d}t$

[I]THEODOR: thermal energy onto divertor

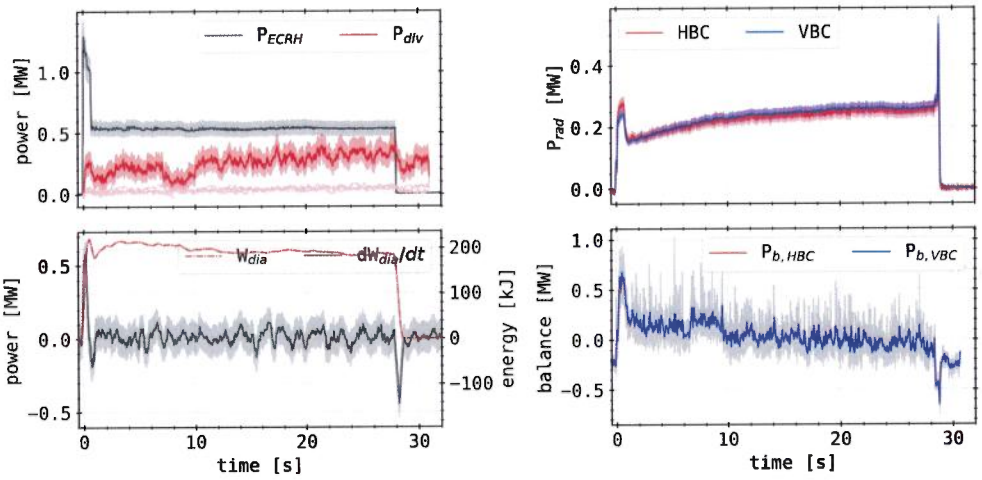

Figure 2.26.: XP20180808.4
Example for power balance as in equation (2.37). **(top-left)**: Microwave power and divertor target heat loads, including individual elements **(top-right)**: Radiative power loss as measured by the bolometer cameras **(bottom-left)**: Plasma stored energy measured by diamagnetic loops and its time derivative **(bottom-right)**: Individual power balance for both bolometer cameras (blue, red) and a general result from the mean with error bar (grey).

rises to 0.6 MW, as W_{dia} goes towards its maximum, and turns over for the enclosed small drop. Over the duration of the experiment, $\mathrm{d}W_{\mathrm{dia}}/\mathrm{d}t$ drifts around zero, although the plasma energy clearly presents a declining slope. At ECRH termination this energy is exhausted from the plasma and its time derivative indicates negative 0.45 MW. → So, the errorbars are 20–100x. !!
The resulting global power balance is generally satisfied within the given error bar, i.e. $P_{\mathrm{bal}} \approx 0$. However, there still persist non-negligible discrepancies in the power balance that are not accounted for in the previously discussed plasma properties. For example, in the beginning of the experiment, an excess of heating power is indicated, as well as the radiation peak after shut-off leads to a large negative balance. Also, one of the drops in target heat load around 8.5 s can not be explained by this model.
Further exemplifying this issue are the results shown in Figure 2.27. This is the same experiment as previously discussed in the examples shown in

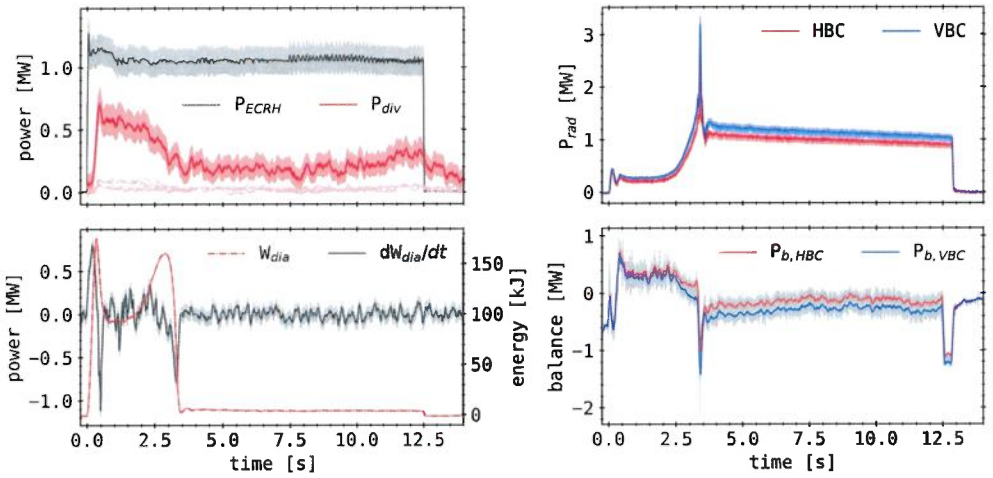

Figure 2.27.: XP20180725.44
Example discharge as previously exhibited. **(top-left)**: ECRH power and divertor target heat loads **(top-right)**: P_{rad} as measured by the bolometer cameras **(bottom-left)**: Plasma stored energy measured in W_{dia} and its time derivative **(bottom-right)**: Power balance for both bolometer cameras (blue, red) and their mean.

section 2.3.2 and figure 2.24 and figure 2.25. The heating power is delivering a constant 1 MW for 12.5 s. The displayed individual heat loads are well below 200 kW. The divertor heat rises with non-negligible retardation to the engagement of the ECRH and only slowly decreases after its shut-off. Following a peak heat load of 0.6 MW around 0.1 s, P_{div} decreases with a rate similar to the increase of P_{rad}. The remaining heat load drifts between 0.2–0.3 MW. Bolometric measurements of this discharge indicate a rapid increase of radiation from the engagement of the heating to 3.0 s, where previously a significant shrinkage of the plasma was discussed in section 2.3.2 with figure 2.24. In the following 2 s the radiation power is substantially larger than the input heating. This is a strong indication for errors in the volumetric estimation of equation (2.25), especially considering the results of P_{bal} and $\mathrm{d}W_{\mathrm{dia}}/\mathrm{d}t$ for those times. From there on, P_{rad} very slowly decreases until plasma termination, about 0.5 s after heating shut-off, where it still measures about 1 MW. The diamagnetic energy sharply rises to its maximum at 0.5 s of 175 kJ and then drops to 100 kJ, before it quickly in-

creases again to 160 kJ towards the plasma collapse at 3.1 s. After that the remaining plasma stored energy almost zeros and is as small as 50 kJ.
The resulting power balance shows large deviations from zero, indicating inconsistencies between the physics of the presented plasma and the model of the power balance equation (2.37). At the start of the discharge P_{bal} in figure 2.27 appears to be a poor measure for energy conservation. After ECRH start-up P_{bal} quickly turns negative and immediately inverts due to the simultaneous increase of P_{rad}, $\mathrm{d}W_{\mathrm{dia}}/\mathrm{d}t$ and the reversal of the latter. Before 3.0 s the power balance indicates an excess of heating power that is not accounted for in any of the above. Towards the maximum of radiation power at 3.1 s, P_{bal} turns negative again, while $\mathrm{d}W_{\mathrm{dia}}/\mathrm{d}t$ is also negative, indicating that P_{rad} greatly overestimates the true radiative power loss in this case. The balance then drifts towards zero until the termination of ECRH, were radiation from the collapsing plasma lead to a negative pedestal that fades with its extinction.
The presented global plasma power balances exemplify the applicability of the model discussed in equation (2.37). One expects scenarios with fast plasma transitions, i.e. strong perturbations and variations in profiles or plasma properties, to be not very well described by this approach. Though it is assumed that steady state conditions are represented much better by this model.

→ conclusion on errorbars:

local 20-100% at low P_H
20-50% high P_H

average 20-50%.
~ 20-30%.

It is a good description that is relatively complete, well-balanced and well structured.

decreasing in contrast to the whole scrape-off layer[129]. One might also say that the limiting surface shifts inward and becomes a *pseudo wall* with steep increase in neutral pressure profile. For a significant plasma power exhaust in the SOL and subsequent profile changes, edge radiation from low- to medium-Z impurities, Z being the atomic number, might be necessary. This is being investigated upon in many magnetically confined plasma fusion experiments[123, 124]. Additionally, the feasibility of a divertor concept is characterised by its stable performance and resilience against thermal or radiative collapse in scenarios with plasma detachment. Among important features are a high efficiency of particle exhaust under conditions of reduced recycling flux. Furthermore, at high radiation power losses, impurities should be transported into and retained inside the scrape-off layer to prevent accumulation of the core plasma. Finally, the most critical attribute and limit of such a divertor is its capability to remove power from the plasma and to dissipate this heat load.

For the stellarator Wendelstein 7-AS, which, in comparison to W7-X, featured a similar magnetic configuration space at a smaller volume, major radius and rotational transform and therefore poloidal mode number of edge islands, EMC3-Eirene simulations indicate that the majority of intrinsic impurity radiation from carbon is located at the *X-points*. Those are intersections of inner and outer separatrices, in-between magnetic islands[130]. Around X-points the radial width of magnetic field lines is largest, which greatly reduces the power transport across the field lines and therefore enables condensation of radiation[122, 131]. Simulations of impurity radiation and transport of the scrape-off layer for Wendelstein 7-X indicate that the radiation is also located around X-points. Additionally, the separatrix impurity density and neutral particle pressure at the divertor depend on the island configuration, i.e.geometry and size. Calculations show an optimum of impurity radiation for the efficiency of recycling neutrals. Around 60% to 70% (from input) of impurity radiation power loss yield adequate particle and power exhaust. The divertor neutral pressure is expected to decrease, while the impurity density and radiation front shifts inward towards the separatrix for power loss fractions of 80% and above - as calculated before in f_{rad} by equation (2.22). It is assumed that detached, higher density scrape-off layers are operational at lower impurity concentrations and higher neutral pressures. For some configurations of SOL islands, the neutral particle recycling flux does not refuel the core plasma, which possibly offers an independent

3 Plasma Radiation Feedback Control

On the way to a magnetically confined plasma fusion reactor it is of ~~up~~ut-most importance to develop a strategy to remove as much energy from the scrape-off layer in order to minimize the thermal power load onto vessel components[121–125]. A ~~decreased plasma flux across the separatrix is also~~ favourable due to the reduction of erosion rates, tritium retention and neutron ~~permeation for potentially all-metal plasma facing elements of such a reactor~~. Strong plasma power losses in the scrape-off layer lead to changes in the density and temperature profiles therein. The resulting ~~transport~~ power flux along the open field lines at ~~this point~~ to the targets, i.e. the *plasma exhaust*, decreases significantly and therefore the load on limiting (divertor) elements is reduced[123]. A theoretical scenario to visualize could be the one proposed by Tenney et al.[126]: the neutral pressure close to the divertor is assumed to be relatively high, while impurity radiation, i.e. from extrinsically seeded argon in this case, causes the plasma temperature to drop tremendously outside the separatrix along the divertor channel. The latter is defined as the collection of open magnetic field lines that cross the limiting surface. This is accompanied by a high particle recycling regime, ~~including incident working gas ion backscattering, trapping, diffusion, re-emission and desorption at or close to the plasma boundary~~[127, 128]. In front of the divertor the recombination rate is increasing to the point where no plasma flux is expected to reach the wall due to the very low temperature, high neutral and low plasma pressure. This state is called ***detachment*** or ***plasma detachment*** and can also occur partially, where only the ion flux close to the separatrix is

rephrase

put to introduction

control of both densities[121].
In order to achieve this desired level of plasma control in magnetically confined fusion devices, the external seeding of impurities is inevitable to increase the power exhaust in the scrape-off layer in a controlled manner[121, 123–125]. However, an unprompted, continuous feeding of the plasma with an extrinsic impurity will eventually corrupt the scrape-off layer and lead to a radiative collapse. A predictive system to describe and inject low- to medium-Z impurities into the SOL of W7-X to increase the radiation power loss and exhaust, potentially achieving controlled plasma detachment, is needed. Similar systems that control the plasma density via ~~high pressure~~ gas ~~boxes~~ have been used and verified in past experimental campaigns at ~~the stellarator~~. They are installed inside the vessel about 20 cm from the last closed flux surface, where each of them can be operated independently with a standalone or predetermined mixture of working gases like H, He, Ar or Ne. Incidentally, plasma density control is one of the most important but equally evident requirements to the experimental exploration of a plasma fusion device[97, 132, 133].
The two-camera resistive bolometer system at W7-X provided a real time evaluation of the global radiative power loss for plasma feedback purposes during the ~~last~~ experimental campaign. Its application has been designed, tested, implemented and verified before and during the procedure of OP1.2b. A set of lines of sight has been used to estimate the radiation level for plasma control, with fast auxiliary gas fuelling as an actuator. Actuator of the ~~impurity seeding~~ was ~~the~~ *thermal helium beam diagnostic*[134].

This chapter will introduce and characterise the real time bolometer feedback system. This also includes a brief introduction of the thermal helium beam and other connected diagnostics that have been designed to achieve plasma control and possibly stable detachment through seeding of impurities. After introducing the hardware and software setup of the system, laboratory tests for the performance of the feedback will be presented. Finally, the results of experiments incorporating plasma radiation feedback are shown, including a comparison to other feedback candidates and a discussion of potential advantages and disadvantages.

3.1. Configuration

During the last experimental campaign, the stellarator Wendelstein 7-X was operated in island divertor configuration for the first time. The corresponding toroidal length of open field lines, which are pathways of heat flux to the wall and eventually end on plasma facing components, increased about ten-fold in comparison to the limiter scrape-off layer, which was explored during the very first W7-X startup campaign. Results of the first divertor experiment campaign, previous to the one mentioned above, presented target heat fluxes that promise stable operation at high density[135]. This operation phase also featured the first, as well as second and third, *boronisation* or *boronised wall* in this machine. Improvement of wall conditions through boronisation is considered a standard technique to reduce the ~~exhaust~~ release of intrinsic impurities, most prominently carbon and oxygen, from plasma facing components into the plasma[136–141]. A thin film of diboron B_2 $(\cdot)$ compounds is deposited onto plasma facing components, which are inert when exposed to molecular oxygen and do not show any oxidation in plasma environments. They are amorphous, transparent and kinetically hard. Boronised walls show overall lower chemical reaction rates, while retaining oxygen and metal to a much better degree[137]. Each of the three performed boronisations led to a significant reduction of intrinsic impurity radiation from carbon and oxygen[142].
Hereafter presented experiments took place after the aforementioned boronisations and were performed, if not mentioned otherwise, in magnetic *standard high mirror* configurations with a *rotational transform* $\iota = 5/5$ [144, 145]. Five individual island bands wrap around and enclose the magnetically confined plasma region in toroidal direction. The magnetic island chains circle helically between upper and lower divertor elements around the torus, which cut through the enclosing field lines and corresponding separatrices in poloidal direction[146]. Figure 3.1 shows the assembly of the ten divertor elements. On the left, each coloured band represents an island chain that revolves around the confined plasma region and cycles between upper and lower divertors in consecutive half-modules[143]. The right shows the five half modules, which each contain an upper and lower divertor, HM10/1 through HM50/1 respectively. Red and blue bands around the torus indicate traced field lines that originate and terminate in target elements, where the thermal helium beam box is located and gas is injected into the scrape-off

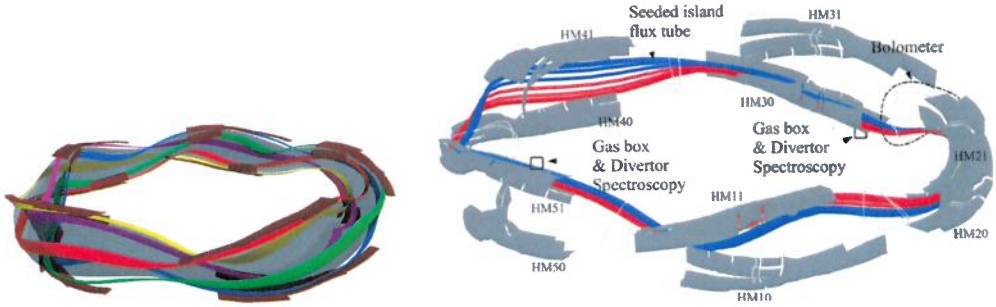

Figure 3.1.: (left): Standard magnetic configuration last closed flux surface (transparent, grey) inside ten divertor modules assembly (dark red). Five flux tubes that helically revolve around the core plasma and follow the island chains in front of the divertors included (red, yellow, purple, green, blue)[143]. **(right)**: Ten divertor elements (half-module HM 1-5, up (1) and down (0)) and helium beam gas boxes with positions of bolometry system (108° toroidally) and field lines that connect at the seeding points (red, blue)[144]

layer. Both traces have a target-to-target connection length in the order of $\mathcal{O}(100\text{–}1000\,\mathrm{m})$ and follow field lines from one (upstream) divertor, in clockwise (red) and counter-clockwise (blue) direction, until they reach another (downstream) target[144].

Thermal Helium Beam Diagnostic

The line ratio spectroscopy of helium is used to measure electron density and temperature in the scrape-off layer and plasma edge. Due to the intrinsic nature of the fully optimized stellarator W7-X, very low temperatures and densities in divertor regions, especially under conditions of plasma detachment, are expected. Therefore, the spectroscopy is extended by seeding of extrinsic impurities through thermal gas injection valves. These low-Z impurities include helium, neon, argon, methane (CH_4) and mixtures thereof. Due to their lower excitation energies, the yield of line radiation at low temperatures is much better[147]. Electron temperature T_e and density n_e can be derived from the ratio of line radiation intensities of atomic helium, which are based off of calculations for emission rate coefficients from a collisional-radiative model.[134, 148]. The thermal helium beam diagnostic consists of

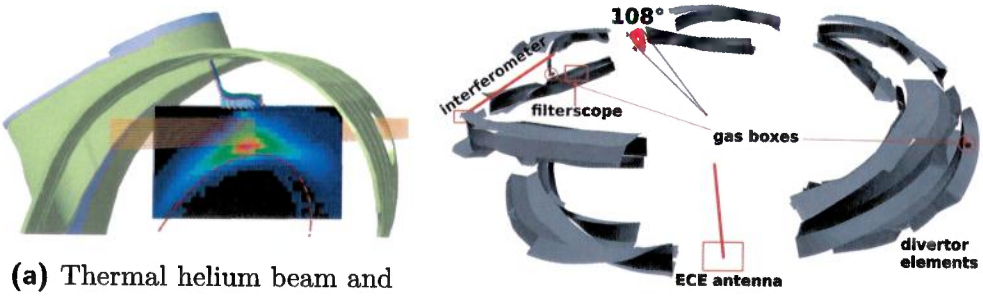

(a) Thermal helium beam and spectroscopy

(b) Toroidal diagnostic locations

Figure 3.2.: **(a)**: Gas injection box at the upper plasma edge with all 5 capillary nozzles as used for divertor operation. Included are spectroscopy lines of sight (orange) perpendicular to the beam and the last closed flux surface (red). Superimposed is the result of one EMC3-EIRENE for He line emission[147]. **(b)**: Relative toroidal position of all involved diagnostics. One filterscope system is located in the same divertor as one of the gas valve boxes, while interferometer and electron cyclotron measurements are done in different locations.

two *in vacuo* boxes at different toroidal locations in one upper lower divertor element. Each is equipped with five, millisecond fast piezo valves that allow for independent gas injection of He, Ar, Ne, N_2, H_2 or CH_4. The nozzles on the gas lines are mounted behind the target elements and directly seed into the same island chain of the $\iota = 5/5$ magnetic standard configuration. Line pressures range from a few mbar to a maximum of 60 bar, where the latter is used for seeding experiments, at around 1.5 km/s exit velocity and an opening angle of 40°.[134, 147]

However, the measurement of electron density and temperature in the divertor region by line ratio spectroscopy is of no concern for the plasma feedback control. The fast acting gas valves of the thermal helium beam diagnostic will be used as an actuator for the injection of extrinsic impurities. Other diagnostics provide experimental information that will be used for the feedback system, which ultimately controls the gas boxes. One of those diagnostics is the dispersion interferometry that provides line integrated core plasma densities in real-time.

Dispersion Interferometry

Interferometry is a fundamental measurement technique to assess the line integrated plasma density. Due to its simple methodology, it is a prime candidate for reliable real-time feedback[149, 150]. An easily tunable laser is split via a frequency doubling crystal. Both beams pass the plasma co-linearly. Because of their differing group velocities, i.e.dispersion of the plasma with its density dependent refractive index, both beams experience different phase shifts based on the plasma density along their path. After a second pass through the crystal, their interference image can be used to calculate the line integrated density. The disadvantages of this, generally very robust measurement method, are phase shifts that are introduced via perturbations perpendicular to the beam direction and potentially unfavourable SNR due to both reference and measurement beam passing the plasma[151]. For the single channel integral electron density dispersion interferometer (IEDDI), a real-time evaluation system based on FPGAs has been implemented. This assembly is capable of providing density measurements with a 23 µs latency, which is dominated by the laser diodes modulation. This has a maximum data rate of 50 kHz. However, the density feedback frequency is mandated by the internal W7-X system at 1 kHz. The latter is used for feedback by the central stellarator control system and plasma fuelling[152]. The density data is forwarded with an error of $2 \times 10^{18}/\mathrm{m}^2$ and signal drift of $6.7 \times 10^{15}/(\mathrm{m}^3\,\mathrm{s})$ from the last performed laser and phase calibration[153].

Besides the dispersion interferometry, there are two other possible candidates for thermal helium beam feedback. One of them is the spectroscopic imaging system, which measures impurity heat and particle fluxes from the plasma onto the divertor target. It can provide spatial-temporally resolved impurity line radiation, e.g. of carbon species like C^{3+}, for feedback purposes.

Filterscope and IR-visible Camera System

Two divertor targets have been under special investigation by the spectroscopic imaging system at W7-X in past experimental campaigns[154]. In one toroidal position, a combination of high resolution visible-infrared cameras and filterscope systems were able to provide the totally calibrated, spatially

and temporally resolved line radiation intensity of H_α, H_β, He-I, He-II, C-II and C-III from and in front of the target. The filterscopes at W7-X are based on the design from the *Oak Ridge National Laboratory*[I]. Lenses located outside the vacuum vessel focus light from the plasma and divertor onto a linear array of optical fibres. At focus lengths of 25 mm and 50 mm, the spatial resolution at the target becomes 3.6 cm and 7.1 cm, respectively. Those fibres are connected outside the machine to individual optical bandpass filters, which are attached to photomultiplier tubes (PMT), whose full-width at half maximum is 1–3 nm for the above emission lines. Data acquisition with a temporal resolution of 100 kHz is taken care of by a LabVIEW® control program. The filterscopes provided measurements of H_α, H_β, He-I, He-II, C-II lines and visible bremsstrahlung[154]. For feedback purposes, the filterscope system has to provide the accurate photon flux as the brightness of the scrape-off layer changes, which challenges the PMT voltage control. In certain scenarios, relative errors as high as 20% after gain normalization can occur. For fast plasma transitions with large increments in emission brightness, occasional clipping of the filterscope signal is unavoidable[155, 156].
The infrared-visible imaging system is based on the design from the *Los Alamos National Laboratory*[I]. It is located outside the vacuum vessel as well, while looking at the divertor plasma from 1.5 m away through a 21.5 cm diameter, 6 mm thick sapphire vacuum window. The infrared camera is acquiring between wavelengths of 3–5 µm at a 125 Hz acquisition rate of 1344×784 pixel resolution images. The calibration of the camera was performed with a 50 mm or 200 mm lens for temperatures of up to 1200 °C. In contrast, the visible system is acquiring 1024 pixel square images at 100 Hz with only a 50 mm lens. Both cameras achieve a 1 mm spatial divertor resolution[157].

After characterising the dispersion interferometry and filterscopes as candidates to control the impurity seeding, one additional constraint to the performance of the thermal helium beam valve box was made. The central line integrated electron temperature needs to be above 2 keV in order to

[I]ORNL; Oak Ridge National Laboratory, Oak Ridge, Tennessee, United States of America; 37831-8072
[I]LANL; Los Alamos National Laboratory, Los Alamos, New Mexico, United States of America

avoid poor ECRH coupling and therefore radiation collapses. The electron cyclotron diagnostic (ECE) is measuring line integrated T_e along a line of sight through the plasma core and along the separatrix, closer to the edge[158–160].
Finally, the real-time radiation feedback system, which provides information about the total radiative power loss of the plasma to the thermal helium beam, will be introduced.

3.2. Real-Time Radiation Feedback System

The goal of the real-time feedback system is to provide an estimate of P_{rad}, as derived in equation (2.25), for each sample during data acquisition, with as small as possible latency to the underlying measurement. This means a calibrated, error and offset corrected, filtered absorber voltage $\Delta\widetilde{U}_{\text{M}}$ needs to calculated within one signal integration cycle. Assuming current results from the *in-situ* calibration routine are available, one is able to find the power onto the absorber for every point in time P_M, as described by equation (2.19). In order to calculate a total radiation power loss in real-time from P_M, information about the line of sight geometry have to be provided via K_M and V_M. For an extrapolation of P_{rad} similar to equation (2.25), the calculation of geometric coefficients is too computationally expensive and can not be performed during the data acquisition. Therefore, K_M and V_M have to be provided beforehand, limiting their specificity towards the experiment scenario, e.g. in regard to the magnetic configuration. Finally, due to computational limits, P_{rad} of the full HBC or VBC arrays can not be calculated within one sample period. Simplifications to equation (2.25) have to be made to achieve a real-time proxy of the radiation power loss. Assume there exists a collection of lines of sight S that measure the radiation power loss from the plasma, so that

$$V_S = \sum_M^S V_M \ ,$$

$$\boxed{P_{\text{pred}}^{(1)} \coloneqq P_{\text{rad},S} = \frac{V_{\text{P,tor}}}{V_S} \sum_M^S \frac{P_M V_M}{K_M} \ , \qquad S \subset (S_{\text{HBC}}, S_{\text{VBC}})} \tag{3.1}$$

the predictive value $P_{\text{pred}}^{(1)} \approx P_{\text{rad}}$ the full set of information. An equivalent requirement is the adequate description of the local emissivity distribution by the set of lines of sight S, though this abstract concept is difficult to quantitatively assess from the standpoint of the bolometer diagnostic alone. However, an attempt for a rigorous and thorough investigation of the accuracy and reliability of $P_{\text{rad},S}$ is made in the later section 4.3. The subset S of the total selection of lines of sight, which are available through the HBC and VBC arrays, needs to be much smaller than the main cameras in order to be a candidate for radiation feedback. A decreased amount of channels for calculation means less computational load and therefore promises feasibility for real-time application. A key distinction between P_{rad} and $P_{\text{pred}}^{(1)}$ is that the prediction has to be limited between 0–10 MW.

$$\begin{aligned} P_{\text{pred}}^{(n)} &\in (0, 10)\ \text{MW}\ , \\ U_{\text{AO},n}\,[\,\text{V}\,] = P_{\text{pred}}^{(n)}\,[\,\text{MW}\,]\ , &\qquad n = \{1, 2\} \end{aligned}$$

On one hand, this is due to the analogue output limitation of the hardware to a range of 0–10 V. On the other, radiation power loss estimations > 10 MW for a total possible heating power of 10 MW do not make sense for the aspired feedback system and its requirements. In equation (3.1), the analogue output voltages that are used to provide feedback to the gas valve control are noted as $U_{\text{AO, n}}$, with $n = \{1, 2\}$.
The performance of the real-time radiation system, especially with respect to latency, is crucial to the achievement of stable plasma detachment through impurity seeding in the scrape-off layer. A calculation like in $P_{\text{pred}}^{(1)}$ takes a certain, non-negligible amount of computation cycles and time, which inevitably increases the latency of the feedback response, relative to the acquisition of the underlying samples. One way around this issue is to make further simplifications to the approach of equation (2.25) or equation (3.1). In steady state scenarios, with slow perturbations and small gradients in the radiation power distribution, let us assume:

$$P_{\text{M}} = F_M \left(\frac{\text{d}\left(\Delta\tilde{U}_M\right)}{\text{d}t} + f_M \Delta\tilde{U}_M \right) \approx F_M f_M \Delta\tilde{U}_M\ ,$$

$$\boxed{P_{\text{pred}}^{(2)} := \frac{V_{\text{P, tor}}}{V_M} \cdot \frac{P_M V_M}{K_M} \overset{!}{=} a_M \Delta\tilde{U}_M\ , \qquad M \in (S_{\text{HBC}}, S_{\text{VBC}})} \tag{3.2}$$

Equation 3.2 yields a different approach to the radiation power loss proxy. Assumptions for $P_{\text{pred}}^{(2)}$ require $\mathrm{d}\Delta\tilde{U}_M/\mathrm{d}t \ll f_M\Delta\tilde{U}_M$ and therefore temporal changes in the radiation distribution to be negligible. This saves additional computational steps by eliminating the derivative. Furthermore, removing the sum in equation (3.1) assumes the radiation to be located mainly in or around one radial position, i.e.one point in the chord brightness profile, which is symmetrically distributed in poloidal and toroidal direction. The channel constant a_M can be calculated in advance to the measurement. For example: with $R_M = 1\,\mathrm{k\Omega}$, $\tau_M = 110\,\mathrm{ms}$ and $\kappa_M = 0.8\,\mathrm{mW/k\Omega}$, which gives $F_M = 0.343$ and $f_M = 0.993$, $K_M = 1.1 \times 10^{-10}\,\mathrm{m^3}$ and a total radiating plasma volume $V_{\mathrm{P,\,tor}} = 45\,\mathrm{m^3}$, the channel constant to upscale the absorber voltage $\Delta\tilde{U}_M$ to feedback proxy becomes $a_M = 141.18\,\mathrm{MW/mV}$. At an absorber signal of $\Delta\tilde{U}_M = 0.1\,\mathrm{mV}$, equation (3.1) will estimate and extrapolate a total plasma radiation of $P_{\text{pred}}^{(2)} = 1.41\,\mathrm{MW}$.
Equation 3.1 will be the reference for a radiation power loss proxy that can be implemented for the scrap-off layer seeding system. Nevertheless, both of the previously introduced concepts have been used during the last experimental campaign to provide radiation power loss predictions. Details of how the implemented diagnostic hardware and a tailored algorithm calculated the radiation power proxy will be described below.
To start, the setup that was used to provide radiation loss information to the thermal helium beam box will be introduced. The center component of the bolometer feedback system is the PCI Express add-in card and multipurpose input/output device NI® 6321. For the purposes of this experiment, only the analogue output capabilities of this device are of interest. The cards specifications have been rated for constant environmental conditions, i.e. temperature and humidity, which are provided by the air-conditioned cabinet in the torus hall, where the bolometer system PC this device has been installed on is located. The NI® 6321 incorporates two analogue output channels that are both able to provide a DC coupled voltage signal in the range of $\pm 10\,\mathrm{V}$, with 16 bit or 0.3 mV resolution. If both channels are being used, the maximum update rate becomes 840 kS/s, which is equal to a 1.2 µs sample time with an accuracy of 10 ns. The output has a buffer array of 8191 samples, where the first sample in is replaced by sample number 8191+1

property	σ_G	s_G	s_r
value	8×10^{-5}	$1.13 \times 10^{-5}/°C$	$5 \times 10^{-6}/°C$
property	σ_{off}	s_{off}	ΔINL
value	5.3×10^{-5}	$4.8 \times 10^{-6}/°C$	1.28×10^{-4}

Table 3.1.: Output and temperature characteristics of NI® 6321.

and so on (FIFO[I], see figure 3.3). The absolute error ΔU_{AO} for output voltage U_{AO} of the device is given by:

$$\begin{aligned} \Delta U_{AO} &= U_{AO}\Delta G + R\Delta U_{off} \\ \Delta G &= \sigma_G + s_G\Delta T_{in} + s_r\Delta T_{ex} \\ \Delta U_{off} &= \sigma_{off} + s_{off}\Delta T_{in} + \Delta\text{INL} \ , \end{aligned} \tag{3.3}$$

where ΔT_{in} and ΔT_{ex} are the temperature difference to the last internal and external calibrations, and R the set output range of the card. The noted properties and their value can be found in table 3.1. For a temperature change relative to the calibrations of 1 °C and 5 °C respectively, an output range of 20 V ($\pm$ 10 V) and voltage of $U_{AO} = 1$ V the analogue error becomes $\Delta U_{AO} \approx 3$ mV. The characterisation of the hardware will later be put into context when addressing the performance and limits.
The NI® 6321 is only tasked with providing signals for the gas valve control. Therefore, the procedure of acquisition and the algorithm that are responsible for real-time feedback need to be presented next. In section 2.2.2, the bolometry system has been described. The following introduction builds on the specifications of the previously implemented system.

Measurement Algorithm

Assume an incoming signal that functions as an event trigger, as is standard for the central W7-X control system, which marks the point in time $T0 = T1 - 60$ s, with $T1$ being the moment the experiment starts - commonly the startup of ECRH microwaves[152]. A bare bone, top level LabVIEW

[I]FIFO: First In – First Out

program, designated to receiving and interpreting any incoming trigger signals as fast as possible, is forwarding a start command to the core bolometer control. The trigger routine is executed before an experiment session and is running with the lowest possible latency, which is $\ll 1\,\mathrm{ms}$. The initialization of the main bolometer LabVIEW routine is following the start signal from the trigger program. The user interface input parameters, which have been set before runtime, are stored in memory for later requests during execution. This includes links to local files containing the line of sight geometry. Thereby provided K_M and V_M are, for reasons stated above, derived from magnetic standard configuration calculations.

A preventative reset and clearing of the bit registers and FPGA states of the NI® AD 7730 is carried out in the beginning of the execution. For each of the following internal routines, the bit programmable registers, which are responsible for the mode, voltage range and frequency of acquisition, are set to appropriate values. For the initial floating potential measurement, which has been mentioned in section 2.2.4, the device is put into full range mode, i.e. $\pm 80\,\mathrm{mV}$ and sample frequency of $0.4\,\mathrm{ms}$. The subsequent measurement of $10\,\mathrm{s}$ yields the offset voltage and measurement noise per channel. Next, the registers are reset again and then put into calibration mode, which enables the NI® AD 7730 to measure the current through individual parts of the Wheatstone bridge. As lined out in section 2.2, a calibration routine incorporating two subsequent heating stages with $1.2\,\mathrm{V}$ and $2.5\,\mathrm{V}$ for $1.6\,\mathrm{s}$ each is then executed. Resulting currents are measured with a sampling time of $0.4\,\mathrm{s}$. This, in total $4\,\mathrm{s}$ long procedure is repeated for both of the reference and measurement parts of the Wheatstone bridge. In succession to the four individual calibration routines, the respective properties κ, τ and R for reference and measurement absorbers are calculated using equation (2.7) and following (see section 2.2.4). Thereafter, filter and mode register are programmed to continuously acquire N data points at the given sample time of 0.8–$6.4\,\mathrm{ms}$ for the measurement of experiment data. At this point, the program indicates a total runtime of 25–30 s, depending on small changes in the PCs execution prioritisation. The remaining part of the $T0 + 60\,\mathrm{s} \rightarrow T1$ section is downtime.

Simultaneously, the NI® 6321 is programmed for two-channel analogue output. A global variable for each channel, i.e. memory address for writing and reading is provided beforehand. The most current radiation values are calculated using $P_\mathrm{pred}^{(n)}$ from equation (3.1) and equation (3.2) individually, inside

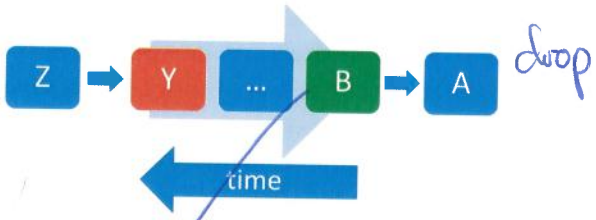

Figure 3.3.: Schematic of a FIFO array. Time progresses from right to left, i.e. sample A is acquired before B, ..., Y and Z. Currently stored samples are B, ..., Y. When sample Z is acquired, sample A is removed from the FIFO array, the oldest data point at this moment.

the acquisition routine, which will be presented further down below. The addresses are read from inside a loop structure separate from the acquisition, which runs as fast as allowed by the output performance of the card.
A certain amount of time, e.g. 5 s before $T1$, the system starts acquiring samples. The main LabVIEW program initialises a sub-routine that only takes care of data acquisition. Required storage arrays and memory addresses are either referenced or created at first runtime. In scenarios where no feedback is required, only the raw data is returned from the sub-routine, with no additional tasks performed during sample cycles. Also, the initialisation of the NI® 6321 is omitted. For feedback purposes, multiple additional arrays have to be prepared. The raw samples ΔU_M of channels that are in the selection S are stored in an array with the number of rows $|S|$, the cardinality of the subset. In order to reduce the impact of signal noise on the prediction value, smoothing like in equation (2.18) has to be applied. In real-time application, performing a full width Savitzky-Golay filter the width of L samples for each channel is not possible. A computationally affordable approach to a boxcar filter is the FIFO array. A schematic can be seen in figure 3.3. Consecutive samples are stored in a container of length $L + 2$. Assume an iterator i that counts the progression of data points in time. For $i \leq L$ samples are placed in the container at index i. Once the iterator reaches $i > L$, the stored samples are replaced by new ones at their location $j \equiv i \pmod{L}$, hence *first in - first out*. For $i = M$, the mean over all elements is stored in column $L + 1$. In the next iteration, entry $L + 1$ is moved to column $L + 2$ and the new mean is calculated in $L + 1$. This is repeated in all following cycles. Hence, data of the real-time feedback

algorithm is stored in a structure the size $|S| \times (L+2)$.
After the required memory space and addresses have been reserved, the data acquisition is started. The enclosing loop over N repetitions is timed by the length of a sample, e.g. 1.6 ms. An acquired data point $\Delta U_M^{(i)}$ for sample number i is subtracted by the previously in-situ measured offset $V_{\text{off},M}$ and stored in the FIFO array at its corresponding location. After M iterations and onwards, for every sample i and channel M, the boxcar filtered $\Delta\tilde{U}_M^{(i)}$ is calculated. The temporal derivative is calculated from columns $L+1$ and $L+2$ using the discrete *forward Euler*[I] *method*:

$$\frac{\mathrm{d}\left(\Delta\tilde{U}_M^{(i)}\right)}{\mathrm{d}t} \approx \frac{\Delta\tilde{U}_M^{(i)} - \Delta\tilde{U}_M^{(i-1)}}{\Delta t} \,.$$

you said above that you drop the $\frac{d}{dt}$ term. Do you know?

By referencing the current calibration results, one finds $P_M^{(i)}$ from the last and second to last column of the FIFO array using equation (2.19). With K_M and V_M provided through input files, the final step is done in equation (2.25), which yields $P_{\text{rad}} = P_{\text{pred}}^{(1)}$. Similarly, $P_{\text{pred}}^{(2)}$ is derived from a separate FIFO array which only stores samples of one channel. The scaling factor a_M is calculated beforehand.
For each iteration $i > L$, both $P_{\text{pred}}^{(n)}$ are written to their respective memory addresses, which are read from in the top-level routine, where the analogue output is carried out as fast as possible. Also, both values are written to individual arrays that are returned to the main program after the measurement loop has been completed. After N samples, P_M, ΔU_M and both $P_{\text{pred}}^{(n)}$ are forwarded to the primary LabVIEW application. The measurement procedure has been successfully completed at this point. Output loop and device status are reset and returned to default for the next experiment. At last, the data will be stored locally and uploaded to the central W7-X archive, including the calibration currents, results and feedback proxies. Measurement, as well as feedback routine and algorithm are shown in a schematic outline in appendix A by algorithm 1.
The performance of the *real-time radiation feedback system* has been tested and benchmarked before its application during the experimental campaign. An uncalibrated diode laser with 7 mW continuous power output was aimed at a single detector absorber, like it was described in section 2.2.2, outside the plasma vessel and inside the measurement cabinet of the bolometer

[I] Leonhard Euler * Apr. 15. 1707 † Sept. 18 1783

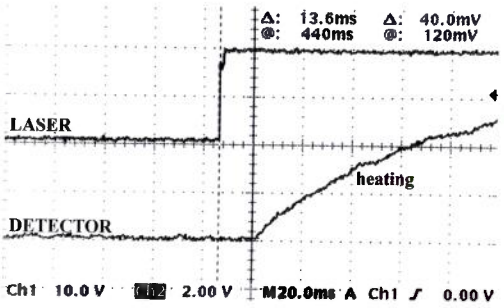

Figure 3.4.: Real-time feedback system benchmark result for 7 mW at 1 Hz **laser** diode power and frequency. The **detector** response was created using the algorithm for $P^{(1)}_{\text{pred}}$ with $M = 1$ the FIFO array length. A total, minimum latency of 13.6 ms was achieved during the test.

diagnostic. A frequency generator with cycle frequencies of 1 Hz-1 kHz and output voltages < 10 V has been powering the laser diode. The detector was connected to a vacant port in the acquisition electronics. In order to find the intrinsic, lowest possible latency of the system, the length of the *FIFO* buffer was set to the minimum $M = 1$. A measurement program was carried out while the laser was adjusted to its maximum 7 mW intensity at a square wave cycle frequency of 1 Hz. The output of the frequency generator was split between the diode and one input of an oscilloscope. The prediction $P^{(1)}_{\text{pred}}$ for the analogue output was calculated using equation (3.1) and was also monitored by the oscilloscope with a separate input. The result of the benchmark can be seen in figure 3.4. A minimum intrinsic latency of the system of 13.6 ms was achieved. Prediction and analogue output using $P^{(2)}_{\text{pred}}$ resulted in the same values. Further temporal delays are subject to the smoothing of the FIFO array over M samples of length Δt:

$$\Delta T \approx \frac{M \cdot \Delta t}{2} .$$

In context of the other feedback candidates and actuator system, this latency is the largest among the individual diagnostics. This will become important when discussing initial results of the bolometer feedback and comparing its achievements to the results other control values.

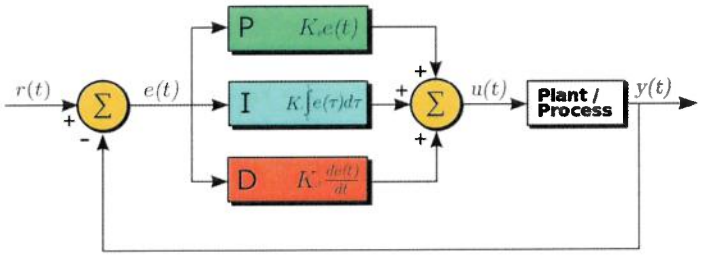

Figure 3.5.: A block diagram of a PID controller in a feedback loop. Desired process value or setpoint SP $r(t)$ and measured process value PV $y(t)$. The control function $u(t)$ is used for feedback[161].

PID Controller

Both of the analogue output channels of the NI® 6321 that provide $P_{\text{pred}}^{(n)}$ are connected via individual, BNC[I] terminated, double shielded cables outside the vacuum vessel to an *Arduino*[II] based *PID*[III] that controls the impurity seeding valves. Such a controller is widely used in control systems that incorporate feedback mechanisms. The PID algorithm continuously modulates a control function, based on an error value $e(t)$ between a setpoint SP $\equiv r(t)$ and process variable PV $\equiv y(t)$. A correction to the feedback control is applied involving a proportional (P), integral (I) and derivative (D) term of $e(t)$. A block diagram of how such a PID works can be seen in figure 3.5. A setpoint $r(t)$ is defined as the desired state of the machine or system. The current state of the system is measured in $y(t)$. Error $e(t)$ is given by the difference of SP and PV. Individually optimized constants K_{p}, K_{i} and K_{d} scale the proportional, integral and differential part of the control function $u(t)$. The impact of the feedback mechanism, which is controlled by $u(t)$, is measured in $y(t)$ and is used for subsequent adjustments to the control. The control function is given by:

$$\begin{aligned} e(t) &= r(t) - y(t) \\ u(t) &= K_{\text{p}} e(t) + K_{\text{i}} \int_{t_0}^{t} e(t')\,\mathrm{d}t' + K_{\text{d}} \frac{\mathrm{d}\,e(t)}{\mathrm{d}t} \,. \end{aligned} \tag{3.4}$$

Figure 3.6 shows how the control function for the same setpoint and response

[I]BNC: Bayonet Neill Concelman, Bayonet Nut Connector or British Naval Connector
[II]open-source electronics platform, based on easy-to-use hardware and software for I/O
[III]PID: proportional–integral–derivative controller

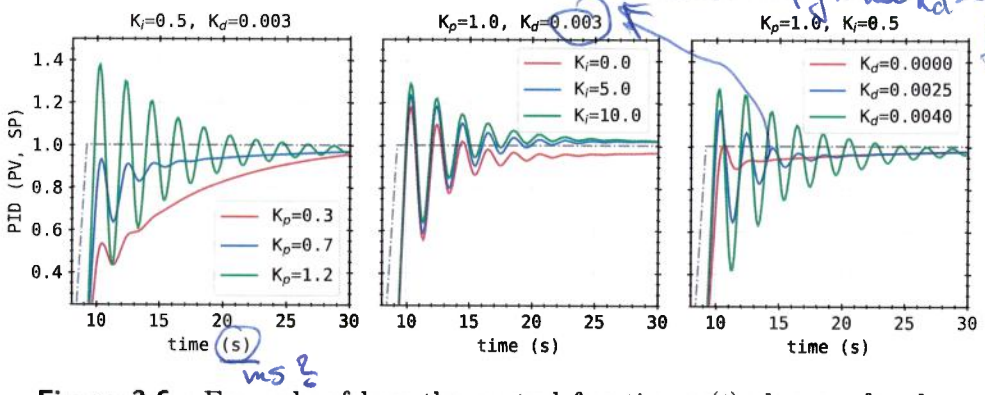

Figure 3.6.: Example of how the control function $u(t)$ changes for the same setpoint SP (grey dashed) and system but different proportional, integrals and differential parts.

changes with different K_p, K_i and K_d. The proportional component determines the approach of $u(t)$ to the setpoint. For larger K_p, the amplitude of the control increases and vice versa, i.e.smaller proportionality leads to a slower adjustment towards the SP. The integral component is responsible for the long-term development of the control. Scaling K_i up eventually can lead to a faster balancing with the setpoint, but too large values will force the control to underestimate the error more consistently. Smaller differential contributions with K_d dampen oscillations in the feedback control, but can also neglect and smooth over fast, transitional responses of the system.
For feedback control with electron density measurements by dispersion interferometry, the factors of proportional and integral part K_p and K_i have been individually optimized based on previous measurements and knowledge about delays in the feedback system itself, i.e. valve opening and closing times. A differential component $K_\mathrm{d} = 0$ is excluded in those scenarios. During real-time radiation feedback-control, a different, also uniquely optimized set of parameters has been used. In this case, also $K_\mathrm{d} \neq 0$ has been included. For both, there are two sets of PID factors that scale either more aggressively or conservatively.

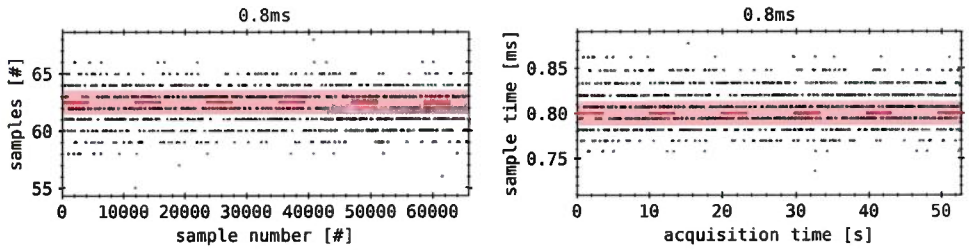

(a) samples per half period **(b)** sample time

Figure 3.7.: Laser test results without real-time radiation feedback. The expected number of samples and average sample time are shown in red. **(left)**: Number of samples per laser half period over sample number **(right)**: average sample time over laser half period, as derived from the leftover acquisition time.

3.2.1. Performance

The previous efforts around the real-time radiation system and underlying algorithm were dedicated to a reliable, low latency performance for detachment control purposes. In order to ensure a consistent sampling of the absorber signal and subsequent radiation power, while also calculating and providing feedback proxies $P_{\text{pred}}^{(n)}$, measurements of the acquisition cycle timings was performed. Therefore, the same setup as for the intrinsic latency test of the radiation feedback system was used. An uncalibrated diode laser with 7 mW continuous power output was aimed at a single detector absorber in a laboratory environment, outside the plasma vessel. A frequency generator with 1 Hz-1 kHz of < 10 V output voltages was powering the diode. The exposed absorber was connected to a vacant port in the diagnostic electronics. In order to measure the actual sample times for the individually set Δt, diagnostic programs were carried out with maximum acquisition length and a square wave signal laser facing the detector. The measurement procedure was performed while the laser was adjusted to its maximum 7 mW intensity with a frequency of 1 Hz. For a set sample time Δt and laser half period of 0.5 s, the number of samples that are expected to measure the laser light is given by:

$$N = \frac{0.5\,\text{s}}{\Delta t} \pm 1 \,.$$

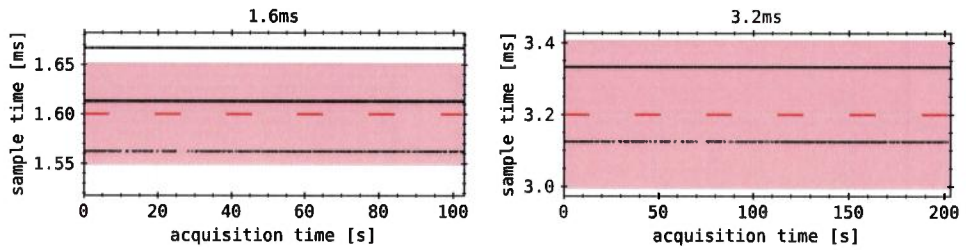

Figure 3.8.: Laser test results without real-time radiation feedback for 1.6 ms and 3.2 s. Both show the average sample times per laser half period over acquisition duration. The expected average sample times are shown in red.

An uncertainty of one sample is assumed, both for errors in distinguishing process of rising and falling slopes in the signal and the smallest possible resolution of the measurement. Rewriting N for Δt yields the *actual sample time* for the respective laser half period.
The results for no real-time radiation feedback, i.e. without the algorithm and calculations related to the proxies, for a set sample time of $\Delta t = 0.8\,\text{ms}$ can be seen in figure 3.7. This is the lowest possible sample time of bolometer data acquisition, regardless of feedback and experiment configuration. The number of data points is limited by the memory of the system. Therefore, for longer periods of acquisition, larger Δt have to be selected in order to cover the experiment duration. For $\Delta t = 0.8\,\text{ms}$, the actual sample time is found to be within 0.05 ms of the set sample time 0.8 ms. A large amount of data points indicate a divergence from the programmed acquisition time Δt, which is supported by the accompanying number of points per laser half period, which show the same behaviour. This is equal to a 6.25% error in sample timing, which is significantly larger than the in section 2.2.5 already discussed minimum resolution of ADC programming and physical properties of the absorber design.
Results for $\Delta t = 1.6\,\text{ms}$ and 3.2 ms are shown in figure 3.8. Similar perturbations of the acquisition timing can be found for 1.6 ms, while the spectrum of measured sample times only consists three values. For $\Delta t = 3.2\,\text{ms}$, the results are within the error bar of the measurement and therefore in agreement with the predicted timing. Larger sample times show the same results and therefore support the findings of this benchmark. An erratic error in

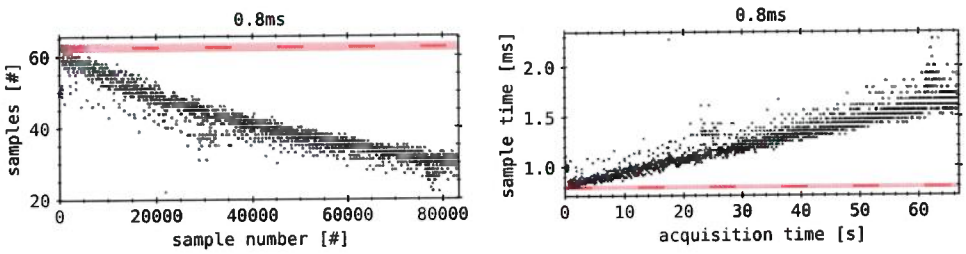

(a) samples per half period **(b)** sample time

Figure 3.9.: Laser test results with real-time radiation feedback. The expected number of samples and average sample time are shown in red. **(left)**: Number of samples per laser half period over sample number **(right)**: Average sample time over laser half period, as derived from the leftover acquisition time.

acquisition sample timing is found for $\Delta t < 1.6\,\text{ms}$, which is presumably caused by the routine of signal integration in LabVIEW®. This specific part of the program is clocked at a fixed frequency for each set sample time Δt. Interferences can be caused by additional task, which are performed during each sample clock of the actual measurement.
In the next step, in order to compare the results without feedback, the same benchmarks are performed for the real-time radiation algorithm. The results for $\Delta t = 0.8$–$1.6\,\text{ms}$ are shown in figure 3.9. From the very first data point and laser period, an increasing sample time is found over the entire measurement duration. The first samples are already substantially longer than the set 0.8 ms, while their length only grows with 0.01 ms/s or 0.01 µs/S. This leads to an increase by factor two of the set sample time after 60 s to $\approx 1.6\,\text{ms}$. For $\Delta t = 1.0$–$1.6\,\text{ms}$, similar results can be seen in figure 3.10. However, an elongation of the sample cycle is found to occur after a certain number of samples have been processed, i.e. $\approx 28\,000\,\text{S}$ for $\Delta t = 1.0\,\text{ms}$. Like before, a linear increase of 0.01 ms/s in sample length is found from this point onwards. For an even longer sample time of 1.6 ms, only single data points deviate from Δt, while the majority of samples is still within the expected timing window of the program. However, in comparison to the previous results without real-time feedback, $\Delta t = 1.6\,\text{ms}$ exhibits greater uncertainties towards the end of the acquisition. Larger sample times show no perturbations due to the feedback algorithm and its interference with

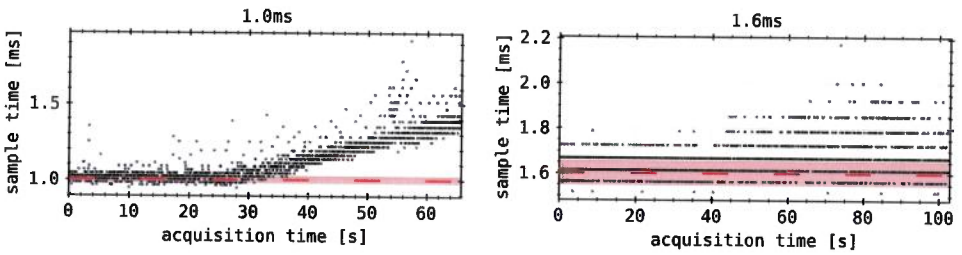

Figure 3.10.: Laser test results with real-time radiation feedback for 1.0 ms and 1.6 ms. Both show the average sample times per laser half period over acquisition duration. The expected average sample time is shown in red.

the acquisition cycle.
In order to be able to rule out any interference of the PC system on the performance on the acquisition timing, the same benchmarks are repeated with a synthetic load of at least 80% of its capacity on the central processing unit of the system. If the stress on the computational unit does have any impact on the calculation speed, with which the algorithm is performed, and therefore timing of the diagnostic, a significant increase in deviation from the set sample time Δt is expected. The results for $\Delta t = 0.8\,\text{ms}$ are shown in figure 3.11. When comparing results to the previously presented measurements without synthetic PC load and real-time feedback, there is no noticeable difference in the number of samples per half period or actual sample time. This is the case for all larger samples times Δt. The computational stress of the computer is found to have no effect on the performance of the bolometer acquisition.
The presented results inevitably show that the real-time radiation feedback is not applicable for sample times $\Delta t < 1.6\,\text{ms}$, or at higher acquisition frequencies for experiment times above 30 s. Furthermore, in its current configuration, the bolometer systems acquisition duration is limited by its memory capacity with regard to the selected sample time Δt. The perturbations in *actual* sample timing can be found for all individual sample time settings Δt. They show random behaviour and protrude in both directions around the set value with similar amplitudes. Both bolometer acquisition programs, with and without real-time feedback, present erratic divergence of the sample timing. However, the latter shows stretching of integration

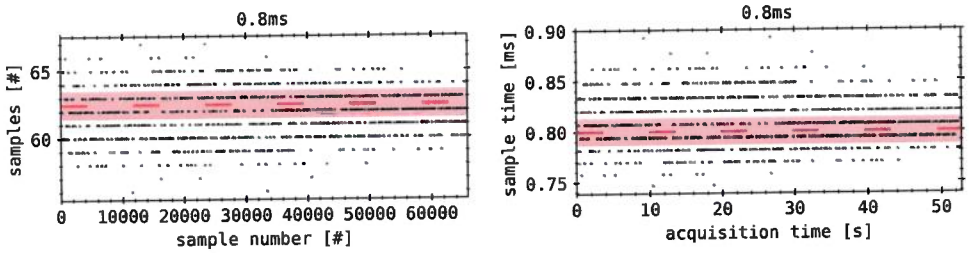

Figure 3.11.: Laser test results without real-time radiation feedback and additional, synthetic PC load. The expected number of samples and average sample time are shown in red. **(left)**: Number of samples per laser half period over sample number **(right)**: Average sample time over laser half period over acquisition time.

periods for lower set sample times. No coherent alteration of experimental data timelines due to random perturbations in sample timing is expected. Though, future bolometer measurements could greatly benefit from a similar setup to be permanently installed at the diagnostic.
The following experimental applications of real-time radiation feedback will incorporate the findings of this benchmark. If not stated otherwise, the set sample time of the bolometer acquisition is 1.6 ms.

3.2.2. Experimental Achievements

After characterising the *real-time radiation feedback* system in the previous section, one can now begin to present and discuss its experimental achievements from the last experimental campaign.

Initial Results

The very first plasma discharge that incorporated radiation feedback control was experiment (number) XP20180920.29. After initial, functional tests of the feedback system, this was the first time the PID controlled gas valve actuator was applied based on radiation measurements. This plasma discharge took place after the first *boronisation*, which significantly decreased the influx of intrinsic impurities oxygen and carbon from plasma facing components and vessel walls. The latter's line radiation was decreased by a factor of

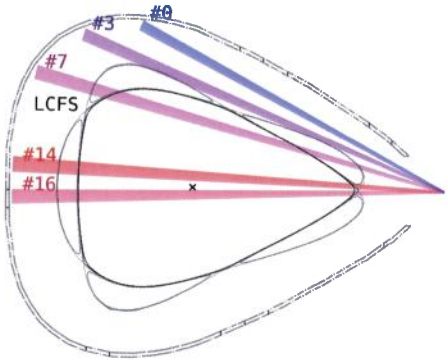

Figure 3.12.: Line of sight selection for experiment number XP20180920.29, only containing of HBC channels from the top and center part of the triangular cross-section, i.e. the bolometer measurement plane around $\varphi = 108°$ toroidally.

up to six[162]. The experiment was planned to include 10 s of 2 MW constant microwave heating. The ECRH was coupled to the second-harmonic extraordinary (X2-) mode of the plasma. For safety reasons, the heating and therefore discharge were terminated early after 1.3 s. The plasma vessel was pre-filled with hydrogen before heating startup by five short bursts of 5 ms each at ≈ 200 mbar L/s. The experiment was performed in standard magnetic field geometry with an $\iota = 5/5$ magnetic island chain configuration. Plasma feedback valves have been seeding helium into the scrape-off layer from port AEH30 in half module no.3. Helium exited the valves at 50 mbar with a flow rate of 6×10^{18} atoms/s, injecting 1×10^{19} atoms in total. The setpoint SP of the PID was programmed for $f_{\text{rad}} = 90\%$, while $P_{\text{rad}} \approx P^{(1)}_{\text{pred}}$ from real-time feedback is assumed to be true. On one hand, this is done according to theoretical and experimental predictions for stable plasma detachment for W7-X, like it was described in the introduction of this chapter. On the other hand, in anticipation of errors in the radiation prediction, as well as retardations of the plasma response to gas injections, this is supposed to prevent oversaturation of the scrape-off layer and plasma with impurities, which can lead to a radiative collapse.

The temporal evolution of available plasma parameters can be seen in figure 3.13. In the top left, the input heating power and plasma stored energy, as well as its derivative can be found. Below, the total radiative power loss from the plasma, measured by both bolometer cameras can be seen. The real-time radiation feedback predictions, calculated by equation (3.1) and 3.2 are shown in the same plot. The prediction for P_{rad} in $P^{(1)}_{\text{pred}}$ was calculated

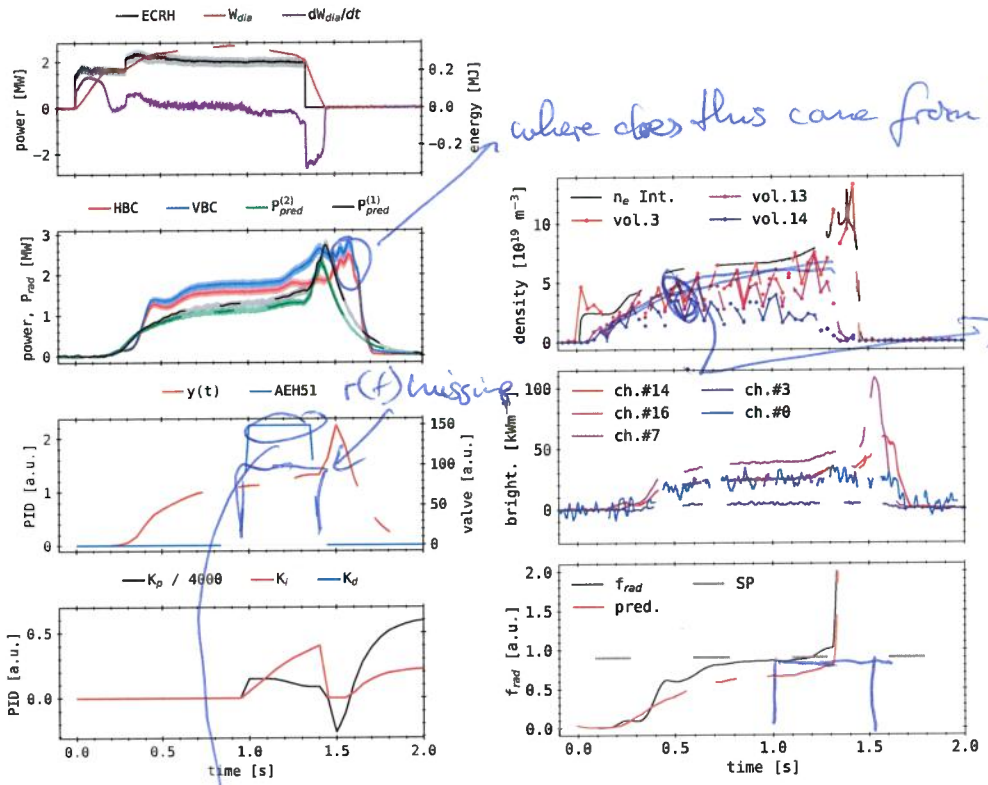

Figure 3.13.: XP20180929.29
Very first radiation feedback controlled plasma discharge. **(top left)**: Microwave heating power, plasma stored energy and loss **(center left top)**: Radiative power loss, both cameras and prediction values **(center left bottom)**: PID control $u(t)$, reference $r(t)$ and valve actuation **(center left bottom)**: Control components **(top right)**: Electron density of selected Thomson scattering volumes and line integrated ECE measurement **(center right)**: Individual bolometer channels, used for $P^{(n)}_{\text{pred}}$ **(bottom right)**: Radiation fraction(s).

using the detector subset $S = \{0, 3, 7, 14, 16\}$, as well as the approximation $P^{(2)}_{\text{pred}} = a_7 \Delta\tilde{U}_7$ with detector 7. This line of sight selection can be seen in figure 3.12. Below, the PID controls process value $u(t)$, the forward model $P^{(1)}_{\text{pred}}$ for comparison and the normalized feedback valve actuation are presented. Only valves located in port AEH30 injected helium into the

scrap-off layer. On the bottom left, the PID components K_p and K_i can be seen. No differential component was used in this case. The line integrated electron density from the dispersion interferometer and *Thomson scattering* for selected volumes $\{3, 13, 14\}$ is shown in the top right. Below, the chord brightness evolution of the bolometer channel subset is presented. Finally, the radiation fraction f_rad, given by equation (2.22), next to the setpoint SP of the controller can be seen on the bottom right.
Both plasma radiation power loss predictions quantitatively roughly mimic the complete P_rad dataset. Like the full camera information set, the predictions feature a late rise from 0.2 s to 1.5 MW at 1.3 s. After, the proxies sharply rise and peak with 2.5 MW at 1.4 s, before rapidly decreasing to zero. Proxy $P_\mathrm{pred}^{(1)}$ is slightly larger and reaches its maximum of 2.8 MW later than $P_\mathrm{pred}^{(2)}$. The radiative power loss P_rad from both cameras has a much steeper increase at 0.35 s, with a small plateau around 1.4 MW. The vertical camera measures an increasing radiation power of 2.7 MW at 1.4 s, where oscillations lead to an abrupt drop off. Similarly, the horizontal camera measures oscillations for a shorter duration at a later point in time around 1.5 s. Generally, the VBC presents a larger P_rad of at least 10% than the HBC, while the latter shows radiation power values of up to 0.5 MW larger than the predictions. Although, in situations of peak radiation, the proxies $P_\mathrm{pred}^{(n)}$ are able to represent the full dataset results within their respective error bars.
The individual chord brightness of the channels used to calculate the predictions show the same behaviour. However, their temporal relation, i.e. the position of the peak before and after 1.5 s varies significantly. Channel no.7 is maximum at 1.55 s, while detectors viewing plasma volumes further inside with smaller $r_{\mathrm{eff},M}$, no.14 and 16, reach their peak about 0.1 s later. Due to its orders of magnitude larger noise $\sigma_{\Delta U}$, channel no.0 has no meaningful contribution to the radiation prediction and must have experienced issues during data acquisition. Channel no.3 already shows very small values and therefore suggests no.0 not containing any more information on the emissivity profile, since the chord brightness indicates that the radiation is mainly located inside the last closed flux surface, which will be discussed further below with figure 3.14.
Similar behaviour can be seen in the Thomson scattering electron density for three different volumes - the volumes are ordered so that vol.0 is located

closest to the magnetic axis or center of the plasma and vol.16 the furthest away. Volume no.3 quickly rises after microwave heating startup and gradually increases towards its maximum of about $1.4 \times 10^{20}/\mathrm{m}^3$ at 1.4 s, before dropping to zero at 1.5 s. The volumes further outward climb much slower and are as much as 50% smaller. They also experience an early drop off from 1.3 s and 1.0 s for vol.13 and 14 respectively. The line integrated measurement of the dispersion interferometry envelops the lines of the Thomson profile, leading up to the same maximum.

The resulting radiation fraction f_{rad} for a constant 2 MW heating quickly rises, after the slight delay in the radiation, to 80% at 0.7 s. It diverges beyond 1.3 s, since P_{ECRH} becomes zero and the radiation power loss reaches its maximum. After the start of the ECRH and within the first 0.2 s, the radiation power is close to zero, while the plasma stored energy is increasing until a plateau at 0.2 MJ. Its time derivative indicates that almost all the heating power is deposited into the plasma. However, probes dedicated to measuring the shine-through of the microwaves through the plasma show that there is a non-negligible portion of the heating power beam which is not absorbed. After $\mathrm{d}W_{\mathrm{dia}}/\mathrm{d}t$ becomes zero, there is a small step in the ECRH power of 0.3 MW, which in turn again increases the stored energy, as well as P_{rad} towards its plateau. After ECRH shut-off, W_{dia} linearly decreases to zero, while the plasma radiation reaches its maximum.

The feedback can be seen on the bottom left of figure 3.13. According to the PV, the valve is opened and closed for injecting helium into the plasma, as is indicated by the actuation of the gas valves. The injection box is located in the diagnostic port AEH30, in the half module of the plasma vessel next to the bolometer measurement plane in counter-clockwise direction. In terms of transport along magnetic field lines, the actuator is one full toroidal rotation away from the bolometer cameras, since the net parallel plasma transport increased to ≈ 200 A in clockwise direction (if viewed from above). Due to the delayed response of P_{rad} and $P^{(1)}_{\mathrm{pred}}$, the control function $u(t)$ triggers the gas injection early. Two smaller gas puffs of < 0.1 s are initiated within the first 0.5 s of the plasma and one longer, 0.35 s inlet after 1.0 s.

Figure 3.14 presents the (top) spatial-temporal resolved chord brightness profiles of the horizontal (left) and vertical (right) bolometer camera, as well as (bottom) selected snapshots of the above profiles for both. The radiation, measured by the HBC, is mainly located inside the last closed flux

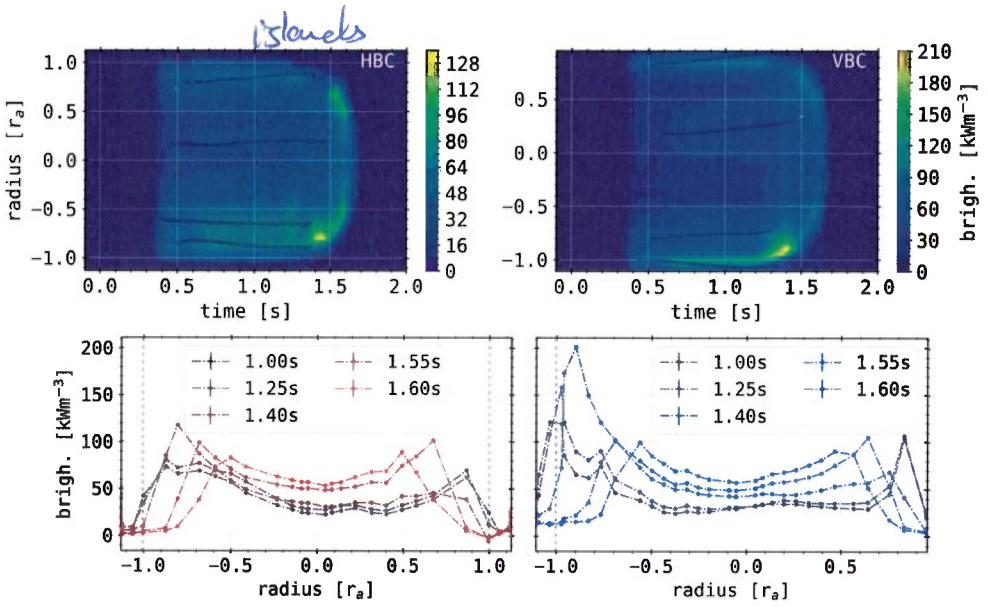

Figure 3.14.: XP20180929.29
Chord brightness profiles **(top)** in two-dimensional contours and **(bottom)** at significant points in time for both cameras HBC and VBC.

surface, i.e. $r_{\text{eff}} \in \{-1, 1\}$. After the delayed increase of radiation power, the chord brightness develops generally symmetric, with slightly larger and wider structures towards the negative end of the scale, or closer to the VBC in the bolometer plane. Very shallow peaks limit the radiation profile on both ends inside the confinement area, while a hollowness with a $20 - 30\%$ reduction around $r_{\text{eff}} = 0$ can be seen. After the second gas injection, the brightness of the peaks increases gradually, until at 1.4 s around $r_{\text{eff}} = 0.75 r_{\text{a}}$ a pronounced maximum appears. This structure is followed by a quickly inwards, i.e. towards the magnetic axis shifting radiation front beyond 1.5 s, which presents not emission after 1.7 s. Similar results are found with the VBC chord brightness profile. Due to the asymmetric line of sight geometry of the vertical camera relative to the magnetic axis, the spatial range is slightly shifted towards the negative, which corresponds to the inside of the vessel or left of the triangular cross-section. The VBC profile features a stronger hollowness of about 50%. Furthermore, the small asymmetry of the HBC chord profile is much more pronounced in the vertical camera. The

exemplary snapshots of the profile underline this circumstance. Shown there is also the inward shift of the radiation over time towards 1.7 s. Both profiles feature the asymmetric maximum at 1.4 s on the lower inside the separatrix, close the aperture of the VBC.
Due to the delayed response of plasma radiation and therefore difference to the setpoint, the controller engages and initiates two, separate gas inlets. One small and large dent in the radiation power can be found following the actuation of the gas valve and ionization of helium in the scrape-off layer. The radiation power increases accordingly after the first gas injection and step in ECRH around 1.0 s, which leads to $f_{\mathrm{rad}} \approx 80\%$. However, due to the discrepancy between prediction and full dataset, the PID is assuming a much smaller radiation fraction, as shown by the red line in figure 3.13:(bottom right). The gas valves are opened again, since f_{rad} plateaued and has not yet reached the setpoint. The following 0.35 s long helium puff first slowly increases P_{rad} until the *actual* radiation fraction crosses 90%, where it again gains significantly beyond 95%. During that time, the electron plasma density collapses from the outside inwards, as at 1.3 s vol.14 is close to zero and vol.13 decreases about 50%. Meanwhile, vol.3, i.e. the core plasma, and central line integrated density reach their peak. At this point, the plasma became nearly transparent for the microwave beam and the discharge had to be terminated early.
Due to the more conservative PID coefficients and underrepresented *true* plasma radiation power by the prediction $P_{\mathrm{pred}}^{(1)}$, the second-long feedback gas puff essentially suffocates the plasma by increasing the impurity content beyond a sustainable level and thereby removes energy through radiative cooling from not only the scrape-off layer, but also the core plasma. Because of the shrinking density and temperature profiles, which changes the gradients, helium is transported inside the last closed flux surface and into the confinement regions core plasma. After 1.0 s, the plasma continuously loses ≈ 0.25 MJ per second, or irradiates 0.25 MW due to seeding. At increasing density and declining plasma energy, the temperature is assumed to be strongly reduced. The previously discussed radiation asymmetries in chord brightness profiles of both cameras in figure 3.14 can be identified as the connected plasma volume of gas injection (see figure 3.1). Once these profile changes have reduced the absorption of the microwaves enough, the ECRH has to be terminated in order to avoid too much stray radiation on plasma facing components. The remaining 0.2 MJ of plasma stored energy

are exhausted over the next 0.1 s at nearly 2 MW. This energy is partially irradiated, as P_{rad} increases by ≈ 0.75 MW. The remaining injected helium also dissipates energy by ionization and excitation in the core. The increasing core plasma density quickly drops, as the diamagnetic energy becomes zero and the remaining ionized gas neutralizes. The subsequent final radiation peak at 1.5 s is the result of the residual plasma and its recombination of hydrogen and impurities.
The radiation feedback XP20180920.29 has failed, since $P_{\text{pred}}^{(1)}$ did not provide the required accuracy for an approximation of P_{rad} and the system was not able to achieve a scenario of (stable) detachment. This led to an oversaturation of the scrape-off layer with helium, which caused plasma profiles to collapse and thus the discharge to be terminated early. Critical towards the efficiency of the feedback as well is the temporal delay, which is further exacerbated by the negligent, conservative scaling of the proportional K_{p} term in the process value $u_{\text{PV}}(t)$. From the chord brightness profile of the vertical and horizontal camera array, the radiation is found to be mainly to be located close the last closed flux surface, inside the confinement area. Therefore, additionally to excluding channel no.0, which was unexpectedly out of order in this experiment, the selection subset S has to be optimized towards this kind of plasma radiation profile. More lines of sight along this radial spectrum have to be included, while channels that do not see any or only small amounts of radiation have be removed from the feedback. However, in order to adequately represent any possible emissivity distribution for varying experiment scenarios, the subset S needs to contain detectors with lines of sight in all plasma regions.

Application Progress

The second application of the radiation feedback occurred in experiment XP20180920.31. Regarding the boronisation, the influx of impurities from the wall and general machine condition are assumed to be same as in the previous experiment. This discharge was also planned with 29.5 MJ of total input energy at 10 MW X2-mode microwave heating for 10 s in a similarly prefuelled hydrogen plasma. Furthermore, the real-time feedback system used the same settings as experiment XP20180920.29, i.e. $S = \{0, 3, 7, 14, 16\}$ and $P_{\text{pred}}^{(2)} = a_7 \Delta\tilde{U}_7$, or as in figure 3.12. However, the injection valves for this experiment are located opposite of the bolometer plane, in half module

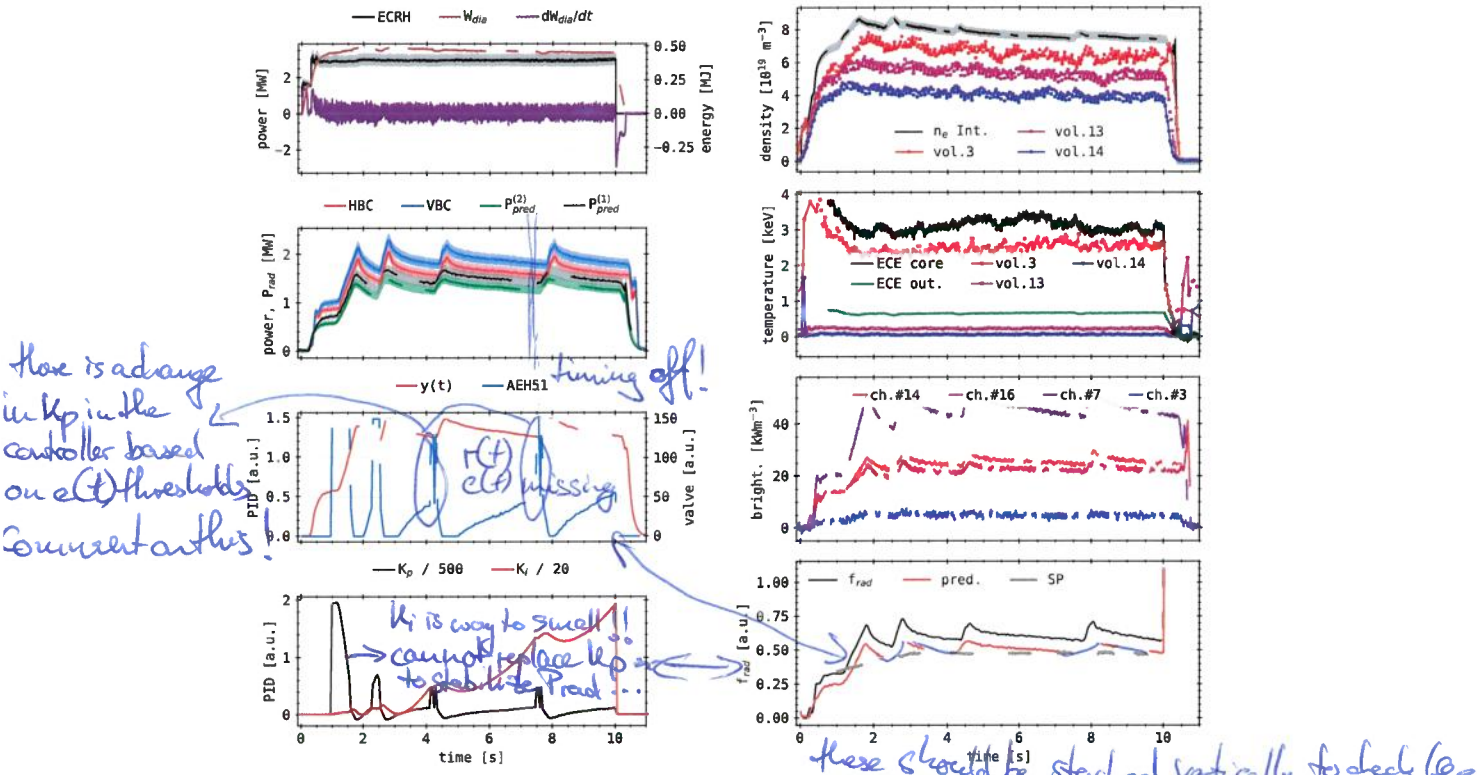

Figure 3.15.: XP20180929.31: **(top left)**: ECRH power, plasma energy and loss **(center left top)**: P_{rad}, prediction values **(center left bottom)**: PID control $u(t)$, reference $y(t)$ and valve actuation **(bottom left)**: Control component(s) **(top right)**: Electron density of Thomson scattering and dispersion interferometer **(center right top)**: Electron temperature of Thomson scattering and ECE **(center right bottom)**: Bolometer channels for $P^{(n)}_{\mathrm{pred}}$ **(bottom right)**: Radiation fraction(s).

no.5 and port AEH51, which is one half toroidal rotation away. The net toroidal current ~~by parallel plasma transport~~ increased over the course of the discharge to $\approx 2\,\mathrm{kA}$ in counter-clockwise direction.
The available plasma properties are shown in figure 3.15. The structure of the plots is generally the same as for the previous experiment. The duration of the discharge is now 10 s, given by the electron cyclotron heating of $\approx 2.9\,\mathrm{MW}$. Additionally, the now accessible electron temperature measure-

ments of both the Thomson scattering and electron cyclotron diagnostics are shown in the second plot on the right.
The heating power starts at 1.7 MW for the first 0.3 s, before increasing to $\approx$ 2.9 MW at 2.5 s, where it remains constant throughout the experiment. Accordingly, the diamagnetic plasma energy rises nearly linearly to 0.2 MJ. After a small plateau, W_{dia} increases more gradually together with the second heating stage towards 0.5 MJ. From there follows a slight decline of about 50 kJ until the termination of the microwave heating. Its time derivative, similarly to the heating power, rises to 1.75 MW and drops again as the stored energy plateaus. The same is repeated for the second stage. Afterwards, this peak decays with the same time constant as the positive slope of W_{dia}. After ECRH shut-off, the plasma stored energy quickly drops to zero within 0.3 s. This is also presented by $\mathrm{d}W_{\text{dia}}\mathrm{d}t$, as the peak dissipation of $\approx$ -3 MW is followed by a sharp increase towards zero, with two small reversals in slope in between around -1.25 MW.
The global radiative power loss of both cameras show similar behaviour, though their discrepancy is generally $>$ 10% for most parts of the experiment. Throughout the discharge, the vertical bolometer camera measures significantly more plasma radiation than its horizontal counterpart. The prediction values are similarly related, as $P_{\text{pred}}^{(1)}$ indicates about 10% more radiation power than $P_{\text{pred}}^{(2)}$, while the former is as much as 10% smaller than $P_{\text{rad, HBC}}$. At 0.25 s the radiation power rises quickly to 0.9 MW within the first 1 s. After a small increase to $>$ 1 MW towards 1.3 s, $P_{\text{rad, VBC}}$ sharply jumps and peaks at $\approx$ 2.2 MW around 1.8 s. Afterwards, the radiation level drops with a gradually decreasing slope. This behaviour repeats three times, with varying levels of P_{rad} and time in-between the peaks. The second follows about 1 s after the first, with a marginal increase in power of 0.2 MW. The subsequent two occur around 1.5 s and 3.2 s later at about the same power loss level as the first. All the peaks and valleys cycle between 1.7–2.4 MW. After ECRH termination at 10 s, the last stage has decreased to 1.8 MW. Beyond, the radiation power drops to 1.4 MW, where, after a small increment, P_{rad} goes to zero before 11 s. Differences between the full datasets and predictions are the less pronounced shape of peaks and slopes, smaller gradients in the rise and conclusion of the radiation and a substantial temporal deviation, which can be noticed around the maximums.
The control $u_{\text{PV}}(t)$ is composed of a proportional and integral part. During

the rise of radiation in $y(t)$, the PV peaks before 0.5 s, accounting for the first heating stage and slower response of P_{rad}. After the gradient in $y(t)$ shallows and ECRH increases, the control triggers a helium gas injection and therefore an increase in radiation. Over the course of the activation, $u_{\mathrm{PV}}(t)$ increases until the valve is closed, where the radiation still rises for ≈ 200 ms and the control conclusively drops. This behaviour is repeated for all subsequent gas puffs. Leading slopes in AEH51 signal are correlated to the increase in gradient in PV between injections.
The underlying system value $y(t)$, and therefore the prediction, underestimate the radiation level in P_{rad} significantly. Initiated actuations of the feedback valve in port AEH51 and subsequent injections of helium precede the peaks in radiation power. In the beginning, one gas puff leads to the first peak in P_{rad}. A second stage is enclosed before the next peak. For the following injections, incremental slopes lead up to the maximum amplitude activation, which increase in both width and height. A final, fifth stage is not completed due to the discharge being terminated beforehand. The behaviour of the valve can be derived from the two PID components the PID, which the control value is based on. The activation of the actuator is dominated by the proportional component of the PID. However, the potential fifth gas puff would have been initiated by the integral part K_{i}, as K_{p} has decreased substantially at this point. The leading slopes in actuator signal later in the experiment are supported by an integral component. Width and shape of the peaks in AEH51 signal are dominated by K_{p}. The line integrated and innermost plasma electron densities exhibit the first step in heating power around $2 \times 10^{19}\,\mathrm{m}^{-3}$, while volumes further outward increase more gradually. From line integrated to core and outward volumes the density reaches about $8.5\text{–}4.5 \times 10^{19}\,\mathrm{m}^{-3}$ respectively, around 1.5 s after the first helium gas injection. Afterwards, additional gas puffs produce small peaks in the line integrated density. Generally, n_{e} decreases over the course of the discharge to $7.5\text{–}4 \times 10^{19}\,\mathrm{m}^{-3}$ from the core further outward. Inversely, the electron plasma temperature is highest after the first ECRH stage at 0.25 ms with 5.5 keV for the innermost Thomson scattering volume. The electron cyclotron emission measurements are not available in the first 0.75 s. Core ECE measurements indicate a higher temperature than volume no.3 of about 0.5 keV. The further outward volumes no.13 and no.14, as well as the ECE measured temperature are significantly lower, well below 1 keV. After shut-off of heating power, the temperature drops quickly to zero,

K_{i} too low to make steady-state → oscillations (combined with K_{p} switching → large overshoots.
refocus: this is the main point of this study to understand the role of K_{x} and how it controls the feedback → discuss and draw conclusions!

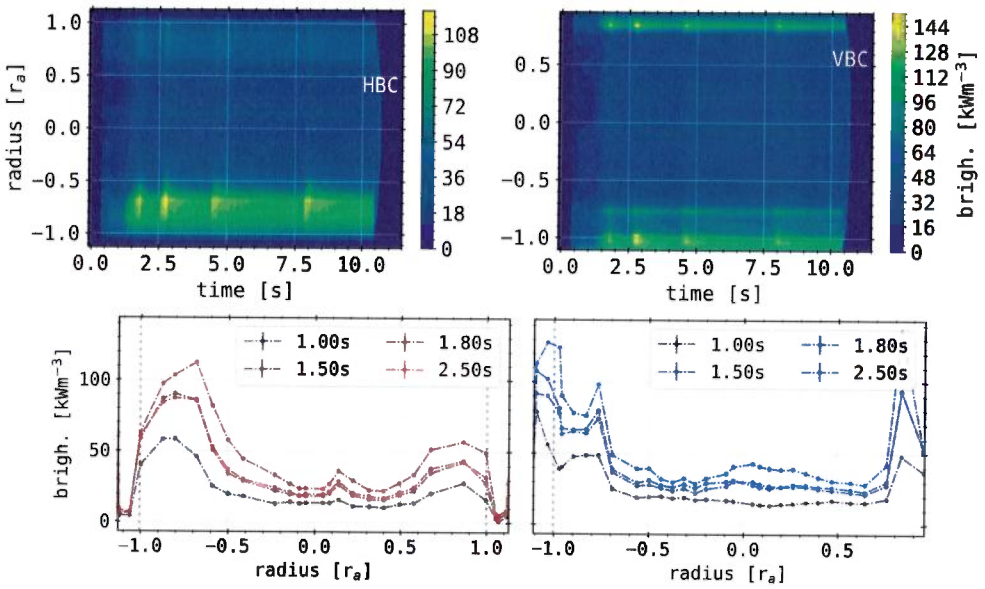

Figure 3.16.: XP20180929.31
Chord brightness profiles. **(top)** Two-dimensional contours **(bottom)** snapshots for both cameras, HBC and VBC around feedback gas puff.

where large oscillations in Thomson scattering measurements can be found. For very low electron plasma densities, the measurement of temperatures by elastic Thomson scattering is not applicable. Hence, before and after the plasma, those values show very large errors.
The chord brightness of the subset that was used to calculate $P_{\text{pred}}^{(1)}$ presents the same behaviour as P_{rad}. As in the previous experiment, the channels further inward, no.14 and no.16 measure overall less radiation power and show smaller response to gas injections than detector no.3, which is viewing close to the separatrix on the inside of the magnetically confined region. Channel no.3 presents the lowest brightness measurement and a negligible reaction to helium seeding. As the plasma collapses after 10.5 s, channel no.7 first drops before peaking and finally decreasing to zero, while no.16 and no.14 do not decrease.
The full chord brightness profile of the HBC and VBC, as well as snapshots from before, during and after the first helium gas injection are shown in figure 3.16. From the perspective of the HBC, the radiation is mainly located

inside the last closed flux surface, i.e. $r \in \{-1, 1\}$, with a strong poloidal asymmetry. The emission level on the bottom of the triangular cross-section, inside the separatrix and close to the VBC aperture, is at least twofold of that on the top. During the first gas injection, the radiation level strongly increases towards approximately 1.9 s, where the maximum has significantly shifted inside. This is reverted after the injection is stopped. An emission front around $\approx 0.75 r_a$ remains until the collapse of the plasma after 10.5 s, in which the following gas puffs each create small local maximums that are located slightly further inside. Radial gradients indicate that the entire radiation distribution is shifted inwards during that time. The same can be found on the top around $0.8 r_a$, however at much lower power densities. The emissivity around the magnetic axis, i.e. $r = 0$, is only 1/3 of the peak on the bottom side. Towards the top, there is a third structure in the brightness profile at $0.2 r_a$, which is consistently below the level of the upper peak. The vertical camera measures a radiation peak, similar to the negative end in the radial spectrum of the horizontal camera, outside and along the separatrix at $r = r_a$. The same behaviour in response of the helium gas puffs as on the left in the HBC can be examined here. The structures radial width however is much smaller, while being distinctly limited on the inside at $-0.95 r_a$. Another structure can be found around $-0.75 r_a$, with about 3/4 of the former intensity. On the opposite end of the radial profile, another emissivity peak can be seen, with comparable amplitudes after gas injections but much narrower radial proportions. A central structure can also be found $\approx -0.1 r_a$, although with a much larger radial gradient as seen by the HBC. The poloidal asymmetry in the horizontal camera measurements is exemplified by the individual chord brightness snapshots of before, during and after the first gas injection. Both response and absolute level of the emissivity close to the separatrix are up to a factor of two larger on the *left*, or close to the VBC aperture on the bottom side of the triangular cross-section. The power density is highest right before the end of the puff, from where it decreases approximately to the level in the beginning of the injection. With the increase in emissivity, the location of maximum intensity also moves inwards. The same can be found for the negative end of the radial spectrum in the vertical camera profiles. Moving inwards, the previously examined gap and second structure is found, with less pronounced maximums and no positional shift. On the other side, increments in radiation power density are significantly larger, while no movement is exhibited.

The *actual* and predicted radiation fraction, based on P_{rad} and $P_{\mathrm{pred}}^{(1)}$ respectively, differ significantly. At most times, and especially during and after gas injections, the prediction underestimates the actual radiation fraction by at least 10%. Furthermore, f_{rad} is well below the setpoint of 90%, reaching a maximum of 73% after the second gas puff. The conservatively set K_{i} was not able to affect and achieve a consistently higher radiation fraction by injecting more helium into the scrape-off layer. For a factor of ten larger K_{i}, the process value $u_{\mathrm{PV}}(t)$ would be dominated by an integral component of error compensation later during the discharge and increase the radiative exhaust. At this point however, the gas injection is insufficient for radiatively cooling the SOL and increasing the radiative power loss to a high enough level for plasma detachment. Furthermore, this combination of K_{i} and K_{p} is unable to maintaining a constant, high radiation fraction $> f_{\mathrm{rad}}80\%$ in this scenario. The large gaps in gas feedback, which cause the radiation fraction to decrease significantly in-between valve activations, are basically defined by K_{p} in the beginning. This can potentially be bypassed and enhanced by a smaller, conservatively scaled differential component K_{d}. The significant drops in P_{rad} after each gas puff could be dampened by a similarly proportioned K_{d} like the previously constructed $10K_{\mathrm{i}}$, since the differential component scales $\propto \mathrm{d}P_{\mathrm{pred}}^{(1)}/\mathrm{d}t$.

To summarize, this conservative set of proportional and integral PID components K_{p} and K_{i}, without a derivative part K_{d}, is not able to achieve stable detachment by helium impurity seeding. The gas injection is insufficient in radiatively cooling the scrape-off layer. A positional shift of peak radiation location can be observed in the chord brightness profile during impurity gas injections, although the outermost electron densities and temperatures do not indicate perturbations during those times. At the achieved radiation fraction of $\approx$ 75%, an improved particle and power exhaust is expected, which is supported by the increasing P_{rad} at relatively stable W_{dia} under the assumption of a constant target heat load P_{div}. The desired, as well as theoretically predicted level of f_{rad}[121], at which a significant inwards shift of impurity radiation and plasma profiles is expected, was not achieved.

The possibility of feedback, based on a real-time radiation prediction was presented. Latency and accuracy of the proxies, defined in equation (3.1) and equation (3.2) as $P_{\mathrm{pred}}^{(n)}$ and calculated by the bolometer system using algorithm 1, are adequate for the application of impurity seeding feedback.

A different combination of proportional and integral error compensation K_p and K_i, or even an entirely new set with a differential contribution K_d can provide the necessary feedback to achieve the desired $f_{rad} = 90\%$. To support this claim, a *synthetic* PID controller, which was previously applied to the system in figure 3.6, has also been used to find different contributions to the control function u_{PV} for achieving the desired 90% level of radiation fraction for the above experiment. In order to adequately address the plasma scenario, the process value is based on the provided $f_{rad,XP}$ through the proxy $P^{(1)}_{pred}$. Two scenarios of PID control are presented: K_p and K_i can be adjusted, as well as K_i and K_d are optimized for a given K_p from the experiment. Assuming the system value to be

$$y(t) = \left(1 - \hat{f}_{rad}\right) u_{PV}(t) + f_{rad,XP} \,,$$

where $\hat{f}_{rad}$ is used to define the cost or efficiency of the control output towards plasma radiation adjustments. For example, to achieve the results shown in figure 3.17, $\hat{f}_{rad} = 0.5$ or 50%. This is in line with theoretical predictions of operational detachment scenarios, where higher density scrape-off layers are stable at lower impurity concentrations and higher neutral pressures. Furthermore, the control is given a 0.5 s penalty, as is the case during the actual experiment in order to avoid to early gas feedback and cooling of the plasma.

In the case of optimized integral and proportional components, K_p roughly mimics the behaviour that was experienced during the actual experiment. In the beginning 0.5 s of feedback, K_p shows fast scale oscillations due to numerical artefacts. The response of K_i is two orders of magnitude larger when compared to the respective quantities in the experiment. The relative level is noted as $K_d : K_i = 1 : 2/3$. The integral compensation also starts early, together with the proportional contribution, in contrast to the experiment. The resulting *synthetic* radiation fraction model quickly, after the penalty time, rises to the setpoint of 90%. The enclosed small steps in K_p, in addition to oscillations in the underlying f_{rad} from the experiment, lead to under- and overshooting of the mimic radiation fraction around the setpoint. Beyond 5 s, the integral K_i has significantly levelled out the process value, which causes K_p to decrease and become negligible. Remaining peaks therein are subject to the underlying $f_{rad,XP}$.

For a synthetic PID control, including a K_p as in the experiment of the

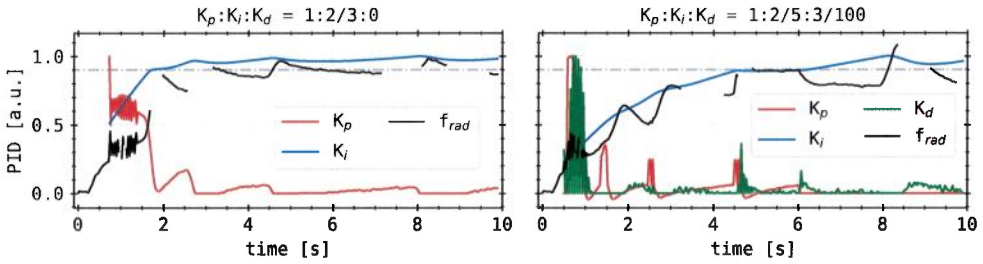

Figure 3.17.: Adjusted, simulated PID controller response based on f_{rad} in XP20180920.31. The impact of the feedback on the radiation fraction was modelled linearly by a cost function around a target $\hat{f}_{\mathrm{rad}}$. The setpoint SP is set to 0.9 or 90%. **(left)**: The algorithm was allowed to control K_{p} and K_{i}. The ratio is noted above, while their values are shown normalized. **(right)**: PID control derived K_{i} and K_{d}. The proportional K_{p} was taken from the experiment data, as seen in figure 3.13.

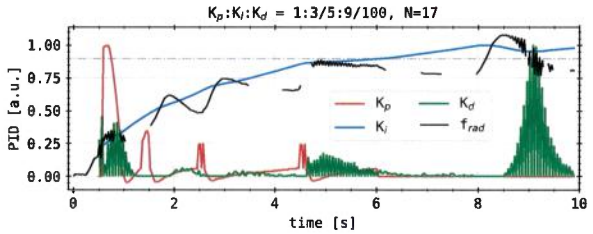

Figure 3.18.: Simulated PID response based on f_{rad} in XP20180920.31 including an ansatz with damping over $N\Delta t$ previous samples. Results are obtained for $\hat{f}_{\mathrm{rad}}$= 0.5 and $N = 17$.

modelled after radiation fraction, results also now feature a differential component K_{d}. The PV increases towards 90% much slower compared to the previous case. At 5 s, $f_{\mathrm{rad}} \approx 0.9$ is reached with a short plateau, after which K_{i} and K_{d} are not able to compensate the missing proportional scaling. Due to the consistently larger error, the integral component increases and adds to the existing peak in $f_{\mathrm{rad,XP}}$ at 9 s. The ratio between the individual contributions therefore also differs significantly, where $K_{\mathrm{p}} : K_{\mathrm{i}} : K_{\mathrm{d}} = 1 : 2/5 : 3/100$. Larger values of K_{d} lead to strong oscillations, since no dampening of the control u_{PV} to $y\,(t)$ is applied. For an ansatz of

$$y(t) = \left(1 - \hat{f}_{\text{rad}}\right) e^{-(t-N\Delta t)} u_{\text{PV}}(t) + f_{\text{rad,XP}} \ ,$$

with exponential dampening over $N \in (5, 20)$ samples of length Δt, results do not improve. Including this model of response, the control in figure 3.18 does not manage to achieve a constant 90% radiation fraction within the 10 s experiment duration. Though, the overshooting of the integral part is slightly reduced by a stronger K_{d}.
With this approach, it is possible to model and discuss the impact of latency and response of the plasma with regard to the feedback control $u_{\text{PV}}(t)$, as well as to study the influence of potential delays between the feedback process value $y(t) = P^{(1)}_{\text{pred}}$ on the *actual* radiation fraction. This is however not within the scope of this work and not further elaborated on.

Using the 3-chamber model as $y(t)$ predictor would have been better.

3.2.3. Radiation Feedback Controlled Discharge

The previously discussed real-time radiation feedback experiments were not able to achieve stable, controlled plasma detachment. However, the experimental results and control data indicate that optimizations of the feedback system and scenario may lead to controlled detachment. It was shown that, on the one hand, the large latency of the radiation feedback and plasma response require a more aggressive setting of the PID controller responsible for the gas injection, and on the other hand, the region of interest and channel selection of the bolometer for feedback purposes has to be optimized in order to adequately support the actuation of the valves. An experiment with a radiation fraction $f_{\text{rad}} \geq 90\%$ and a significant reduction of target heat loads, involving the injection of hydrogen into the scrape-off layer based on real-time approximations of the radiative power loss will be discussed hereafter.

This is not clearly elaborated that it is the lag that is the problem. The issue here seems to be suboptimal flux radius!

The experimental data can be seen in figure 3.20. Discharge number XP20181010.32 consisted of 9.2 s of plasma with maximum 6.23 MW of electron cyclotron heating power and total input energy of 55 MJ. This plasma was heated by microwave radiation coupling to the second-harmonic ordinary (O2-) mode. The plasma vessel was pre-filled by five, 5 ms gas puffs of hydrogen at $\approx$ 200 mbar L/s. The fast thermal gas injection system also seeded hydrogen at 750 mbar into the scrape-off layer. The responsible gas injection valves are the same as in the previously presented experiment. However, the net toroidal current increased to $\approx$ 0.9 kA over the course of the discharge in

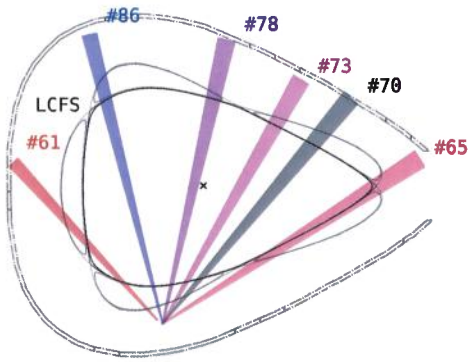

Figure 3.19.: Line of sight selection for experiment number XP20181010.32, only containing VBC channels. The LOS cones cover all magnetic islands, as well as the core region and parts of the in-between X-points of separatrices.

this was done so far as well with HBC?!
Why change now and why/how is this more consistent?

counter-clockwise direction.
In order to provide a more representative radiation power loss proxy for a scenario involving SOL gas injections, the lines of sight selection was changed accordingly. The subset $S = \{65, 78, 61, 73, 86\}$ was adjusted to consist only of channels from the vertical bolometer camera. The line of sight selection can be seen in figure 3.19. Previously discussed results showed significant differences between the chord brightness measurements, as well as their toroidal, global power loss extrapolation between the two cameras. The vertical camera, thus far, has seen a greater response of the plasma radiation around the separatrix to the feedback gas injections and overall higher maximum emissivities due to its respective line of sight geometry. Because of the connection along the magnetic field lines between the seeding valves and lower scrape-off layer of the triangular cross-section, the vertical camera is assumed to be more suitable to measuring the impact of gas feedback. So far, the chord brightness indicated the impact of radiation feedback on P_{rad} to be largest close to the VBC aperture and around the magnetic islands on the inboard and lower part of the triangular cross-section, where the bolometer is located. The above line of sight selection of vertical camera detectors covers those particular areas, as well as the in-between located X-points, where at very high radiation fractions $f_{\mathrm{rad}} \rightarrow 100\%$ condensation of radiation is expected.
Within the first 0.5 s, the ECRH increases to 2.3 MW and 4 MW for ≈ 0.2 s respectively. After, the input power is raised again to 6.1 MW between 1–1.5 s. For the following 7 s, the microwave power is kept constant at 5.5 MW, with three smaller steps from 8.5 s to 9.2 s down to zero. The diamagnetic en-

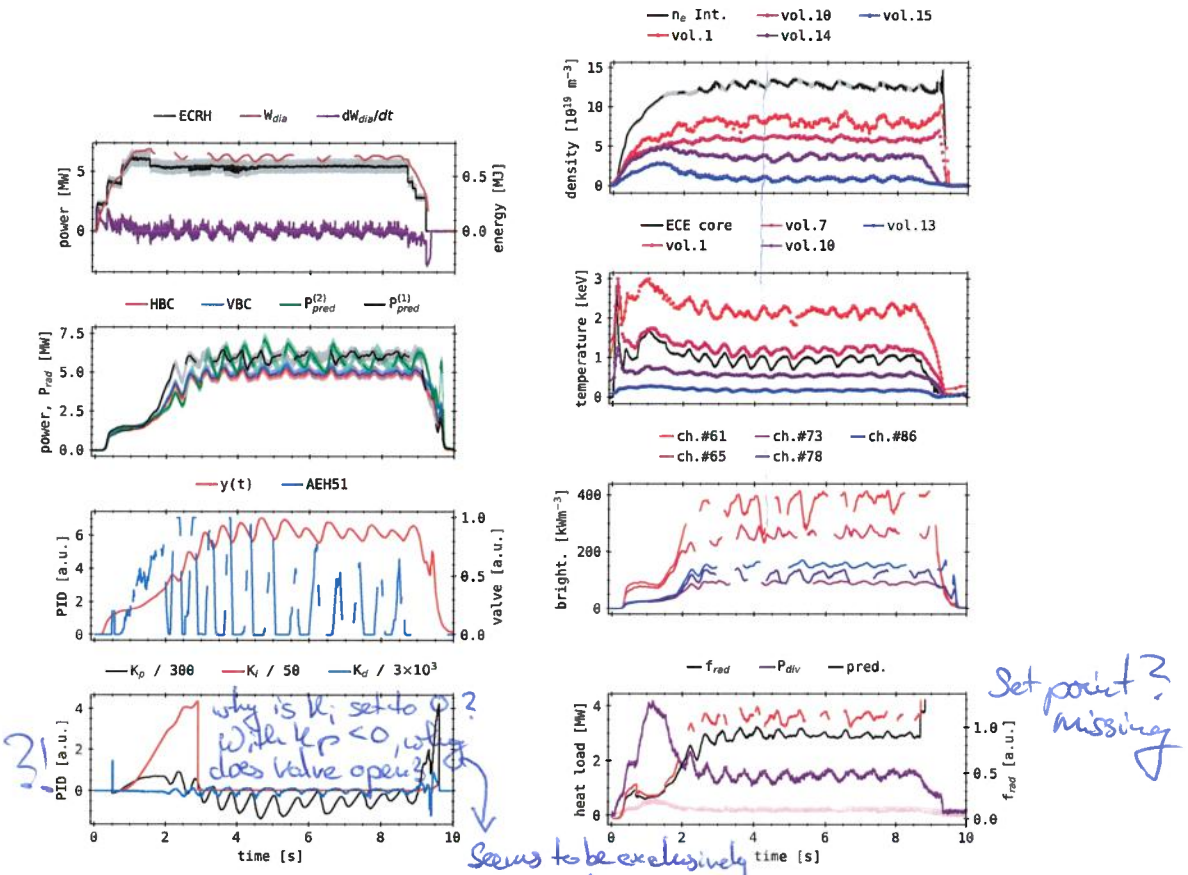

Figure 3.20.: XP20181010.32:
(top left): ECRH power, plasma energy and loss **(center left top)**: P_{rad}, prediction values **(center left bottom)**: PID control $u(t)$, process value $y(t)$ and valve actuation **(bottom left)**: Control components **(top right)**: Electron density **(center right top)**: Electron temperature **(center right bottom)**: Bolometer channels for $P^{(n)}_{\text{pred}}$ **(bottom right)**: Radiation fractions and target heat loads (individual, integrated).

ergy rises more gradually, with small changes in slope for each ECRH stage, to 0.75 MJ at 1.5 s. Afterwards, the level of W_{dia} decreases slightly over the course of the discharge to 0.65 s, on which oscillations of 50 kJ amplitude are superimposed. Those perturbations are in sync with the activation of the gas feedback. After the ECRH drops from 5.5 MW, the plasma energy declines within 0.5 s to zero. The resulting $\mathrm{d}W_{\mathrm{dia}}/\mathrm{d}t$ indicates that the initial heating stages are absorbed with up to 2 MW per increment by the plasma, while the power deposition decreases with increasing plasma energy towards the following microwave power step. Following the last ECRH stage before 1.5 s, the plasma energy exhaust oscillates accordingly between −1–1 MW, until the heating power steps down and W_{dia} drops to zero. Conclusively, $\mathrm{d}W_{\mathrm{dia}}/\mathrm{d}t$ represents the energy dissipated from the plasma with −3 MW from 9.2 s on until W_{dia} is zero.
Within the first two ECRH stages, the radiation power climbs to 1 MW, after which it shortly plateaus and slowly increases to 4.5 MW towards 2.2 s. On top of a slight increment of base level P_{rad} to 5 MW, superimposed oscillations as in W_{dia} with amplitudes of up to 0.5 MW can be seen. However, these perturbations are *retarded* to the activation of the gas valves, i.e. peaks in P_{rad} occur 0.2–0.3 s after the respective gas injection. They also decrease over the course of the discharge. After ECRH shut-off, the radiation power declines sharply, with a conclusive peak due to particle recombinations as the plasma collapses. The horizontal and vertical camera measure a P_{rad} that is within their respective error bars, while $P_{\mathrm{rad,\,VBC}}$ is consistently larger. Both of the real-time proxies show larger radiation powers than the full camera extrapolations. Before the second oscillation in P_{rad} around 3 second, the single channel approximation $P_{\mathrm{pred}}^{(2)}$, based on a vertical camera channel no.70, indicates smaller values, however with greater perturbation amplitudes afterwards. The subset prediction $P_{\mathrm{pred}}^{(1)}$ increases early and presents an up to 1 MW consistently larger radiation power loss. Oscillations therein have slightly smaller amplitudes compared to the other proxy, while both level around 6 MW.
The control function $u_{\mathrm{PV}}(t)$ generally follows the behaviour of the process value $y(t)$. The gas injection valves are activated when, on the one hand, the overall radiation level as presented by the PV in the beginning is too low, or on the other hand, during falling edges in the oscillations thereof, directly caused by the subsequent gas puffs. At first, during the initial $y(t)$ plateau, the valves gradually increases gas injection to 75% of its maximum

until 2 s. Within the next 2 s, the valve is opened four times fully for ≈ 0.3 s each. Afterwards, a similar frequency and duration is maintained at a significantly lower, over time decreasing intensity until 8.75 s. The individual PID components below indicate a dominant proportional and differential contribution K_p and K_d for most parts of the feedback. In the beginning however, for the increasing seeding before 2 s, an integral K_i equally contributes to the actuation of the gas valves. Hence, K_p and K_i trigger the system in the beginning, where the radiation level is still low and therefore f_rad far away from the setpoint of 90%. As soon as $y\,(t)$ indicates > 5 MW of radiation power, K_p and K_d particularly shape the control function and valve activation. The proportional component is compensating, for one thing, the individual oscillations due to the feedback, and then again a slight increase in process value, which in itself overshoots the setpoint. The significantly faster reaction of the differential K_d enhances the feedback response to the intrinsic oscillations. After 9 s, when the ECRH decreases and the discharge is eventually terminated, the PID components produce large values, which are not relevant to the feedback anymore.

The presented volumes of the electron density measurement by Thomson scattering have been changed with respect to the previous experiments, though their ordering remains the same. After a steep increase until 1.5 s into a plateau, the electron density of both line integrated interferometer and Thomson scattering measurements show oscillations similar to the ones in P_rad with varying intensity. The line integrated n_e goes up to $\approx 1.4 \times 10^{20}\,\mathrm{m}^{-3}$ during the on and off of the feedback. From the inside out, the Thomson scattering volumes show descending electron densities of $9 \times 10^{19}\,\mathrm{m}^{-3}$, $6 \times 10^{19}\,\mathrm{m}^{-3}$, $3.5 \times 10^{19}\,\mathrm{m}^{-3}$ and $1 \times 10^{19}\,\mathrm{m}^{-3}$ respectively. The further inward volumes no.1 and no.10 increase slightly during and beyond the initial gas injection up to 2 s, however no.14 and no.15 decrease after $P_\mathrm{rad} \approx 3$ MW around 1.5 s. Line integrated interferometry measurements show sawtooth-like perturbations of the electron densities of $1 \times 10^{19}\,\mathrm{m}^{-3}$ in sync with the actuation of the feedback valves. Thomson scattering volumes no.1 and no.10 indicate no or negligible oscillations. Similar, but less pronounced peaks and drops compared to the interferometry are visible in volumes no.14 and no.15. All densities drop to zero after ECRH shut-off at 9.4 s.

The electron temperatures are presented for different Thomson scattering, as well as a central electron cyclotron emission volume. A large maximum

of 3.4 keV is found in the first 0.2 s after the start of ECRH. In descending order, this peak is shown by two innermost volumes no.7 and no.1, as well as the ECE core measurement and volume no.10. A further outward electron temperature measurement displays no such peak. By the initial ECRH stages, T_e increases again after a drop from the previous maximum to up to 3 keV in the innermost Thomson scattering volume. Number 7, ECE and no.10 respectively show lower electron temperature values down to 0.9 keV. During the first, longer gas injection, T_e collectively decreases for all measurement locations, with decreasing impact from the inside outwards. Volume no.10 and no.13 show only very little impact of the radiation feedback, though subsequent perturbations by the valve activations are still noticeable. The ECE and two inner Thomson scattering volumes indicate larger responses to the gas injection of up to 0.4 keV around their respective average of 0.8 keV, 2.2 keV and 1.2 keV. Further outwards, the electron temperature T_e in volumes no.10 and no.13 is around 0.6 keV and 0.2 keV, with variations of at most 0.1 keV. These oscillations are anticyclical to the gas injections and radiation power loss measurements, i.e. when P_{rad} increases due to a hydrogen puff in the scrape-off layer, the temperatures decrease and vice versa. After 8.5 s, where the ECRH starts to decrease, the electron temperature quickly drops to zero in all locations before 9.5 s.
The chord brightness of the subset $S = \{61, 65, 70, 73, 78, 86\}$ for radiation prediction $P_{pred}^{(1)}$ and channel no.70 for $P_{pred}^{(2)}$ largely resemble the already presented P_{rad} and aforementioned proxies. The line integrated radiation power density greatly differs among the selected channels and lines of sights. The colour of the plots matches the in figure 3.19 presented lines of sight. Channels no.70, no.86, no.73 and no.78 share a shallower slope than the overall P_{rad}. They also present similar or slightly larger average emissivities like in XP20180920.31 of 80–160 kW/m^3. A noticeable temporal shift between the aforementioned channels can be seen, i.e. no.70 has peaks where no.78 and no.86 have local minima, while maxima are found later the higher the emissivity. The response to the gas injection is within 40 kW/m^3 for those channels during this experiment. The radiation intensities measured by channel no.65 and no.61 greatly differ from the previous ones. Both show a very steep rise during the initial heating stages, with a subsequent plateau and slight decrease until 1.5 s. After, channel no.65 goes up to average $\approx$ 290 kW/m^3, with oscillations of up to 60 kW/m^3. Channel no.61 reaches

a baseline of 360 kW/m^3, from which perturbations due to the gas injection vary between 40–100 kW/m^3 over the course of the discharge. Between 4–5.5 s and around 6.75 s, the peaks and drops in no.61 are extraordinarily larger than during other gas puffs. These oscillations appear retarded to the hydrogen injections by around 0.2–0.3 s. A small increase in baseline of $\approx$ 40 kW/m^3 during the cycling of the feedback is also visible in channel no.65 and no.61. Their local maxima and minima occur later than the previous channels, which measure lower emissivities. However, after the ECRH step down at 8.5 s, the radiation intensity starts to decrease first in those channels, before no.73, no.78, no.86 and no.70 peak and sharply drop to zero around 9.5 s.

So is the LOS now better as discussed above?

The resulting radiation fractions of both the presented proxy $P^{(1)}_{\text{pred}}$ and mean between $P_{\text{rad,HBC}}$ and $P_{\text{rad,VBC}}$ are shown next to the heat load of the individual divertors and the integrated P_{div}. Both proxy and P_{rad} show an overall similar behaviour of f_{rad}, though, as seen before in $P^{(1)}_{\text{pred}}$, the total radiation power loss is being overestimated by the prediction, which leads to a larger and even greater than unity ($P_{\text{rad}} > P_{\text{ECRH}}$) radiation fraction. During the initial stages in microwave heating, f_{rad} quickly increases to 30-40%, before dropping again after the final ECRH power is reached. By the first, longer gas injection, the radiation fraction goes up to 80%. Subsequent valve actuations increase $f_{\text{rad}} > 90\%$ towards 3.5 s. For the power loss derived from the mean P_{rad} of both camera arrays, the following gas puffs cycle the radiation fraction between 90%-100%. Towards the end of the experiment, i.e. 9 s, the perturbation amplitude decreases and the mean $f_{\text{rad}} \rightarrow 90\%$ due to compensations in control $u_{\text{PV}}(t)$ and reduced gas injection. Since $y(t) = P^{(1)}_{\text{pred}}$ and the prediction overestimates P_{rad}, the radiation fraction provided to the feedback control is significantly larger than 100% during the alternation of the valve control. In accordance to P_{rad} and the adjustments in gas injection, the perturbations in f_{rad} decrease over time, where in the beginning variations of up to 15% can be seen. From prediction $P^{(1)}_{\text{pred}}$, f_{rad} even reaches 120% and oscillates between 115-105%. The integrated target heat load increases quickly until the maximum microwave heating is achieved at $\approx$ 1 s to 4.2 MW. Afterwards, by the initial long and subsequent shorter hydrogen injections, P_{div} decreases to 2 MW at first and then averages around 1.4 MW over the following gas puffs. Similar to P_{rad}, the response in target heat load to the later valve actuations decreases to-

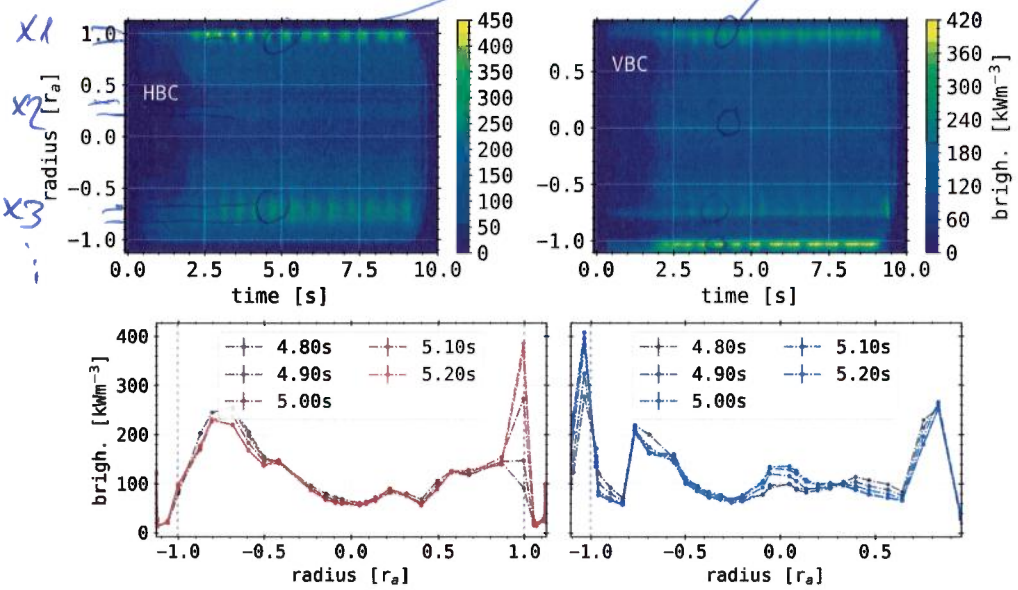

Figure 3.21.: XP20181010.32
Chord brightness profiles. **(top)** Two-dimensional contours **(bottom)** snapshots for both cameras, HBC and VBC around feedback gas puff.

wards 8.5 s. After the final gas puff, P_{div} decreases to 0.8 MW, from which it drops to zero at 9.3 s. The heat load of the individual targets is largely symmetrically distributed. However, the divertors HM51 and HM10 indicate a non-negligible, larger thermal power of 50–100 kW, or 20-40% more than the other modules. In direction of the counter-clockwise, net toroidal plasma current, the targets HM51 and HM10 in the respective half modules no.5 and no.1 are connected with each other by parallel transport along field lines. Furthermore, with respect to figure 3.1, this also connects to the responsible gas valves in module HM51, as well as the lower and inside magnetic islands. In figure 3.21 the chord brightness profiles of both vertical and horizontal camera, as well as temporal snapshots around one hydrogen gas puff at $f_{\mathrm{rad}} \approx 90\%$ can be seen. Similar to the previous experiment, the majority of emissivity is located at or around $r_{\mathrm{eff}} = \pm r_{\mathrm{a}}$. The poloidal asymmetry in chord brightness as measured by the HBC is reversed compared to before, with local maxima being strongly radially focused at the separatrix $r_{\mathrm{eff}}/r_{\mathrm{a}} = 1$. For each of the gas puffs and subsequent peaks in P_{rad}, a concur-

rent peak in the chord brightness profile with an overall radial inward shift of emissivity can be found. The temporal snapshots emphasize the (radial) asymmetry during gas injections, as well as show the evolution of the maximum emissivity at the separatrix $r_{\text{eff}} = r_{\text{a}}$. At $-r_{\text{a}}$, the emissivity increases from 80–380 kW/m^3 for one hydrogen injection. The small inward shift is visible in the peak position on the negative end of the radial spectrum. The absolute maximum is located opposite of the peaks that have been measured during the previous experiments. The responsible lines of sight cover areas that are opposite to the aperture of the VBC and do not overlap with the magnetic island on the inboard side. The chord brightness of the vertical camera now shows a small poloidal asymmetry, which is supported by the individual profiles below. Local maxima can be found around the separatrix at $r_{\text{eff}} = -r_{\text{a}}$ after gas injections, with parallel inward shifts of the radiation on both sides of the profile. As in the top of the HBC chord brightness, the radial gradients are much stronger on the bottom of the vertical camera profile. In addition, there is a significant gap in the radial evolution of the emissivity on the inside of the separatrix of the inboard side. In comparison to the peak evolution for a single gas puff in the horizontal profile, the vertical camera measures only an increase of $\approx 33\%$ around $-r_{\text{a}}$.
The resulting power balance for this discharge can be seen in figure 3.22. Within the first 2 s $P_{\text{bal}} = 0$ is satisfied inside its error bars, though the individual lines for P_{rad} indicate an underestimation of losses of ≈ 1 MW. After the first gas injection, the power balance starts to oscillate with the individual gas puffs, as seen in the radiation power loss P_{rad}, plasma energy W_{dia} and its derivative, as well as the divertor heat load P_{div}. On average, P_{bal} indicates a significant overestimation of the cumulative power losses of ≈ 1.5 MW. Perturbations due to the feedback injections cycle around this level by about 1 MW, with decreasing impact of each gas puff towards the end of the discharge. Due to the large error bar of ≈ 0.8 MW, the power balance can be assumed to be occasionally off by only 0.3 MW following individual valve activations. After the ECRH starts to step down, P_{bal} declines in two drops due to the collapse of the plasma and dissipation of the stored energy to -2.5 MW and -4 MW.
The measurement data of this experiment presents evidence of *feedback controlled stable plasma detachment.* Hydrogen gas injection into the scrape-off layer, controlled by real-time radiation power loss measurements was able to achieve and maintain a radiation fraction $f_{\text{prad}} > 90\%$ for extended dura-

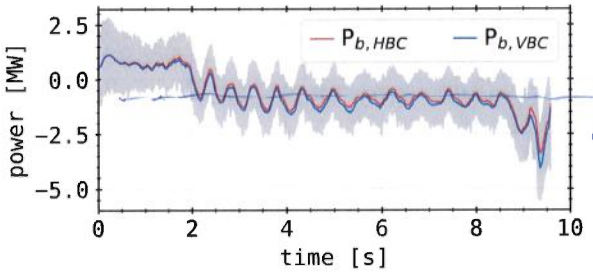

Figure 3.22.: XP20181010.32
Power balance for both P_{rad} of the individual camera arrays and a (grey) mean with error bar, derived from the intrinsic errors of the contributing physical quantities.

tions. Its application raises the overall radiation level, as well as significantly increases the emissivity along and close to the magnetic separatrix. The achievement of $f_{rad} \geq 70\%$ is accompanied by an inward shift of radiation towards the separatrix and center of the confined region. This is supported by the fact that the response to the individual gas puffs is, on the one hand, varying strongly in amplitude across the chord brightness profile, and on the other, temporally retarded with respect to different parts of the profile and their respective peaks and drops. The chord brightness profiles suggest radiation condensation, after increasing the radiation fraction $> 80\%$, in the inboard magnetic island and X-points towards the neighbouring islands on the top and bottom of the triangular cross-section. Therefore, the lines of sights covering those areas measure factor two to three larger emissivities compared to detectors mainly viewing the magnetically confined region. The magnetic island located on the inboard side is connected to the responsible feedback valves in half module no.5 (AEH51) by the plasma transport along field lines. The focussing of radiation power loss at X-points and close to the separatrix, i.e. in magnetic islands at significantly higher $f_{rad} > 70\%$, was predicted by results from the similarly configured W7-AS experiment and simulations of impurity radiation using EMC3-EIRENE[121, 122, 131]. In addition, there is no degradation of the plasma stored energy, as W_{dia} only increases until $f_{rad} > 80\%$ and only small perturbations of the overall level due to individual gas injections can be found. The line integrated electron density presents similar behaviour, where n_e starts to plateau at

$f_{\mathrm{rad}} \approx 80\%$ and then slightly increases over the subsequent hydrogen injections. Individual Thomson scattering volumes close to the magnetic axis indicate smaller densities, though with comparable development as the line integrated density at lower values. No concurrent perturbations due to the gas puffs can be seen. The two outermost scattering volumes indicate a drop following their initial increase after the radiation fraction reaches 40%. They present, in contrast to the volumes further inwards, significant perturbations due the gas injections, which are anticyclical to f_{rad}. The electron density close to the separatrix inside the confined area decreases $\approx 30\%$ when the radiation fraction goes from 90% to 100% and vice versa. Contrary, the electron temperature measured in the innermost volumes and from cyclotron emissions presents inverse behaviour to f_{rad}, while volumes further towards the separatrix display negligible interference by hydrogen injections. Also, the prior similarly drop from their respective maximum after $f_{\mathrm{rad}} > 40\%$. Towards high radiation fractions $f_{\mathrm{rad}} > 70\%$, a significant decrease of the plasma density close to the separatrix is expected, which leads to a steepening of the profile. For $f_{\mathrm{rad}} \approx 90 - 100\%$ the perturbations in volumes closer to the separatrix, opposite to changes in radiation fraction, indicate the inward shift of the plasma and therefore reduction of perpendicular transport to the scrape-off layer. However, in this case the accompanying temperature distribution flattens and only changes significantly closer to the magnetic axis. Though, assuming constant temperature profiles close to the separatrix, the net perpendicular plasma flux across field lines is reduced due to smaller gradients and the decreased density. Lastly, the integrated divertor heat load supports the previous arguments. After the radiation fraction increases beyond 40%, P_{div} decreases with increasing f_{rad} until it is more than halved at $f_{\mathrm{rad}} \approx 80\%$. With each subsequent gas injection and peak to 100% radiation fraction, the target heat load decreases further, before receding again with the concurrent drop in f_{rad}. The significantly larger heat loads of divertor modules HM51 and HM10 suggest a substantial contribution of the plasma radiation to the incident power of plasma target components in scenarios with very high f_{rad} and controlled radiative cooling in neighbouring plasma volumes. In this particular case, the parallel transport along field lines directly links the aforementioned modules, feedback gas valves and, indirectly in the second to next half module, inboard magnetic island in the bolometer measurement plane. The chord brightness reflects this as well, where the emissivity is twofold of that on the opposite side of

the profile and at $400\,\mathrm{kW/m^3}$ extraordinarily high when compared to the previous experiments.
In conclusion, this radiation feedback controlled experiment has achieved *stable plasma detachment* by gas injections into the scrape-off layer. The target heat load was significantly reduced by a factor of over two, while a radiation fraction and therefore radiative power loss $> 90\%$ of the input heating power was maintained by the PID controlled feedback system. During the gas injection, neither degradation of the plasma stored energy nor the core electron density, i.e. close to the magnetic axis, was found. However, the evolution of the electron temperature profile in its entirety indicates a stronger coupling to the radiation fraction than the electron density. A small but noticeable inward shift of the radiation distribution profile is measured by both bolometer cameras. The feedback control is able to consistently increase the radiation fraction $> 80\%$ by controlled injection of hydrogen, in this case the working gas in contrast to low- to medium-Z impurities, like helium in the previous experiments. In succession to reaching $f_{\mathrm{rad}} \approx 90\%$, the feedback input underestimates the impact of the individual gas injections, which leads to strong oscillations in P_{rad} of up to 10% of the heating power for full activation of the valves. Towards the end of the experiment however, the PIDs differential component can steadily reduce the overshooting of the control and therefore reduce the oscillations in P_{rad} and conclusively f_{rad}. Another significant factor to the cycling of PID control and valve activation is the latency of the feedback prediction and response of the plasma to the injections. Although the radiative power loss proxy $P^{(1)}_{\mathrm{pred}}$ is consistently larger than P_{rad} from either cameras' measurement, the adjusted channel selection S in figure 3.19, consisting of detectors from the vertical camera arrays viewing the magnetic islands and X-points, has improved the quality of the feedback.

You need to discuss that all exp. were not driven by W_i and hence not properly controlled in steady-state. So, it was not completed to demonstrate the PID settings that are useful/optimal.

3.2.4. Comparison to Different Feedback Control

The real-time radiation feedback system was able to perform plasma control based on other properties than the radiative power loss. In section 3.1, the dispersion interferometer, measuring the line integrated electron density, and optical fibre filterscopes, with lines of sight parallel to the divertors were introduced as additional candidates for plasma detachment control with the thermal helium beam gas valves as an actuator. In order to fully discuss the

also I think there is a strong P_{rad} & W_{int} correlation that should be discussed and that makes 3.13 possible

quality of the radiation feedback and categorize its results, a comparison to the achievements of the different control proxies is imperative.

Electron Density From Dispersion Interferometer

Similar to XP20181010.32, which featured controlled detachment by radiation feedback, this example of electron density feedback in experiment number XP20181016.16 consisted of hydrogen gas injections in half module HM51 by the same valves. Measurement results of this pre-filled hydrogen plasma can be seen in figure 3.23. A constant 5 MW of O2-mode microwave heating was applied for 21 s, after two initial, smaller steps at 3–4.5 MW within the first 1 s, before decreasing to 4.5 MW for the remaining 9 s. The plasma energy increases with small changes in slope, according to the steps in heating power, to 0.65 MJ. After the feedback gas injection starts at 2 s, there is a small drop in W_{dia}, which is followed by a decline towards 0.6 MJ until the step-down in ECRH. This is also reflected in the plasma energy. Besides the initial heating of the plasma and its collapse after 32 s, the plasma power loss $\mathrm{d}W_{\mathrm{dia}}/\mathrm{d}t$ presents high frequency, random perturbations between -0.1–0.1 MJ, which decrease slightly towards the end of the discharge.
Radiation power loss P_{rad} from both bolometer cameras are within their respective error bars. Following the heating stages in the beginning, P_{rad} plateaus around 2 MW before increasing to 4.15 MW after the hydrogen gas feedback starts at 2 s. The radiation power increases ≈ 0.1 MW before the step-down in ECRH. Afterwards, P_{rad} also steps down with the heating power to 4.05 MW, from which it drops to zero as the plasma collapses after 31.5 second.
The process value and feedback variable of this detachment experiment was the line integrated electron density, which was provided by the dispersion interferometer. A slowly declining n_{e} ramp around $1.1 \times 10^{20}\,\mathrm{m}^{-3}$ for this microwave heating and feedback configuration was developed from experiences of previous experiments. The density setpoint for this feedback was designed to achieve a constant, high plasma radiation fraction $f_{\mathrm{rad}} > 90\%$[158]. Consequently, the proportional PID component K_{p} prohibits gas injections before 2 s, as n_{e} sharply rises towards its setpoint value. The following gas valves activation is exclusively determined by the integral component K_{i}. When the downward ramp in density begins, K_{i} also decreases similarly to the valve actuation by a factor of two. The subsequent hydrogen gas injec-

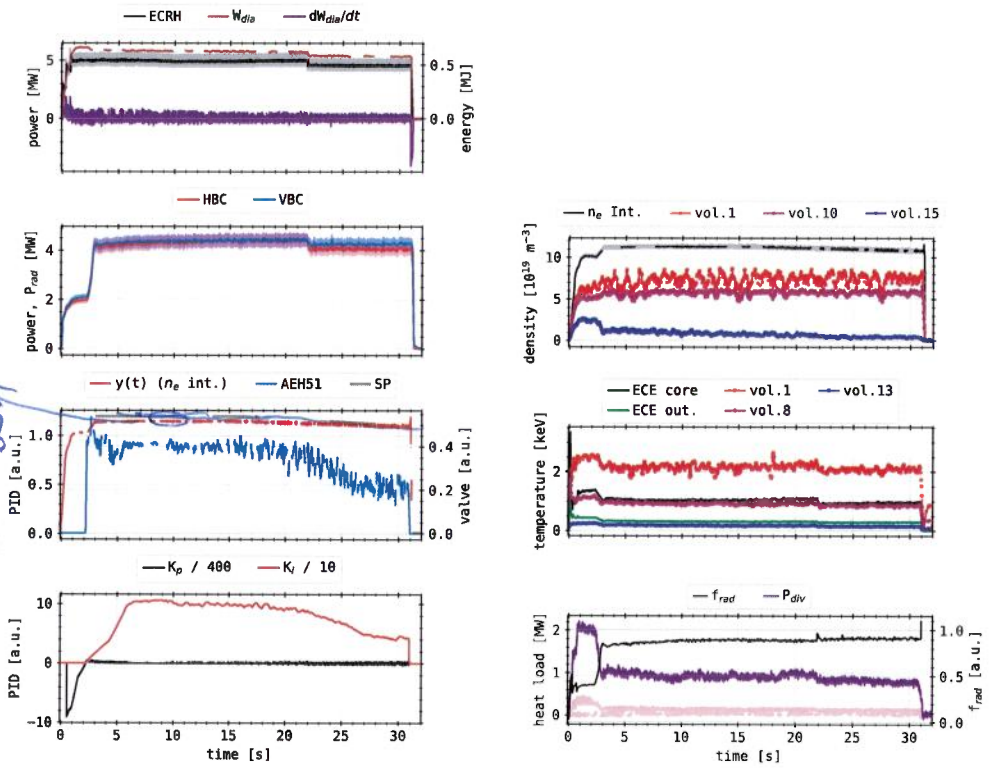

Why kp so small and Ki not increasing? There is an offset in SP here, right?

Figure 3.23.: XP20181016.16:
(top left): ECRH, plasma energy and loss **(center left top)**: P_{rad} **(center left bottom)**: Process value $y\,(t)$ and valve actuation **(bottom left)**: Control components **(top right)**: Electron density **(center right)**: Electron temperature **(bottom right)**: Radiation fractions and target heat load.

tion starts at 2 s, which increases n_{e} from 1–1.15 $\times\, 10^{20}\,\mathrm{m}^{-3}$. After 17 s, the electron density declines to 1.08 $\times\, 10^{20}\,\mathrm{m}^{-3}$ toward the end of the discharge. Thomson scattering volumes further inward exhibit similar behaviour, however at lower values and with smaller responses to the hydrogen injection. Volume no.15 shows a decline after 2 s and a stronger ramp down than the line integrated density towards 31 s, while n_{e} of inside volumes increases minutely. The electron temperature initially increases quickly to its maximum 2.6 keV in the innermost Thomson scattering volumes. Afterwards, T_{e}

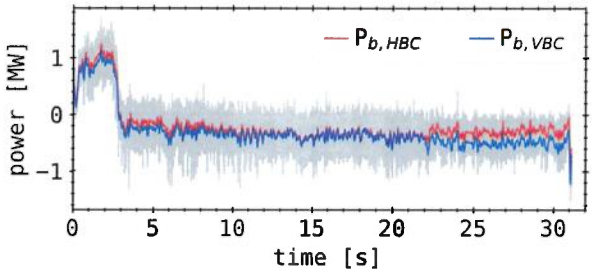

Figure 3.24.: XP20181016.16
Power balance for both P_{rad} (red, blue) of individual camera arrays and a (grey) mean with error bar.

declines with the gas feedback and then again with the downward step in heating power. This behaviour is found for all temperature measurements, at lower values further outward and closer to the separatrix. Overall, the average electron temperatures are comparable to measurement results in XP20181010.32.
The resulting radiation fraction and target power adjust accordingly to the increase in radiation fraction. As the gas injections increase n_{e} to its ramp-like setpoint, the divertor heat load P_{div} drops by 50%, while f_{rad} rises to 80% with a small incline to 90% towards 10 s. Integrated heat load and radiation fraction remain relatively constant throughout the rest of the discharge. Similar to XP20181010.32, two divertor modules in HM51 and HM11, close to the gas valves and along the direction of parallel plasma transport, show significantly larger heat loads in comparison to the others. Also, similar to the radiation feedback detachment, P_{div} already starts to decrease substantially as $f_{\mathrm{rad}} \approx 50\%$ and above, as well as T_{e} and n_{e} of volumes further outward begin to decline.
The global power balance for this experiment is shown in figure 3.24. There is a surplus of 1 MW of heating power in the initial 2.5 s, which is not accounted for in loss terms. After the feedback starts injecting hydrogen, P_{rad} increases by over 2 MW and P_{div} drops by 1 MW. The resulting power balance adjusts accordingly and indicates ≈ -0.2 MW, while $P_{\mathrm{bal}} = 0$ is satisfied within the error bar. From 20 s and following the step-down in heating power, P_{bal} begins to increasingly deviate from zero over time. The individual lines for either cameras P_{rad} start to diverge more, with P_{bal} from radiative power

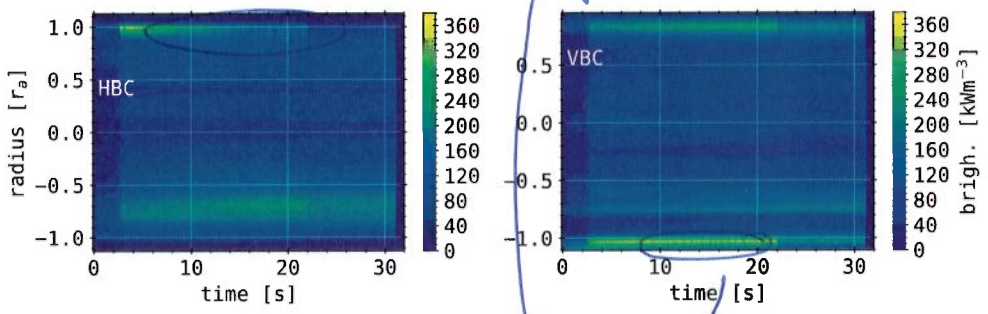

Figure 3.25.: XP20181016.16: Chord brightness profile of HBC and VBC.

loss measurements of the horizontal camera being closer to zero than from the vertical.

The chord brightness profile for both bolometer cameras can be seen in figure 3.25. Very similar results to XP20181010.32 are presented. The HBC measures a strong poloidal asymmetry, with the maximum emissivity on the top of the triangular cross-section throughout the entire discharge. A similar structure on the inside, closer to the magnetic axis, is found for $f_{\text{rad}} > 50\%$. The peaks on both ends of the radial spectrum are located in the same position as before, i.e. $r_{\text{eff}} = r_a$, $0.8r_a$. Poloidal asymmetries for $f_{\text{rad}} > 50\%$ in the HBC chord profile decrease towards the step-down in heating power at 22 s. The maximum in brightness shifts to the other side at $r_{\text{eff}} \approx 0.7r_a$, while the peak on the negative end of the radial spectrum has almost entirely flattened. Vertical camera measurements also present local maxima at $r_{\text{eff}} = -r_a$, $0.9r_a$ for the entire duration of the discharge, with a substantial gap on the inside of the separatrix and negative end of the radial spectrum in the chord brightness. There is no reversal of the local maxima after 22 s in the VBC profile. However, the peak around $-r_a$ has decreased significantly to a similar level of the local maximum at $0.8r_a$. A small inward shift towards the magnetic axis of the chord brightness can be seen. For both cameras profiles, in agreement with the temporal evolution of P_{rad} and in contrast to XP20181010.32, there are no oscillations in the profiles due to cycling of gas injections. Furthermore, the total radiative power loss is 0.5 MW lower than the average during the radiation feedback detachment. The maximum chord brightness however is about is up to 20% and 15% lower for the horizontal and vertical camera, respectively. With

the step-down in heating power at 21.8 s, the chord emissivity also decreases slightly.
In conclusion, the electron density feedback results in a significant reduction of divertor heat load by radiatively cooling the scrape-off layer and increasing the radiation fraction, like it was discussed for the case of radiation feedback. The gas injection system aims to achieve a high performance plasma in terms of core electron density, which is defined by the previously explored n_e setpoint at $1.1 \times 10^{20}/\mathrm{m}^3$. Additionally, a slow ramp down in electron density is programmed in order to compensate for a gradual increase in P_{rad} over time due to a slowly increasing amount of intrinsic impurities. Accordingly, the radiation fraction is well adjusted above 80%, which leads to the already alluded to shaping of the electron density and temperature profiles. The more direct coupling, with less latency when compared to the radiation feedback, of hydrogen gas injections to the feedback proxy n_e yields much smoother and reliable results, without oscillations, in target heat load reduction.

C-III Radiation From Filterscopes

The third candidate for plasma feedback control was the C^{3+} (carbon) radiation intensity in front of the target, which is measured by filterscopes. The results of XP20180920.32 can be seen in figure 3.26. Like before, hydrogen is seeded into the scrape-off layer of a pre-filled hydrogen plasma by thermal gas injection valves in AEH51. In contrast to the previous experiments, this plasma was heated by microwave radiation coupling to the second-harmonic extraordinary (X2-) mode. After an initial step at 1.5 MW, a constant 3 MW of ECRH was applied to the plasma for 9.5 s. The plasma energy increases to 0.5 MJ, from which it declines towards the termination of the discharge. When the gas feedback sets in at 2 s, there appears a small increase in W_{dia}. Its time derivative reflects this behaviour, as two initial increments in heating power and the plasma collapse at 10 s can be distinguished in $\mathrm{d}W_{dia}/\mathrm{d}t$. Both bolometer cameras measure similarly behaving radiation powers, while the VBC indicates $\approx 10\%$ larger values than the HBC. After the start of the ECRH, P_{rad} plateaus at 1 MW, with a minor incline slope until 2.5 s. Following the beginning of gas injections, the radiation power loss gradually increases, until slowly equilibrating around 8 s at ≈ 2 MW. About 0.5 s after the ECRH is shut off, P_{rad} drops to zero as the plasma collapses.

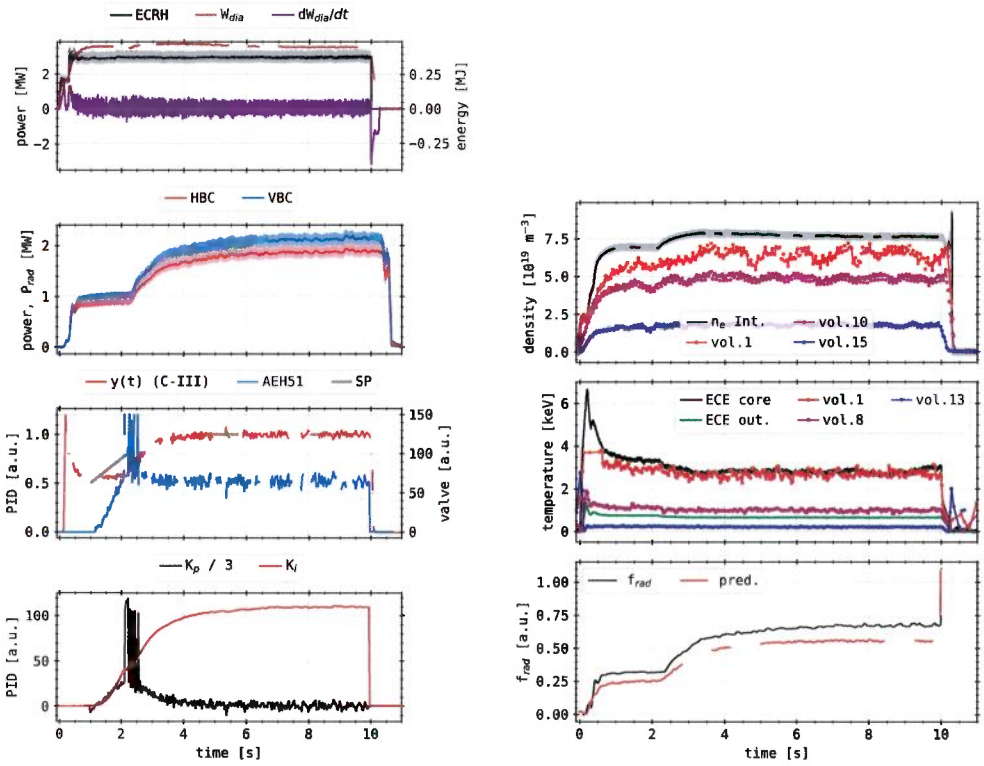

Figure 3.26.: XP20180920.32:
(top left): ECRH, plasma energy and loss **(center left top)**: P_{rad} **(center left bottom)**: Process value $y\,(t)$ and valve actuation **(bottom left)**: Control components **(top right)**: Electron density **(center right)**: Electron temperature **(bottom right)**: Radiation fractions and target heat load.

The PID process value for this feedback control is the ionisation radiation of triple ionized carbon C^{3+}, as measured by the filterscopes from their lines of sight, parallel to the divertor module HM51. The goal of this kind of control is to reduce the radiation from this intrinsic impurity species closest to the target and shift it towards the separatrix. The implication is that C^{3+} can be taken as an indicator of the scrape-off layer temperature and density profile for detachment purposes. Due to its ionization coefficients, it is assumed that a significant shift in C^{3+} radiation position represents an adequate particle

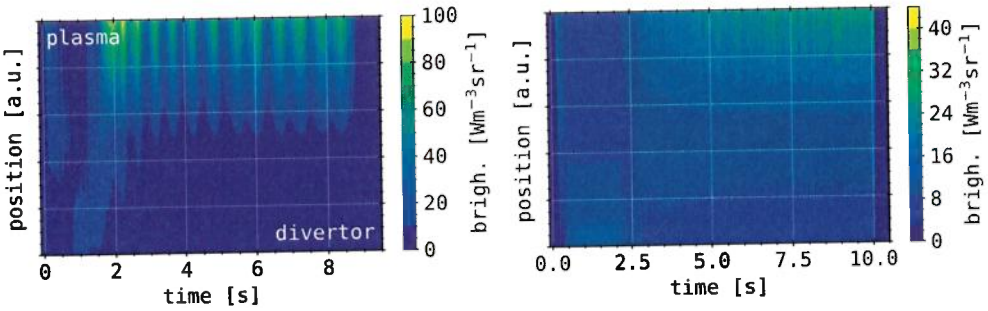

(a) XP20181010.32 **(b)** XP20180920.32

Figure 3.27.: Spatial-temporal evolution of C^{3+} radiation in front of the divertor in HM51. Plasma and target facing side (direction) are indicated. The measurements are performed by the same filterscopes, i.e. same lines of sight.

as the ionization front detaches from the target

and power exhaust reduction to the divertor by changing the perpendicular transport. The specific line of sight is measured from location AEI51, which is, in this specific case, the furthest away from the target. Therefore, the setpoint aims to increase the radiation in this location. The control function activates the valves after 2 s in order to radiatively cool the scrape-off layer and increase $y(t)$. After the process value reaches the setpoint, the valve actuation equilibrates in order to maintain the emissivity. Beside the initial opening of the valves, the control function is dominated by the integral PID component K_i.

Electron temperature and density are largely constant throughout the discharge, with minor perturbations due to the hydrogen gas injections. Closer to the magnetic axis, the plasma reaches a maximum density of $8 \times 10^{19}\,\mathrm{m}^{-3}$ at $\approx 3\,\mathrm{keV}$. Further outward and closer to the separatrix, the electron density and temperature decrease to $2 \times 10^{19}\,\mathrm{m}^{-3}$ at $< 200\,\mathrm{eV}$.

The resulting radiation fraction is significantly lower than during the previously presented detachment experiments. After the start of the gas injections, f_{rad} reaches a maximum 70% at the end of the discharge. In order to further discuss the results of this feedback experiment, the full set of filterscope measurements have to be compared to XP20180920.32. Their respective profiles can be seen in figure 3.27. Experiment XP20181010.32 shows emission closer to the separatrix at the start and during the early development of the

plasma radiation, i.e. at low radiation powers. Afterwards, during the first hydrogen injections, the emissivity is higher closer to the target. After f_{rad} increases > 80%, the C^{3+} radiation detaches from in front of the divertor and moves towards the plasma, where the maximum intensity for this set of lines of sight is found. The previously discussed oscillations in radiation intensity due to the cycling of the gas injections are also present here. The individual peaks appear in sync with the plasma radiation and with retardation to the respective gas puffs. By the results of the filterscopes, there is no emission of C^{3+} ionisations close to the divertor for $f_{rad} > 70\%$. A similar evolution of ionisation radiation from C^{3+} is found for XP20180920.32. At the start of the plasma, the emissivity is largest on the plasma side. This is inverted before the hydrogen injection starts. The emissivity profile changes again with the activation of the gas valves. The local maximum C^{3+} radiation is found on the plasma side. However, the emissivity closer to the divertor is not zero, indicating residual carbon ionisations in this location.
From the results of the filterscope measurements, a significant shift in temperature and density profiles is expected. With respect to the Thomson scattering and ECE electron temperature and density measurements, both feedback experiments show similar results closer to the separatrix. A reduction of impurity radiation close to the target and shift towards the core plasma is found. Presumably, ~~the perpendicular particle and energy transport across the separatrix and scrape-off layer, as well as~~ heat load of the divertor are reduced. In contrast to before, this method does not achieve higher radiation fractions $f_{rad} > 70\%$. Previous feedback experiments have shown similar results of temperature and density profile changes, as well as reduction of target heat loads for smaller radiation fractions $f_{rad} < 70\%$. This is also reflected here, as the emissions from C^{4+} are reduced by a factor of two to three for $f_{rad} \approx 50\%$. Since the impurity radiation is strongly coupled to the underlying n_e and T_e plasma profiles, and the filterscope measurement provides much lower latencies and higher acquisition rates than the radiation proxy, much smoother and more reliable results without oscillations are achieved by C^{3+} emission feedback. The overall plasma performance during the detachment process, in terms of electron density and temperature profile, radiation power and divertor heat load, does not compare to the other experiments due to their inherently different microwave heating configuration[163].

3.3. Conclusions

In this chapter, the radiation feedback system was introduced. This system has been designed to achieve stable, controlled plasma detachment in cooperation with fast acting, thermal gas valves. Actuation of these valves, which either injected low-Z impurities, like He, Ne or Ar, or working gas into the scrape-off layer, was controlled by an integrated PID. The goal of the radiation feedback control is to achieve and maintain $f_{\mathrm{rad}} > 80\%$, which is expected to significantly reduce the perpendicular particle and heat transport across the separatrix and SOL onto the divertor.
In order to find low latency, high accuracy real-time representations of P_{rad}, two different proxies for predicting the total radiative power loss of the plasma have been established. Due to the intrinsic nature of the comparatively slower radiation measurement of the bolometer and the limited computational performance of the electronics, several assumptions about the radiation distribution have to be made. A subset S of the full set of lines of sight from both cameras is used to calculate $P_{\mathrm{pred}}^{(1)}$ in a similar approach to equation (2.25) in equation (3.1). This simplification is based on the assumption that the radiative power loss can be adequately extrapolated from measurements taken in a smaller area of the chord brightness profile in the bolometer plane. Additionally, information about the line of sight geometry and magnetic configuration, necessary to calculate P_{rad} after the experiment, have to be provided beforehand, therefore limiting the flexibility of the prediction. The second radiation proxy $P_{\mathrm{pred}}^{(2)}$ is based on the measurements of a single absorber $\tilde{U}_{\mathrm{M}}$, further reducing the contributing area from the triangular cross-section to the feedback. This approach also eliminates the time derivative in the bolometer equation (2.19), which requires relatively slowly transitioning or constant radiation distributions. In order to minimize the impact of noise to the feedback, an algorithm within the measurement procedure has been developed, featuring a FIFO array for smoothing and computational load reduction. A minimum total latency of the system of 13.6 ms for sample times of 1.6 ms was found. However, the M sample FIFO array further exacerbates this delay by smoothing over the absorber response with $\approx M\Delta t/2$ width.
Initial feedback experiments with helium lead to a radiative collapse of the plasma by oversaturation with impurities. The latency of the real-time system and the delayed response of the plasma radiation to gas injections can

not be compensated by the conservatively programmed PID control. For a more aggressive set of integral and proportional control components K_i and K_p, the system is able to consistently achieve radiation fractions $f_{rad} > 50\%$. Synthetic benchmarks for such a scenario of a virtual PID controller indicate that a set of parameters exists that is capable of increasing and maintaining $f_{rad} \approx 80\%$ with minor oscillations.

Experiment XP20181010.32 shows results of radiation feedback that present stable plasma detachment. For a radiation fraction of 50%, a substantial reduction of target heat load and transport is found. The PID controlled gas injections increase the radiative power loss to a level of $f_{rad} > 85\%$ with remaining oscillations from cycling in valve actuation due to the large latency. Divertors close to the gas valves and along the parallel transport show a significantly larger heat load. The total integrated P_{div} is reduced by at least a factor of two for $f_{rad} \geq 90\%$. From filterscope measurements of C^{4+} ionisation radiation, plasma detachment can be seen for much lower radiations fractions of $\approx 50\%$.

In comparison to other feedback candidates, the latencies of plasma response and measurement complicate the application of real-time radiation predictions. Electron density and impurity radiation feedback perform more reliable and smooth detachment experiments. However, P_{pred} does not require preceding explorations of plasma parameters, like electron density feedback, and the plasma radiation intrinsically provides a scale for detachment quality through f_{rad}. In the current state, real-time radiation control is not feasible for sample times $\Delta t < 1.6\,\text{ms}$ due to the perturbations of the bolometer measurement timing by the feedback algorithm. In the future, a similar setup to the benchmark for actual samples times can be used with a blind absorber, outside the vessel, in order to disentangle the plasma radiation latency and errors in the measurement process.

The real-time radiation system was proven successful in achieving stable plasma detachment. In upcoming experimental campaigns, the application of such feedback is supported by the results presented in this chapter. Assumptions about the radiation distribution and its evolution remain valid for the purpose of providing predictions P_{rad} for this purpose.

Feedback impact and line of sight sensitivity analysis

The presented results and findings of the previous chapter have posed various challenges towards a more detailed understanding of the impact and effects of the real time bolometer feedback system with the thermal gas injection as an actuator. As repeatedly marked throughout the discussion in chapter 3, three major questions remain regarding the optimisation and evaluation of the feedback mechanism and the corresponding evolution of plasma parameters.

1. Is there, and if so what is the correlation of the activation of the thermal gas valves, the real time bolometer feedback system and the underlying plasma characteristics?

2. Does an optimal set of lines of sight S for the real time bolometer feedback system exist?

3. What is the dominant contributor towards the line of sight selection sensitivity of the real time bolometer feedback system?

The answers to those questions are, but not necessarily have to be, very much entangled with each other. On one hand, findings regarding the optimisation of the line of sight selection S inevitably will support or contradict evaluations towards the local sensitivity of the bolometer LOS geometry and the enclosed real time feedback. On the other hand, any correlation between the thermal gas valve activation and evolution of plasma characteristics will have to play a large role in the selection of the ideal set of lines of sight for

the bolometer feedback.
This chapter will attempt to, as thoroughly as possible within the scope of this work, answer those questions, using a combination of different physical models and variations thereof, available sets of data from feedback experiments and simulated plasma profiles from the equilibrium transport code STRAHL. Following the proposal of the above questions will be a quantitative analysis of the thermal gas valve feedback experiments data set. Subsequently, a simple impurity seeding model is explored and applied to experimental data from the bolometer diagnostics. An extensive evaluation of the quality of LOS selections S, also with respect to core plasma characteristics is enclosed. Finally, the previous findings are employed together with the equilibrium impurity transport code STRAHL.

Comment on why we have not used flux in Ch. 3 (and Ch. 4 is moved up front).

4.1. Prediction of Feedback Impact on Plasma Parameters

In order to adjust and optimise the real time bolometer feedback system with thermal gas valves as actuators, the temporal and quantitative correlation between activation and reaction of plasma parameters has to be understood. Varying injection durations and amounts of gas from the feedback valve have equally varying impact on the evolution of plasma profiles. Furthermore, the latency between feedback action and plasma reaction can greatly change the effect the injected gas has on the discharge characteristics. This also may play a large role when reevaluating the applicability and performance of the real time bolometer feedback system.
In an attempt to find possible correlations between the activation of the thermal gas valves and change in plasma parameters, data from the entire set of accomplished feedback experiments has been evaluated using an algorithm that *finds peaks (local maxima)* and compares them between the actuator and given profiles. An example of such a *peak-finding-and-matching* can be found in figure 4.1. Two sets of results for different algorithm parameters but the same profiles are shown here. The origin profile, i.e. the evolution of the actuator, from which found peaks are used to look forward in time for correlating reactions in other profiles, is represented by the activation of the AEH51 thermal gas valve. The *target profile*, i.e. the line represent-

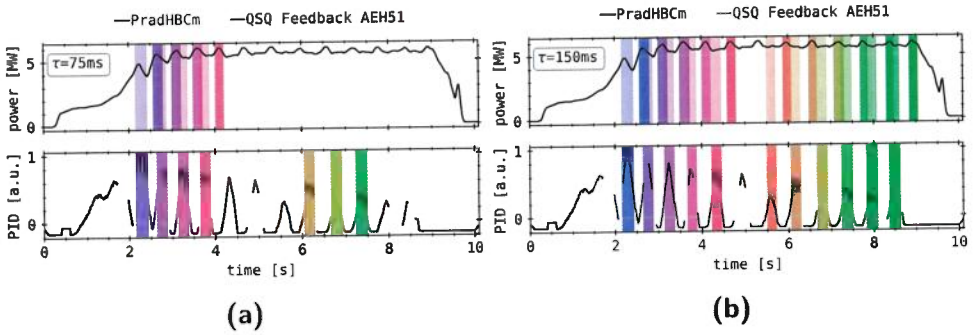

Figure 4.1.: XP:20181010.32:
Example of how peaks in experimental data are detected. Shown here is $P_{\mathrm{rad,HBCm}}$, as well as the feedback valve control in port AEH51. The peaks found in the lower plot are transparently overlaid onto the upper. Same colours indicate cause and effect relation between seeding and plasma parameter ($P_{\mathrm{rad,HBCm}}$) changes. Algorithmic peak detection width set to **(a)** 75 ms and **(b)** 150 ms.

ing the reaction to the *origin profile* (feedback activation), in which the algorithm looks for corresponding maxima to the previous peaks from the origin, is given by the P_{rad} of the horizontal bolometer camera. Depending on a provided *width, distance* and *prominence*, the algorithm searches for local maxima in the origin, which are colour coded with transparent bars and matched in the same colours to peaks in the target profile. The corresponding maxima in the activation are interlaced with higher transparency in the same plot. Such a match is produced if a local maximum is found in the target profile within a certain time interval, i.e. T_{peaks} <450 ms, after the location of the peak in the activation. For multiple occurrences, the first maximum forward in time is chosen. In the provided examples, peaks for a given minimum width and distance in-between of τ=75 ms and 150 ms are shown. The prominence of local maxima with significant width and distance to other peaks are evaluated based on the surrounding profile: for an increase of $> 100\%$ of the variation within $\tau/2$ in the profile around the peak, a local maximum is found by the algorithm. For further details, see the documentation of the underlying core routine in [164].
The provided examples for different peak widths and distances τ in figure 4.1 showcase the importance of careful adjustment of the selected algorithm

parameters and their influence. For smaller τ, potentially fewer local maxima are detected for the same prominence as for larger τ, while increasing width and distance inevitably lead the algorithm to produced false positive matches. Reducing the interval in which corresponding peaks can be found to match also, on one hand act as a cut-off for false positives but on the other hide high latency responses in the target plasma profiles. Within the range of τ =75–150 ms and, depending on the profile, T_{peaks} <450 ms the algorithm works best with the provided feedback experiment data. However, as is already presented by the above examples, not all local maxima are found for the given parameter selection. A manual procedure to find peaks in the lines of data from feedback experiments that were related to the activation of the thermal gas valves is, given the large number of plasma parameters to search through and discharges performed, not within the scope of this work. That said, if not stated otherwise, the following results have been achieved with τ =150 ms and the previously outlined prominence - an increase > 100% of the variance within $\tau/2$ around a local maximum. For electron density measurements of the dispersion interferometer, the interval was set to T_{peaks} =150 ms, while for P_{rad} from the bolometer camera system required a larger setting of T_{peaks} =450 ms. Data from central electron densities measurements n_{e} and heating power P_{ECRH} for points in time of both origin and target profile peak have also been collected simultaneously.
The results for the above described procedure from all thermal gas injection feedback experiments that featured hydrogen as the injected gas are presented in figure 4.2. The compiled data points show the results for the horizontal and vertical bolometer cameras as the target profile individually. The top left shows the increase in P_{rad} over the change in gas flow or valve activation Γ - assuming constant gas pressure and temperature they are synonymous. The absolute gas flow is not known for all data points, hence a presentation in arbitrary units in favour of comparability is chosen. Below that the increase in radiative power loss as a function of gas injection duration T_Γ can be seen. The top right image shows the change in P_{rad} over the total injected amount of gas, i.e. the integrated valve activation peak $\int \Gamma$ over the interval T_Γ.
The presented results in figure 4.2:(top left) show that for a large range of gas pulse strengths, ΔP_{rad} changes almost always with small increments, while few exceptions with no coherent pattern exist across the entire spectrum of valve activations. For smaller injection gas flows, i.e. between 5–10 a. u.

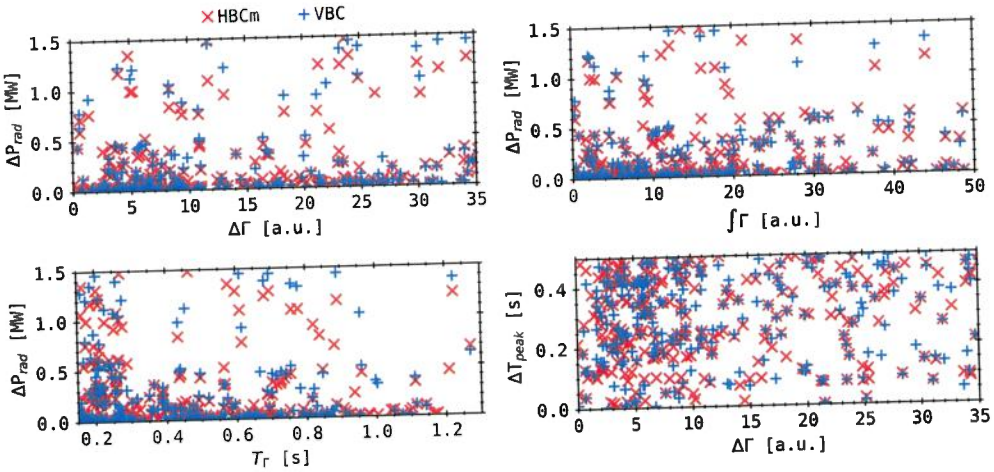

Figure 4.2.: Peak database of P_{rad} for both bolometer cameras individually from hydrogen seeding experiments. Changes in radiation power are shown for **(top left)** the change in seeding control, **(top right)** the approximate injected gas amount, **(bottom left)** the time between the maximum peak values and **(bottom right)** the time delay between peaks over the respective seeding control change.

a small group of points with larger corresponding ΔP_{rad} for both cameras can be seen, indicating that with a reduced flow rate the respective change in radiation increases. The aforementioned exceptions at higher radiation increments might be attributed to varying plasma parameters, which will be examined at a later point in this chapter. Similar findings are presented in the bottom left plot, where the majority of results are found at small ΔP_{rad} across the entire spectrum of seeding durations T_{Γ}. However, a larger number of results for a radiation increase >0.25 MW is found for smaller durations, i.e. 0.15–0.3 s by both cameras equally. Again, singular data points at high ΔP_{rad} across all T_{Γ} show no distinct behaviour. This is also reflected in figure 4.2:(top right), where for small to medium amounts of injected gas, i.e. up to 20 a. u., the majority of results are found below 0.5 MW for both bolometer cameras. This can be linked to the previously discussed plots by either assuming small gas flows for longer injection durations or more intense, shorter pulses. Finally, the last image on the bottom right displays a significantly higher data point density for smaller gas flows and larger

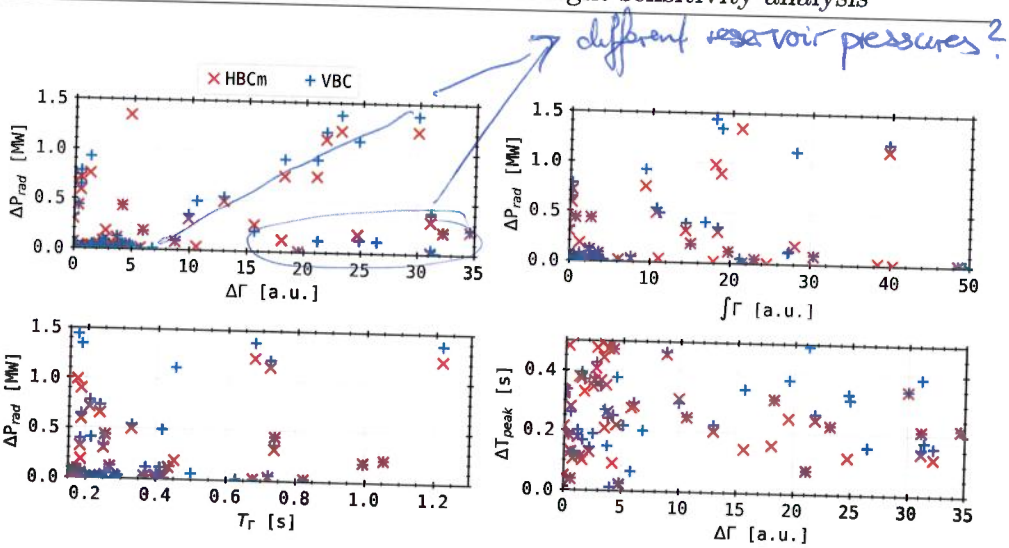

Figure 4.3.: Similar plot as figure figure 4.2, with the gas used for seeding being helium. Peak searching algorithm parameters are kept the same.

latencies between action and reaction in plasma radiation between 0.2–0.5 s. For higher injection intensities, more results are found at $\Delta T_{\text{peak}} > 0.3$ s, further suggesting that higher gas flows do not necessarily, if at all lead to greater or quicker plasma radiation reactions.
The same layout and presentation of data has been used to collect and display results of the algorithm for *helium impurity seeded* experiments, where the feedback controlled thermal gas valve was fed with molecular helium in figure 4.3. Far fewer results have been produced by the algorithm for the same set, or a selection of different sets of parameters at that, than for hydrogen seeded feedback experiments. This is attributed to the greatly smaller number of performed experiments under such conditions. As for figure 4.2, the top left image shows most of the points at $\Delta P_{\text{rad}} < 0.2$ MW, while across the rest of the spectrum in gas flow no coherent pattern can be recognized. Similar findings are presented by the top right plot - the majority of the results show small injection gas amounts at $\Delta P_{\text{rad}} < 0.5$ MW. Consequently, the point density in the bottom left image is highest up to $T_\Gamma < 0.5$ s and very small radiation power loss increments, while fewer results can also be found at up to $\Delta P_{\text{rad}} \sim 1$ MW. Finally, the latency between injection of helium and changes in plasma radiation power, which is shown in the bottom right plot of figure 4.3, is generally found to be between 0.1–0.5 s at small gas flows.

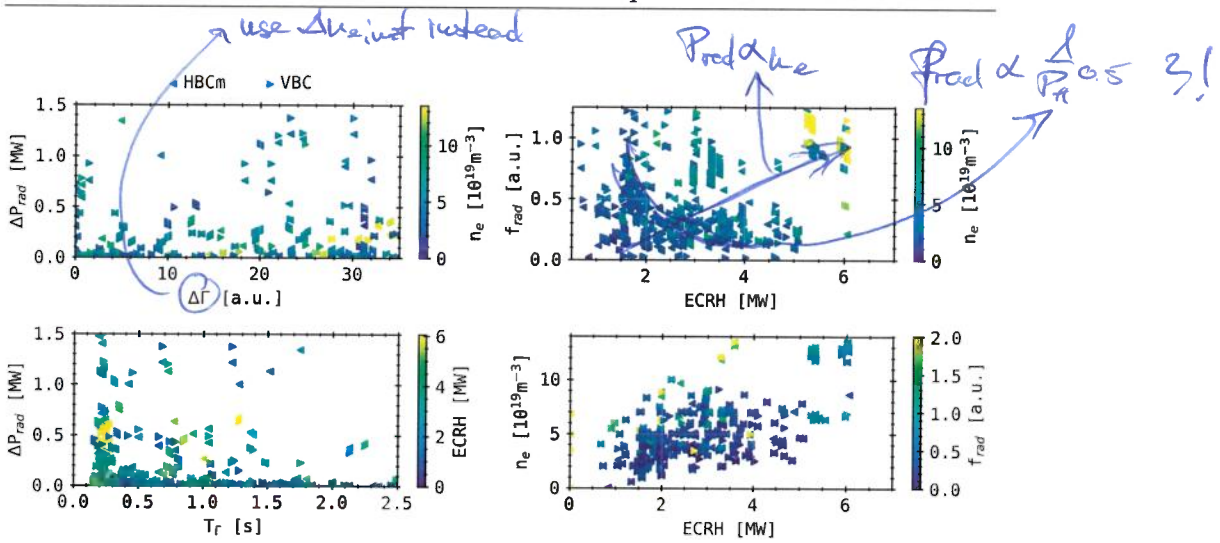

Figure 4.4.: Selected experiment parameters for previously presented peaks in P_{rad} from seeding experiments. **(top left)** change in radiation power over change in seeding control with electron density colour map **(top right)** radiation fraction over heating power with n_e map **(bottom left)** radiation power delta over temporal peak delay with ECRH colour code **(bottom right)** electron density by heating power with radiation fraction map.

For larger flows, no significant pattern is displayed here. In conclusion, very similar, results are presented by the algorithmically collected data points for helium injected feedback experiments as for their hydrogen counterparts. On one hand, this underlines the interpretation of the previously discussed figure 4.2, since the experimental approach and goal were the same. On the other hand, this poses the question as to why a different impurity produces quantitatively comparable results to the injection of working gas. Hence, a more thorough analysis of the dataset is required, involving a larger set of evaluated plasma parameters than just P_{rad} of the bolometer camera system.
The extended database of results previously shown and discussed in figure 4.2 and 4.3, including core plasma parameters f_{rad}, P_{ECRH} and n_e is shown in figure 4.4. Results in all plots were reduced due to availability of the corresponding plasma parameters. The presentation of data points is very similar to the prior, where results are plotted for both bolometer cam-

eras individually. Furthermore, the axis and abscissa on the two left images are kept the same. The two right figures feature, on the top, the radiation loss fraction f_{rad} and, on the bottom, electron density n_{e} over cyclotron heating power P_{ECRH}. In all four plots, a colour grading is imposed on the scattered points: the electron density is used on the top two images, while the bottom left shows the heating power and the bottom right the radiation fraction.
The superimposed core electron density on the top left plot in figure 4.4 indicates no noticeable behaviour across the entire spectrum of gas flows and radiation powers. On the bottom left plot, P_{ECRH} is higher for larger changes in radiation power loss ΔP_{rad}, while no correlation to the latency between feedback action and plasma reaction therein is found. The plot on the top right features a clear trend of higher electron densities for higher heating powers and radiation loss fractions, i.e. peaks have been found for $f_{\mathrm{rad}} \sim 100\%$ and $P_{\mathrm{ECRH}} = 6\,\mathrm{MW}$ at $n_{\mathrm{e}} \geq 10/\mathrm{m}^3$. One should note here that radiation fractions greater than unity are found by the searching algorithm, since momentary power exhaust from the discharge through radiation can be greater than the input heating power under the assumption that plasma stored energy is lost. Finally, the last image on the bottom right supports the observations of the previous plot, where larger heating powers and electron densities are also accentuated with higher f_{rad}.
The results presented in the two left images of figure 4.4 promote no further insight into possible correlations of feedback seeding and changes in plasma radiation, besides the indication of a decreased latency between action and reaction. However, the findings in the top and bottom right plots describe an evident connection between the input heating power, electron core density and radiation loss fraction. Similar results have been previously examined and discussed for different divertor and magnetic field configurations, mainly under steady state conditions[102, 165, 166], implying that the feedback seeding reactions are governed by the same plasma power scaling laws. Here, at higher heating powers $> 3\,\mathrm{MW}$, peaks in the plasma radiation have been found for electron densities $n_{\mathrm{e}} > 5 \times 10^{19}/\mathrm{m}^3$ and loss fractions $f_{\mathrm{rad}} \in \{0.2, 1.2\}$. Concurrently, for higher values of P_{ECRH} and n_{e}, radiation power loss fractions significantly greater than unity, i.e. $f_{\mathrm{rad}} > 1$ are found. Examinations of the previous chapter 3 and especially section 3.2.4 have shown that higher electron densities combined with P_{rad} close to the input heating power - $f_{\mathrm{rad}} \geq 80\%$ - are favourable to an improved radiative cooling

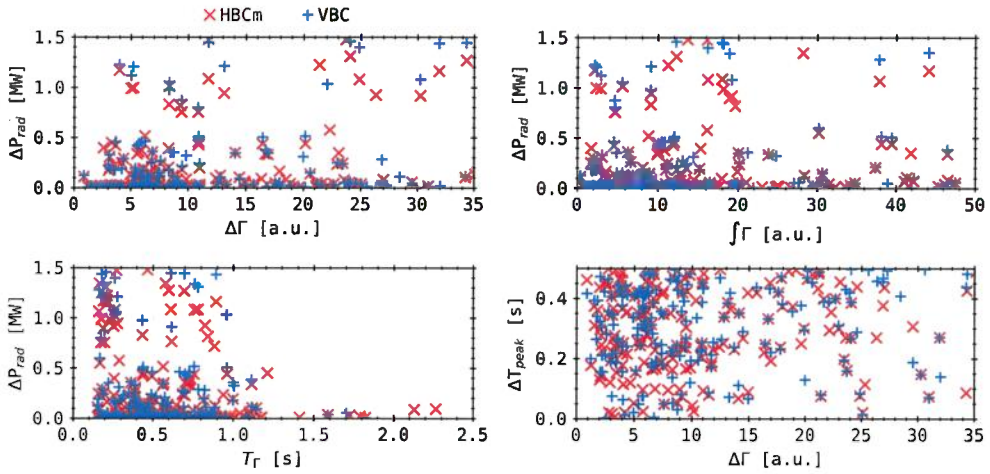

Figure 4.5.: Peak database from main gas valve. Changes in radiation power P_{rad} of both cameras for **(top left)** the change in gas flow, **(top right)** the approximate injected gas amount, **(bottom left)** the time between the maximum peak values and **(bottom right)** the time delay between peaks over the respective gas flow.

of the scrape-off layer and target heat load reduction. The data presented in figure 4.4 therefore overall supports and is consistent with the findings of the latter chapter, however they so far do not exhibit any dependencies whatsoever that could be used to improve the performance of the real time radiation feedback.

4.1.1. Comparison with Non-Feedback Gas Injection

In order to reference the results gathered from the peak finding algorithm for the thermal gas injection valve and feedback activation, the same has to be conducted for the main gas valves located around W7-X. The corresponding data points for both working gases, helium and hydrogen and a minimum peak width of $\tau = 150\,\mathrm{ms}$, like in figure 4.2 and figure 4.3, can be found in figure 4.5. The structure of plots and quantities displayed here are the same as before. One should note here that the scale for Γ is again in arbitrary units, though the absolute value thereof is not necessarily comparable to that of the thermal gas valves of the helium beam diagnostic, since nozzle

and gas injection characteristics, as well as pressures and temperatures of the gases are different.
In the top left image of figure 4.5, a similar behaviour as for the feedback gas valve is seen, where across the spectrum of gas flows $\Delta\Gamma$, the radiation power loss changes with small increments. For smaller fuelling intensities, i.e. <10 a. u. the response in ΔP_{rad} increases like before, quantitatively and qualitatively, while also no coherent pattern can be seen for larger ΔP_{rad} along the abscissa. The bottom left picture features a much narrower distribution of points than before. Up to $T_\Gamma \leq 1\,\mathrm{s}$, a significant increase in radiation power loss is found towards $T_\Gamma \sim 0.15\,\mathrm{s}$ with $\Delta P_{\mathrm{rad}} > 1\,\mathrm{MW}$. Furthermore, the majority of peaks is now located around an injection duration between 0.3–0.6 s below 0.5 MW. This may be attributed to, on one hand the method of injection - main gas valves are applied before the start of the discharge and again, if necessary, to feed the plasma during the experiment - and on the other the valve latency and their distance to the SOL. Beyond $T_\Gamma \sim 1.2\,\mathrm{s}$ the point density is greatly reduced and almost no results can be found beyond this point. Scattered results at $\Delta P_{\mathrm{rad}} > 0.5\,\mathrm{MW}$ show no coherent pattern. In combination of the latter two, the top right plot presents a continuation of the previous findings: around lower to medium amounts of injected gas, $\int \Gamma \leq 20$ a. u. the response in P_{rad} is increased up to 0.5 MW, while beyond that no significant differences can be seen. Finally, the last image on the bottom right also presents a higher data point density up to medium gas flows, $\Delta\Gamma \leq 10$ a.u and higher latencies between injection and reaction $\Delta T_{\mathrm{peak}} \geq 0.2\,\mathrm{s}$. However, no results are found for very small gas flows $\Delta\Gamma$ <2 a. u. up to very high latencies of 0.4 s. At higher injection intensities, this density decreases greatly and for higher latencies $\Delta T_{\mathrm{peak}} > 0.3\,\mathrm{s}$ slightly more peaks are found still. This is in agreement with figure 4.2: higher gas flows do not necessarily imply quicker or stronger reactions in radiation power loss, while slower, more moderate injections appear to yield better results for cooling the plasma.
In order to complete the comparison between the injection valves with respect to their impact on the radiation power loss, a counterpart to figure 4.4 involving additional plasma parameters has to be provided. The corresponding result can be found in figure 4.6. The procedure to acquire the data points, as well as their presentation in the plots is the same as before.
In the top left of figure 4.4, the superimposed core electron density slightly increases with larger ΔP_{rad} for smaller gas flows. At higher injection intens-

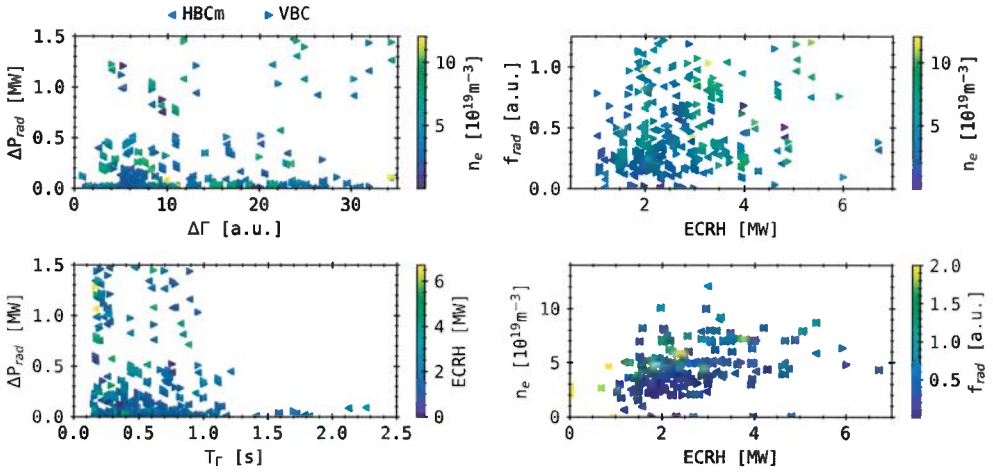

Figure 4.6.: Experiment parameters for main gas valve. **(top left)** change in radiation power over change in seeding control with electron density colour map **(top right)** radiation fraction over heating power with n_e map **(bottom left)** radiation power delta over temporal peak delay with ECRH colour code **(bottom right)** electron density by heating power with radiation fraction map.

ities, few data points scattered along the ordinate and at very low radiation impact also indicate higher n_e. Similar to figure 4.4, on the bottom left larger ΔP_{rad} for small injection durations are noted with increasing input heating powers. The two right-hand plots show the same quantitative picture as before, where with larger P_{ECRH} both electron density and radiation power loss fraction f_{rad} increase. Furthermore, the overall structure of the data point distributions are very similar. The top right image however does not feature an accumulation of points towards very high f_{rad} and heating powers with $n_e \geq 10/m^3$.

From figure 4.2 through figure 4.6, one can summarize that, in general, a gas injection with moderate intensity and duration is most suited for radiatively cooling the scrape-off layer and thereby potentially improving its overall performance with regard to increasing electron density and temperature. Besides the apparent differences in application, i.e. construction and methodology, no significant qualitative change in plasma radiation response between thermal gas feedback valve and main gas inlet is found. That said,

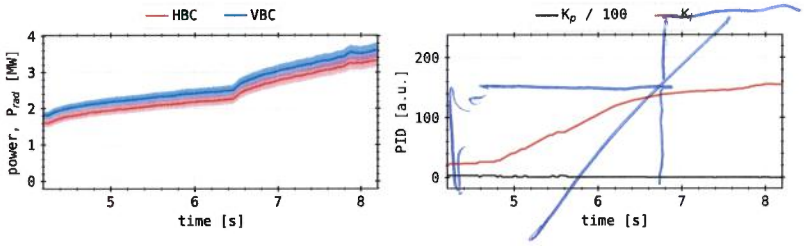

Figure 4.7.: XP20180920.49:
Experimental data of P_{rad} for both bolometer cameras and PID components of gas seeding valve controller. This is an excerpt between 4.2 s and 8.2 s where two consecutive seeding stages where applied and the radiation power responded accordingly.

this is concluded with respect to the implied direct causality (algorithm), where the action-reaction connection between the gas pulse and peak in radiation power loss is implied. As stated before, and supported by the very similar results in figure 4.6, the algorithmically established peak database adheres to the same plasma (performance) scaling laws which have been established for steady state conditions. Finally, in reference to the scientific questions posed in the beginning of this chapter 4, so far no correlation between the activation of the feedback system, the radiation power loss and underlying plasma parameters could be established.

4.2. Impurity Seeding Modelling

The results presented in chapter 3 have shown a direct connection between the change in plasma radiation and gas injected through the valves of the feedback system. During experiments with interferometer-measured electron density feedback, a continuous gas injection resulted in the increase and quick saturation of the radiative power loss at constant heating power. Throughout the establishment and configuration of the feedback procedure, this pattern has been repeated multiple times, with occasionally multiple saturated *plateaus* in the radiation power. An example of this behaviour can be found in figure 4.7, which shows an excerpt from XP20180920.49. The left plot features the individual P_{rad} measurements from HBC and VBC. The right side shows the feedback valve activation, as has been presented

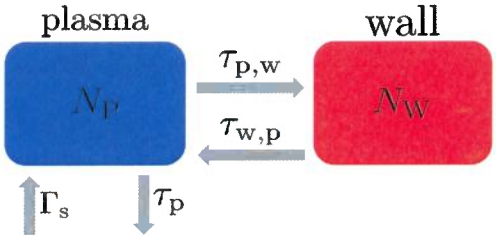

Figure 4.8.: Two chamber model schematic, with N_p the plasma chamber population and N_w the wall chamber population, including their respective source and loss rates $\tau_{x,y}$ and Γ_s.

previously throughout chapter 3, which is directly linked to the gas flow. Over an interval of 4 s, two changes in injection intensity are applied. The first appears just before 5 s and linearly increases until 6.2 s, where the slope of the integral PID component flattens. A similar behaviour can be found in the left plot from either radiative power measurement, although the respective slopes behave differently. This suggests that an equilibration takes place at a given flux of gas particles from the valves into the scrape-off layer. With respect to the overarching questions of this chapter, this observation facilitates another possibility to answer the question of connection between radiation reaction and feedback.

not feedback controlled was feed forward!!

slow increase imply some buffering of puff → wall pumping for N
as timescale >> $\tau_{transport}$

4.2.1. Two Chamber Model

In a first attempt to better understand the saturation process, a simple model is established for comparison. The schematic representation of this model can be found in figure 4.8. Here, the total amount of gas is split into two separate populations, i.e.the feedback injected impurity. In this scenario, the gas flow Γ_s contributes directly to the population inside the plasma chamber, including the SOL, N_P, neglecting any scattering processes or losses. This, in turn, is connected through particle exchange with the second population of the reactor walls (chamber) N_W. The different exchange flows are noted by their respective rate coefficients $\tau_{p,w}$, for transport from the plasma to

the wall, $\tau_{w,p}$ vice versa, and τ_P exclusive losses from the plasma. The first order differential equations for both populations are as follows:

$$\begin{aligned}\frac{d}{dt}N_p = \dot{N}_p =& \Gamma_s + N_w\tau_{w,p} - N_p\left(\tau_{p,w}f + \tau_p\right) \ , \\ \frac{d}{dt}N_w = \dot{N}_w =& N_p\tau_{p,w}f - N_w\tau_{w,p} \ .\end{aligned} \tag{4.1}$$

The first order differential equations of the individual quantities are composed of the respective sources and losses, where the term denoting the plasma-to-wall exchange $\tau_{p,w}$ is modified by an additional parameter f to satisfy the equilibrium requirement at the threshold population. Therefore, the equation for the wall chamber population can be solved for approaching $N_{w,lim}$ the limit value at equilibrium, where its first order temporal derivative from equation (4.1) becomes:

$$\begin{aligned}\lim_{N_w \to N_{w,lim}} \dot{N}_w \stackrel{!}{=} 0 &= N_p\tau_{wp}f - N_{w,lim}\tau_{w,p} \\ \rightarrow f &= \frac{N_{w,lim}\tau_{w,p}}{N_p\tau_{p,w}} \ .\end{aligned} \tag{4.2}$$

The final equation for the plasma and wall chamber population then become:

$$\begin{aligned}\dot{N}_w =& \left(N_{w,lim} - N_w\right)\tau_{w,p} \\ \dot{N}_p =& \Gamma_s + N_w\tau_{w,p} - N_{w,lim}\tau_{w,p}N_p - N_p\tau_p \ .\end{aligned} \tag{4.3}$$

Note that the above equations are no longer a function of the parameter $\tau_{p,w}$.

In order to understand the behaviour of the above two chamber model in equation (4.3), the included parameters are varied independently and their individual impact on the development on the plasma and wall chamber populations recorded. A straightforward explicit first order differential equation integration method (*4th order Runge-Kutta method*[167]) is used. The results can be found in figure 4.9. For each variation of one variable, the evolution of the populations have been calculated for an interval of 10 s each, while all other parameters have been kept constant. If the respective variable is not changed, the initial values are - all in arbitrary units (a. u.) or a. u./s - as follows: $\tau_{w,p}$ =1 a. u./s, $N_{w,lim}$ =10 a. u., τ_p =1 a. u./s, Γ_s =1 a. u./s, $N_{p,0}$ =10 a. u., $N_{w,0}$ =10 a. u. The first plot in figure 4.9:(a)

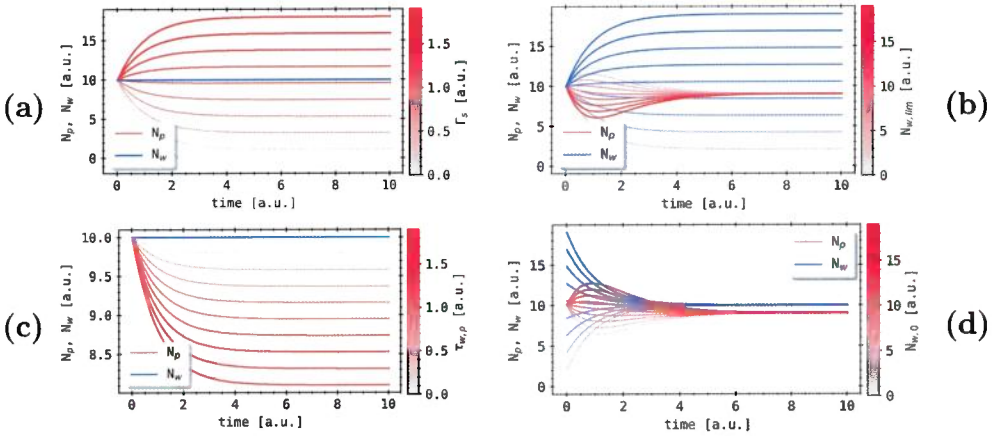

Figure 4.9.: Parameter variation for two chamber model in equation (4.3). Included are variations of seeding rate **(a)** Γ_s and limit parameter **(b)** $N_{w,lim}$, as well as wall-to-plasma loss rate **(c)** τ_p and initial population value **(d)** $N_{w,0}$, while the other model parameters have been kept constant.

shows the variation of the injection flow Γ_S between $\{0, 2\}$a. u. Recorded results for both populations are displayed for each injection intensity, while the corresponding lines are drawn also with a colour scale between grey and red for N_p and blue for N_w. With increasing Γ_S, the equilibrium plasma chamber population increases proportionally, while N_w remains constant at its initial value. Within the first 4 s, the plasma population grows or shrinks at the same rate with a (inverse) *square root-like* trend. The tipping point from increasing to decreasing plasma chamber population is evidently reached at $\Gamma_S = \tau_p$ - for $\tau_{w,p} = \tau_{p,w}$) -, i.e. where the absolute loss from the plasma chamber population is balanced by the input gas flow. At very small Γ_s, N_p even becomes negative at 2 s for this combination of parameters, providing an invalid solution for equation (4.3). The second plot in figure 4.9:(b) shows the variation of the limit parameter $N_{w,lim}$ between $\{0, 20\}$a. u. For smaller $N_{w,lim}$, N_p increases within the first 4 s before levelling off at 9 a. u., while for larger limit values the plasma chamber population decreases and then approaches its equilibrium. The wall chamber population develops accordingly, where larger values of $N_{w,lim}$ lead to equally larger equilibria and vice versa. The variation of the wall-to-plasma loss rate $\tau_{w,p}$ between $\{0, 2\}$ a.u is

presented in the third plot in figure 4.9:(c). For small values of $\tau_{w,p}$, only a small reduction in plasma chamber population from its initial value is found, while for increasing $\tau_{w,p}$ the drop in N_p grows, i.e. 2 a. u. for $\tau_{w,p} \approx 2$ a. u. The plasma chamber population equilibrates around 4 s. No changes in N_w are found here. Finally, the last plot in figure 4.9:(d) shows the variation of the initial wall chamber population $N_{w,0}$ between $\{0, 20\}$a. u. A similar, but inverted behaviour of N_p as in plot (b) can be seen, since larger $N_{w,0}$ correspond to initially increasing plasma chamber populations and the other way around. Again, N_p equilibrates at 9 a. u. while the wall chamber population levels off at 10 a. u., the limit value $N_{w,lim}$ here, after increasing or decreasing from its respective smaller or larger starting point. With respect to the information presented in the plots of figure 4.9, variations of the not previously presented and hence remaining parameters $N_{p,0}$, $\tau_{p,w}$ and τ_p result in no additional insight into the evolution of the model. Changes in the initial plasma chamber population mimic the behaviour of N_w when $N_{w,0}$ is varied, while τ_p determines the boundaries of N_p in a trivial way. If the plasma chamber loss vanishes, its respective population does not equilibrate and becomes infinite. For smaller τ_p the equilibrium of N_p increases and vice versa.

After introducing a simple two-chamber model in equation (4.3) and benchmarking it, one can now apply it to the experimental data presented in figure 4.7 in order to examine its suitability for reproducing the observed behaviour of the plasma radiation. The accompanying feedback activation data show two distinct injections steps, hence the model is applied similarly. A simple least-square fit procedure is employed to find the best parameter set representing the first and successive second stage. Only positive parameter solutions are allowed, since all particle exchange directions are accounted for by individual coefficients. The resulting populations N_p and N_w of the initial injection step up until 2.2 s of the feedback application are used as input for the evolution of the second stage for another 2 s. This fit is conducted assuming an injection rate of 200% intensity of the priors. A presentation of this fit over the normalized experimental data, next to the temporal evolution of the individual populations can be found figure 4.10. The corresponding parameters are noted below.

This simple model is evidently very well capable of reproducing the behaviour of P_{rad} in this example, though under the vastly simplifying assumption of direct proportionality between $P_{rad} \propto N_p$. The wall chamber population

motivated by $n_{imp} \propto c_{imp} \propto P_{rad}$

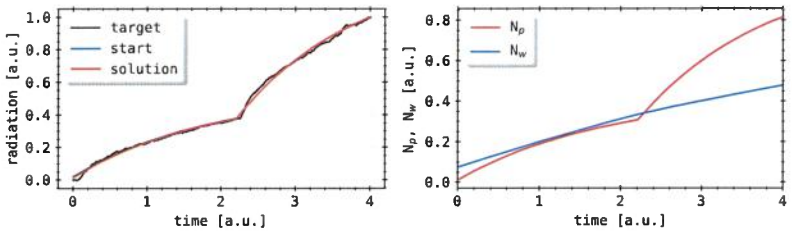

Figure 4.10.: Application of model equation (4.3) on experimental data from XP20180920.49 in-between 4.2 s and 8.2 s. The respective parameters of this solution are Γ_s =0.648 a. u./s, $\tau_{w,p}$ =0.1 a. u./s, $N_{w,lim}$ =1.388 a. u., τ_p =0.436 a. u./s, $N_{p,0}$ =0.011 a. u. and $N_{w,0}$ =0.075 a. u.

has a very small positive slope, which is reflected by its comparatively large capacity ($N_{w,lim}$) of 1.388 and $\tau_{w,p}$:$\Gamma_s - \tau_p$. The ratio between the net growth of both chambers, $\dot{N}_p \sim \Gamma_s - \tau_p$ and $\dot{N}_w \sim \tau_{w,p}$ determines the development of the populations. Initial values $N_{p,0}$ and $N_{w,0}$ are negligible and can be accounted for by remaining gas in the discharge environment from previous experiments.
Although this trivial two-chamber model offers only a superficial understanding of the behaviour of the plasma radiation evolution in relation to the feedback gas injection, it is of significant interest explicitly for its simple approach and ability to reproduce the experimental data. Furthermore, this approach is also capable of reproducing the behaviour in presence of a second feedback stage for the same set of parameters and with continuity at the transition. Therefore, the model and its respective implications, i.e. two separate compartments with finite capacity in exchange with each other and a single source and sink, provide a possible explanation for the correlation between feedback gas injection and plasma radiation from the initially posed questions. It also shows that a direct proportionality as searched for in 4.1 is not obvious if the wall and time constants plays and important role.

4.2.2. Three Chamber Model

The three-chamber model is a simple extension of the two-chamber model to the case of three separate chambers and is based on the latter. A scrape-off layer chamber (population) N_s is added in-between the wall and plasma chamber as an additional buffer, which in this case features the single source

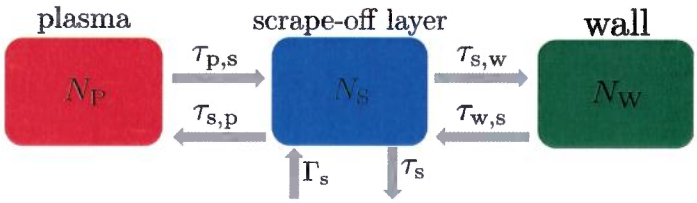

Figure 4.11.: Three chamber model schematic, with the plasma chamber population N_p, N_w the wall chamber population and an additional chamber for a scrape-off layer population N_s. The seeding location has changed to the SOL, including the loss channel from there. There is also a second pair of respective source and loss rate terms between the individual model chambers.

and sink like the plasma chamber did before. This is assumed to be a more exact model for the feedback gas reservoirs in a discharge. A schematic can be found in figure 4.11. Plasma and SOL, as well as SOL and wall chamber are connected through two exchange terms and accompanying coefficients for both particle flow directions respectively. Source and sink are again represented by Γ_s and τ_s (from N_s). Here, the *finite capacity* boundary condition applies to the plasma and wall chamber. This model will also be applied to the experimental data in figure 4.7 in same manner as before.
Given figure 4.11, the first order differential equations describing the populations in this model are as follows:

$$\begin{aligned}
\dot{N}_w &= N_s \tau_{s,w} f_w - N_w \tau_{w,s} \ , \\
\dot{N}_s &= \Gamma_s + N_p \tau_{p,s} f_p - N_s \left(\tau_{s,w} f_w + \tau_{s,p} + \tau_s\right) \ , \\
\dot{N}_p &= N_s \tau_{s,p} - N_p \tau_{p,s} f_p \ .
\end{aligned} \tag{4.4}$$

Again, the respective source and loss terms of the scrape-off layer chamber are modified by two individual parameters f_w and f_p to satisfy the equilibrium condition of before, which is applied here to the wall and plasma chamber

populations, N_w and N_p. More specifically, when approaching equilibrium populations $N_{p,lim}$ and $N_{w,lim}$, the respective derivative should be zero.

$$\begin{aligned}
\lim_{N_w \to N_{w,lim}} \dot{N}_w &\stackrel{!}{=} 0 = N_s \tau_{s,w} f_w - N_{w,lim} \tau_{w,s} \\
\lim_{N_p \to N_{p,lim}} \dot{N}_p &\stackrel{!}{=} 0 = N_s \tau_{s,p} - N_{p,lim} \tau_{p,s} f_p \\
\rightarrow f_w &= \frac{N_{w,lim} \tau_{w,s}}{N_s \tau_{s,w}}, \qquad f_p = \frac{N_s \tau_{s,p}}{N_{p,lim} \tau_{p,s}}
\end{aligned} \tag{4.5}$$

Finally, the equations for plasma, scrape-off layer and wall chamber populations in this simple model become:

$$\begin{aligned}
\dot{N}_w &= (N_{w,lim} - N_w)\, \tau_{w,s} \ , \\
\dot{N}_s &= \Gamma_s + \frac{N_p N_s \tau_{s,p}}{N_{p,lim}} - N_{w,lim} \tau_{w,s} - N_s (\tau_{s,p} + \tau_s) \ , \\
\dot{N}_p &= N_s \tau_{s,p} - \frac{N_p N_s}{N_{p,lim}} \ .
\end{aligned} \tag{4.6}$$

Note that the final set of equations no longer contains terms of $\tau_{s,w}$ and $\tau_{p,s}$, reducing the set of parameters to six and increasing it by two from the previous model.

Variation.

Similar to before, the model is benchmarked with respect to the influence of the different parameters on the evolution of the individual chamber populations. This is done using the *4th order Runge-Kutta* integration method for first order ODEs. The parameters are varied in the same way as before, whereas the initial values are set to $\tau_{s,p} = 1\,\text{a. u./s}$, $N_{p,lim} = 7\,\text{a. u.}$, $\Gamma_s = 20\,\text{a. u./s}$, $N_{w,lim} = 5\,\text{a. u.}$, $\tau_{w,s} = 1\,\text{a. u./s}$, $\tau_s = 1\,\text{a. u./s}$, $N_{p,0} = 0$, $N_{s,0} = 1\,\text{a. u.}$ and $N_{w,0} = 0$ if not stated otherwise. The results can be found in figure 4.12. Each model is calculated for an interval of 10 s, while one of the parameters is changed and the rest is kept constant. Presentation and schematic of the corresponding figures are the same, with the only difference being the additional lines for N_s.

The first plot in the top left, figure 4.12:(a) features the temporal evolution of the three populations at varying values of $N_{w,lim}$ between $\{0, 10\}$a. u. All variations of wall and SOL chamber populations propagate with a *square root-like* increase similar to before, and equilibrate around 6 s. However, this

is only the case for N_p at smaller $N_{w,lim}$, while its slope flattens with increasing values. Larger values of equilibrium wall chamber population evidently lead to higher plateaus in N_w, while the opposite is true for the steady state of N_s, which decreases with growing $N_{w,lim}$. The value of $N_{p,lim}$ is not affected by this, i.e. the equilibrium remains at 7 a. u., though it takes significantly longer to equilibrate for smaller wall chamber capacities.
The second plot in the top right, figure 4.12:(b) shows the results for variations of $N_{p,lim} \in \{0, 20\}$a. u. A similar behaviour in N_s to before is found, where higher values of $N_{p,lim}$ correspond to smaller SOL chamber equilibria. The respective range in variation is twice the size of the previous, so the impact of changes in $N_{p,lim}$ on the capacity of N_s evidently are smaller than the prior, since the corresponding spectrum of N_s is roughly the same. Concurrently, the wall chamber capacity $N_{w,im}$ is not affected by changes in $N_{p,lim}$ and remains at 5 a. u. For constant exchange coefficients, source and loss rates, the plasma chamber population takes longer to reach its maximum capacity the higher the value of $N_{p,lim}$, which is to be expected from equation (4.6).
In figure 4.12:(c), the evolution of the populations for SOL-to-plasma exchange rates $\tau_{s,p}$ between $\{0, 2\}$ a. u./s is shown. The same overall behaviour presented in the previous figure can be seen here. Only small differences across the spectrum of the parameter variation can be noted, i.e. the decrease in equilibrium of N_s is smaller. The lower the value of $\tau_{s,p}$, the longer it takes the plasma chamber population to reach is capacity $N_{p,lim}$, though itself is not affected by it. The evolution of N_w does not change.
The next image in figure 4.12:(d) presents the results for changes in the gas feeding rate Γ_s over a large interval of $\{15, 60\}$ a. u./s. For the given set of parameters, the SOL chamber population increases strongly with larger values of Γ_s, while its equilibration latency stays the same throughout the spectrum. Again, N_w is not perturbed by the change in gas injection rate, and its capacity remains at 5 a. u. For smaller Γ_s the process of reaching the steady state $N_{p,lim}$ takes longer, though the equilibrium value stays constant at 7 a. u.
figure 4.12:(e) shows the evolution for variations of the wall-to-SOL chamber loss rate $\tau_{w,s}$ in the interval $\{0, 2\}$ a. u./s. A similar behaviour in N_w and N_p is noted, where their respective equilibria stay constant at 5 a. u. and 7 a. u. throughout the perturbation spectrum and the corresponding latency changes with $\tau_{w,s}$. For larger values, the slope in wall chamber population

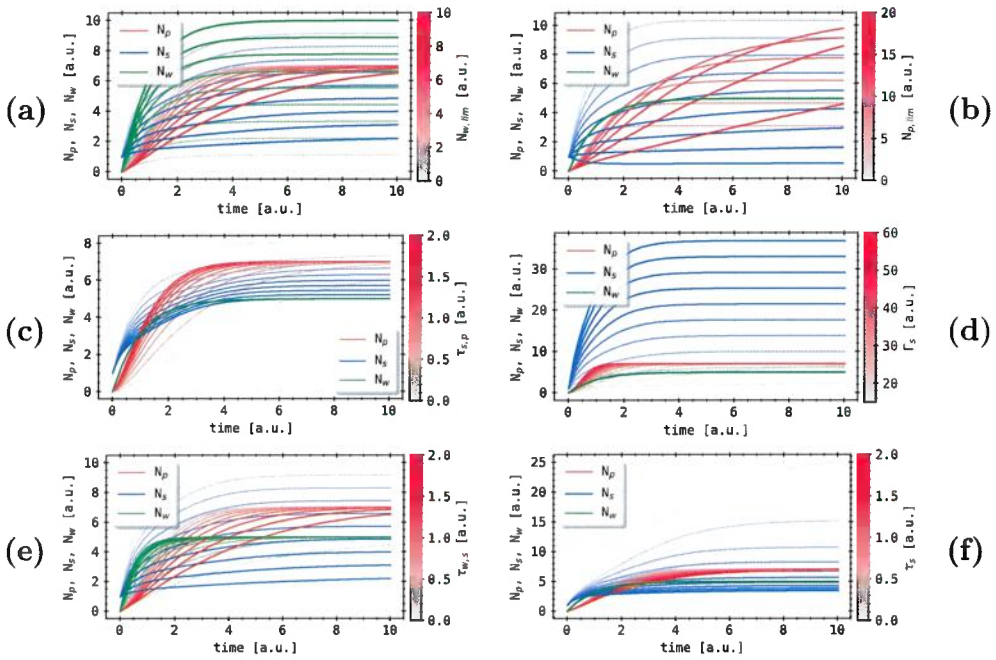

Figure 4.12.: Parameter variation for three chamber model in equation (4.3). Included are variations of limit parameters **(a)** $N_{\mathrm{w,lim}}$ and **(b)** $N_{\mathrm{p,lim}}$, plasma source and feedback injection rates **(c)** $\tau_{\mathrm{s,p}}$ and Γ_{s}, as well as **(e)** $\tau_{\mathrm{w,s}}$ source and **(f)** τ_{s} loss rates of the plasma scrape-off layer, while other model parameters have been kept constant.

increases, as for the plasma chamber population it is the other way around and vice versa. Instinctively, one would expect larger wall-to-SOL loss rates to lead to higher equilibria in N_{s} for a given set of $N_{\mathrm{w,lim}}$, Γ_{s} and τ_{s}. However, the presented results show otherwise, i.e. increasing $\tau_{\mathrm{w,s}}$ causes smaller plateaus of SOL chamber population, which is indeed in agreement with the model described by equation (4.6).
The final image in figure 4.12:(f) presents the results for the variation of τ_{s} in between $\{0, 2\}$. No change in N_{w} is found for perturbations in the scrape-off layer loss rate. With $\tau_{\mathrm{s}} \to 0$, the equilibrium SOL population increases until the system evidently becomes unbounded at $\tau_{\mathrm{s}} = 0$, since there is no more exhaust of gas particles. On the other end of the spectrum, the impact on the equilibrium value of N_{s} decreases with larger SOL loss rates. The value

discuss role of τ_p τ_s to set ratio of impurity content → enrichment.

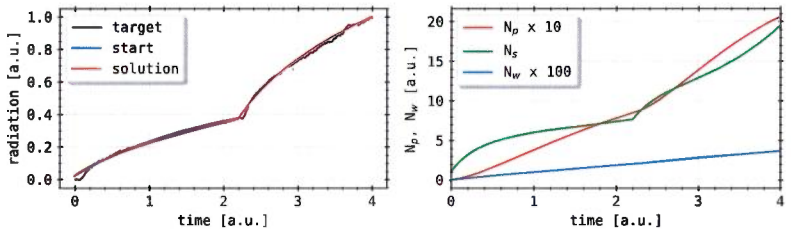

Figure 4.13.: Application of the model from equation (4.6) on the experimental data of XP20180920.49 in-between 4.2 s and 8.2 s. The final set of parameters from a least-square fit is $\tau_{s,p} = 0.1$ a. u./s, $N_{p,lim} = 17.9$ a. u., $\tau_{p,s} = 14.931$ a. u./s, $\Gamma_s = 18.08$ a. u./s, $N_{w,lim} = 2.579$ a. u., $\tau_{w,s} = 2.561$ a. u./s, $\tau_s = 2.772$ a. u./s, $N_{p,0} = 0$, $N_{s,0} = 0$, $N_{w,0} = 1$. The weighting factor is $f = 10.957$.

of $N_{p,lim}$ is not affected by the variation, though the equilibration latency of the plasma chamber population increases with τ_s.

The benchmark of the model and its accompanying parameters is thereby completed. The addition of the scrape-off layer chamber, which also incorporates the source and sink of the system, was found to act as a buffer for the injected feedback gas and an exchange reservoir of the remaining two plasma and wall chambers. Evidently, N_w is only affected by changes in its respective chamber capacity and $\tau_{w,s}$, not however by perturbations in the plasma or SOL chamber populations. The behaviour of N_p is as expected, where larger transfer coefficients in this direction and/or higher capacities in the neighbouring SOL chamber lead to accelerated population of the plasma chamber.

With its introduction in equation (4.6) and the corresponding benchmark in figure 4.12, the three chamber model can now also be applied to reproduce the results of figure 4.7 with the same approach as in figure 4.10. Again, a least-square fit is used to find the best parameter solution for $N_p + f N_s \propto P_{rad}$ from the distinct two stage injection. The difference to the prior fit is that the scrape-off layer is now incorporated into the modelling of the plasma radiation. A weighting factor f between the two contributions is also included in the fit. Only a set of positive parameters is allowed. The model is applied to the first 2.2 s of the injection, after which the resulting populations are used as input for further calculations beyond that point in time. The fit is performed to find a set of parameters that represents the first and second

feedback stage best while satisfying the above requirement.
Figure 4.13 shows the results from the fit. The left plot presents the original experimental data with the superimposed sum of $N_p = fN_s$. A line of the fit for the first stage only is also included, verifying the results for the complete data set. On the right the evolution of the individual three populations can be found, scaled up by separate factors for better visibility. From the corresponding display scaling factors and the value of $f \sim 11$, one can immediately determine the dominating contribution of this model solution to the representation of P_{rad}. The final input of N_p to the plasma radiation is more than 10^2 times smaller than that of the SOL chamber population. . Plasma and wall chamber populations increase steadily throughout the entire interval, with a positive change in slope of N_p when the injection intensity increases. No such behaviour is seen in N_w. The individual populations of N_w and N_p are significantly smaller than N_s. The content of the wall chamber is a factor of 10^2 smaller than those of the others and can be neglected. Furthermore, its respective capacity and exchange rate - read *loss rate* - $\tau_{w,s}$ to N_s are small and of almost the same magnitude, which means particles transported into that chamber immediately are lost to the neighbouring SOL. The plasma chamber population is about 10 times larger and features an increased positive slope compared to the latter. This is the result of the large ratio between $\tau_{p,s}$:$\tau_{s,p} \approx 150$, which also greatly impairs this population to grow. By about a factor of ten, the scrape-off layer chamber population is the largest in this model. During the initial feedback injection, N_s increases quickly and begins to equilibrate towards 2 s. For the given injection intensity and model loss rate, the SOL is beginning to saturate towards the end of this first step, when the term $\propto N_s(\tau_s + \tau_{s,p})$ becomes larger than the net gain of N_s in equation (4.6). This appears to repeat after the second stage is engaged, but the equilibration process quickly inverts around 3 s and the SOL population starts to increase more strongly towards the end of the interval. At this point, the term $N_p N_s \tau_{s,p}/N_{p,lim}$ becomes dominant, while the rest of the contributions to $\dot{N}_s$ are constant or scale only with N_s.
The presented results in figure 4.13 are consistent with the measurements in figure 4.7 and results in figure 4.10. They underline the previous findings and show that the extended model is also capable of reproducing the experimental data through $P_{rad} \propto N_p + fN_s$. Furthermore, it offers a deeper understanding of the behaviour of injected gas during feedback experiments.

By extending the prior set of equations and adding a scrape-off layer compartment, into which the gas is injected, this model is able to mimic the effects of radiative cooling through seeding of impurities, like it was pursued by the underlying experimental setup. The results from the fitting procedure of $P_{\mathrm{rad}} \propto N_{\mathrm{p}} + fN_{\mathrm{s}}$ show a strong correlation between the SOL impurity content and the radiation power loss. On one hand, the contribution of N_{s} to P_{rad} is, comparatively, ten times larger than that of the plasma chamber population. And on the other hand, the absolute content of the SOL is largest among the three chambers in this model by at least a factor of ten. This results in a very dominating contribution of that species to the radiation power loss prediction. In section 3.2.4 and especially the C-III emission measurements of figure 3.27, it was seen that, with higher gas injection intensity, the radiation in the edge of the plasma and SOL increased, suggesting an accumulation of externally seeded impurities in that region. Although these findings fit the conclusions from the respective experimental results rather well, there still remain discrepancies either between both the corresponding models and measurement data. In the extended three chamber model, no equilibration process is seen in the evolution of the final parameter set of figure 4.13, contrary to the results in figure 4.10 or figure 4.7. This behaviour is expected of the wall chamber population, where the physical plasma boundary, i.e. a steel wall, is able to retain a certain amount of impurity gases through kinetic or chemical deposition[137]. Similarly, there exists a maximum, sustainable impurity concentration of the core plasma. Beyond this level of saturation, a radiative collapse of the discharge through removal of plasma stored energy by radiation is very likely[168].

This concludes the analysis of the saturation behaviour in radiation power loss during gas injection plasma feedback experiments. Simple two and three chamber models have been established and explored, through which the impact of extrinsically seeded impurities on the plasma radiation can be better understood. Applying said models to measurement data from the bolometer diagnostic has yielded plausible results which coincide with experimental data. With regard to the initially posed questions at the beginning of this chapter 4, this partially answers *item 1.*, since a strong correlation between the impurity contents of the scrape-off layer and plasma edge from extrinsic seeding and plasma radiation was found.

4.3. Line of Sight Sensitivity Evaluation

A key feature and issue at the same time of the real-time bolometer feedback system is the extrapolation and application of a limited line of sight selection S to the control variable $P_{\text{rad,S}} \stackrel{!}{=} P_{\text{pred}}$ - in this section, only the formerly introduced $P_{\text{pred}}^{(1)}$ from equation (3.1) is of interest, hence the simplification. To approach this challenge and adequately evaluate the capabilities of the prediction, a metric for measuring the quality of the individual LOS selection has to be established and thoroughly exercised across a wide selection of experimental data sets that ideally represent as many different plasma scenarios as possible. This in itself poses another problem, in which a single such metric might not be sufficient to address this task. For example, in section 3.2.2 and lastly section 4.1, the latency and frequency between the feedback injection and reaction of the plasma radiation were found to play a large role in the success of the experiment. A simple, normalized deviation between the prediction and full set P_{rad} across the experiment time interval is not capable of representing the difference in spectral densities between the two quantities. Hence, a variation of different metrics will be adequately introduced and applied individually on the same set of experimental data to thoroughly evaluate the impact of LOS selection for feedback control quality.

4.3.1. Evaluation Metric

In order to establish a unified terminology for all metric variations for the sake of simplifying equations, references and plots, first a basic set of equations and maps have to been introduced. The underlying prediction for the plasma radiation power loss, as measured by the bolometer diagnostic, for a line of sight selection S shall be the same as previously introduced in equation (3.1):

$$P_{\text{pred}} \stackrel{!}{=} P_{\text{S}} = \frac{V_{\text{P,tor}}}{V_{\text{S}}} \sum_{M}^{S} \frac{P_M V_M}{K_M} , \qquad S \subset (S_{\text{HBC}}, S_{\text{VBC}}) \ .$$

Two functions have to be defined next. First, one providing a metric for the quality of the prediction relative to the *full LOS set* P_{rad}. The domain of this function is the time interval of the experiment. Second, a function that

transforms the result of the latter from the temporal or frequency domain to a single number. This value then represents the quality of the prediction for the LOS set S with respect to the corresponding metric. The following are therefore introduced:

$$\boxed{\begin{aligned}\varphi &:= f\left(t, S, P_{\text{rad}}\right) : \mathbb{N}^m \times \mathbb{R} \to \mathbb{R} \\ \vartheta &:= h\left(S,\, P_{\text{rad}}, \varphi\right) : \mathbb{N}^m \times \mathbb{R} \to \mathbb{R}\end{aligned}} \tag{4.7}$$

For simplification, from here on $\varphi = \varphi\left(t\right)$ will be called metric and $\vartheta = \vartheta\left(S\right)$ map to the prediction quality. The evaluation process is repeated for all following metrics in the same way. In the beginning, before beginning the calculations for the first $\varphi\left(t\right)$, a large collection of LOS sets is established. These contain combinations of three, five and seven channels individually, where each is constructed using all possible permutations of the respective three, five or seven subset ranges of channels from the horizontal *or* vertical bolometer camera. For example, for LOS sets of three channels from the HBC, permutations of from ranges $\{1, \ldots, 10\}, \{12, \ldots, 21\}$ and $\{22, \ldots, 30\}$ resulted in a total collection of *nine hundred* different sets S. The individual subset ranges are also later easily deductible in the plots presenting the results, i.e. figure 4.15. The selection of underlying experiments for conducting the feedback evaluation is the same as for the investigations earlier in this chapter in section 4.1, the entire set of feedback controlled discharges from the previous campaign. For every provided *full* P_{rad} of every individual experiment, all $P_{\text{pred}} = P_{\text{pred}}\left(S\right)$ of the corresponding permutations S are calculated using equation (3.1). Applying those results to equation (4.7) yields the prediction qualities $\vartheta\left(S\right)$ for the corresponding permutations of LOS and incorporated metric φ. Finally, evaluation of this data set for each channel n and combination size m produces an average *line of sight sensitivity in plasma feedback scenarios* $\overline{\vartheta}_{\text{n}}^{(\text{m})}$.

$$\begin{aligned}\overline{\vartheta}_{\text{n}}^{(\text{m})} &= \frac{1}{N^{(\text{n,m})}} \sum_{S} \vartheta\left(S^{(\text{m})}\right) \\ N^{(\text{n,m})} &= \sum_{S} \delta_{\text{n}}\left(S^{(\text{m})}\right) \\ \delta_{\text{n}}\left(S\right) &= \begin{cases} 1, & n \in S \\ 0, & \text{else} \end{cases}\end{aligned} \tag{4.8}$$

Here, $N^{(\mathrm{n,m})}$ is the amount of permutations of size m that feature channel number n. The left-hand expression of the first equation in equation (4.8) can be seen as the contribution of channel n to the expected quality of the prediction with selection size m. In other words, $\vartheta_{\mathrm{n}}^{(\mathrm{m})}$ describes the sensitivity of channel n to local plasma radiation emissions and therefore significance to the representation of the total power loss P_{rad}.
Finally, after calculating the quality using equation (4.7) for the given metric, the full set of experimental data with all permutations of size 3, 5, and 7 channels individually, the evaluation is concluded. This strategy is applied to every following metric $\varphi(t)$ and map $\vartheta(S)$ and their results are examined and compared with each other.

Weighted Deviation

The first metric introduced in equation (4.9) will be referred to as a *weighted mean deviation*. This map is defined by the ratio between prediction P_{pred} and the full data set P_{rad}. The closer to the expected value and therefore more accurate the prediction, the larger the value $\varphi(t)$. However, the metric only yields values in the temporal interval of the experiment and for predictions with deviations to P_{rad} smaller than the respective reference. This punishes LOS sets S that greatly overestimate P_{rad} by not producing a contribution in such cases. Hence, assuming $P_{\mathrm{rad}} > P_{\mathrm{pred}} > 0$, the metric is positive-definite, and or more specifically $\varphi \in (0, 1)$. The quality ϑ of LOS selection S and corresponding prediction is calculated by integrating the metric across the experiment interval and normalizing by $T_{\mathrm{stop}} - T_{\mathrm{start}}$.

$$\begin{aligned} \varphi(t) &= \begin{cases} 1 - \frac{\|P_{\mathrm{pred}} - P_{\mathrm{rad}}\|(t)}{P_{\mathrm{rad}}(t)} & , (\|P_{\mathrm{pred}} - P_{\mathrm{rad}}\| < P_{\mathrm{pred}}) \wedge \\ & \qquad (T_{\mathrm{start}} < t < T_{\mathrm{stop}}) \\ 0 & , \text{else} \end{cases} \\ \vartheta &= \frac{1}{T_{\mathrm{stop}} - T_{\mathrm{start}}} \int_{T_{\mathrm{start}}}^{T_{\mathrm{stop}}} \varphi(t)\,\mathrm{d}t \end{aligned} \tag{4.9}$$

The corresponding results for equation (4.9) are presented in figure 4.15. On the left-hand side, an example of how such a metric for a LOS selection of *three channels* and experiment XP20181010.32 looks like can be seen. Also indicated here is a dotted black line, which represents the *norm* of $\vartheta(t)$, i.e. the metric of a selection S that yields the largest possible quality $\vartheta(S)$ or

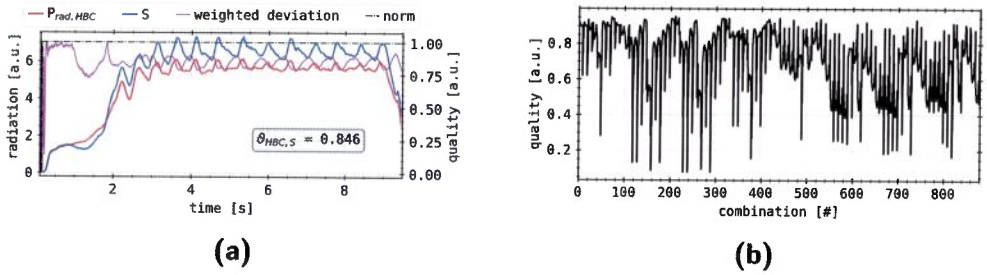

Figure 4.14.: Example of how the quality of the prediction for the *weighted deviation* metric is calculated for the previously discussed XP20181010.32. **(a)** Comparison of traces $\varphi(t)$, calculated using equation (4.9), P_{rad} and $P_{\mathrm{pred}}^{(1)}$ for a subset of three channels of the HBC. **(b)** Overview of 900 different combinations of three channel subsets for ϑ.

for $P_{\mathrm{pred}} = P_{\mathrm{rad}}$. The calculated value of $\vartheta(S)$ with respect to $P_{\mathrm{rad,HBC}}$ is noted with 0.846. The left ordinate corresponds to the values of radiation power loss, while the right refers to the quality of the LOS set in a. u.. The right-hand side plot shows the overall results ϑ for equation (4.9) for the same experiment as on the left, number XP20181010.32, and all LOS selections with three channels, $m = 3$.

The example on the left achieves a good overall prediction quality with an adequate representation of the temporal behaviour of the corresponding $P_{\mathrm{rad,HBC}}$, though its estimate consistently surpasses the former by around 10% above 5 MW. The oscillations, caused by the cycling of the underlying gas feedback valves, are visibly featured in P_{pred} as well as $P_{\mathrm{rad,HBC}}$, however this metric does not take temporal or spectral correlations explicitly into account. Hence, this LOS selection yields a quality of $\sim$ 85%. The spectrum of $\vartheta(S)$ on the right reaches from 0.1 to 0.95, with the majority of results above 0.5. The combinations are not sorted, hence their quality does not show any particular behaviour whatsoever. Values may differ from one combination to the other, where for example only one channel has been exchanged, by > 0.5.

The averaged quality ϑ of three, five and seven channel LOS selections for the *weighted deviation metric* is calculated using equation (4.8) and shown in figure 4.15 for both bolometer cameras P_{rad} individually. The left and right plot show the results for the HBC and VBC respectively, with differ-

ent colours and markers, including errors bars derived from the standard deviation in $\vartheta(S)$. On the lower ordinate, the channel number is noted and on the upper the corresponding minimum, effective plasma radius along the LOS. The *sensitivity* of the horizontal camera is generally, except for number 20 for combinations of three channels, well above 0.7. In cases of $m = 3$, the average quality of the channels is around 0.8, with LOS around $\pm 0.5 r_a$ having higher sensitivities of up to 0.9. A small local minimum of 0.75 can be found around $\sim -r_a$, as well as a local maximum at the opposite side at r_a with ~ 0.85. Lines of sight viewing the plasma core close to the magnetic axis $r \sim 0$ all have a similar sensitivity of 0.83. Channel number 20, which is viewing the center of the triangular plane and area close to the inboard, lower magnetic *X-point*, features a much lower sensitivity than any other of 0.58. The error bars on the individual channels do not exceed ± 0.05, where most have noticeably smaller ones. Especially LOS closer to the magnetic axis have smaller deviations than those around the local extremes. The two gaps in the channel coverage for combinations with $m = 3$ are small and indicate a continuous interpolation. For $m = 5$, the average quality is significantly increased and fluctuations between the individual channels in their contribution to the prediction are reduced. The expected quality of P_{pred} is between 0.84 - 0.9. Again, a local minimum and maximum can be found around $\pm 0.5 r_a$, respectively. The error bars are reduced, similarly to before. Gaps in locations where the prior subsets have been covered can therefore be supported by the underlying results and vice versa. This is clearly seen at $0.5 r_a$, where the missing channels for combinations of $m = 3$ in the next larger combination set show a similar trend as the surrounding LOS in the prior. And again the same is repeated for the average sensitivity of channel selections of the HBC with size $m = 7$. Here, the overall prediction quality is increased even more to between 0.91 - 0.92. The spectrum is hence narrowed further, with negligible error bars and almost no variations across the channels. Around $\pm 0.75 r_a$, where the local extremes in the previous profiles have been observed, deviations from the average sensitivity are found, indicating that the highest prediction quality is achieved by those lines of sight.
On the right-hand side, the sensitivity of the vertical bolometer camera is presented in the same way. Again, for all combination sizes, the average quality is generally above 0.8. Lines of sight with $r \sim -0.5 r_a$, as well as $-0.1 r_a$ for $m = 3$ have higher sensitivities of up to 0.9. However, for higher m there is a local minimum instead of a maximum at $-0.13 r_a$. The results

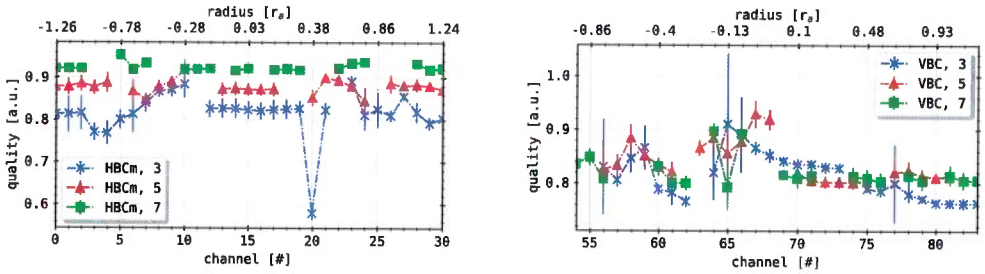

Figure 4.15.: Average prediction quality ϑ over a large number of experiments for combinations of three, five and seven channels using the *weighted deviation* metric. Prediction selections were limited to one of the individual camera arrays **(a)** HBCm and **(b)** VBC.

for combinations with $m = 3$ show the highest uncertainties, while the error bars decrease with larger prediction selection size like before. More specifically, channels number 56, 65 and 77 feature especially large uncertainties of up to 0.1 or $\sim 20\%$. The profiles of different m again provide visual aid for the gaps in their respective counterparts. Though, distinct differences can be noted in comparison to the results of the horizontal bolometer camera. There is no correlation between selection size m and average LOS sensitivity and a gap remains in the spectrum around $-0.36r_a$.
In summary, the *weighted deviation* metric shows that the expected prediction quality and therefore sensitivity of the individual channels for LOS selections of at least three channels is above 70% for both subsets of HBC and VBC lines of sight. In case of the horizontal camera, this increases proportionally to the amount of channels m in the selection, simultaneously reducing the variation in ϑ between combination predictions. Local minima in the sensitivity profile of the horizontal camera are found at radii that view the plasma core and inboard side X-points, while maxima are produced by lines of sight integrating through the center and opposite the camera located magnetic island. The vertical camera achieves result of similar quality, though the sensitivity does not scale with selection size. Maxima can be found again for LOS that mainly view the plasma core and inboard side magnetic island edges. Here, the peak height in sensitivity correlates with the integration length through the triangular plane, as is expected for this

type of analysis. Due to the camera orientation, the single local minimum is found at a different location. However, this still corresponds to a LOS viewing an inboard side X-point. The discrepancy between the profiles around $-0.13 r_\mathrm{a}$ can be attributed to the poor variation in the $m = 3$ sensitivity.

Correlation

The next metric and sensitivity map incorporate the *correlation* integral between the prediction P_pred and the full data set P_rad. The approach is analogous to the prior weighted deviation method in equation (4.9), where the metric yields a function in temporal space $\varphi(t)$ and the map transforms and normalizes this to a single prediction quality value for the subset S $\vartheta(S)$. The *(cross) correlation* integral describes the likeness of signals along the same domain, calculating a profile in which higher deviations from the self-correlation φ^* - the cross correlation of a signal with itself - correspond to lesser similarity between them. Assuming P_rad, $P_\mathrm{pred} > 0$, the metric and quality map both yield positive-definite results, which are presented in arbitrary units.

$$\begin{aligned} \varphi(t) &= \int_{-\infty}^{\infty} P_\mathrm{pred}(\tau)\, P_\mathrm{rad}(t+\tau)\,\mathrm{d}\tau \\ \vartheta &= \frac{1}{T_\mathrm{stop} - T_\mathrm{start}} \int_{T_\mathrm{start}}^{T_\mathrm{stop}} |\varphi^*(t) - \varphi(t)|\,\mathrm{d}t \\ \varphi^*(t) &= \int_{-\infty}^{\infty} P_\mathrm{rad}(\tau)\, P_\mathrm{rad}(t+\tau)\,\mathrm{d}\tau \end{aligned} \tag{4.10}$$

An example for this metric and selection quality ϑ can be found in figure 4.16. The plot on the left-hand side is presented in a way similar to before, including a line representing the *metric norm* or self-correlation. The results shown for $\varphi(t)$ are calculated using a LOS selection with $m = 7$ from the horizontal bolometer camera and achieve a quality of $\vartheta(S) = 1.1\,\mathrm{a.u.}$ Experiment number XP20181010.32 is again chosen as the comparing data set and example here. The temporal link between reference and prediction is strong in this case, where local minima, maxima and inflection points correspond well with each other. However, the prediction continuously overestimates the plasma radiation power loss compared to the full camera LOS set. Around 6 MW, the discrepancy in absolute value increases to up to 1 MW. On the right-hand side, a plot of the spectrum of selection qualities,

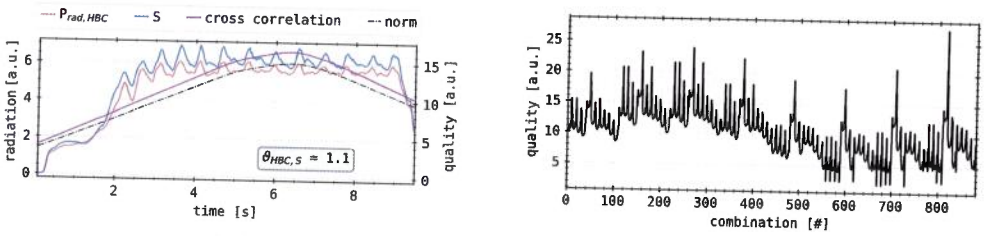

(a) (b)

Figure 4.16.: Example of how the quality of the prediction for the *correlation* metric is calculated for the previously discussed XP20181010.32. **(a)** Comparison of traces $\varphi(t)$, calculated using equation (4.10), P_{rad} and $P_{\mathrm{pred}}^{(1)}$ for a subset of three channels of the HBC. **(b)** Overview of 900 different combinations of three channel subsets for ϑ.

calculated using equation (4.10) for the same ~ 900 combinations and experiment XP20181010.32 as before with $m = 3$ can be found. The results are again not sorted and also show no coherent behaviour. Values range from 1–28 a. u. and vary between single instances of S with one channel exchanged up to 12 a. u.

In figure 4.17, the averaged line of sight sensitivity for selection sizes of three, five and seven channels from both bolometer cameras for the *cross-correlation metric* are displayed similarly to before in figure 4.15. The left plot shows the results of the HBC, with colours, corresponding ordinates and error bars alike to the presentation above. The profiles depict an entirely different behaviour than those calculated using the weighted deviation metric. Channel sensitivities have little variation across the camera array, except for two very distinct local maxima around $-0.9r_{\mathrm{a}}$ and $0.85r_{\mathrm{a}}$. The different selection sizes are congruent here, though $m = 3$ features two additional, smaller peaks further inward at $0.2r_{\mathrm{a}}$ and $0.38r_{\mathrm{a}}$. The minimum quality is 8 a. u., with most channels between 9–10 a. u. and maxima with up to 15 a. u. The error bars are, compared to the prior metric, very large with up to 4 a. u. and only barely decrease in size with increasing LOS selection size m. The data points of the individual profiles are all within their adjacent standard deviations, which increase around the location of local maxima. Again, gaps in the results are covered and qualitatively very well supported by the neighbouring lines for different m. In contrast to before,

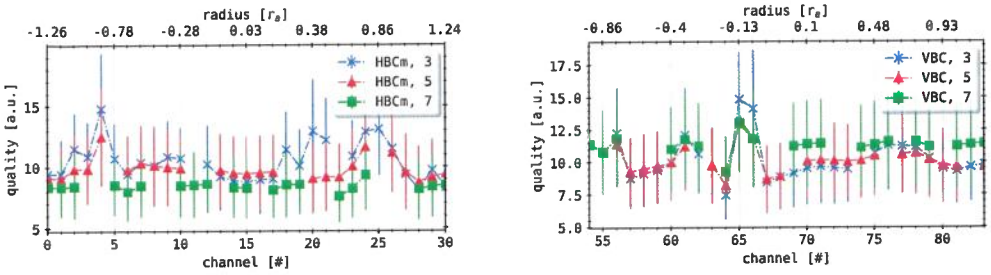

(a) **(b)**

Figure 4.17.: Average prediction quality ϑ over a large number of experiments for combinations of three, five and seven channels using the *correlation* metric. Prediction selections were limited to one of the individual camera arrays **(a)** HBCm and **(b)** VBC.

the orientation of the quality ordinate is different here due to the definition in equation (4.10), where smaller values equal higher sensitivity of the channels to the prediction results. This means that the previously noted maxima correspond to less sensitive lines of sight for the plasma radiation power loss. Larger selection size profiles show slightly smaller average values, indicating a generally improved prediction quality for those sets of S.
The right-hand side of figure 4.17 shows the results for the vertical bolometer camera in the same way as the left-hand side. A similar image can be seen here, with comparatively large error bars and nearly congruent profiles for the different LOS selection sizes m. The variation across the individual profiles is slightly larger than that of the HBC. Average channel sensitivities are again around 10 a. u.. Small local maxima of up to 12.5 a. u. can be found at $-0.8r_a$, $-0.35r_a$ and $0.65r_a$, while the global maximum is at $-0.13r_a$ with 15 a. u. Around that location two local minima of 7.5–8 a. u. are noted. The results for the different m are also in agreement with each other with consideration of the aforementioned error bars. However, in contrast to before, the larger size LOS selections yield higher average values and therefore lower local sensitivity for $r > 0$. On the other end of the spatial spectrum the profiles are congruent.
The correlation metric provides an entirely different approach to measuring the efficacy and quality of the plasma radiation power loss prediction for varying sizes m of the LOS selection. This method focuses on both the

likeness in absolute value and congruence in temporal behaviour between P_{pred} and P_{rad}. Most channels, with exceptions for the local extremes, of the horizontal and vertical bolometer camera feature a sensitivity around 10 a. u. In comparison to the weighted deviation, the lowest prediction qualities for the HBC are found for channels that previously presented local maxima, i.e. the highest radiation sensitivity. Lines of sight viewing along the inside of the separatrix and SOL across the triangular plane of W7-X and the inboard side located X-points show the lowest prediction quality for this metric. With respect to the prior analysis, this can also be said for the results of the VBC on the right-hand side - the less sensitive channels, measured by the correlation metric, of the vertical array only watch part of the core and the inboard X-points. For the VBC, detectors viewing the edges of the magnetic island adjacent to those X-points present profile minima and therefore higher local sensitivities. Contrasting results for increasing prediction selection sizes are found for the different cameras. The HBC shows the highest sensitivity for $m = 7$, while the VBC depicts the opposite behaviour for fewer channels or no correlation between size m and average quality. In both cases, increased standard deviations are found for all selection sizes, thus the prediction metric variation is very large. To some extent, the results from the weighted deviation metric analysis are supported by those findings, however the local extremes are orientated the other way and underline the opposite argument. This metric finds lines of sight from those ranges to contribute worse to the overall prediction quality than others, indicating that they provide unfavourable temporal correlation between prediction and total radiation power loss.

Is this because it is a local disturbance (due to puff?) and not the change of overall plasma conditions by the puff? This would make it consistent, no?!

Mean Deviation

The third metric is introduced in equation (4.11) and uses a modified variance to calculate a *mean deviation*. The corresponding prediction quality is defined by the square root of the integral of that mean deviation, normalized by the length of the measurement interval. In contrast to the weighted deviation from above, a smaller profile is equal to a higher likeness or better congruence between prediction and full data set. The opposite is true for the quality map due to its inverse correlation with the metric. This prediction evaluation method does not take the temporal relation between the two signals into account explicitly, similar to the prior weighted deviation

metric, however it does so without cut-offs in the spectrum of P_{pred}. Both expressions in equation (4.11) yield positive-definite results.

$$\begin{aligned} \varphi(t) =& \frac{1}{T_{\text{stop}} - T_{\text{start}}} \left(P_{\text{rad}}(t) - P_{\text{pred}}(t)\right)^2 \\ \vartheta =& \sqrt{\left(T_{\text{stop}} - T_{\text{start}}\right) \left(\int_{T_{\text{start}}}^{T_{\text{stop}}} \varphi(t)\,\mathrm{d}t\right)^{-1}} \end{aligned} \tag{4.11}$$

An example of the mean deviation metric is shown in figure 4.19. The left-hand side plot shows the results for a single LOS selection and horizontal bolometer camera measurement from discharge XP20181010.32 for comparison in the same way as before. The average prediction quality ϑ for this set of S is calculated to 5.12×10^{-6} a. u. This is an exceptionally small value, as is reflected by the profile of φ in the same figure, which corresponds to a strong agreement between prediction and P_{rad}. Hence, the *norm* here is a baseline at zero. From 2 s on, there are only small deviations between the two signals, underlining the previous statements. In this example, larger values of $\vartheta(t)$ of up to 7 a. u. are only found during the ramping up and collapse of P_{rad} and for temporally decoupled structures, i.e. peaks.
The right-hand side in figure 4.19 shows all, unsorted prediction qualities in reference to XP20181010.32 for line of sight selections with $m = 3$. Results for those circumstances range from 0.51×10^{-5} a. u. down to near zero, which is underlined by the plot on the left and the corresponding ϑ. Again, no particular behaviour is found here, while individual selections S with one channel exchanged can differ by up to 0.4 a. u..
The averaged prediction quality ϑ of three, five and seven channel line of sight selections for the *mean deviation* metric, calculated by equation (4.11) is shown in figure 4.19. The left and right side plot show the results for the horizontal and vertical bolometer camera respectively the same way as before. Profiles of both cameras are in the range of 2.5×10^{-5}–2.5×10^{-4} a. u. On the left, the results of the HBC show clearly separated lines for the different selection sizes m. The highest values, i.e. qualities generally with $\sim 1.2 \times 10^{-4}$ a. u. are achieved by $m = 7$, while the respective variation across the spectrum of channels is lowest. No distinct local extremes can be found here and standard deviations are comparatively large at 3×10^{-5} a. u. or $\sim$40%. The profile for $m = 5$ is more akin to the results for $m = 3$, although higher overall and hence presenting higher local sensitivities than the lat-

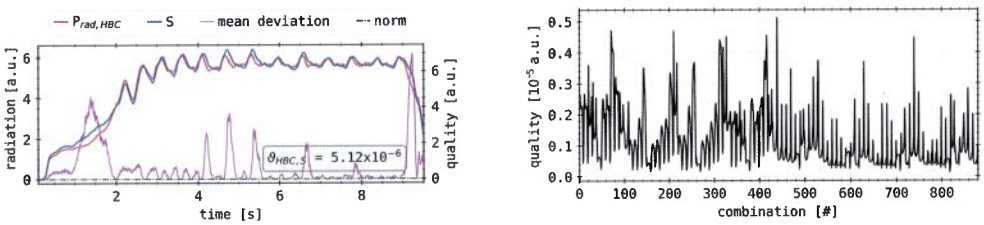

Figure 4.18.: Example of how the quality of the prediction for the *mean deviation* metric is calculated for the previously discussed XP20181010.32. **(a)** Comparison of traces $\varphi(t)$, calculated using equation (4.11), P_{rad} and $P_{\mathrm{pred}}^{(1)}$ for a subset of three channels of the HBC. **(b)** Overview of 900 different combinations of three channel subsets for ϑ.

ter. Error bar sizes remain the same, as there are now three local minima around $-0.75r_{\mathrm{a}}$, $0.35r_{\mathrm{a}}$ and $0.85r_{\mathrm{a}}$. The average quality here is ~25% lower at 9×10^{-5} a. u. Two less pronounced local maxima can be found at $-0.4r_{\mathrm{a}}$ and $0.5r_{\mathrm{a}}$ with up to 1×10^{-4} a. u. Lastly, the profile for $m = 3$ is lowest in this plot with values between 4.5–8.5 $\times 10^{-5}$ a. u. and features even more prominent extremes in similar locations to the ones before. However, the accompanying uncertainties are smaller than for the higher selection sizes at around 20%, though still unfavourable with respect to the prediction quality reliability.

The right-hand side plot shows the results for the vertical bolometer camera in the same manner. Similar to the HBC on the left, the highest values are achieved by selection size $m = 7$, while the respective variation across the spectrum of channels is smallest. The average sensitivity here is around 1.75×10^{-4} a. u. with error bars of up to 5×10^{-5} a. u. or ~25%. Only one minor local minimum and maximum each can be found at $-0.15r_{\mathrm{a}}$ and $-0.1r_{\mathrm{a}}$, respectively. Very similar results are found for $m = 5$, with only slightly smaller average prediction qualities, comparable error bars and local extremes. The latter are more pronounced here with respect to the increase variation across the camera array, while their position did not change. Finally, the profile for $m = 3$ is lowest in this plot with values between 1–1.7 $\times 10^{-4}$ a. u. and features even more prominent extremes in similar locations to the ones before. An additional local minimum can be

found around $0.7r_a$. However, in contrast to the horizontal camera results, the accompanying uncertainties are similar in size to before.
The *mean deviation* metric offers another approach to analysing the difference in quality of individual channel selections. In the above results, the local extremes are in the same locations as for the weighted deviation, though being far less pronounced in both cameras. However, some features are missing when comparing to the latter, i.e. the small minimum and maximum outside the separatrix on both ends of the spectrum are absent here. More prominently, the profiles standard deviation is overall unfavourable with at least 20% and an order of magnitude larger than that of the weighted deviation and similarly sized compared to the correlation metric. No outliers in local radiation sensitivity are found with this method. Contrary to before, this metric promotes horizontal camera channels from the center of the array, around $-0.5 - -0.5r_a$, to be best suited for predicting P_{rad}. Lines of sight from that area mainly view the plasma core and eventually pass through the inboard magnetic island and adjacent X-points. The global maximum of the vertical camera profiles is also located in the same position as in the previous analysis. Scaling of the quality ϑ with selection size m is small or negligible. Qualitatively, the VBC results are very similar to the average prediction quality of the VBC as calculated by the correlation metric. Hence, the local minima here also consist of LOS that view one lower inboard and one lower outboard X-point. Overall, with a selection size $m = 7$ (or larger), a consistently high prediction quality can be achieved for any channel combination from both cameras according to the mean deviation metric. With respect to the previous prediction evaluation methods, no additional insight is gained from this approach. The respective mathematical formulas in equation (4.11) do not yield significantly different results comparing to figure 4.15, i.e. temporal and absolute deviations are not weighted differently like the correlation does. However, that said, the exceptionally large error bars have to be taken into account during later assessments of the real-time radiation feedback.

Is there a commonality in combinations with lowest quality ?
Can we rather rule out sets/subset of channels ?

Fourier Transform Correlation

The final evaluation method is the *Fourier transform correlation* metric. This uses the established and widely applied *Fourier transform* $\mathcal{F}(\cdot)$ and previously used cross correlation to calculate the likeness between P_{rad} and

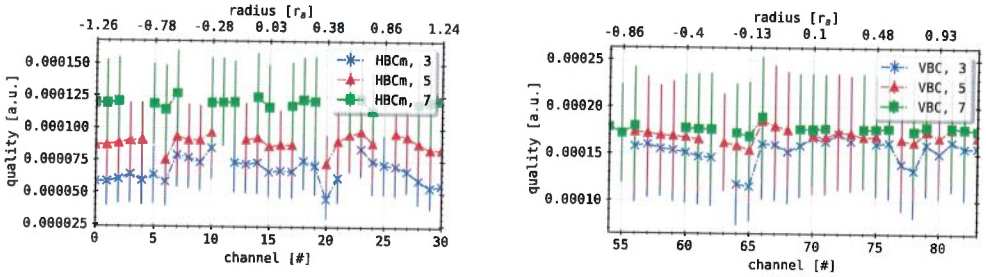

(a) **(b)**

Figure 4.19.: Average prediction quality ϑ over a large number of experiments for combinations of three, five and seven channels using the *mean deviation* metric. Prediction selections were limited to one of the individual camera arrays **(a)** HBCm and **(b)** VBC.

the prediction P_{pred}. This transform finds the continuous frequency spectrum - the spectral function - for the provided aperiodic signals and calculates the similarity between them. The definition of the individual (spectral) transforms $\gamma_{i/j}$ can be found in equation (4.12), including the map of both signals from their temporal to a frequency domain using the cross correlation.

$$\begin{aligned} \gamma_i &= \mathcal{F}\left(\int_{-\infty}^{\infty} P_{\text{rad}}(t-\tau)\,\mathrm{d}\tau\right)(\omega) \\ \gamma_j &= \mathcal{F}\left(\int_{-\infty}^{\infty} P_{\text{pred}}(t-\tau)\,\mathrm{d}\tau\right)(\omega) \\ g_{i,j}(\omega) &= \frac{1}{T}\int_{-\infty}^{\infty} \gamma_i(\omega)\,\gamma_j(\omega-\nu)\,\mathrm{d}\nu \end{aligned} \tag{4.12}$$

To calculate the individual Fourier transforms of the temporally sampled signals for all pre-composed LOS combinations, a *discrete fast Fourier transformation* routine (DFFT) from the integrated *NumPy*[I] package, a mathematical Python[II] library is used[169]. The resulting spectral function $\gamma_{i/j}$ describes the contribution of a frequency bin $\mathrm{d}\omega$, a discrete part of the

[I] NumPy is the fundamental package for scientific computing in Python; provides multidimensional array objects (masked and matrices), fast operations, including mathematical, logical, manipulation, sorting, selecting, I/O, discrete Fourier transforms, basic linear algebra, basic statistical operations, random simulation

[II] high-level, interpreted, general-purpose programming language; designed with code readability as a priority

spectral domain $[0, N/(2\mathrm{d}t)]$, to the corresponding signal[170]. This is also referred to as spectral (power) density and $g_{\mathrm{i,j}}$ as cross-spectral density. The latter provides a measure for the likeness of the two corresponding signals, as it was already applied by the previous correlation metric. Hence, a larger $\gamma_{\mathrm{i/j}}(\omega)$ corresponds to a larger contribution of that frequency bin to the signal and therefore $g_{\mathrm{i,j}}(\omega)$ likewise to a stronger correlation between the two spectral profiles. A metric is defined by $\varphi(\omega)$, analogous to the *(magnitude-squared) coherence*[171], together with a respective map to a prediction quality ϑ in equation (4.13).

$$\varphi(\omega) = \sqrt{\frac{|g_{\mathrm{i,j}}^2|}{|\gamma_{\mathrm{i}}\gamma_{\mathrm{j}}|}}, \qquad \vartheta = \int_{-\infty}^{\infty} \varphi(\omega)\,\mathrm{d}\omega \tag{4.13}$$

The metric $\varphi(\omega)$ applies the coherence relation, however the spectral densities $g_{\mathrm{ii/jj}}$ are exchanged with the absolute value of the product of the above Fourier transforms $\gamma_{\mathrm{i/j}}$. The coherence estimates the relation between two signals, measuring the probability that one is reproducible by or predictable through the other. For the purpose of this evaluation, this appropriation provides adequate normalization and finds φ in units of spectral power per frequency, i.e. spectral (power) density. Finally, the prediction quality ϑ for a LOS selection S is calculated by integrating φ over the spectral interval provided by the DFFT, yielding a single value in units of spectral power - here noted as a.u. for consistency.
An example for the results from equation (4.12) and equation (4.13) can be found in figure 4.20 on the left. Like before, for a combination of $P_{\mathrm{rad,HBC}}$ and prediction P_{pred} from a LOS selection with $m = 3$, the metric $\varphi(\omega)$ and subsequent quality ϑ are calculated and presented on the left. The spectral density profile is superimposed with a different abscissa in units of frequency on the top. The final prediction quality is noted in the bottom right corner. Due to the nature of the DFFT routine, the spectral profile extends to the negative frequency range and, in this case, is mirrored around zero. Frequency bins with $\omega < 0$ correspond to the imaginary part of the spectrum. If the complex contributions are identical to the real, i.e. the negative is the mirror image of the positive part, the provided signals and their coherence are found to be exclusively real[172]. On the right-hand side, the full results of all three channel combination predictions for the Fourier transform metric is shown.

Immediately, when examining the results on the left, a stark contrast to the previous metrics is noticeable. When comparing to the results of all three channel combinations on the right, this prediction appears to yield favourable results, however, the two signals P_{rad} and P_{pred} are particularly disjoint. The prediction profile overestimates the actual radiation value continuously and occasionally by over 300% or 15 MW during local extremes. Furthermore, the initial phase up to 2 s of the discharge looks significantly different in the prediction compared to P_{rad}, while the decline to zero after 9 s is much sharper and more abrupt in the prior. As already noted, the spectral density is symmetric around $\omega = 0$, where it is also lowest. At 0.9 Hz, the first local maximum with a magnitude of 5 a. u. can be found. A small step around 2.7 a. u. is located in-between the global minimum and this peak. Multiple small oscillations around 3 a. u. follow, until at 1.8 Hz the global maximum of 7.3 a. u. is reached. This again is succeeded by a second minimum around 2 Hz and concluding maximum towards 2.1 Hz. The rest of the spectral density profile comprises oscillations with decreasing amplitude from 0.2 a. u. around 3.4 a. u.. Beyond 8 Hz, the spectrum is nearly constant with negligible variations.

This metric measures the similarity between the profiles spectral powers in the spectral domain, hence the favourable prediction quality value despite the large difference in profile amplitudes and shape. The resulting φ shows a strong correlation around the frequency of the primary injection oscillation, i.e. 1.8 Hz. The secondary and tertiary maxima at 0.9 Hz and 2.1 Hz respectively can be attributed to the small, superimposed variations on the larger fluctuations from the gas inlet. In contrast, the lower correlation towards the global minimum at 0 Hz underlines the large discrepancy in absolute value and small contribution of very slow oscillations to both signals. The latter is also true for the profile between 0.9–1.8 Hz. Following the conclusive local maximum, the fading oscillations with increasing frequencies are attributed to the similarity in noise content and spectrum. With respect to the investigations and results in the introductory section 2.2.5, this is dictated by the particular performance of the individual channels in the selection S used for P_{pred}.

The plot on the right of figure 4.20 shows all unsorted prediction qualities ϑ as calculated by equation (4.13) for selections with $m = 3$. The spectrum of results reaches from 2×10^3–3.4×10^4 a. u., while the majority of LOS selections S achieve qualities around 1×10^4–1.5×10^4 a. u.. Individual pre-

The frequency response is quite an interesting parameter for designing the controller. I don't understand its relevance as a quality metric (yet). Results seen inconclusive in the present form → drop.

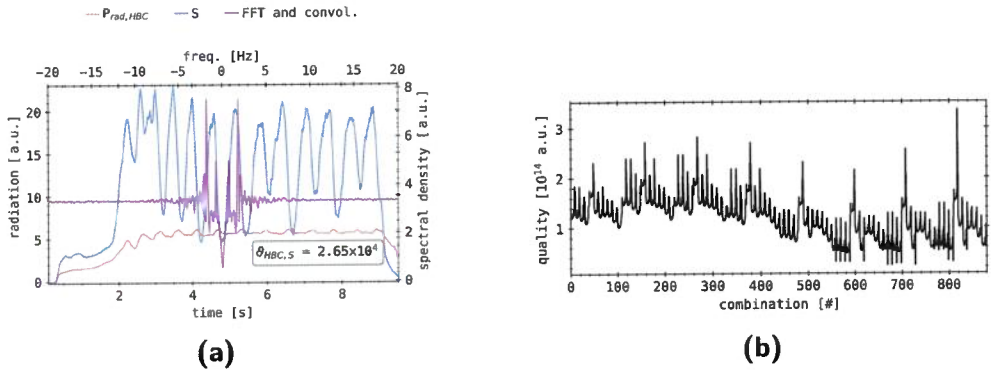

Figure 4.20.: Example of how the quality of the prediction for the *FT correlation* metric is calculated for the previously discussed XP20181010.32. **(a)** Comparison of traces $\varphi(t)$, calculated using equation (4.11), P_{rad} and $P^{(1)}_{\mathrm{pred}}$ for a subset of three channels of the HBC. **(b)** Overview of 900 different combinations of three channel subsets for ϑ.

dictions differ up to 2×10^4 a. u. or $> 50\%$ with one channel exchanged. In this case, the second half of the spectrum of combinations shows consistently smaller values of ϑ than the other, while the corresponding local and the global maxima contrast the former much stronger. This range of three channel selection permutations collectively yields generally less accurate predictions of the plasma radiation loss, which already indicates a significantly weaker sensitivity of at least one or more channels to the overall measurement.

The collected and averaged LOS sensitivity for three, five and seven channel selection sizes are shown in figure 4.21. The plots are constructed the same way as for the previous evaluation metrics, featuring the results for all selection sizes m of the horizontal bolometer camera on the left and of the vertical camera on the right. All profiles are, with the exception of the global maxima of 8.5×10^4 a. u. around $0.38 r_{\mathrm{a}}$ for the HBCm and 8×10^4 a. u. at $-0.13 r_{\mathrm{a}}$ for the VBC, in the range of $2\text{–}6 \times 10^4$ a. u. On the left, the different selection sizes yield qualitatively and, along most of the radial spectrum, quantitatively very similar values. Gaps in the channel coverage of the individual lines are again supported in qualitative trend by the other results. In fact, the profile for $m = 5$ and $m = 7$ are respectively lower than the prior, except around the center LOS no. 15 of the HBC. The results for

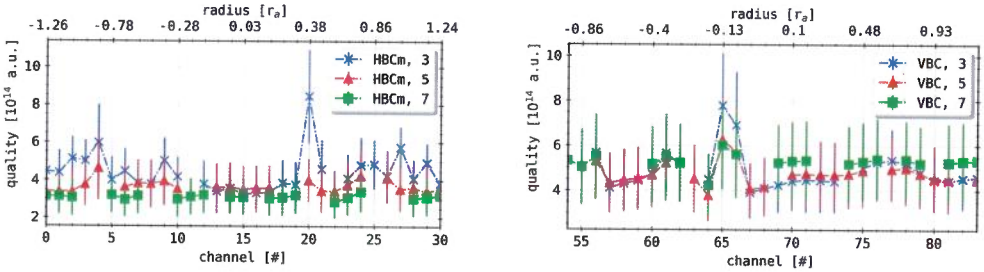

Figure 4.21.: Average prediction quality ϑ over a large number of experiments for combinations of three, five and seven channels using the *FT correlation* metric. Prediction selections were limited to one of the individual camera arrays **(a)** HBCm and **(b)** VBC.

$m = 7$ are consistently between 2.5–4 $\times$ 10^4 a. u. Only on both ends of the camera fan, i.e. towards $\pm 1.25 r_a$ and at the global maximum location, the LOS combinations with $m = 3$ provide higher prediction accuracy according to the above spectral Fourier metric. However, in those locations, the latter also has larger uncertainties as indicated by the accompanying error bars. Local maxima of up to 6 $\times$ 10^4 a. u. are also found here towards r_a, though smaller ones can also be seen around $-0.4 r_a$ and $0.7 r_a$. The individual average prediction quality uncertainties decrease with selection size, while they are increased for the local maxima, especially the global maximum at $0.38 r_a$. They are in the range of 0.75–3 $\times$ 10^4 a. u. or 25% - 37.5% for the profile for $m = 7$ and global maximum respectively.
The results for the vertical bolometer camera on the right-hand side generally are in strong quantitative and qualitative agreement with each other, while in contrast to the HBC profiles on the left, $m = 7$ shows the overall largest average prediction quality. The plotted lines are in the range of 3.5–8 $\times$ 10^4 a. u. Except for the radial interval of $-0.13 r_a$-$0.4 r_a$, the individual plots are nearly congruent and hence well within their respective error bars of less than 2 $\times$ 10^4 a. u. or 30%. The latter are mostly constant across the selection sizes, however they increase around and at the local and global maxima. The quality profile for predictions with seven LOS yields higher results between the global maximum and $0.5 r_a$. Channel no. 16, i.e. $-0.13 r_a$ shows the highest ϑ at 6 $\times$ 10^4 a. u. for $m = 5$, 8 or 8 $\times$ 10^4 a. u. for $m = 3$. In

contrast to the HBC, two LOS yield significantly higher prediction qualities. Additionally, shallower local maxima are located around $-0.75r_a$, $-0.35r_a$ and $0.65r_a$ with values between 5–6 $\times$ 10^4 a. u. The global and a local minimum are located either side, adjacent to the maximum in $-0.2r_a$ and 0 with 3.5×10^4 a. u. and 4×10^4 a. u. Again, gaps in the coverage of each line in the radial spectrum are quantitatively well-supported by the neighbouring profiles. Generally, $m = 7$ provides the highest average prediction quality, except for measurements involving LOS between no. 64 and 6, where $m = 3$ shows the best results.

The *Fourier transform correlation* focuses on the spectral correlation between the prediction and full data set P_{rad}. The above results in figure 4.21 show very similar features and characteristics as can be found in figure 4.17 for the *correlation metric*. The global maximum in the prediction profile of the vertical bolometer camera is located at the same radius and features a nearly identical contour on both sides of the LOS spectrum. The relation between the individual selection size lines, with respect to the absolute level of ϑ, and the qualitative plot profile also are virtually congruent to that in the latter figure. The only noticeably difference, besides the quantitative details, are the relative size of the error bars and intensity of the local extremes towards the negative end of the radial spectrum, i.e. $-1.25r_a$, which are more pronounced in figure 4.17. However, this does not hold entirely true for the HBC predictions on the left. The negative part of the selection profiles generally reflect the results of the correlation metric, besides the quantitative differences and relative error bar sizes. Again, location and shape of the local maxima here are similar, while also being less intense than in the previous image. Contrary to figure 4.17, the global maximum is featured on the right side of the radial spectrum in $0.38r_a$ instead of $-0.85r_a$. Beyond that, additional maxima can be found only for the Fourier transform correlation with significantly lower relative peak height than the secondary extremes in the prior plot.

The presented quality profiles provide a measurement of the spectral likeness between the prediction and P_{rad}, contrasting the previously examined correlation metric by excluding quantitative contributions to the above results. Again, the horizontal bolometer shows that LOS viewing along the inside of the separatrix and SOL, as well as across the triangular plane and inboard side located X-points present the lowest prediction quality. However, channel no. 20 viewing the upper inboard facing X-point is an exception, which

for $m = 3$ features the global maximum - this is also indicated by channel no. 9, at a much lower intensity however, watching the corresponding lower magnetic island intersection. Average prediction qualities are higher outside the separatrix and inside the scrape-off layer, indicating a similarly increased sensitivity for feedback frequency responses of P_{pred} in P_{rad}. Lines of sight viewing this part of the plasma yield line integrated measurements along the separatrix, from multiple upper and lower magnetic islands, as well as X-points. In particular, channel no. 4 focuses on the lower inboard X-point and no. 27 the upside located counterpart. Increased values of ϑ towards $\pm 1.25 r_{\mathrm{a}}$ indicate similar contributions from both midplane and outboard islands, including the corresponding SOL separatrix intersections. The variations in-between those local maxima are more pronounced towards the positive end of the radial spectrum. Results of the vertical bolometer camera support the above examinations, where the global maximum also views the upper inboard X-point. The less intense secondary and tertiary extremes also align with the location of the different X-points around the triangle shaped plasma core. Lines of sight watching only the plasma core and surrounding magnetic islands show relatively decreased average prediction qualities, which in context of the above observations about the separatrix intersections underlines the latter results. Conclusively, the Fourier transform correlation finds the largest local sensitivity of spectral representations in P_{rad} to come from channels viewing X-points in the scrape-off-layer and more specifically the one located upside inboard of the triangular bolometer plane. With respect to the very similar results of the *correlation metric* in figure 4.17, the only significant qualitative change can be found in the radial location of the global maximum of the HBC prediction profile. Exclusion of the contribution of absolute values to the prediction quality yields a shift of the maximum from the top inboard magnetic islands to the below neighbouring X-point.

This concludes the application and examination of the individual evaluation metrics for the same multifaceted, large set of experiments with feedback application. For all metrics, the plasma radiation prediction has been characterized for different selection sizes m and the local sensitivity of such towards the full set P_{rad} explored. Different functional patterns towards a singular quality measure for this kind of prediction have been exercised and their impact measured. The results are used to understand the contribu-

tion of individual lines of sight, given the manifold of metric characteristics magnetic configuration of W7-X, to the predictability of qualitative and quantitive features in P_{rad}. With respect to the initially posed questions in the beginning of this chapter 4, findings from the above investigations point to lines of sight of the HBC at or close to the separatrix and scrape-off layer to be most promising for predicting the radiative power loss from a smaller data set. More specifically, when also looking at channels of the VBC, information from the upper inboard magnetic island and X-point yield the largest contribution towards favourable P_{red} for feedback experiments.

Highlight! also for m=7 there is basically no selection bias anymore ...

Section could be condensed significantly in the result description of the plots. Which channels can we forget? (inverse analysis) See above

4.3.2. Sensitivity Analysis

Analogous to the collection of experimental data in section 4.1, and more specifically figure 4.1, median values of the central plasma parameters, i.e. microwave heating power P_{ECRH}, outboard electron temperature T_{e} and radiative plasma power loss P_{rad} have been collected for all, in the previous section examined discharges. Based on this information, the results from, e.g. the *weighted deviation* in figure 4.15 or any other metric can be used to correlate their findings with the governing plasma parameters. For the sake of clarity, the aforementioned weighted deviation and its prediction results where chosen to apply the above approach. The results can be found in figure 4.22. For a selection S of m channels, the weighted deviation metric φ^* finds a quality value ϑ for the calculated P_{pred}, given P_{rad} and accompanying plasma parameters. Conclusively, this yields a map from LOS selection and characteristic plasma parameters, including P_{ECRH}, P_{rad}, $T_{\text{e,out}}$ etc., to one singular measure for prediction efficacy

$$\vartheta := f\,(S,\, \varphi^*,\, \textit{plasma parameters}) : \mathbb{N}^m \times \mathbb{R}^n \to \mathbb{R}\ . \tag{4.14}$$

This section will only focus on the results for $m = 3$ in figure 4.15, producing the coloured, two-dimensional height map in figure 4.22. The top line of plots shows the combined individual selection prediction qualities of HBC and VBC from before with their corresponding median plasma heatings powers P_{ECRH}. The following two figures below correlate the previous profiles with the median radiative power loss P_{rad} to find the radiation fraction f_{rad}. Due to differences in the two bolometric measurements, the colour scales are different here between the cameras. Finally, the last two images

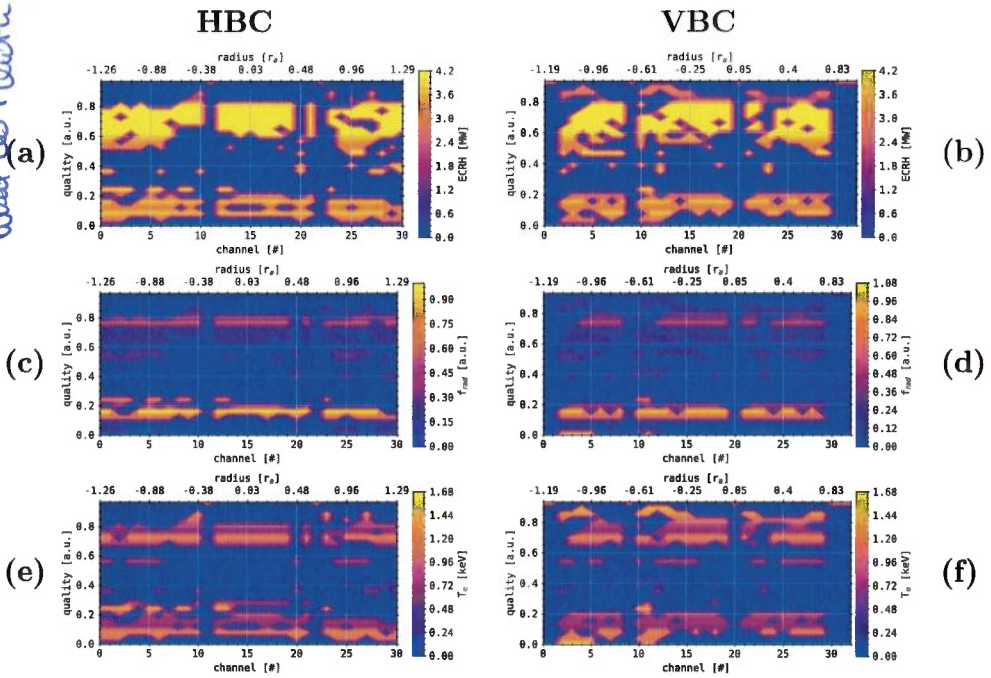

Figure 4.22.: Experiment parameter analysis for the *weighted deviation* metric and the corresponding sensitivity results shown in figure 4.15. Included are maps of both cameras each for parameters **(a)**, **(b)** microwave heating P_{ECRH}, **(c)**, **(d)** radiation fraction f_{rad} and **(e)**, **(f)** core electron temperature T_{e}.

show the same results superimposed with the median core electron temperature T_{e}. All plots span the same ordinate ranges of $r \in [-1.26,\ 1.29]\, r_{\mathrm{a}}$ or $[-1.19,\ 0.95]\, r_{\mathrm{a}}$ for the HBC and VBC respectively, as well as abscissa range of $\vartheta \in [0, 0.95]$ a.u.

On the top row, figure 4.22:(a) and (b), the resulting P_{ECRH} brightness profiles show heating powers of up to 4.2 MW for both cameras and feature very similar structures. The images are presented with distinct gaps between 0.25–0.5 a. u. across the entire radial spectrum with few bright spots for exceptions. Algorithmically omitted HBC channels no. 11 and 22, as well as VBC channels no. 9 and 20 produce the same features vertically and therefore separates each of the profiles into three individual structures at the top and bottom. Indicated heating powers for lower prediction qualities

$\leq$0.3 a. u. are noticeably reduced with $\leq$3.5 MW when compared to higher $\vartheta \geq$0.5 a. u. at $\geq$4 MW. The latter shows no visible structures in colouring or shape of the profile besides a minor descending gradient towards lesser quality values. At 0.75 a. u. and 1.5 a. u., the bottom part of the plots features two characteristic lines with similar gradients in vertical direction. In between and above 0.85 a. u., single points with >0 MW appear sporadically distributed and random. For the HBC, edges of the top and bottom part of the image are generally unspecific, though the left- and rightmost portion with $\leq -0.35 r_\mathrm{a}$ and $\geq 0.7 r_\mathrm{a}$ consistently show lower qualities than the center. Similar features can be found at the bottom, while on the left the metric produces slightly higher ϑ for the given selection of LOS and experiments. The VBC shows an increased amount of structures with lower brightness or P_ECRH above 0.8 a. u. The upper left and right section at $< -0.65 r_\mathrm{a}$ and $> 0.1 r_\mathrm{a}$ of the profile also extend further downward when compared to the HBC, which is also true only for the bottom left part below $-0.4 r_\mathrm{a}$.
The next line of plots, figure 4.22:(c) and (d), shows the radiation fraction f_rad as a brightness profile over the minimum plasma radius along the LOS and mean deviation prediction quality in the same way as before. Due to the correlation $f_\mathrm{rad} \sim P_\mathrm{rad}/P_\mathrm{ECRH}$, both images largely show the same results, with vertical gaps at the omitted channel numbers and a large void in the center of the quality spectrum like above. However, since $P_\mathrm{rad,HBC} \neq P_\mathrm{rad,VBC}$, the radiation fraction or brightness ranges from 0–1 a. u. or 1.08 a. u. for the individual cameras respectively. The top part of the HBC plot is very similar in outline, but features a reduced brightness or smaller values of f_rad of 0.2–0.4 a. u. Within the smooth profile is a bright line at 0.75 a. u. across the entire radial spectrum with a radiation fraction of $\approx$0.65 a. u.. At the bottom, a singular bright structure is located at 0.15 a. u. with $f_\mathrm{rad} \sim$0.9 a. u., while results for lower prediction qualities are negligible. The same image presents on the other side in figure 4.22:(d) for the VBC, where the top part of the distribution is similarly shaped but significantly decreased in brightness or f_rad, and the bottom is reduced to one bright feature at the same ϑ as in the HBC plot.
The last row of images shows the brightness profile of the core electron temperature T_e from the same set of experiments as before. Results for the horizontal bolometer camera on the left in figure 4.22:(e) are largely very similar in shape to the two prior plots. The gap in-between the top and bottom part is slightly increased due to the reduced distribution for

higher prediction qualities >0.65 a. u. This also features a higher brightness between 0.7–0.75 a. u. of ≈1.3 keV and a local maximum towards 1 a. u. of 1.45 keV. At the bottom, the profiles structures are much more strongly separated, with an increased temperature of 1.2 keV between 0.05–0.1 a. u. The global brightness maximum of 1.6 keV can be found at 0.2–0.25 a. u. between $-1.25 - -0.05 r_a$. Finally, the same is true for figure 4.22:(f), where the structure of the VBC electron temperature profile is a combination of the prior two, and the brightness distribution features pronounced local extremes at the top and bottom. Most prominently, the highest brightness of 1.65 keV is located between 0.85–0.95 a. u. and $-1.15 - - -0.25 r_a$, with an additional local maximum below around 0.7 a. u. across the radial spectrum. Similarly, the bottom part shows two characteristics with distinctly higher temperatures of ∼1.5 keV: around the same radial space as the maximum at up to 0.05 a. u. and a singular bright spot at $-0.55 r_a$ and 0.25 a. u. Also, a slightly increased temperature can be seen just below 0.1 a. u. for a few LOS with $> -0.25 r_a$.
The presented results in figure 4.22 all outline a very similar picture due to the underlying LOS prediction quality profile, calculated from the same experimental data set using the *weighted deviation* metric. Small variations in the shape of the plots are due to the evaluation of the corresponding plasma parameter, which potentially yield negligible or no results, i.e.∼ 0. In this case, this is interpreted as the background colour, since omitted channels and combinations of $\{r_a, \vartheta_S\}$ that yield no results also correspond to 0. The most notable feature is the distinguishable gap in ϑ between ≈0.3–0.5 a. u., containing only few single spots with no pattern whatsoever. On one hand, qualitatively, profiles of the two cameras match very well throughout the series of plots, where overall shape, global extremes location and absolute values are in good agreement. On the other hand, the brightness profiles greatly differ for each camera across the individual colour axis, i.e. P_{ECRH}, f_{rad} etc. At the top, a large range of prediction qualities 0.5–0.85 a. u. is found for the highest heating power of 4.2 MW, while the bottom of the same plot features a decreased brightness of 3.6 MW and narrower profile shape. Correspondingly, the highest f_{rad} >0.8 a. u. yield the lowest ϑ <0.3 a. u., with higher predictions qualities linked to slightly reduced radiation fractions above 0.75 a. u. for both cameras. This plot also does not provide results at the bottom below 0.1 a. u. Finally, in the last set of images, electron temperatures of >0.9 keV coincide with the full spectrum of prediction qualities for

all featured LOS combinations and radii. However, increased T_e >1.2 keV can be found for ϑ <0.15 a. u. or at 0.7 a. u. consistently and for a small range of LOS towards the negative end of the radial spectrum across all qualities.
The presented results in figure 4.22 provide a detailed insight into the correlation between central plasma parameters and the efficacy of individual bolometer channels towards a radiation power loss prediction. First and foremost, this shows that either the applied *weighted deviation* evaluation metric yields no results for, or that combinations with a medium prediction quality, i.e. ~0.5 a. u. correspond only to negligible plasma parameters. Considering the manually selected combination of experiments and evaluation procedure, the latter is the more plausible cause. Within the scope of the above analysis, this is synonymous with the fact that only ϑ significantly below or above 0.5 a. u. are found for the selection of LOS combinations. Furthermore, higher heating powers P_{ECRH} correlate with an overall increased predictability of P_{rad}, while this is inversely linked to the respective radiation fraction f_{rad}. However, around prediction qualities of ~0.75 a. u., a significantly increased f_{rad} compared to the surrounding profile of <0.5 a. u. can be found, indicating that at higher radiation loss fractions there exists an improved ϑ. Finally, a similar picture is found for electron temperature measurements, where around the same prediction quality of 0.75 a. u. and above 0.9 a. u. a relatively higher value of 1.3 keV is found across all LOS. However, consistently greater T_e and also its global maximum are located at distinctly lower weighted deviation metric results <0.4 a. u. Furthermore, the latter applies only for LOS with $r < 0.4 r_a$, i.e. towards the lower inboard side of the triangular plane, close to the aperture of the VBC camera array and two neighbouring islands. In conclusion, both camera datasets are in very good agreement with each other, from which very confidently experimental configurations can be preset to achieve good plasma radiation predictability. Discharges with medium to high heating powers, ≥3.5 MW, core electron temperatures of ~1.3 keV and radiation loss fractions >0.75 a. u. consistently fit well to the above methodology across all LOS combinations.

This section serves as a robust study for the application and local sensitivity of plasma radiation feedback for future experiment campaigns. Hence, closing this particular investigation and referring back to the originally posed questions in the beginning of this chapter, sets of discharge configurations and

I don't understand what I can extract of this data.
I would drop the section.

corresponding line of sight combinations have been identified to positively correlate with the quality of the real-time radiation prediction. Therefore, there *does exist an optimal set S of LOS for a range of given plasma parameters.* The following section will try to answer the remaining question, posed in the beginning of this chapter, regarding the cause of the plasmas behaviour and LOS sensitivity under feedback conditions.

4.4. STRAHL Modelling drop!

The one-dimensional transport simulation code STRAHL is designed to analyse the radial distribution and radiation profile of impurities within the plasma bulk. It solves the radial continuity equation for each ionization stage of the impurity in a one-dimensional geometry and uses an ansatz of anomalous diffusivities and radial drift velocities. STRAHL can incorporate full neoclassical transport treatment as needed. The simulation focuses on dynamics of impurity transport and its radiative effects, using parameters derived from experimental data for the background plasma and is therefore used to understand and predict their behaviour.

4.4.1. Introduction

STRAHL solves the radial continuity for each ionisation stage i, i.e. of particle density $n_{\mathrm{i,Z}}$ of a given impurity Z by the above paradigms. Let $S_{\mathrm{i,Z}}$ be sources and sinks of said ion population. The simulation focuses on transport perpendicular to the flux surfaces (FS), assuming a constant $n_{\mathrm{i,Z}}$ along them, however poloidal variations in distance between them also leads to a net impurity density and temperature gradient and hence flux. For establishing a differential expression to solve numerically, one finds the flux surface average of $n_{\mathrm{i,Z}}$ and applies that to the continuity equation, producing a cylinder coordinate form in which an ansatz of diffusive and convective

terms for the flux is applied. This gives, taking the flux surface averaged radial diffusion coefficient D^* and drift velocity v^*:

$$\begin{aligned} \frac{\partial n_{\mathrm{i},Z}}{\partial t} &= \frac{1}{r}\frac{\partial}{\partial r} r \left(D^* \frac{\partial n_{\mathrm{i},Z}}{\partial r} - v^* n_{\mathrm{i},Z} \right) + S_{\mathrm{i},Z} \ , \\ D^* &= \left\langle D\left(\theta\right) |\nabla r|^2 \right\rangle_{\mathrm{FS}} := \frac{1}{4\pi^2 R_{\mathrm{M}} r} \oint_{\mathrm{FS}} D\left(\theta\right) |\nabla r| \mathrm{d}S \\ v^* &= \left\langle v\left(\theta\right) |\nabla r| \right\rangle_{\mathrm{FS}} = \frac{1}{4\pi^2 R_{\mathrm{M}} r} \oint_{\mathrm{FS}} v \mathrm{d}S \ . \end{aligned} \tag{4.15}$$

Outside the separatrix, the one dimensional model is not very well suited and the parallel transport to the divertor or limiter is considered by a loss time $\tau_{||}$, which is considered by an additional term $-n_{\mathrm{i,Z}}/\tau_{||}$ in the SOL on the right-hand side of the modified continuity equation. The sources and sinks $S_{\mathrm{i,Z}}$ are described by coupling neighbouring ion stages with their respective rate coefficients $Q_{\mathrm{i,Z}}$ for ionisation (*ion*), radiative and di-electronic (*rec*) as well as charge exchange (*cex*) recombination.

$$\begin{aligned} S_{\mathrm{i},Z} = &-n_{\mathrm{i},Z} \left(n_{\mathrm{e}} Q_{\mathrm{i},Z}^{\mathrm{ion}} + n_{\mathrm{e}} Q_{\mathrm{i},Z}^{\mathrm{rec}} + n_{\mathrm{H}} Q_{\mathrm{i},Z}^{\mathrm{cex}} \right) + n_{\mathrm{e}} Q_{\mathrm{i},Z-1}^{\mathrm{ion}} n_{\mathrm{i},Z-1} + \\ & n_{\mathrm{i},Z+1} \left(n_{\mathrm{e}} Q_{\mathrm{i},Z+1}^{\mathrm{rec}} + n_{\mathrm{H}} Q_{\mathrm{i},Z+1}^{\mathrm{cex}} \right) \end{aligned} \tag{4.16}$$

Neoclassical transport is accounted for by two individual tools in STRAHL. *NeoArt* is another simulation code by Arthur Peeters, solving the set of linear coupled equations for the parallel velocities in arbitrary toroidally symmetric geometry for all collision regimes[173]. The second approach finds approximative analytical expressions for the diffusion and drift according to Hirshman and Sigmar et al.[174]
The result in equation (4.15) for a number of Z transport equations can be expressed and solved algebraically and therefore numerically, using $\vec{n}$ the density of said impurity as well as $\mathbf{D}$, $\mathbf{v}$, $\mathbf{S}$ and $\mathbf{R}$ (diagonal) matrices of transport and rate coefficients. The latter two denote products of the previously mentioned parameters and electron number densities n_{e}. A source term for neutral ionisation is given by $\vec{d} = \vec{e}_1$.

$$\begin{aligned} \frac{\partial \vec{n}}{\partial t} = &\mathbf{D} \frac{\partial^2 \vec{n}}{\partial t^2} + \left(\left(\frac{1}{r} + \frac{\mathrm{d}}{\mathrm{d}r} \right) \mathbf{D} - \mathbf{v} \right) \frac{\partial \vec{n}}{\partial r} - \\ & \left(\frac{1}{r} + \frac{\mathrm{d}}{\mathrm{d}r} \right) \mathbf{v}\vec{n} - \mathbf{S}\vec{n} - \mathbf{R}\vec{n} + \vec{d} \end{aligned} \tag{4.17}$$

The stable and computationally effective *Crank-Nicholson*[I][175] method finds an equation for temporal iteration to $\vec{n}^{(l+1)}$:

$$\begin{aligned} \vec{n}^{(l+1/2)} &= \frac{\vec{n}^{(l)} + \vec{n}^{(l+1)}}{2} \\ \frac{\vec{n}^{(l+1)} - \vec{n}^{(l)}}{\Delta t} &= \left[\mathbf{D}\frac{\partial^2}{\partial r^2} + \left(\left(\frac{1}{r} + \frac{\mathrm{d}}{\mathrm{d}r}\right)\mathbf{D} - \mathbf{v}\right)\frac{\partial}{\partial r} - \right. \\ &\qquad \left.\left(\frac{1}{r} + \frac{\mathrm{d}}{\mathrm{d}r}\right)\vec{v} - \mathbf{S} - \mathbf{R}\right]\vec{n}^{(l+1)} + \vec{d}\,. \end{aligned} \tag{4.18}$$

Neutrals (impurities) have so far only been accounted for as sources to the first ionisation stage. In STRAHL, they are modelled as uniformly moving radially inwards, decaying in density with decreasing radius as the plasma is assumed to be sufficiently dense and hot to fully ionize the influx of particles. This equilibrium impurity transport and radiation simulation is employed to investigate the previously discussed results of the local LOS sensitivity towards the real time bolometer feedback. In particular, the calculated one-dimensional impurity emission profiles will be used to find possible correlations between the results in section 4.3, experimental kinetic data and transport coefficients, which are varied as input parameters into STRAHL. The goal is to link data from the previously thoroughly examined results of experiment XP20181010.32, which is the prime candidate for radiation feedback control, to particular variations in the chord brightness profiles and impurity radiation around the separatrix that have been observed in the previous chapter. For given profiles of electron temperature and density, transport coefficients, magnetic field geometry and strength, impurity sources and atomic spectral and energy data, STRAHL solves equation (4.15) and finds the corresponding distribution and emissivity profile. One should keep in mind that this approach is not very well suited for the SOL, where approximative terms for parallel transport to the plasma limiting surface are considered, while the kinetic profiles are estimated to decay exponentially outside and the magnetic geometry has to be extrapolated from the LCFS. A more detailed inspection with additional background information can be found in [176–178].

[I] an implicit, finite difference method used for numerically solving the heat equation and similar partial differential equations; giving second-order convergence in time

First, a series of STRAHL output plots are shown, which are achieved using experimentally measured kinetic profiles T_e and n_e from discharge XP20181010.32 for four different radiation fractions, f_{rad} ={1/3, 2/3, 90%, 100%}. If not stated otherwise, the STRAHL configuration is the same for all presented results. An inexhaustible neutral gas background was considered for collisions with the modelled impurity ion species. For convenience, local quasi-neutrality $n_e(r) = n_i(r)$ and equilibrium $T_e(r) = T_i(r)$ is assumed. Corresponding data for atomic energies levels and spectral information were collected from the central *Atomic Spectra Database*[179] and/or using *ADAS*[180]. As was extensively explored at the stellarator W7-X during its past experimental campaigns and its predecessors[114], in general, the most relevant impurities towards radiative power loss and plasma performance were oxygen and carbon[40, 162, 165]. Helium, which during previous operational phases and before the first boronisation also played a large role in plasma-wall interactions, will be omitted in the calculations, since the above data are collected after treatment of the reactor wall by plasma-chemical deposition of boron. If not stated otherwise, a set of default parameters, modelled to represent a plasma environment as encountered during the feedback experiments, is deliberately chosen and used throughout the different calculations. Magnetic field data and grid point information, i.e. location of separatrix etc. are picked using the standard configuration. Neutral impurities are injected, modelling the exhaust and pumping of the wall, with an energy of 1 eV at a rate of 9×10^{20}/s from r_{LCFS}+7.5 cm, where r_{LCFS} is the radial location of the separatrix in STRAHL, while recombinations are configured to occur at the surface or close to it. The impurity density, as well as the T_e and n_e profile decay length is set to 5 cm outside the separatrix, which mimics profile shapes across magnetic islands. A limiting surface, i.e. the divertor is placed at r_{LCFS}+6.5 cm, whereas the calculation boundary is at +8 cm. Any provided grid-based data, like the experimental Thomson scattering measurements for electron temperatures and densities, are smoothed upon ingest by STRAHL through *cubic spline interpolation* to ensure stability during numerical iteration.
In figure 4.24, the set of kinetic radial profiles n_e and T_e of the first two selected radiation fraction stages f_{rad} = 33% and 66% is shown next to the corresponding STRAHL simulation results of radial, total radiation intensity profiles for carbon and oxygen. The Thomson scattering measurements and

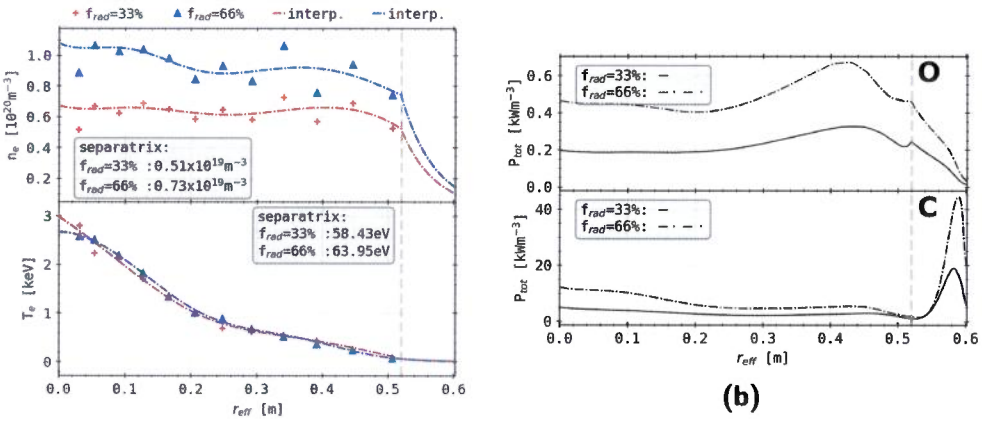

Figure 4.24.: Comparison between *Thomson scattering* data and corresponding STRAHL simulation results for $f_{\mathrm{rad}} = 33\%$ and 66% from experiment XP20181010.32. **(a)**: Thomson scattering electron density and temperature data with individual second order spline interpolated lines (*interp.*), which were used as input for STRAHL simulations. **(b)**: One-dimensional STRAHL simulation results of total carbon impurity radiation intensity.

interpolations on the left are extracted from the results of XP20181010.32 at 0.621 s and 2.22 s, respectively. The position of the separatrix r_{a} is indicated by a dotted, grey line around 0.52 m. In the bottom left and top right of the respective kinetic profile plots, the separatrix temperatures and densities for the individual radiation fractions are noted for comparison. On the right, the top and bottom plots show the total impurity radiation power density profile for oxygen and carbon respectively for the corresponding f_{rad} and input data on the left. They represent the sum of all considered ionization stages integral emissivity per radial bin in STRAHL. For both radiation fraction stages, the radial temperature profiles show little or negligible differences between them. In particular, the separatrix temperature $T_{\mathrm{e,sep}}$ is $\sim$5 eV or 9% higher for double the total radiation power loss. At higher f_{rad} of 2/3rd, a slightly increased temperature is found between 0.05–0.25 m or $\sim 0.1 - -0.5 r_{\mathrm{a}}$ and a decreased $T_{\mathrm{e,core}}$ at the center of the profile. At that location, shown by the innermost data points and their spline interpolation,

the profile for $f_{\mathrm{rad}} = 66\%$ has a shallower slope, indicating a plateau around the center of the plasma. The density plots show a different picture, with a distinct increase in separatrix, median and core electron densities. At the LCFS, $n_{\mathrm{e,sep}}$ grows by $\sim 30\%$ or $2 \times 10^{18}/\mathrm{m}^3$ between the different radiation fractions. For $f_{\mathrm{rad}} = 33\%$, n_{e} remains at or around $6.5 \times 10^{18}/\mathrm{m}^3$, with outliers at up to 5–7.5 $\times\, 10^{18}\, 1/\mathrm{m}^3$, and can be considered plateau-like. At the higher radiation fraction of 2/3rd, the electron density increases towards the plasma center to $1.05 \times 10^{19}/\mathrm{m}^3$, with stronger scattering of data points around the interpolated line. Closer to the separatrix, discrepancies of up to $1.5 \times 10^{18}/\mathrm{m}^3$ can be found. For both plots, the shape of the profiles outside the LCFS, where no data can be collected from the Thomson Scattering diagnostic, is defined by the previously introduced generalization about kinetic decay lengths in the SOL of 5 cm. On the right, the corresponding impurity emissivities for both f_{rad} stages immediately show a strong mismatch in the absolute values and shapes of the radial plots between the two elements. In particular, the radiation power loss through oxygen impurities $P_{\mathrm{tot,O}}$ is $10^1 - 102$ times smaller than the corresponding exhaust through carbon. For both impurities and radiation fraction levels, the general shape of the radial radiation plots are very similar. The emission from the plasma core is consistently higher with $0.65\,\mathrm{kW/m}^3$ than from the SOL for oxygen, while carbon impurity particles irradiate the strongest at $45\,\mathrm{kW/m}^3$ beyond the separatrix. At both radiation fraction levels, $P_{\mathrm{tot,O}}$ has its maximum close to $0.8r_{\mathrm{a}}$ with a plateau or local minimum and small incline towards the center of the plasma to 0.2–$0.45\,\mathrm{kW/m}^3$. Towards and outside the LCFS the radiation level declines rapidly towards 10–$20\,\mathrm{W/m}^3$ at the very edge of the simulation domain. In particular, the absolute levels so far scale linearly with f_{rad}, i.e. a factor of two is directly represented in P_{tot} by both impurities. Due to the intrinsic ansatz for particle transport, the emissivity for oxygen has distinct features at the separatrix that are significantly different from the surrounding profile. However, such characteristics can not be found in carbon, where in fact the global minimum in emissivity is located at the LCFS.

Based on the above observations about the total amount of radiation, the following evaluations will omit oxygen as a factor to the analysis of radial emissivity profiles from impurities under feedback conditions. Hence, figure 4.26 only focuses on the individual ionization stages of carbon and their corresponding fractional abundances, i.e. $f_{\mathrm{A,Z}} = n_{\mathrm{i,Z}}/n_{\mathrm{tot,C}}$, as well as

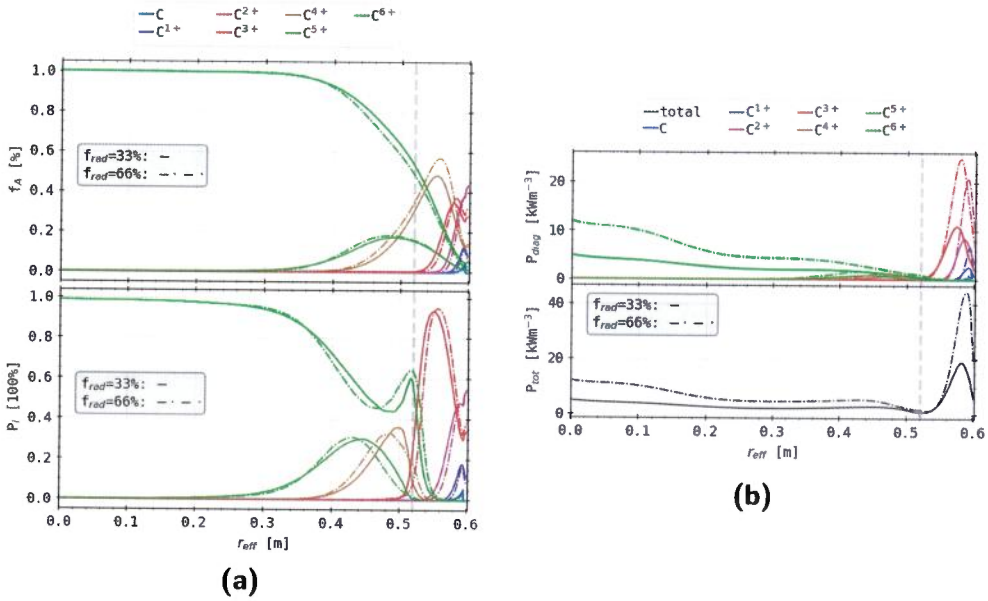

Figure 4.26.: Comparison between STRAHL simulation results for $f_{\mathrm{rad}} = 33\%$ and 66% from experiment XP20181010.32. **(a)**: one-dimensional STRAHL simulation results of carbon impurities for n_{e} and T_{e} on the left. The top shows the fractional abundances of the individual ionisation stages of carbon, while the bottom depicts the corresponding radiation intensities and total power density. **(b)**: Individual and total radiation intensities for carbon, corresponding to the previously shown results in figure 4.24.

radiation power loss contributions. On the left, the relative density (top) and emissivity (bottom) of each carbon ion species across the radius for the previous radiation fractions of 33% and 66% is shown. The presented results correspond to the same kinetic input profiles as before in figure 4.24. Carbon impurity species are exclusively represented by the fully ionized C^{6+} up until $\sim 0.6r_{\mathrm{a}}$, where its fractional abundances decreases and those of the next lower stages, C^{5+} and C^{4+} begin to increase. Their maxima appear around $0.95r_{\mathrm{a}}$ and $1.05r_{\mathrm{a}}$, at just below 20% and 50%, before all decline to zero at the boundary. Outside the separatrix, the lesser ionized particle counts start to increase. Carbon atoms can only be found at the very end of the domain with a sharp cut-off towards the edge and steep decline from

$< 5\%$ inwards. This is due to recombination reactions at the plasma limiting surface, acting as a source of neutral impurities. The remaining C^{3+}, C^{2+} and C^{1+} have their maxima of 35%, 45% and 10% either right at or beyond the divertor, while the impact of the recombination process is easily visible in their individual abundances as a local minimum. The change in f_{rad} has a varying impact on the individual ion abundances. Increasing the radiation fraction leads to a slight reduction of fully ionized C^{6+}, whereas the next two lower stages show a small uplift and shift in their maximum location inwards and outwards for C^{5+} and C^{4+} respectively. The latter is also true for C^{3+}, where the whole profile also moved towards the simulation boundary. In C^{2+}, C^{1+} and atomic carbon, no radial displacement is visible, though their fraction is similarly reduced.
The bottom left figure in figure 4.26 shows the relative radiation power loss fraction of each of the above ionization stages. With respect to the individual line radiation coefficients and kinetic temperature and density profiles, they directly correspond to the previous fractional abundances. Therefore, up until $\sim 0.6r_{\mathrm{a}}$ nearly all of P_{rad} is represented by fully ionized carbon. Beyond $0.7r_{\mathrm{a}}$, C^{6+} emissions greatly decrease to below 50% just before the LCFS, while the power loss from C^{5+} and C^{4+} increase accordingly, with their maxima of 30% and 35% slightly inwards and closer to the separatrix than the prior. Immediately at the edge of the plasma core, the emissivity of fully ionized carbon has an additional local maximum of 60%, while the next two lower stages nearly drop to zero, whereafter the prior quickly vanishes before $1.2r_{\mathrm{a}}$. Simultaneously, emissions from C^{3+} rise rapidly just before the LCFS until they reach >90% of the total radiation power at the very position where the loss from the higher ionized particles are negligible or disappear entirely. After its peak outside the separatrix at $1.1r_{\mathrm{a}}$, P_{3+} decreases to 30% at the divertor. Shape, location and relative height of the remaining two ions and atomic carbon are very similar or identical to their respective fractional abundances. Notable differences are only in the absolute value of P_{2+}, which reaches 55%. Changing the radiation fraction from 1/3rd to 2/3rds and incorporating their corresponding kinetic profiles again has varying impact on the individual ion emission levels. For C^{6+}, the profile is slightly increased and shifted inwards inside the plasma core, while the peak at the separatrix is broadened. The next lower ionization stage shows minor tapering of the emission line shape and shift towards the center, whereas C^{4+} presents the opposite when increasing f_{rad}. All preceding carbon ion

radiation profiles feature minor tapering and radial variation towards the plasma limiting surface, at which again a small contribution from carbon atoms can be found.
The right side of figure 4.26 shows the same data as on the bottom left in terms of absolute levels of radiation, including the individual ion emission profiles for each level of f_{rad} as before, as well as their sum across the radius of the simulation domain. Like before, for $f_{\mathrm{rad}} \sim 1/3$ emissions from C^{6+} of up to $5\,\mathrm{kW/m^3}$ are dominating the radiation composition almost up until the separatrix, with negligible to equalling contributions around $2\,\mathrm{kW/m^3}$ from the next two lower ion stages towards r_{a}. Beyond the LCFS, radiation from C^{3+} and C^{2+} dictate the total emissivity profile shape. Their respective negative square function shaped peaks at 8–$10\,\mathrm{kW/m^3}$ around $1.1r_{\mathrm{a}}$ make up the total emission line maximum in the lower plot. Emissions just in front of the limiting surface from the remaining ions stay below $2\,\mathrm{kW/m^3}$. In total, the sum of the individual particle emissivities yields a radiation level inside the plasma core at or below $5\,\mathrm{kW/m^3}$. The SOL counterpart has the aforementioned peak $\sim$1 cm in front of the divertor at $19\,\mathrm{kW/m^3}$. Like previously examined in figure 4.24, increasing the radiation fraction to 66% is directly proportional reflected in both the absolute radiation level of the individual carbon ions and the total plot below. The core profile, i.e. C^{6+} emissions and the sum respectively, reach $12\,\mathrm{kW/m^3}$ at the center. Changes in the SOL here are a reflection of the aforementioned radial shifts in the fractional abundances and relative emissivities, which yields a more than twofold increase in power to $21\,\mathrm{kW/m^3}$ and $25\,\mathrm{kW/m^3}$ for C^{3+} and C^{2+} between the radiation fractions. The remaining ions and carbon atoms indicate far lower or, to the absolute emission level, negligible variations in both shape and height of their profiles. Accordingly, P_{tot} amounts to $44\,\mathrm{kW/m^3}$ at the peak beyond the separatrix, which is now also closer to the plasma limiting surface.
Continuing the presentation of simulation results for two radiation fraction levels, their corresponding experimental Thomson scattering profiles and constant domain geometry, magnetic configuration and transport coefficients is figure 4.28. Shown here are the radial fluid drift and diffusion coefficient profiles, applied in STRAHL for all calculations equally, on the left and on the right the particle density concentrations c_i of the individual ionization stages and carbon atoms. The anomalous diffusion profile is general and experimentally motivated, as indicated by Wegner et al. and the *Laser Blow-*

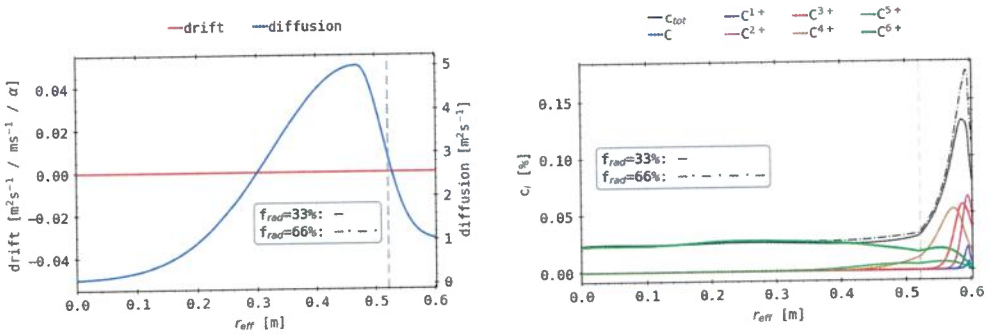

Figure 4.28.: Comparison between input transport profiles and STRAHL simulation results corresponding to the calculations in figure 4.26. They are based off of the same experimental measurements (XP20181010.32) and compare $f_{\mathrm{rad}} = 33\%$ and 66%. **(a)**: radial fluid drift and diffusion profiles, which were used as input for the STRAHL calculations. **(b)**: one-dimensional STRAHL simulation results of carbon impurity concentrations, relative to the total amount of atomic carbon in the simulation domain.

Off system[181]. The convective drift was conveniently kept constant at zero, as it was not well understood and very much subject to current investigation at the time of calculation. Anomalous diffusion is found to be more than two orders of magnitude larger than the neoclassical transport, strongly suggesting dominant turbulent transport[181]. Therefore, the chosen profile indicates a larger diffusivity of carbon impurities in the core towards the separatrix, while their transport outside the LCFS is still greater than at the plasma center. The individual particle concentrations on the right are shown in relative amounts, i.e. their sum equals c_{tot} at any point across the radius and c_i of stage i is in units of $n_{\mathrm{i}}/n_{\mathrm{e}}$. For the given temperature and density profiles, as well as injection and ASD/ADAS rates, the dominant species throughout the simulation domain are C^{6+} with ca. 2.5%. Up until $0.7r_{\mathrm{a}}$ almost only the fully ionized impurity can be found, whose concentration has a plateau up until $0.75r_{\mathrm{a}}$. All other concentrations begin to grow accordingly and peak near to or at the limiting surface between 2% - 7%, while the lower the charge state the sharper and closer to it the maximum can be found. However, c_{6+} decreases steadily, with a small plateau outside

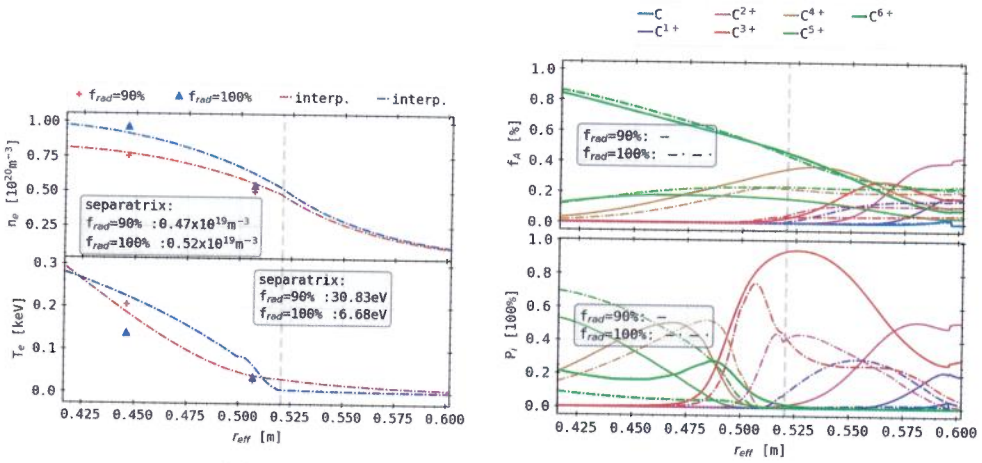

Figure 4.30.: Comparison between *Thomson scattering* data and corresponding STRAHL simulation results for $f_{\text{rad}} = 90\%$ and 100% from experiment XP20181010.32. **(a)**: Thomson scattering electron density and temperature data with individual second order spline interpolated lines (*interp.*). **(b)**: STRAHL simulation results of carbon impurities. The top shows the fractional abundances and the bottom the radiation intensity fractions of the ionisation stages for carbon.

the separatrix, until the domain boundary. The total carbon concentration inside the core is largely defined by C^{6+} and the steady reallocation of carbon impurities at lower temperatures near the LCFS. Beyond, the shape and size of the c_{tot} profile is determined by the peaks of the lower ionization stages close to the divertor, where it rapidly increases towards 13%. Here, the total concentration peak in the SOL increases by ~5% between the two f_{rad} levels, while the rest of its profile remains qualitatively unchanged.
figure 4.30 extends the previously displayed set of radiation fractions, kinetic profiles and accompanying STRAHL simulation results. Here, the data and results for $f_{\text{rad}} = 90\%$ and 100% are presented. In contrast to before in figure 4.26, only the very edges of the plasma core and the SOL are shown by the remaining plots in order to focus on the most relevant areas for the intended investigation of chord brightness characteristics. Again, the left image shows the different experimentally measured electron temperature and

density profiles from the Thomson scattering and their respective spline interpolations. Their corresponding separatrix values are noted as well. When looking back at n_e and T_e for $f_{rad} \sim$ /33% and 66%, significant changes around the separatrix and of the temperature values at the LCFS can be noted, which were at 58 eV and 64 eV before respectively. The separatrix temperature decreases by roughly half when going to 90% and again about 80% when reaching $P_{rad} = P_{ECRH}$ or $f_{rad} = 100\%$. The latter especially shows a much sharper drop towards the LCFS and virtually $T_e = 0$ in the SOL. However, it should be noted that the measurement values closest to the SOL are roughly equal between the two shown profile, though the overall shape allows for the given interpolation. Minor variations in the separatrix electron density of about 10% with increasing power loss here come after a drop from $0.73 \times 10^{19}/m^3$ at a radiation fraction of 66%. Their shape remains largely similar to before.
The right image again shows the individual ion stage fractional abundances and relative radiation power loss contributions. At the top, f_{6+} steadily declines until the separatrix for both radiation fractions. Only outside beyond $1.1r_a$ there is a significant difference, where for $f_{rad} = 100\%$ the relative fully ionized carbon density is higher by $\sim 15\%$, while both level off around the divertor location to 10% and 25% respectively. A similar behaviour can be noted for C^{5+}, which exhibits an even larger change from 5% to 25% at the domain boundary, though f_{5+} has a local maximum closer of to the separatrix on the inside before going into a plateau and declining in the SOL. For $f_{rad} = 90\%$, C^{5+} has its maximum around $0.85r_a$ at 15% after which its fractional abundance decreases across the separatrix and SOL. For the next two lower ionization stages C^{4+} and C^{3+}, a very similar profile shape can be found, with the global maximum of 35% and 27% outside the LCFS and a decline with plateau around 10% and 15% towards the divertor at $f_{rad} = 90\%$. At 100%, the maximum of 23 % and 7% is located at or inside the separatrix and their fractional abundances level off around 20% and 5% afterwards respectively. Qualitatively comparable results are shown by C^{2+} and C^{1+}, for which the profile increases from the LCFS outward and the individual maxima of 45% and 18% can be found directly at the limiting surface.
The relative emissivities of the individual ions on the bottom present very strong differences around the LCFS between the two f_{rad} levels. At 90%, fully ionized carbon emissions decrease towards the SOL, but have a local

maximum around $0.9r_a$ at $\sim 27\%$ after which they quickly drop to zero. For $P_{rad} = P_{ECRH}$ the peak vanishes and P_{6+} steadily falls from 10% to zero before the separatrix. The latter behaviour can be found for both profiles of relative C^{5+} emissions, which continuously decrease from 55% and 70% and disappear before r_a, while at $f_{rad} = 100\%$ the radiation power is about 10-15% higher. The emissivity of C^{4+} has its maximum at $0.85r_a$ with 50% and then quickly drops to zero before $0.95r_a$. Increasing the radiation fraction leads to an outside shift towards the LCFS by $\sim$5 cm at constant peak values and change rates. With focus on the aforementioned local sensitivities towards radiation changes around the separatrix, the most significant variations between the different levels of f_{rad} can be found for C^{3+} and C^{2+}. At 90% both feature their maximum outside the LCFS and have the majority of their emissions take place in the SOL. However, P_{4+} begins to rapidly increase inside the core around $0.9r_a$ before reaching its peak of 93% just beyond r_a and then more steadily decreasing towards 25% at the plasma boundary. Emissions from C^{2+} only begin to increase at the separatrix and have their maximum of 53% around $1.12r_a$, after which they slightly level off towards the divertor. Going to $f_{rad} = 100\%$ causes P_{3+} to significantly shift closer to and around the LCFS. Particularly the smaller maximum of 75% is now in front of the separatrix and much more tapered, while it also already begins to drop before r_a and subsequently finds a small plateau around 25% in front of the limiting surface. Similarly, P_{2+} now starts to increase and has its peak at 45% just inside the plasma core, still featuring the bulk of the relative radiation power loss in the SOL. After a small local minimum at r_a, C^{2+} emissions increase slightly again before steadily decreasing towards the domain boundary. For C^{1+}, $f_{rad} = 90\%$ yields a contribution of 22% at the divertor with continuous decline radially inwards. Going to 100% radiation fraction brings P_{1+} to a maximum of 30% at $1.1r_a$ with a nearly symmetrical profile shape in both directions. The relative emissivity of carbon atoms is negligible for both f_{rad} levels.

Concluding the exploration and evaluation of carbon impurity radiation simulations using STRAHL at various radiation fraction levels and experimentally measured kinetic profiles is figure 4.31. Shown here are the individual and total absolute impurity emissivities close to and outside the separatrix for $f_{rad} = 90\%$ and 100% as before. For convenience, a more detailed description of the respective profiles for C^{6+} through C^{4+} will be omitted, since it has been established multiple times up until this point

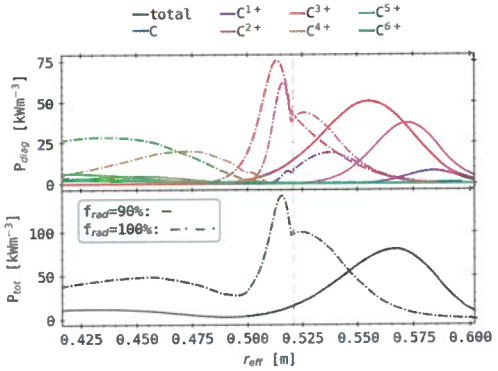

Figure 4.31.: Individual and total radiation intensities for carbon, corresponding to the previously shown one-dimensional STRAHL simulation results in figure 4.30, for $f_{\mathrm{rad}} = 90\%$ and 100%.

that their contribution is largely, if not entirely limited to the plasma core and does not yield particular impact on the local emissivity around the LCFS. Note however that the emission inside the separatrix of P_{3+} and P_{4+} are greatly increased for $f_{\mathrm{rad}} = 100\%$. Emissions from C^{3+}, with a peak of $50\,\mathrm{kW/m^3}$ at $1.15r_{\mathrm{a}}$ and steady slopes, are mostly located in the SOL at a radiation fraction of 90%. They radically shift radially inwards and constitute a much sharper maximum at $0.975r_{\mathrm{a}}$ of $75\,\mathrm{kW/m^3}$. The descending slope towards the outside boundary is defined by an inverse decay of the previously defined constant length of 5 cm. Very similar characteristics are found for C^{2+}, with a slightly lesser maximum of $37\,\mathrm{kW/m^3}$ further outside at $1.2r_{\mathrm{a}}$, and comparable shifts and changes for a higher radiation fraction. However, the descent on the outside is separated by the LCFS into two distinct parts. One is a steady continuation of the trend after the peak, and the second is a remainder from the prior profiles peak and shape, intersected by the separatrix after a shift inwards, which in itself is characterized by the constant decay length again. This is also true for the emissivity of C^{1+} at $f_{\mathrm{rad}} = 100\%$, though its maximum is defined by the SOL profile with $18\,\mathrm{kW/m^3}$ at $1.05r_{\mathrm{a}}$ and the inside peak is nearly unnoticeable. No radiation from carbon atoms can be noted in this plot window.
For all ionization stages large quantitative, and in particular for the lowest four charge states also qualitative changes can be observed when increasing the radiation fraction from 90% to 100%. This is then, most dominantly

by differences in the profiles of C^{3+} and C^{2+}, reflected in the total radiation power density profile in the last plot. At the lower f_{rad}, the sum of emissivities coincides with the SOL emissions of the three first ion stages at $80\,\mathrm{kW/m^3}$ and their symmetrical decay therein. For $P_{\mathrm{rad}} = P_{\mathrm{ECRH}}$, the same structure around the separatrix as for C^{3+} and C^{2+} is found with a peak of $140\,\mathrm{kW/m^3}$ on the inside. The outside shape is similar to that of the second-lowest ion stage, though it is still larger than the prior levels maximum at $100\,\mathrm{kW/m^3}$, while towards the plasma center C^{5+} and C^{6+} dominate with up to $50\,\mathrm{kW/m^3}$ in total.

The STRAHL simulation results for four different sets of experimentally measured kinetic profiles of electron temperature and density at specific radiation fraction levels from discharge XP20181010.32 with constant geometry, magnetic configuration and transport coefficients have thereby been presented. So far, the significance of carbon in this particular case has been underlined, while showing that radiation from oxygen impurities is at least 10^2 times smaller than emissions of the prior. Due to the peaked temperature profile shape and intrinsic transport of convection and diffusion, as indicated by figure 4.28, the most relevant part of the simulation domain towards the LOS radiation sensitivity and chord brightness profiles for feedback scenarios is found to be centred around the separatrix. Furthermore, by comparing the T_{e} and n_{e} profiles next to their corresponding transport and radiation calculation results, the importance of shapes and absolute values in the input data is highlighted. At lower radiation fractions, i.e. 33% and 66%, a more than twofold increase in SOL emissivity is found for increments as small as 6 eV or $\sim$ 10% in separatrix temperature and 43% in density. Results from the second step in f_{rad} support this fact, since for a 10% higher power loss, T_{e} at and beyond the LCFS is greatly reduced. Subsequently, the profiles of f_{A} and P_{diag} are changed drastically both quantitatively and qualitatively. The first set of comparisons is exhibited under nearly unchanged factional abundances, relative emissivities and $\sim$ 5% higher peak carbon concentration directly at the divertor. The population of carbon ions is largely dominated by fully ionized C^{6+} up until the LCFS in any case. At around 0.5 keV and below, lower charge states begin to appear. At even lower temperatures and therefore further outside and into the SOL, the impurity species are rearranged (in-)to the next lower, and finally doubly/singly charged $C^{1/2+}$ or carbon atoms at the limiting surface - due to recombina-

tions and seeding from the divertor. However, those lesser charged carbon ions exist at a significantly higher concentration in the SOL due to the reduced background plasma density and radiate much stronger than C^{6+} in the core. Hence, STRAHL finds the maximum of the one-dimensional radiation distribution for this set of coefficients to be in the SOL for all but one level, $f_{\mathrm{rad}} = 100\%$. With the limited validity of STRAHL simulations beyond closed flux surfaces in mind, only the very last set of results is of relevance towards this particular investigation. Variations in the corresponding T_e profile around the separatrix coincide significantly with the changes in the individual carbon ion emissivity profiles and resulting radiation distribution. This combination of parameters yields the only results relevant for modelling feedback scenarios in STRAHL towards the LOS sensitivity of the bolometer diagnostic. Furthermore, the STRAHL profiles in figure 4.31 are especially interesting for predicting and understanding (controlled) detachment under those circumstances, which ultimately is among the prospects for the real time radiation feedback system.

Given the bad quality of exp. data and the absence of comp. of rad. profile with bolometer data, I would drop this. If the rad. happens in the SOL, the STRAHL 1D assumption is inherently very wrong. If you keep it, I would only use it to show the sensitivity to transport profiles of Prad.

4.4.2. Parameter Variation

The above results have been produced utilizing a deliberate and very limited set of parameters. In order to verify and better understand the provided profiles, variations of said set of coefficients and reiteration of the simulations have to be carried out. Beyond that, a thorough variation also exercises the robustness of the chosen experiment and respective input kinetic profiles towards changes in the parameter space and might highlight features and discrepancies in the established approach.
For sake of comprehension and convenience, the following changes are limited to the transport coefficient profiles D, the kinetic profile decay length λ, the location of the impurity source and the absolute height of the separatrix electron temperature and density, while all other parameters are kept constant, if not stated otherwise. The impact of each individual variation will only be examined for the data collected at $f_{\mathrm{rad}} = 100\%$.

Diffusion Coefficient Variations

Chaning the transport profiles will be conducted in two steps: first, a displacement of the significant peak is examined, after which another set of

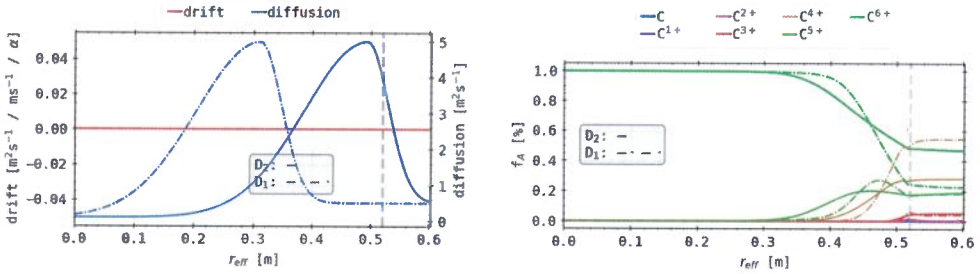

Figure 4.33.: Comparison between two sets of radial transport coefficient profiles and corresponding STRAHL simulation results - the fractional abundance is shown here -, both for $f_{\mathrm{rad}} = 100\%$ from experiment XP20181010.32. **(a)**: normalized drift velocity profile and diffusion coefficient. **(b)**: fractional abundances of carbon from STRAHL simulation results, corresponding to the different profiles on the left.

different absolute height is applied in the simulation.
In figure 4.33, the first two diffusion coefficient D profile variations are shown alongside their corresponding impact on the fractional abundances of the previously described carbon ion species. For now, with respect to the first introduced diffusion coefficients, the new set of profiles are produced by a radial shift either 0.05 m towards (D_2) or 0.15 m away (D_1) from the separatrix, while the respective maximum and peak shape remains the same. The convective drift velocity is unchanged. For D_2, the fractional abundances of carbon impurities on the right feature significantly less steep slopes inside the plasma core. When looking back and comparing with figure 4.30, both sets of diffusion coefficients yield far larger plateaus, spanning nearly the entire SOL. Also, fully ionized carbon C^{6+} remains the dominant species throughout the domain, while for D_1 its abundance f_{6+} drops below 40% and the next lower stage C4+ increases to 55% at the LCSF. All other ion stages show negligible changes outside the separatrix. For D_1, C^{5+} has a much more tapered and slightly larger maximum of 27% at $0.95r_{\mathrm{a}}$.
figure 4.35 shows the corresponding relative emissivities and their respective absolute and total radiation powers of the individual carbon ion stages. From here on, the focus is again on the radial spectrum close to and outside the LCFS. No significant changes for C^{6+} can be noted. The next lower

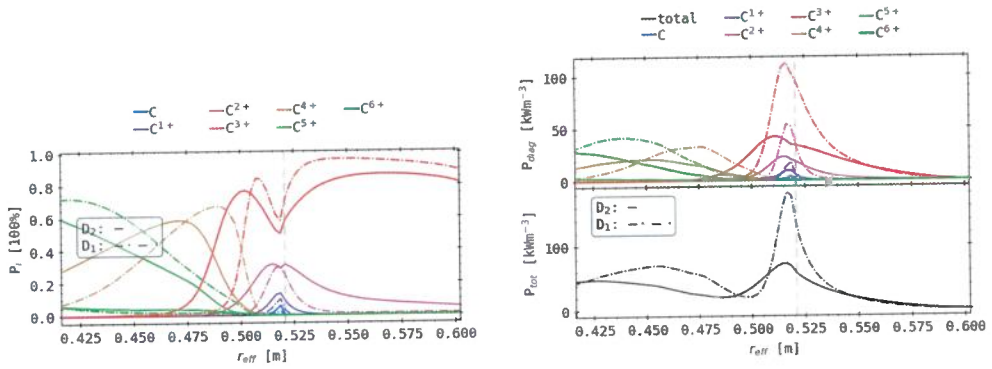

(a) (b)

Figure 4.35.: STRAHL simulation results of relative and total impurity radiation from carbon for the previously presented sets of radial drift and diffusion profiles in figure 4.33 for $f_{\mathrm{rad}} = 100\%$ from experiment XP20181010.32. **(a)**: relative radiation intensity for each individual ionisation stage of carbon. **(b)**: Absolute radiation power and integrated loss for the same ion species.

ionization level features a 5%-7% higher emissivity overall for D_1, whereas C^{4+} shifted radially outward by 0.15 m and increased by 7% at its maximum of 67% in $0.9r_a$. Inside the separatrix, similar changes for C^{3+} are visible, with a shifted and sharper, ~7% higher peak of 85% closer to the LCFS at $0.95r_a$. The overall 5% increase is mimicked in the SOL as well. Comparing with the initial results in figure 4.35, P_{3+} here also has a significant relative emissivity outside for $f_{\mathrm{rad}} = 100\%$ and both diffusion profiles. Its maximum is also higher than before. The remaining impurity emissions of C^2 through atomic carbon are, for D_1 and D_2, centred close to or around the LCFS. Results for C^{2+} and D_2 are very similar to the initially presented profile, though smaller in value, however for D_1 the SOL emissivity is strongly reduced with increasing distance from r_a. The lowest charge state C^{1+} previously had almost no emissions inside and the majority outside the separatrix. Here, for both sets of transport coefficients, P_{1+} is slightly larger and nearly symmetrical around r_a. The same is true for carbon atoms.
On the right, the individual absolute carbon emissivities largely reflect the results on the left, where the relative changes in C^{6+}, C^{5+} and C^{4+} align and both only yield contributions of below $40\,\mathrm{kW/m^3}$ to the plasma core for

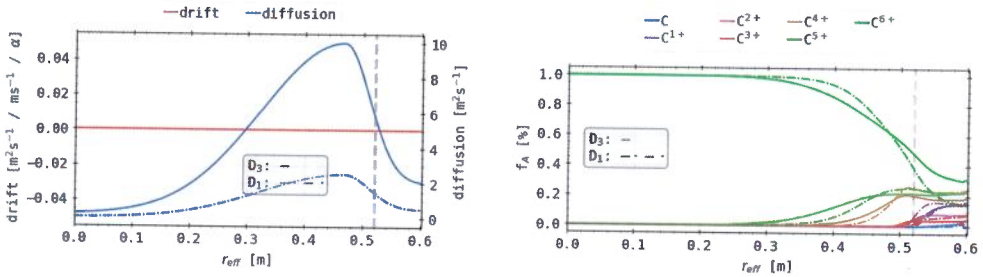

(a) (b)

Figure 4.37.: Comparison between two sets of radial transport coefficient profiles and corresponding STRAHL simulation results - the fractional abundance is shown here -, both for $f_{\mathrm{rad}} = 100\%$ from experiment XP20181010.32. **(a)**: normalized drift velocity profile and diffusion coefficient. **(b)**: fractional abundances of carbon from STRAHL simulation results, corresponding to the different profiles on the left.

every - including the original set - D_{i} profile. The SOL part of C^{3+} radiation is a steady continuation of the pronounced inside profile peak of 110 kW/m^3 for D_1. For D_2, the much lower and broader maximum of 40 kW/m^3 is more akin to the initial result in figure 4.35, where beyond the LCFS the profile is defined by the decay length. This is also the case for both sets of profiles for C^{2+} and C^{1+}, though with decreasing intensity. Hence, D_1 yields a much higher and sharper radiation power loss maximum inside the separatrix with 180 kW/m^3 than D_2, which still produces a similarly peaked profile at 70 kW/m^3. With respect to the first P_{tot}, both plots decrease more quickly in the SOL and have no addition local maxima.
The next set of images contain the second variation of diffusion profiles D, where the absolute value instead of radial location is changed. Here, in figure 4.37, D_3 represents the initially used profile and D_1 a much lower but similarly shaped version of the latter. One should note that D_3 is consistently below zero, indicating a dampened impurity transport around its maximum close to the separatrix. Accordingly, the individual fractional abundances on the right for both sets of transport coefficients from the left indicate minor differences. The relative amount of fully ionized carbon increases for D_3 in the core, while its value at and beyond the LCFS is reduced by up to 50% to 15% at the domain boundary. The f_{A} profiles of the next two

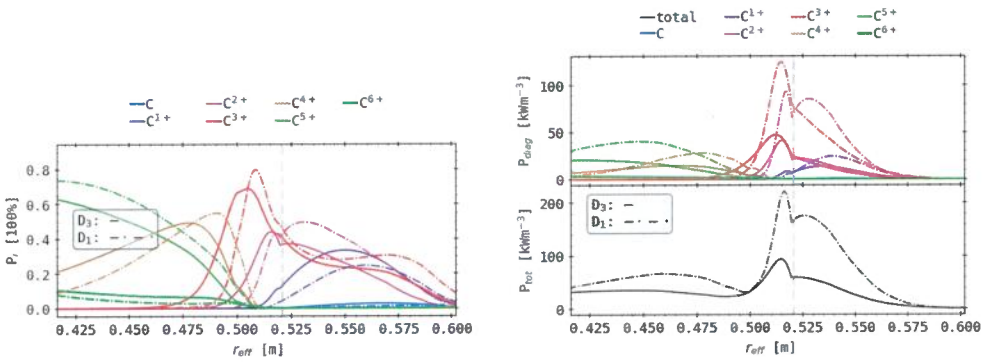

(a) (b)

Figure 4.39.: STRAHL simulation results of relative and total impurity radiation from carbon for the previously presented sets of radial drift and diffusion profiles in figure 4.33 for $f_{\mathrm{rad}} = 100\%$ from experiment XP20181010.32. **(a)**: relative radiation intensity for each individual ionisation stage of carbon. **(b)**: Absolute radiation power and integrated loss for the same ion species.

lower charge states therefore have shifted towards the SOL and increased where f_{6+} is reduced. Both grow steadily from $0.6r_{\mathrm{a}}$ until a maximum before the separatrix, after which they plateau between 18-25%. The remaining ion stages behave similarly, though only featuring significant abundances outside the LCFS with decreasing relative contributions the lower the ionization. Furthermore, for a reduced diffusivity of D_3, C^{3+} and C^{1+} show inverse proportionality in the SOL with increments of 4% and 7% to 9% and 17% respectively. Again, carbon atom numbers increase closer to the divertor, with negligible influence of the different transport coefficient profiles.
The corresponding relative emissivities, as well as absolute impurity ion emissions and total radiation power loss for the above diffusion coefficient profile variation can be found in figure 4.39. On the left, the previously examined impact of changing from the initial transport coefficients D_3 to D_1 is reflected here in a similar way. Radiation from C^{6+} is slightly reduced in front of the separatrix, while the next lower ion stage emissions are increased by 5% in the same spatial range. Again, P_{4+} is shifted towards the LCFS similarly to its fractional abundance profile. However, no emissivity can be found in the SOL despite the plateau in f_{4+}. All other carbon

ions behave accordingly to their respective observed differences in fractional abundance, while their individual emissions decrease with the distance to the domain boundary. Most prominently, C^{3+} features a much sharper and slightly higher maximum of 80% 5 cm closer to separatrix and 2%-10% larger relative emissivity in the SOL.
figure 4.39:**(b)** presents the corresponding total radiation power loss for each individual ionization level at the top and the carbon impurity emissions as a whole on the bottom. Profiles and their changes between the different input coefficients are generally in strong agreement with the noted variations in their fractional abundances. For D_1, C^{5+} and C^{4+} have significantly increased emissions only from the core by up to $30\,\mathrm{kW/m^3}$ to their maximum of $30\text{–}40\,\mathrm{kW/m^3}$. Both of the next two lower ion stage peaks slightly shift towards the LCFS and grow by $50\text{–}70\,\mathrm{kW/m^3}$ to 90 and $125\,\mathrm{kW/m^3}$. Outside the separatrix, C^{3+} decays like before with a constant λ, while C^{2+} has a greatly more intense second local maximum of $80\,\mathrm{kW/m^3}$ at $1.05r_\mathrm{a}$ from which a similar slope follows. Contrary to the relation between the two f_{1+} profiles, P_{1+} is larger for D_1 by $\sim 80\%$. In summary, the variations through increase in C^{5+} and C^{4+} emissions in the core, as well as C^{4+} and C^{3+} close to and beyond the LCFS with their respective shift towards r_a dominate the changes in P_tot on the bottom. Around the separatrix, a more than twofold increase can be noted to up to $215\,\mathrm{kW/m^3}$.
For both parameter variations in the radial diffusivity profile D from figure 4.33 and 4.37, a significant increase in relative density f_a close to and beyond the separatrix for C^{4+} and lower ionization stages can be found. Consequently, this also entail a reduction of C^{5+} and C^{6+} population in those areas. This, due to the respective atomic radiation coefficients and the greatly reduced plasma background electron and ion temperature and density, also leads to similar changes in P_diag and a growth in maximum total radiation power loss inside the LCFS of up to $115\,\mathrm{kW/m^3}$ or 120%. This indicates that a reduction of particle transport in locations of low T_e and therefore ionization regimes greatly dictates the resulting carbon impurity emissions in shape and absolute value.

Electron Profile Decay Length Variation

The second STRAHL input parameter variation is done using different constant SOL decay lengths λ of 5 cm and 2 cm. Primarily, this dictates

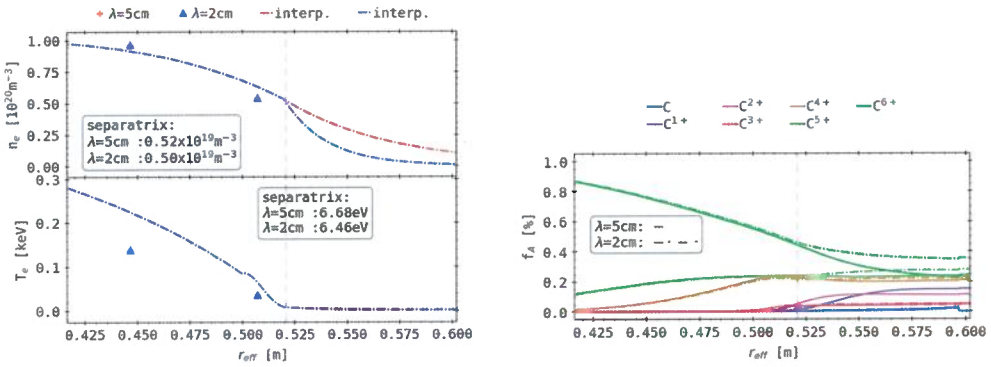

(a) (b)

Figure 4.41.: Comparison between two sets of input electron profiles and corresponding STRAHL simulation results around the separatrix - the fractional abundance is shown here -, both for $f_{\text{rad}} = 100\%$ from experiment XP20181010.32. The decay length of the extrapolated profiles, beyond the last closed flux surface was varied. **(a)**: Electron density and temperature profiles from Thomson scattering measurements as before, where the decay length beyond the LCFS has been altered. **(b)**: fractional abundances of carbon from STRAHL simulation results, corresponding to the different profiles on the left.

the shape and value of the input kinetic profiles for T_e and n_e outside the separatrix through changing the extrapolation methods coefficients. Like pointed out before, λ =5 cm is modelled after the plasma profile decay across a magnetic island inside the SOL, while 2 cm is more akin to the drop over just open field lines. The respective kinetic input profile plots around the LCFS and carbon ion fractional abundances can be found in figure 4.41. On the left, expectedly, the impact of variations in λ is limited to the SOL, where for a decay length of 2 cm n_e drops significantly faster from the separatrix outwards, while only very small changes are visible for T_e. In both cases, the plasma core profiles are unaltered and their values at the LCFS are basically unchanged. The corresponding fractional abundances of carbon impurity ions on the right feature only very small or negligible differences in the core between the two λ. Inside the SOL, the relative C^{6+}, C^{5+} and C^{4+} counts increase by 12%, 5% and 2%, respectively. Accordingly, the populations of C^{3+}, C^{2+} and C^{1+} remain at or decrease to 5% by 6% and 10%. All f_A

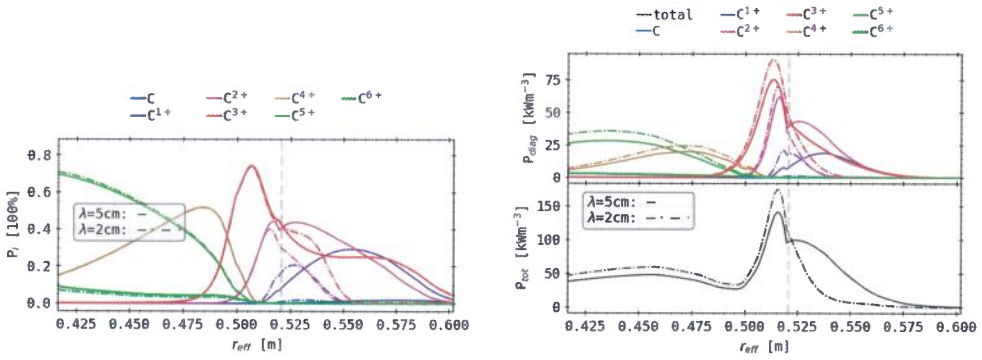

Figure 4.43.: STRAHL simulation results of relative and total impurity radiation from carbon for the previously presented sets of electron density and temperature profiles around the separatrix in figure 4.41 for $f_{\mathrm{rad}} = 100\%$ from experiment XP20181010.32. **(a)**: relative radiation intensity for each individual ionisation stage of carbon. **(b)**: Absolute radiation power and integrated loss for the same ion species.

profiles are relatively continuous or flat outside the separatrix and reach their individual plateau up until $1.1r_{\mathrm{a}}$.
figure 4.43 shows the individual relative emissivities P_{i} on the left and their absolute value P_{diag}, as well as the total sum as the radiation power loss profile P_{tot} on the right like before. Up to $0.9r_{\mathrm{a}}$, there is no noticeable significant difference between the STRAHL results of the two sets of decay length λ. Beyond, at λ =2 cm, C^{1+} is significantly compressed radially with a constant starting point in the core and its maximum slightly reduced to 20% from 30%. Therefore, P_{1+} has its peak very much closer to the LCFS and a larger contribution to the plasma core radiation. In contrast, the factional abundance of C^{2+} shows a minor reduction before and much stronger one at the LCFS. Outside f_{2+} no longer has a second local maximum like before and almost linearly drops to zero with C^{1+}. Lastly, the SOL part of C^{3+} abundance appears strongly contracted towards the separatrix, which leads to an initially shallower drop and a conclusive sharp decline to zero before $1.15r_{\mathrm{a}}$.
The individual absolute carbon ion emissions in the top right reflect the changes examined on the left generally rather well, however their relative

impact here varies between the species. For C^{5+} and C^{4+}, their absolute emissivities are increased drastically when comparing to the variance in their fractional abundances, where they grow by at least $7\,kW/m^3$ in their local maximum. Inside the LCFS, similar differences are presented by C^{3+} and C^{2+}, for which the increments are higher at 10–$30\,kW/m^3$. Here, P_{diag} of C^{1+} has its maximum just in front of the separatrix at $20\,kW/m^3$ instead of in the SOL for $\lambda = 2\,cm$. Beyond r_a, the latter three ionization stages all decrease with a constant decay length equally, before reaching zero around $1.1r_a$. Besides C^{1+}, no radial shifts can be noted. Conclusively, the above variations are very clearly represented in P_{tot} on the bottom. The plasma core radiation increments of 5–$30\,kW/m^3$ are reflected directly, whereas the previously found second maximum in the SOL is lost to the constant decay featured by the three lowest carbon ion charge states above.
Parameter variations in the plasma edge decay length λ, through changes in the SOL part of the kinetic inputs n_e and T_e, greatly impact the shape and height of the outside emissivity profiles. Furthermore, through transport, this indirectly also influences the absolute value of the core portion of said quantities. For large differences in the edge, small qualitative changes to the core part are possible, though no systematic radial shift inside each individual emissivity or the total radiation power can be found.

Radial Impurity Source Variation

In order to further verify the robustness of the presented STRAHL results, the parameter model impurity source S location, which is assumed to be the divertor at r_a+7.5 cm, will be varied. Contrary to before, this directly changes the impurity ion populations instead of the kinetic input plasma background or its extra- or interpolation. Therefore, figure 4.45 only shows the fractional abundances on the left and the corresponding individual absolute emissivities and total impurity radiation on right. The previously presented n_e and T_e profiles for $f_{rad} = 100\%$ in figure 4.30 remain the same in this case. Akin to the changes in f_A profiles in figure 4.41, differences between the individual fractional abundances for two radial source locations are almost exclusive to the SOL. Shifting the carbon impurity source S to the separatrix leads to an increase of relative C^{6+}, C^{5+} and C^{4+} population in the SOL by $\sim 7\%$ at the domain boundary. From the LCFS outward, the respective difference grows with distance until their plateau from $1.1r_a$

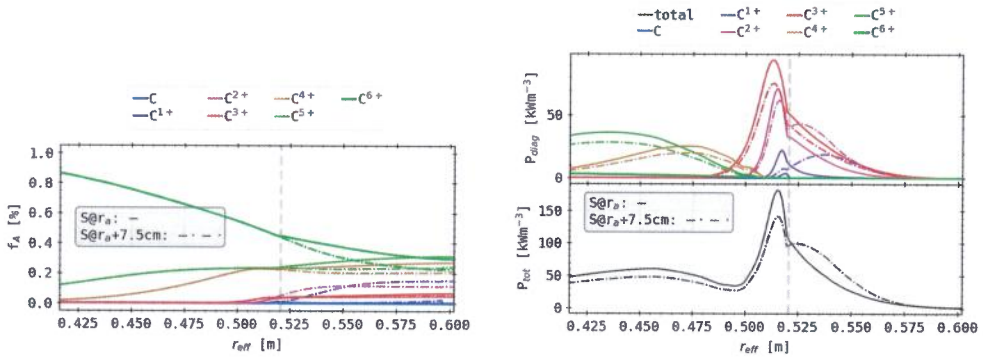

Figure 4.45.: STRAHL simulation results for different radial positions of the carbon impurity source around the separatrix in figure 4.41 for $f_{\mathrm{rad}} = 100\%$ from experiment XP20181010.32. **(a)**: fractional abundance of each individual ionisation stage of carbon. **(b)**: Absolute radiation power and integrated loss for the same ion species.

onward. Concurrently, the fractional abundances of C^{2+} and C^{1+} outside the separatrix decrease much more significantly from 11% and 15% to 4% and 1%. For C^{4+} and C, the variations are very small, with a 1% increase in f_{4+} and a missing step at the divertor in carbon atom population for $S \rightarrow r_{\mathrm{a}}$.

On the right, the absolute radiation levels in P_{diag} and P_{tot} are, besides minor differences in the SOL decay rates, nearly congruent with those shown in figure 4.43. Here, the results for a source located at the LCFS would correspond to a set of STRAHL calculations with λ =2 cm. At the top, the plasma core emissivities for $S \rightarrow r_{\mathrm{a}}$ are equal, within negligible variations in absolute height, to those for λ =2 cm. Outside the separatrix, the profile shape of all three lower ionization stages are defined by a steady decay from their value at the LCFS to zero before $1.15 r_{\mathrm{a}}$. However, in contrast to the above comparison, carbon atom emissions can be found just inside the core of up to 5 kW/m^3. Conclusively, the total impurity radiation below is also a near copy of the results for a reduced SOL decay length, although with a less steep drop outside r_{a}.

Changing the location of the impurity source S and shifting it to the separatrix yields very similar if not equal results in core emissivity as a reduced

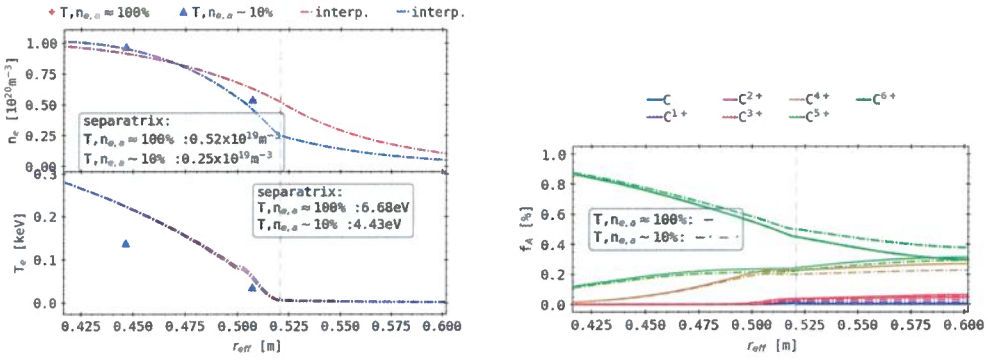

(a) (b)

Figure 4.47.: Comparison between two sets of input electron profiles and corresponding STRAHL simulation results around the separatrix, both for $f_{\mathrm{rad}} = 100\%$ from experiment XP20181010.32. The Thomson scattering measurement of electron density and temperature which is radially closest to the separatrix was rescaled. **(a)**: Electron density and temperature profiles from Thomson scattering measurements. **(b)**: fractional abundances of carbon from STRAHL simulation results, corresponding to the different profiles on the left.

kinetic profile decay length. More so, the corresponding SOL radiation is reduced and additional local maxima are missing. Therefore, no radial displacements of the individual and total carbon impurity emissions are found. The injection of carbon atoms at the LCFS yields a higher population of C^{6+}, as they are fully ionized at higher electron temperatures and densities and transported outward. Coincidentally, lower ion stage counts are greatly decreased or disappear entirely since much less carbon exists at radial locations where the respective reactions rate coefficients have a signal yield.

Seperatrix Electron Profile Variation

Finally, the last parameter variation performed within the scope of this section is a re-scaling of the input electron separatrix temperature and density. The very last input grid point for both quantities is reduced to, in this particular case, only 10% of the original value and the intrinsic STRAHL ingest extra-/interpolation is used to yield continuous profiles to calculate

off of. In order to achieve reasonable gradients in either kinetic input on both sides, the respective numbers at the LCFS are not scaled down directly. The resulting plots can be found, next to their corresponding fractional abundances, in figure 4.47.
At a re-scaled separatrix electron density of 10%, the spline interpolated profile in the top left features a roughly halved absolute value at the location of the LCFS and a shallower decay in the SOL between 2.5×10^{18}–$5 \times 10^{17}\,1/\mathrm{m}^3$. Due to the lower $n_{\mathrm{e,a}}$, and a consequently steeper slope close to the separatrix, the spline fits a slightly higher core electron density towards $0.8r_{\mathrm{a}}$. Only very minor differences in T_{e} profiles between the two scalings can be found, with negligible changes in the core and a slightly smaller local characteristic close to the LCFS. At r_{a}, the electron temperature is reduced by $\sim$1/3 to 4.43 eV, beyond which the SOL characteristics are virtually indistinguishable.
On the right, the fractional abundance of fully ionized C^{6+} increases along the radius for a reduced separatrix electron temperature and density with respect to the initial profile. At r_{a}, f_{6+} is 5% and at the domain boundary 10% higher than before, while the general shape remains the same. Similarly, the relative amounts of C^{5+} and C^{4+} are reduced by 2% and 5% respectively. The same is true for C^{3+} and C^{2+} with a reduction of 1% and 2%. Towards the divertor, f_{1+} increases by a miniscule amount, whereas no change in carbon atom abundance is visible.
The conclusive relative emissivities and absolute radiation powers of the individual carbon ionization stages, as well as the total loss through impurity emissions can be found in figure 4.49. For a scaled down electron temperature and density input profile, the relative emissivities on the left of all impurity ions are shifted inwards by 2–5 cm. The relative height of P_i inside the separatrix for C^{2+}, C^{4+} and C^{5+} are slightly reduced by 2-5%, while those of atomic carbon, C^{2+} and C^{6+} remain the same. However, P_{1+} increases by 4%. Outside the LCFS, all ions besides C^{1+}, which rose by 4%, are significantly decreased by at least 15%.
On the right, the previously observed shift and reduction in intensity inside the separatrix is now true for all ionization stages. A relative shift of 2–5 cm and varying decrease in absolute peak value can be found, where C^{3+}, C^{2+} and C^{1+} feature the largest changes of $25\,\mathrm{kW/m^3}$, $20\,\mathrm{kW/m^3}$ and $3\,\mathrm{kW/m^3}$. The further inward profiles for C^{6+}, C^{5+} and C^{4+} and that of atomic carbon show smaller, negligible changes in their height. Outside the

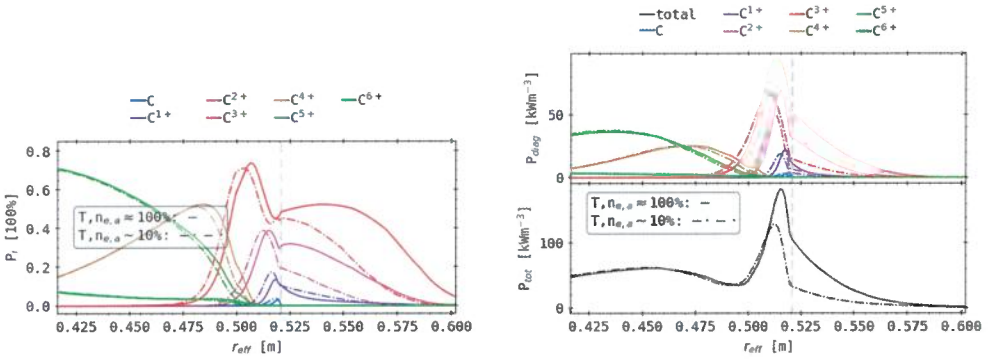

Figure 4.49.: STRAHL simulation results of relative and total impurity radiation from carbon for the previously presented sets of electron density and temperature profiles in figure 4.47 for $f_{\mathrm{rad}} = 100\%$ from experiment XP20181010.32. **(a)**: relative radiation intensity for each individual ionisation stage of carbon. **(b)**: Absolute radiation power and integrated loss for the same ion species.

LCFS, the emissivity all contributing species is reduced by an increasing amount the higher the respective value at r_{a}, i.e. C^{3+} drops by $35\,\mathrm{kW/m^3}$ and C^{2+} by $22\,\mathrm{kW/m^3}$, while their profile shape remains very similar. This observation is directly reflected in the bottom total radiation power from carbon impurities for a lower separatrix electron temperatures and density of $\sim$10%. Its peak close the LCFS is moved 5 cm inwards and reduced by $25\,\mathrm{kW/m^3}$, while the corresponding SOL decay is equally decreased.
Rescaling and thereby decreasing the input electron temperature and density close to the LCFS leads to a significant reduction of total impurity emissions inside and outside the separatrix, as well as a minor inward shift of the individual and therefore cumulated carbon radiation power. The observed changes between the scaling in the fractional abundances can be attributed to the corresponding reaction coefficients of the individual ionization stages, i.e. fully ionized carbon is transported further out due to the significantly lower electron density and therefore collision and recombination rate. Furthermore, at the given kinetic inputs and for constant transport coefficients, dictated by the atomic spectral rates, both the total and individual maximum carbon impurity emissivities are displaced towards the plasma center.

Most prominently, C^{3+} and C^{4+} experience the largest reduction and shift before and outside the separatrix, while also contributing the strongest to the aforementioned maximum. Coincidentally, the core emissions only exhibit negligible changes. The input and impact of this approach are found to be more akin to the differences between $f_{\mathrm{rad}} = 90\%$ and 100% than the previous parameter variations.

This concludes the STRAHL input parameter and profile variations. With respect to the initially posed objective, only changes in transport coefficients and kinetic profiles around the separatrix yield relevant results towards the shape and value of the emission profile on the inside and close to the LCFS. Both a reduction in absolute diffusivity and in electron density and temperature close to r_{a} impact the impurity radiation in such a way that underlines and supports the findings in section 4.4, in which the profiles peak shifts inwards, indicating a certain level of detachment. These approaches also reflect the experimentally measured changes between the previously exercised radiation fraction stages, where n_{e} and T_{e} are gradually decreasing with increasing f_{rad} and an accompanying reduction of transport in that area.

keep this subsection. This is the relevant conclusion section of the above. –

4.4.3. Impact on Chord Brightness Profile

The final step of evaluating the one-dimensional impurity transport simulation results from STRAHL is calculating the corresponding chord brightness profiles using the bolometer diagnostics local sensitivities provided through equation (2.26), 2.27 and figure 2.22. In order to find the two-dimensional radiation distribution $\hat{g}$ for any given STRAHL profile one takes advantage of the poloidal (ϑ) invariance of the results and therefore extends the emissivity along the angular spectrum by 2π, thus yielding $\hat{g}\,(r, \vartheta)$. Given the camera geometry matrix $\mathbf{T}\,(r, \vartheta)$, the radiation power loss as measured by the bolometer $\vec{b}$ becomes

$$\begin{aligned} \hat{g}_{\mathrm{sim}} &:= \hat{g}_{\mathrm{sim}}\,(r, \vartheta) \equiv \hat{g}_{\mathrm{sim}}\,(r) \;\Rightarrow\; \vec{x}_{\mathrm{sim}}\,, \\ \text{chord brightness:} \qquad & \mathbf{T}\vec{x}_{\mathrm{sim}} = \vec{b}_{\mathrm{sim}} \quad . \end{aligned} \tag{4.19}$$

A comparison of the results produced by equation (4.19), using the horizontal bolometer camera geometry, for the previously employed radiation fraction stages and their corresponding experimentally measured and modelled after profiles can be found in figure 4.51. This particular camera is

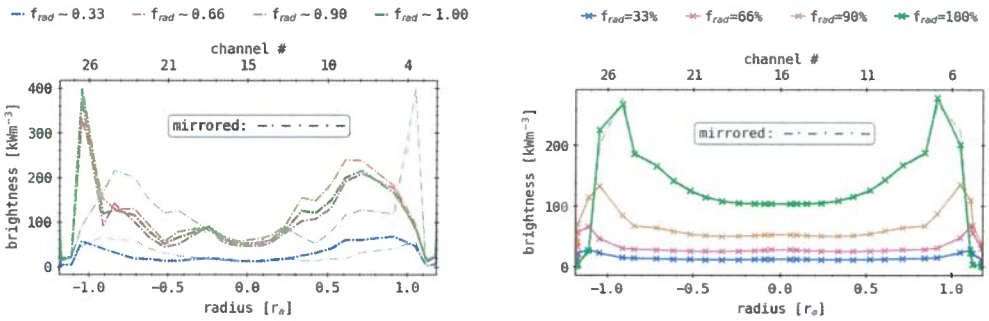

(a) **(b)**

Figure 4.51.: Forward integrated chord brightness profiles for the HBC at different f_{rad} for **(a)** from experiment XP20181010.32 and **(b)** STRAHL simulation results of total carbon impurity radiation distributions from previously presented electron density and temperature profiles in figure 4.26 and figure 4.30 of XP20181010.32.

chosen because it provides a full and even coverage of the triangular plane. The results for the HBC on the left are found for the same electron temperature and density profiles as the STRAHL calculations on the right are performed with, i.e. of experiment XP20181010.32 and at different radiation fractions. The underlying simulation results correspond to the initially calculated profiles without input parameter variations. In both images, reflections of the opposite side profiles - mirrored at $r = 0$ - are superimposed semi-transparently with a dash-dotted line in order to find any asymmetries more easily. On the left, the HBC finds a relatively flat brightness inside the separatrix at $f_{\mathrm{rad}} = 0.33$, i.e. between $-r_{\mathrm{a}}$ and r_{a}, with lower emissivity in the plasma center of $10\,\mathrm{kW/m^3}$ and higher towards and at the separatrix of $80\,\mathrm{kW/m^3}$. Beyond the LCFS the brightness quickly falls to zero on both ends of the radial spectrum, while the transparent line clearly shows a slightly higher and more prominent emission from the positive side of the profile. For $f_{\mathrm{rad}} = 0.66$, 0.9 and 1.0, the chord brightness is very similar, with minor differences between the fraction levels. The local maximum of 200–$220\,\mathrm{kW/m^3}$ on the right is distinctly inside the separatrix and is the largest and furthest inside around $0.7r_{\mathrm{a}}$ at 0.9. Its shape is hollow, with an emissivity of only 60–$80\,\mathrm{kW/m^3}$ and the global maximum just outside at $-1.05r_{\mathrm{a}}$ of 340–$400\,\mathrm{kW/m^3}$. The mirrored lines make the discrepancies

between left and right half of the profile even more obvious, with large differences in respective radial position and absolute height in each radiation fraction level. On the left, this peaks location, as produced by the HBC geometry, corresponds to the inboard portion of the separatrix and its lower side and midplane magnetic islands. The right side of the profile is linked to the outboard side and tip of the triangular plane with its two SOL islands. The image on the right shows the STRAHL results, created using the same camera geometry as on the left and equation (4.19). Chord brightness profiles of the same order of magnitude can be found, however with a much more clear separation between the individual f_{rad} stages and higher level of symmetry. For a radiation fraction of 33%, a similar emissivity in the core and up to $\pm r_{\mathrm{a}}$ as on the left, though with a SOL located and less pronounced peak of $30\,\mathrm{kW/m^3}$ is presented. The profiles mirror reflection is congruent with the original on both sides. At $f_{\mathrm{rad}} = 66\%$, the location of the local maxima and the profiles symmetric shape remain the same, though with a generally increased intensity of 40–$75\,\mathrm{kW/m^3}$. Going to 90% leads to a shift of the two maxima towards $\pm r_{\mathrm{a}}$, however still outside in the SOL, with an overall growth in emissivity to $60\,\mathrm{kW/m^3}$ in the core and $140\,\mathrm{kW/m^3}$ at the peaks. Negligible variations between the left and right reflection of the profile can be found around the separatrix. For a radiation fraction of 100%, both local maxima are now located inside the LCFS and decrease sharply beyond $\pm r_{\mathrm{a}}$ to 0 before the beginning and end of the LOS radial spectrum. The chord brightness increases to 275–$280\,\mathrm{kW/m^3}$ in $\pm 0.92 r_{\mathrm{a}}$ and $105\,\mathrm{kW/m^3}$ in the plasma core. The discrepancy in peak is also reflected by the misalignment of the mirrored profile on both sides, where the right is slightly higher and decreases quicker than the left. Since the underlying impurity emission distribution calculated by STRAHL and extended in poloidal space is intrinsically symmetric, this can only be explained by minor differences in the LOS geometry of the upper and lower half of the HBC camera.

Next, in order to further evaluate the impact of the STRAHL input parameter variations, a comparison between the impact of the separatrix n_{e} and T_{e} reduction and transport coefficient profile changes is presented in figure 4.53. The results are achieved in the same way as before, using equation (4.19) and the horizontal bolometer camera geometry.

On the left, the plot for T, $n_{\mathrm{e,a}} \approx 100\%$ is the same as the previously shown chord brightness at $f_{\mathrm{rad}} = 100\%$, while the lower profile of a reduced sep-

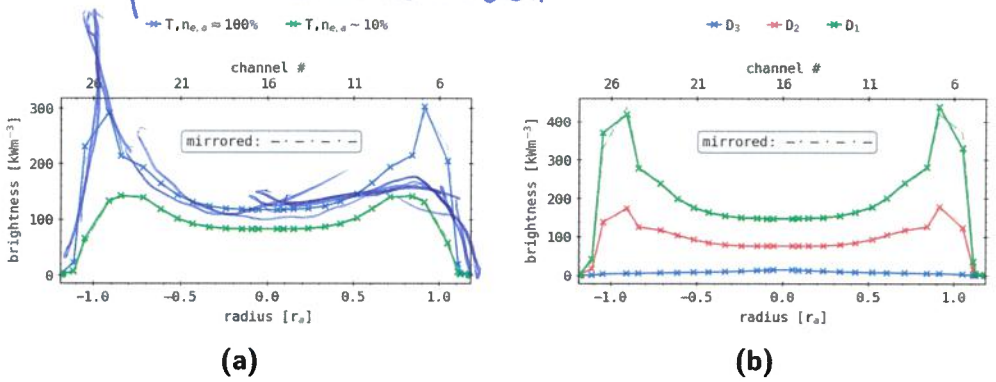

Figure 4.53.: Forward integrated chord brightness profiles for the HBC from STRAHL simulation results of total carbon radiation distributions for **(a)** different electron density and temperature profiles **(b)** varying transport coefficient profiles from figure 4.33 and figure 4.37, based on data from experiment XP20181010.32 at $f_{\text{rad}} \approx 100\%$.

aratrix temperature and density corresponds to the results in figure 4.49. The latters reduced total radiation power is underlined by a 40 kW/m^3 lower plasma core emissivity and a roughly halved peak intensity of 150 kW/m^3 on both sides. However, their maxima location is now further inward around $0.8r_a$ and the decay towards the boundary consequently shallower. On the right, the chord brightness profile of diffusion coefficient profile D_1 is akin to the initial results in figure 4.51 at $f_{\text{rad}} = 100\%$, while D_2 and D_3 are calculated using the emissivities in figure 4.35 and 4.39. For D_2, the overall emissivity is reduced to 80 kW/m^3 in the core and 180 kW/m^3 at the edges, which corresponds to a 50-130% decrease. The location of the local maxima is unchanged and remains inside the LCFS. With a transport coefficient profile of D_3, the chord brightness as measured by the HBC is greatly reduced to a peaked profile of 20 kW/m^3 in the plasma center and linear decay to the SOL. No addition peaks or local features can be found here.
Finalizing the forward modelling of the STRAHL results and their parameter variation using the bolometer camera geometry is figure 4.55. Both images show the same approach, where the individual carbon impurity ion emissivities are used with equation (4.19) to find their respective chord brightnesses and split them each into a SOL and plasma core portion, i.e. how much of the radiation in P_{chord} is located outside or inside the separatrix.

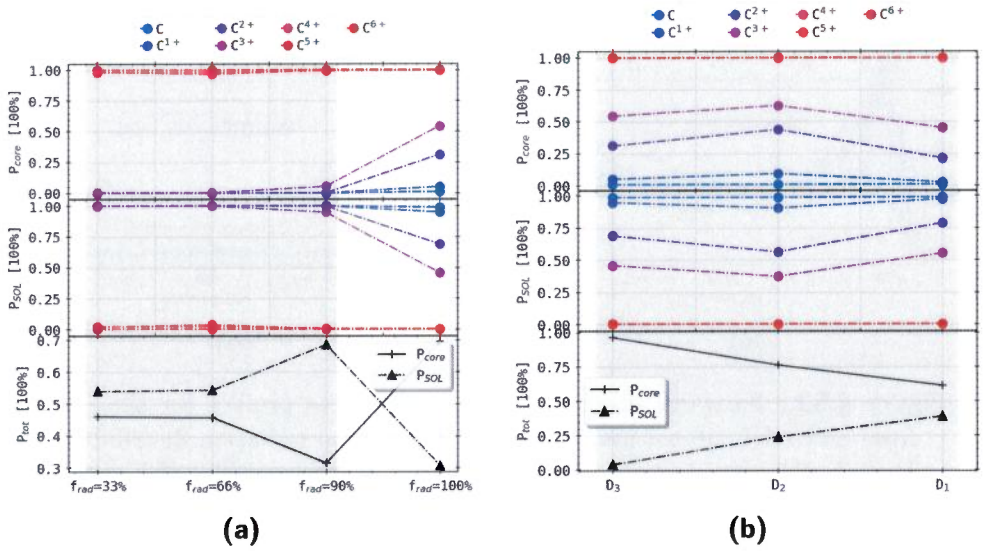

Figure 4.55.: Individual and total radiation power loss from carbon impurities, separated into core and SOL parts, for **(a)** different levels of f_{rad}, which are modelled from electron temperature and density profiles of experiment XP20181010.32, and **(b)** $f_{\mathrm{rad}} \sim 100\%$ with similar underlying profiles but varying transport coefficients - they are the same as in figure 4.33 and figure 4.37.

Because the conservation of volumes along magnetic field lines is no longer valid outside the separatrix, a simple geometric approach for calculating the impurity emissions can not be used. An experimentally motivated method that also can be used for measured data will be introduced. Let us assume that the LOS cone of channel j has a volume of $V_{\mathrm{j}}^{\mathrm{core}}$ in the core and $V_{\mathrm{j}}^{\mathrm{SOL}}$ in the SOL - for example, the outermost HBC channels have no plasma core volume. The respective total powers for camera C, i.e. the horizontal bolometer camera, become

$$P_{\mathrm{core}} = \frac{V_{\mathrm{P,tor}}}{\sum_{j}^{C} V_{\mathrm{j}}^{\mathrm{core}}} P_{\mathrm{rad,C}} \ , \quad P_{\mathrm{SOL}} = \frac{V_{\mathrm{P,tor}}}{\sum_{j}^{C} V_{\mathrm{j}}^{\mathrm{SOL}}} P_{\mathrm{rad,C}} \ . \tag{4.20}$$

Both of the above, P_{core} and P_{SOL} are toroidal extrapolations from the bolometer plane, which implicitly assumes a constant distribution of radiation in the machine. However, this was already true for the initially posed

equation (2.25) for P_{rad}, which has generally proven to be valid in most scenarios[181, 182], particularly with a stronger irradiating plasma core.
The left of figure 4.55 shows the radiation distribution as calculated using equation (2.25) and equation (4.20) for the initial STRAHL simulation results at $f_{\mathrm{rad}} = 33\%$, 66%, 90% and 100%. A grey background is added to underline the distinction between core and SOL emission majority. The figure is split into the core (top), SOL (center) and relative (bottom) radiation parts, where the latter only features the total power of the prior two. On the top and in the center, the individual carbon ion emissivities are split into their relative core and SOL portion. One can immediately note that C^{6+} through C^{4+} emissions are entirely, besides a small deviation at $f_{\mathrm{rad}} = 66\%$, represented in the plasma center. The same is true for C^{3+} through C^{1+} and outside the separatrix until a radiation fraction of 66%. Beyond, P_{SOL} of atomic carbon and C^{1+} remains above 95%, while that of C^{3+} and C^{2+} drop to 70% and 45% at $f_{\mathrm{rad}} = 100\%$. Consequently, P_{core} presents nearly no change for the prior and an increase in the latter two to 30% and 55% respectively. At the bottom, the relative integrated impurity radiation from the core and SOL are shown for the same f_{rad} as above. Using the same approach as equation (4.20) and two prior plots with P_{tot} instead of the individual ion emissivities, this plot shows a distinct turnover between plasma core SOL emission from 90% to 100% radiation fraction.initially, P_{core} to P_{SOL} are distributed 54%-46% until $f_{\mathrm{rad}} = 66\%$. Beyond that, the bolometer measured radiation power loss from the core increases to 68%, while the SOL part drops to 32% accordingly. At 100% radiation fraction, this ratio is now inverted and $P_{\mathrm{core}} = 0.7$, $P_{\mathrm{SOL}} = 0.3$.
The plot on the right of figure 4.55 shows the same type of results, i.e. the core and SOL portion of the individual carbon impurity ion emissions and their cumulative total radiation power loss over the different transport coefficient profiles that have been discussed in the previous sections. For all of D_3 through D_1, where D_3 is equal to the diffusion parameter used on the left, C^{6+}, C^{5+} and C^{4+} exclusively feature radiation from the core and atomic carbon from the SOL. The next two lower ionization stages C^{3+} and C^{2+} have a P_{core} between 45%-60% and 20%-45%, while their respective plasma emissions are highest for D_2 lowest for D_1. Their P_{SOL} is presented accordingly, satisfying $P_{\mathrm{core}} + P_{\mathrm{SOL}} = 100\%$. Lastly, C^{1+} shows only 2%-10% of its emissions in the core similarly as the next higher charge states. The relative integrated P_{tot} at the bottom presents a near linearly declining core

radiation and hence increasing relative SOL emissivity. At D_3, the result from the left set of plots is mirrored, from which e.g. P_{SOL} grows to 25% for D_2 and 40% at D_1. The core radiation decreases from 100% to 75% and conclusively 60% respectively.

The comparison between experimental and STRAHL chord brightness profiles in figure 4.51 shows acceptable agreement in absolute intensity at low to high f_{rad}. However, the stark contrast between the highest radiation fraction emissivities, especially at the center of the plasma indicates inaccuracies in the evaluation of STRAHL profiles using the bolometer geometry for this purpose. A homogenous, poloidal distribution of radiation power, which was assumed for the forward STRAHL calculations, does not apply to the experimental case. The relation between the highest three emission levels in the bolometers' chord brightness profiles, which are all within their respective error margins across the radius, is not supported by the simulation. Furthermore, those experimentally measured lines feature a strong asymmetry, which also can be found for the simulated data, although to a much smaller degree. The high-side inboard located local maximum inside the separatrix though supports the STRAHL results at $f_{\mathrm{rad}} = 100\%$ and their shifted peaks inward of r_{a}.
Incorporating the previous separatrix temperature and density and transport coefficient parameter variations with this approach achieves figure 4.53. The individual diffusivities show quantitative, though insignificant qualitative differences besides D_3, which yields negligible emissivities overall. A decrease in impurity transport inside the core and close to the separatrix alone does not produce the necessary detachment of plasma radiation from the divertor to inside the LCFS. Reducing the electron profiles n_{e} and T_{e} at the separatrix and consequently inside the SOL on the other hand produces a smaller, though noticeably further inward shifted chord brightness at $f_{\mathrm{rad}} = 100\%$. Most prominently, a strongly reduced $T_{\mathrm{e,a}}$ corresponds to a reduced ionization of carbon and a shift in fractional abundances towards lower charge states at that location, which in turn yield a higher emissivity at that temperature.
Lastly, the results in figure 4.55 further reinforce the latter results and again underline the qualitative shift in relative radiation distribution between the core and SOL. In addition, this alleviates the intrinsic inaccuracy in STRAHL for emissions outside closed flux surfaces, since the majority of

P_{rad} now comes from inside at $f_{\mathrm{rad}} = 100\%$ and more so for lowered n_{e} and T_{e} at the separatrix. In turn, this therefore strongly supports the initially posed hypotheses, that at very high radiation fractions in feedback scenarios, plasma radiation detachment was observed by the bolometer and that carbon impurities played a major role. All the above has also reiterated the importance of LOS channels close to and around the separatrix. They especially measure the relevant maxima and shifts, which again provide an important tool to accurately qualitatively and quantitatively assess emissivities. Conclusively, this also expands the so far acquired understanding of feedback radiation scenarios and the local LOS sensitivities towards such plasma.

4.5. Conclusions

This chapter was introduced with a set of three questions regarding the activation of the thermal gas feedback, the real time bolometer system, its LOS geometry and the underlying plasma parameters. This also included a model evaluation for the injection of gas into the SOL and its transport to the plasma and walls. Finally, the one-dimensional impurity transport and radiation code STRAHL was employed to verify and further explore the behaviour of oxygen and carbon emissivities for various parameter combinations, using experimentally measured data and motivated coefficients as input.
A thorough evaluation of a very large number of thermal gas feedback experiments revealed no particular correlation between the activation of the valves and impact on central plasma parameters, especially the radiation power loss. In general, the impact of the feedback gas injections follow the established steady state scaling laws with respect to the underlying plasma profiles, while no significant difference to the effects of the main inlet could be established with this methodology. However, it was found that a moderately scaled, i.e. of medium length and intensity, gas injection is best suited to achieve radiative cooling of the SOL. Rudimentary models proposing a two and three chamber system for such impurity injections from the SOL or plasma core presented all the capability to reproduce experimentally observed radiation profiles of a two-stage feedback injection. With respect to its simplistic approach, those models have provided plausible results that

find a strong correlation between the injected impurities in the SOL and the target plasma emission. The parameter space exploration of said two and three chamber models has also given insight into the relation of, therefore likely, impurity transport and radiation across the separatrix.
Calculation and comparisons of the LOS selection prediction quality, using a variety of measurements metrics, selection sizes and the previously issued large number of feedback experiments as input data have been performed in this chapter. The many, functionally very different metrics have provided results that point to a higher local sensitivity towards feedback scenarios for channels that view around or at the separatrix, especially in the horizontal bolometer camera. Such lines-of-sight also might focus at the inboard and/or lower side magnetic islands and X-points. Introducing the collected underlying central plasma parameters to the selection variation space of the weighted deviation metric results only finds experimental contributions for significantly higher or lower prediction qualities than 0.5 a. u. Also, higher heating powers and radiation losses, thus also explicitly larger radiation fractions, correspond to increased predictabilities. Conclusively, the same is true for higher electron temperatures and densities. For all the above, both bolometer camera datasets are generally in good agreement, supporting the individual results and conclusions.
Finally, the one-dimensional impurity radiation and transport simulation code *STRAHL* was employed to model plasma profiles and transport coefficients that yield a significant contribution to local emissivities inside and around the separatrix that correlate to the previous findings of LOS prediction qualities. Electron density and temperature data from the prime bolometer feedback experiment XP20181010.32 at four distinctly different levels of radiation fraction, i.e. 1/3-1/1 and experimentally motivated transport coefficients, as well as results from *ADAS* were used as input for calculation. Initially, oxygen and carbon were considered, where it was found that the latters total radiation emission is insignificant already at very low f_{rad}. The base model simulation featured a large shift of impurity emissions - from outside the SOL - towards the plasma center when going to very high radiation fractions, as was measured by the bolometer for the very same profiles and f_{rad}. Extended input parameter variations in STRAHL have revealed that, in this scenario, both a reduction of diffusivity and electron temperature and density around the separatrix provided such results that underlined the experimental findings of the bolometer diagnostic and the findings of the

LOS sensitivity evaluation, where a shift of the maximum emissivity from the SOL to inside r_a and beyond is found. The experimentally measured and STRAHL simulation profiles therefore together suggest some form of plasma (radiation) detachment for $f_{rad} \Rightarrow 1$.
Conclusively, a comparison between horizontal bolometer camera measured and calculated chord brightness profiles was performed. The large asymmetry in the experimental data is not reproduced by the forward model results, where the poloidal extrapolation of the radial STRAHL profile yields only negligible variations due to the minor differences in the underlying HBC LOS geometry. This indicates that there is both a significant inadequacy in the forward modelling approach and a stronger poloidal asymmetry in the actual plasmas' emissivity, i.e. a higher power loss closer to the VBC and lower inboard X-points where the magnetic field lines from the feedback gas valves connect to. The simulated chord brightness provides the desired and experimentally recorded inward shift of the maximum emissivity - though the model does so from outside the separatrix to inside, while the bolometer finds all peaks there - and the corresponding high-side inboard located local maximum inside the separatrix for very high f_{rad}. Incorporating the parameter variations in STRAHL further underlined the previous assessments. Evaluations of the core and SOL radiation distribution from the forward model profiles gave additional credibility to this application of a one-dimensional impurity transport code. The application of STRAHL here thereby supports the initial hypotheses of feedback driven plasma radiation detachment towards very high radiation fractions, while also providing a prominent contributor for such scenarios in carbon impurities. Previously recorded LOS sensitivities are underlined by the latter chord brightness comparisons due to the correspondingly positioned local maxima and shifts in their respective profiles.
Circling back to, at the beginning of this chapter posed questions, one can answer confidently as follows:

1. There exists, given the current state of investigations, no particular correlation or scaling between the thermal feedback gas valves activation and underlying plasma characteristics. No such relation could either be found for the bolometer measured P_{rad} in particular that goes beyond established steady state laws.

2. No explicitly best set of 3, 5 or 7 LOS for finding P_{rad} exists. However, for feedback purposes, an established and robust selection of few vertical or/and horizontal bolometer camera channels can be provided that generally can achieve at least 85% prediction accuracy when compared to the full data set. Such LOS are among those looking at inboard and low-side located X-points and magnetic islands or along the separatrix.

3. Carbon impurity is found to be a significant contributor towards the observed crucial changes in emission distribution for plasma radiation detachment scenarios that are aimed for by the application of the feedback system. Similarly important is the reduction of both separatrix and SOL electron temperature and density.

Nice questions, results on 1. in wrong conclusions
For 2. too much analysis for little conclusions
but good/reliable results
For 3: well done for shitty data, but
results only partly relevant
→ 1 page sufficient